Numerical Modelling of Stirling Cryocoolers

Thomas Rawlings
Department of Space & Climate Physics
University College London

A thesis submitted for the degree of
Doctor of Philosophy

January 2022

Declaration

I, Thomas Rawlings, confirm that the work presented in this thesis is my own. Where information has been derived from other sources, I confirm that this has been indicated in the thesis.

Abstract

A new Stirling cryocooler model has been developed that is able to simulate the interactions between the loss mechanisms in the cold finger of the cooler. This one-dimensional, finite difference model can simulate single and two-stage cryocoolers. The model uses the latest friction factor and heat transfer correlations from the literature and simulates turbulence generation and thermal penetration depths. It runs fast enough to be useful for optimisation, thanks to a robust artificial convergence technique. The model includes a full representation of the cold finger, including the displacer motion and the flow past the displacer.

A two-stage Stirling cooler has been developed, and the model has been validated against measurements of its performance. The model predictions have also been compared to the predictions of a commercially available model and to the measured performance of single-stage Stirling coolers. The model is able to accurately predict a variety of measured values, including pressure swings and cooling powers. The model results show that there are significant interactions between the loss mechanisms of the simulated cryocoolers. The model was also used to investigate changes to the cold finger geometry of a single-stage cooler that would be difficult to simulate using other models; the model predicted that significant performance improvements could be made.

Impact Statement

Stirling cryocoolers are a key enabling technology for a wide range of space applications. They are used extensively in Earth observation satellites to cool infrared detectors [1] and are often an integral part of the cooling chain of large space telescopes [2]. Emerging quantum technologies, such as single photon superconducting nanowire detectors for laser ranging and quantum key distribution, will require cooling that could be provided by Stirling cryocoolers [3]. The development of Stirling cryocoolers for these space applications is greatly aided by computer modelling. By simulating the performance of potential designs, the design can be optimised to target attributes such as low mass and high thermodynamic efficiency without requiring a lengthy prototyping process.

Many of the Stirling models in the literature use a modular approach to represent the system components [4][5]. Each different flow region is contained within a separate module. This has the advantage of making the models flexible but can make it more difficult to simulate complex interactions between the modules. The model developed as part of this project takes a different approach. It simulates the cold finger of the cooler as a single system. This allows it to realistically simulate heat transfer between the different flow paths and account for the motion of the displacer.

Analysing the results of the new model showed that there was a great deal of interaction between the loss mechanisms that would not be simulated by a model that considered each flow path separately. This new model should provide a more accurate assessment of the interactions between the loss mechanisms in a cooler and hence give a more accurate prediction of the performance.

The new model was also used to simulate changes to cooler geometry that could only be investigated by simulating the cold finger of the cooler as a single system. It was found that some of these geometry adjustments had a significant effect on the predicted cooling power. The performance of Stirling

coolers could be improved by using the model to find the optimum values of these geometry adjustments.

This thesis describes the operation of the new model in detail and should enable other researchers to incorporate the techniques used by this model into their own work. Hopefully, this will result in lighter and more efficient Stirling cryocoolers that are better suited to the active cooling requirements of spacecraft.

Acknowledgements

I am extremely grateful to my supervisors, Prof. Ian Hepburn and Dr. Jo Bartlett for their support and advice throughout this project.

I would also like to thank the staff of the Cryogenics and Magnetics group at the Rutherford Appleton Laboratory. In particular, Dr. Martin Crook and Dr. Matthew Hills, who provided invaluable feedback when I was developing and validating my model, and Mr. Sam Chung and Mr. Chris Pulker, who assisted me with the design and assembly of the two-stage cryocooler.

Finally, I would like to thank my wife, Emma, for her support throughout this project.

This work has been funded in part by the European Research Council under the European Union's Horizon 2020 research and innovation programme (grant agreement: IRIS, no. 648604).

Contents

1 Introduction **27**

2 Background **30**

2.1 Cryocooler Applications 30
2.2 Types of Cryocooler 31
2.3 Stirling Cryocoolers Developed at RAL 42
2.4 Stirling Machine Models 47

3 Model Development **56**

3.1 Model Scope 56
3.2 Modelling Approach 58
3.3 Model Discretisation 61
3.4 Solution Variables 65
3.5 Differential Equations 70
3.6 Cell Correlations 79
3.7 Heat Transfer to Moving Cells 99
3.8 Radiation Loads on the Cold Finger Tube 100
3.9 Wall Surface Temperature Fluctuations 102
3.10 Interpolation of Gas Properties 108
3.11 Differential Equation Solver 119
3.12 Initial State 123
3.13 Convergence Acceleration 124
3.14 Non-Interacting Losses 136
3.15 Model Outputs 138

4 Breadboard Cooler Development **141**

4.1 Breadboard Cooler Requirements 141
4.2 Breadboard Cooler Design 142
4.3 Breadboard Cooler Operation 151

5 Model Validation **152**
5.1 Validation Against the Small Scale Cooler 152
5.2 Validation Against the CryoBlue Cooler 173
5.3 Validation Against the Breadboard Cooler 181
5.4 Clearance Seal Measurements 196
5.5 Summary of the Model Validation 200

6 Model Applications **205**
6.1 Appendix Gap Geometry 205
6.2 Cold Tip and Regenerator Overlap 209
6.3 Cold Head Body and Regenerator Overlap 213
6.4 Summary of Geometry Modifications 216

7 Conclusion **217**
7.1 Summary of Work Done 217
7.2 Key Findings 220
7.3 Suggestions for Future Work 222

A Model Details **223**
A.1 Alternative Cooler Configurations 223
A.2 Cold Finger Geometry Definition 228
A.3 Model Input and Output Files 230

B Material Properties **238**
B.1 Gas Properties 238
B.2 Solid Properties 239

References **244**

List of Figures

2.1 A diagram showing the idealised stages of a Stirling cryocooler's thermodynamic cycle. 33
2.2 A plot of pressure against the total gas volume for the ideal Stirling cycle. 34
2.3 Diagrams showing two common Stirling cooler configurations. . . 36
2.4 A diagram showing the cold head of a two-stage Stirling cryocooler. 38
2.5 A diagram showing a section view of a typical single-stage RAL Stirling cryocooler. 43
2.6 A photograph showing one of the compressor motors of the RAL Maxi compressor. 44
2.7 A photograph of the RAL Small Scale Cooler. 46
2.8 A photograph of the RAL Maxi compressor attached to a cold head. 46

3.1 A flowchart showing the main steps of the model. 60
3.2 A diagram showing the relationship between the cells and nodes in the model. 62
3.3 A diagram showing the connections between cells when simulating a two-stage cooler with annular heat exchangers. . . . 63
3.4 A diagram showing the physical locations of the cells of a two-stage cold finger with annular heat exchangers. 64
3.5 A diagram showing the relationship between the gas cells and the momentum control volumes. 66
3.6 A flowchart showing the steps taken to calculate the gas properties at the cells and nodes from the solution variables. . . . 69
3.7 A diagram showing different options for calculating pressure forces when there is a change in flow area. 72
3.8 Diagrams showing how the cells of a single-stage cold finger are divided into subcells. 100

3.9 A diagram showing the arrangement of the solid cells used by the model to simulate the wall surface temperature fluctuation when the interior temperature is variable. 103
3.10 A diagram showing the thermal circuit that represents the interactions between the solid cells of the model when the interior temperature is variable. 104
3.11 Plots showing the temperature fluctuations predicted for a solid 2δ deep with a sinusoidal heat flow rate on one side and zero heat flow rate on the other. 105
3.12 A plot showing how the surface temperature fluctuations plotted in Figure 3.11 are affected by increasing the sinusoidal heat flow rate frequency by a factor of five. 106
3.13 A diagram showing the arrangement of the solid cells used by the model to simulate the wall surface temperature fluctuation when the interior temperature is fixed. 107
3.14 A diagram showing the thermal circuit that represents the interactions between the solid cells of the model when the interior temperature is fixed. 107
3.15 Plots showing how the schemes discussed in Section 3.10.2 interpolate the values at the nodes from the cell values. 115
3.16 A plot comparing the relationship between the number of regenerator cells and cooling power for different stagnation temperature interpolation methods. 116
3.17 Plots showing the temperature variation of a cell over a cycle for the central differencing and QUICK interpolation schemes. 117
3.18 A typical Jacobian matrix sparsity pattern calculated by the model. 122
3.19 A diagram showing the thermal circuit approximation for a single-stage cooler used by the energy flow equalisation method. 129
3.20 A diagram showing the extension of the thermal circuit approximation of Figure 3.19 for two-stage coolers. 132

4.1 A photograph of the Breadboard Cooler. 142
4.2 A photograph of the cold head of the Breadboard Cooler. 144
4.3 A section view of the cold head of the Breadboard Cooler. 145
4.4 A photograph of one of the indium seals of the Breadboard Cooler. 146
4.5 A photograph of the displacer of the Breadboard Cooler. 146
4.6 A photograph of the displacer shaft seal of the Breadboard Cooler. 148

4.7 A plot showing the predicted change in diameter of the bush and displacer shaft with temperature. 149
4.8 Plots showing the predicted thermal expansion of the cold finger tube and displacer tube for both stages of the Breadboard Cooler. 150
4.9 A photograph showing the displacer alignment procedure of the Breadboard Cooler. 150

5.1 A plot showing how the modelled cooling power predicted by the RAL Third-Order Model is affected by the number of regenerator cells for the 78 K case of the 2018 Small Scale Cooler. 155
5.2 A photograph of the 2018 Small Scale Cooler undergoing performance testing. 156
5.3 A plot comparing the measured cooling powers of the 2018 Small Scale Cooler at different cold tip temperatures with the cooling powers predicted by the RAL Third-Order Model and Sage. 157
5.4 A plot of the expansion chamber pressure-volume loops predicted by the RAL Third-Order Model and Sage for the 78 K case of the 2018 Small Scale Cooler. 159
5.5 A plot of the gross cooling power, net cooling power and total losses predicted by the RAL Third-Order Model and Sage for the 78 K case of the 2018 Small Scale Cooler. 159
5.6 A plot comparing the losses predicted by the RAL Third-Order Model with the losses predicted by Sage for the 78 K case of the 2018 Small Scale Cooler. 161
5.7 A plot of the variation in cooling power for the 78 K case of the 2018 Small Scale Cooler predicted by the RAL Third-Order Model when each of the inputs is increased to the upper limit of its uncertainty. 163
5.8 A plot of the variation in cooling power for the 78 K case of the 2018 Small Scale Cooler predicted by the RAL Third-Order Model when the rates of heat transfer in each region are increased by 10%. 165
5.9 A plot of the variation in cooling power for the 78 K case of the 2018 Small Scale Cooler predicted by the RAL Third-Order Model when the friction factors in each region are increased by 10%. . . 166
5.10 A photograph of the 2014 Small Scale Cooler undergoing loss mechanism testing. 167

5.11 A plot comparing the measured static losses of the 2014 Small Scale Cooler at different cold tip temperatures with the static losses predicted by the RAL Third-Order Model. 168
5.12 A plot comparing the measured dynamic losses of the 2014 Small Scale Cooler at different displacer strokes with the dynamic losses predicted by the RAL Third-Order Model. 169
5.13 A plot showing the effect that increasing the compressor seal radial clearance by 50% and 100% has on the net cooling power predicted by the RAL Third-Order Model for the 2018 Small Scale Cooler. These results are compared to the measured cooling power. 171
5.14 A plot showing the change in the gross cooling power, net cooling power and total losses predicted by the RAL Third-Order Model for the 78 K case of the 2018 Small Scale Cooler when the sizes of the compressor clearance seal gaps and appendix gap are increased. 171
5.15 A plot showing the change in the losses predicted by the RAL Third-Order Model for the 78 K case of the 2018 Small Scale Cooler when the sizes of the compressor clearance seal gaps and appendix gap are increased. 172
5.16 A photograph of the cold head of the CryoBlue Cooler. 173
5.17 A plot showing how the cooling power predicted by the RAL Third-Order Model is affected by the number of regenerator cells for the 57 K case of the CryoBlue Cooler. 175
5.18 A plot comparing a measured load line of the CryoBlue Cooler to the performance predicted by the RAL Third-Order Model. 175
5.19 A plot of the gross cooling power, net cooling power and total losses predicted by the RAL Third-Order Model for the 57 K case of the CryoBlue Cooler. 176
5.20 A plot showing the losses predicted by the RAL Third-Order Model for the 57 K case of the CryoBlue Cooler. 177
5.21 A plot showing the pressure waveform measured in the transfer line for the 57 K case of the CryoBlue Cooler. This is compared to the results of the RAL Third-Order Model which was run with the measured appendix gap and with the gap increased by 50%. 178
5.22 A plot showing the measured and derived forces acting on the displacer for the 57 K case of the CryoBlue Cooler. 179

5.23 A plot comparing the gas forces calculated by the RAL Third-Order Model for the 57 K case of the CryoBlue Cooler with the gas force derived from measurements, shown in Figure 5.22. . . . 180
5.24 Plots showing the performance of the Breadboard Cooler at three different fill pressures without the cryogenic pressure sensors. . . 182
5.25 A plot showing how the cooling power predicted by the RAL Third-Order Model is affected by the number of regenerator cells for the Breadboard Cooler. 184
5.26 Plots comparing the measured cooling powers of the Breadboard Cooler with the cooling powers predicted by the RAL Third-Order Model. 185
5.27 Plots showing the gross cooling power, net cooling power and total losses predicted by the RAL Third-Order Model for the no pressure transducer, 10 bar, 1 W, 0.5 W case of the Breadboard Cooler. 187
5.28 Plots showing the losses predicted by the RAL Third-Order Model for the no pressure transducer, 10 bar, 1 W, 0.5 W case of the Breadboard Cooler. 188
5.29 Plots comparing the measured and modelled pressure waveforms for the 10 bar, 1 W, 0.5 W case with cryogenic pressure sensors installed. 190
5.30 Plots of the variations in cooling powers of the Breadboard Cooler predicted by the RAL Third-Order Model when each of the inputs is increased to the upper limit of its uncertainty. 193
5.31 A plot of the variations in cooling powers predicted by the RAL Third-Order Model for the Breadboard Cooler when the heat transfer coefficients in each region are increased by 10%. 195
5.32 A plot of the variations in cooling powers predicted by the RAL Third-Order Model for the Breadboard Cooler when the friction factors in each region are increased by 10%. 196
5.33 A diagram showing a clearance seal consisting of an eccentric piston in a bore. 198
5.34 Plots showing the flow resistance measurements of the Ariel compressor piston clearance seals. The modelled relationships between pressure drop and flow rate are also plotted for the measured and increased gap sizes. 200

6.1 Diagrams depicting an appendix gap of a constant size and a tapered appendix gap. 206
6.2 Plots of the cooling power predicted by the RAL Third-Order Model for tapered and constant appendix gaps of different mean sizes. 207
6.3 A plot showing the volumetric flow predicted by the RAL Third-Order Model for three different sizes of tapered appendix gap. 208
6.4 A diagram showing the cold tip and regenerator overlap. 209
6.5 A plot of the cooling power predicted by the RAL Third-Order Model as a function of the mean overlap between the cold tip and the cold end of the regenerator. 211
6.6 A plot showing the cycle-averaged regenerator temperature profile predicted by the RAL Third-Order Model for two different values of mean cold tip overlap. 212
6.7 A plot of the expansion chamber pressure-volume loops predicted by the RAL Third-Order Model for two different values of mean cold tip overlap. 212
6.8 A diagram showing the cold head body and regenerator overlap. . 213
6.9 A plot of the cooling power predicted by the RAL Third-Order Model as a function of the mean overlap between the cold head body and the warm end of the regenerator. 214
6.10 A plot showing the cycle-averaged regenerator temperature profile predicted by the RAL Third-Order Model for two different values of mean cold head body overlap. 215
6.11 A plot of the expansion chamber pressure-volume loops predicted by the RAL Third-Order Model for two different values of mean cold head body overlap. 215

A.1 A diagram showing the connections between cells when simulating a single-stage cooler with an annular heat exchanger. . 224
A.2 A diagram showing the physical locations of the cells of a single-stage cold finger with an annular heat exchanger. 225
A.3 A diagram showing the connections between cells when simulating a two-stage cooler without annular heat exchangers. . 226
A.4 A diagram showing the physical locations of the cells of a two-stage cold finger without annular heat exchangers. 227

A.5 A schematic showing the model input dimensions of a two-stage cold finger with annular heat exchangers. 229

B.1 A plot of the thermal conductivity correlations used in the model. 240
B.2 A plot of the specific heat capacity correlations used in the model. 242

List of Tables

2.1 A table comparing different types of Stirling system models. . . . 54

3.1 A table listing the points that are interpolated to calculate the emissivity of the cold finger tube. 101

3.2 A table showing how the schemes used for interpolating the stagnation temperatures are selected based on the position of the node relative to the interfaces between different regions. 117

5.1 A table showing the measured and modelled pressures of the compressor backshell and transfer line of the Breadboard Cooler for the 10 bar, 1 W, 0.5 W case. The table also shows the differences between the two pressures and the mean piston offsets calculated from these pressure differences. 191

5.2 A table showing the measured gap sizes of the Ariel compressor piston clearance seals and the gap increases required to fit the modelled flow resistances to the measured values. 199

5.3 A table showing the measured dimensions of the clearance seals simulated by the model where the flow resistance had not been measured. The table also shows the gap increase required to fit the modelled cooling power to the measured value for cases where the cooling power was strongly influenced by the gap size. These clearance seals are compared to the piston clearance seals of the Ariel compressor, presented in Table 5.2. 201

A.1 A table showing an example of the input parameters required by the model. 230

A.2 A table showing an example of the output values produced by the model. 236

B.1 A table listing the sources of the thermal conductivity correlations used in the model. 239

B.2 A table listing the sources of the specific heat capacity correlations used in the model. 241
B.3 A table listing the densities of the materials used in the model. . . 243

Nomenclature

Latin Letters

A	Flow area	m^2
a	Clearance seal radial gap size	m
A_s	Solid cross-sectional area	m^2
C	Heat capacity	$J\,K^{-1}$
c	Specific heat capacity	$J\,K^{-1}\,kg^{-1}$
c_P	Specific heat capacity at constant pressure	$J\,K^{-1}\,kg^{-1}$
c_V	Specific heat capacity at constant volume	$J\,K^{-1}\,kg^{-1}$
d	Diameter	m
d_h	Hydraulic diameter	m
E	Energy	J
F	Force	N
f	Frequency	Hz
f_D	Darcy friction factor	
f_P	Pressure calculation factor	
f_T	Temperature calculation factor	$K\,kg\,J^{-1}$
h	Heat transfer coefficient	$W\,m^{-2}\,K^{-1}$
I	Current	A
i	Imaginary unit	
k	Thermal conductivity	$W\,m^{-1}\,K^{-1}$
K_L	Minor loss coefficient	
m	Mass	kg
$\dot{m}$	Mass flow rate	$kg\,s^{-1}$
$m_{\mathcal{T}}$	Turbulent mass	kg
N_k	Conduction enhancement factor	
Nu	Nusselt number	
P	Pressure	Pa
p	Momentum	$kg\,m\,s^{-1}$
Pr	Prandtl number	
Q	Heat	J
$\dot{Q}$	Heat flow rate	W
$\dot{q}$	Heat flux density	$W\,m^{-2}$

R	Thermal resistance	$\mathrm{K\,W^{-1}}$
r	Radial distance	m
R_g	Specific gas constant	$\mathrm{J\,kg^{-1}\,K^{-1}}$
Re	Reynolds number	
$Re_{\mathcal{T}}$	Turbulent Reynolds number	
S	Surface area	$\mathrm{m^2}$
s	Surface area per unit length	m
T	Temperature	K
t	Time	s
$\mathcal{T}$	Turbulence intensity	
U	Internal energy	J
u	Specific internal energy	$\mathrm{J\,kg^{-1}}$
V	Volume	$\mathrm{m^3}$
v	Velocity	$\mathrm{m\,s^{-1}}$
$\dot{V}$	Volumetric flow rate	$\mathrm{m^3\,s^{-1}}$
Va	Valensi number	
W	Work	J
w	Weighting	
x	Length	m
y	Solution variable	
z	Width	m

Greek Letters

γ	Heat capacity ratio	
δ	Thermal penetration depth	m
ϵ	Absolute roughness	m
λ	Compression component calculation factor	$\mathrm{K\,Pa^{-1}}$
ϵ_0	Emissivity	
ε	Eccentricity	
ε_0	Arbitrarily small positive constant	
θ	Gradient ratio	
K	Turbulence kinetic energy	J
κ	Specific turbulence kinetic energy	$\mathrm{J\,kg^{-1}}$
μ	Dynamic viscosity	Pa s
ρ	Density	$\mathrm{kg\,m^{-3}}$
σ	Stefan-Boltzmann constant	$\mathrm{W\,m^{-2}\,K^{-4}}$
τ	Tortuosity	

ϕ	Porosity	
ψ	Slope limiter	
ω	Angular frequency	rad s^{-1}

Subscripts

0	Initial or steady-state
A	Amplitude
a	Advection
b	Backshell
c	Compression
e	Enhanced
g	Gas
I	Interior
i	The i^{th} cell
j	The j^{th} node
L	Laminar
m	Mesh
s	Solid
T	Turbulent
W	Wall
w	Working volume

Notation

$y^{\dagger}$	y is relative to the motion of the cell or node
y^{*}	y has been modified to account for a change in flow area
$\bar{y}$	Mean of y over a cycle
Δy	Change of y
$\dot{y}$	First derivative of y with respect to time
$\ddot{y}$	Second derivative of y with respect to time
$\boldsymbol{y}$	$\boldsymbol{y}$ is a complex-valued function
$\Re(\boldsymbol{y})$	Real component of $\boldsymbol{y}$
$\Im(\boldsymbol{y})$	Imaginary component $\boldsymbol{y}$

This thesis uses the IUPAC sign convention where W indicates the work done on the system, Q indicates the heat transferred to the system and $\Delta U = Q + W$ [6, p. 56].

Abbreviations

2D	Two-dimensional
3D	Three-dimensional
ALMA	Atacama Large Millimetre Array
BDF	Backward Differentiation Formula
CFD	Computational Fluid Dynamics
CFL	Courant–Friedrichs–Lewy
CMM	Coordinate Measuring Machine
CoP	Coefficient of Performance
ESA	European Space Agency
GM	Gifford-McMahon
IUPAC	International Union of Pure and Applied Chemistry
NASA	National Aeronautics and Space Administration
ODE	Ordinary Differential Equation
RAL	Rutherford Appleton Laboratory
MLI	Multi-Layer Insulation
MRI	Magnetic Resonance Imaging

Glossary

Annular heat exchanger	An annular flow passage located between the displacer outlet and the expansion chamber.
Appendix gap	The narrow annular gap between the displacer tube and the cold finger tube. It is a type of clearance seal.
Ariel	An ESA space telescope, scheduled for launch in 2029.
Backshell	The regions of a Stirling cooler that contain the motors. They are separated from the working volume by clearance seals.
Breadboard	Hardware that demonstrates the function of the system, without respecting the final form or fit.
Breadboard Cooler	The two-stage Stirling cooler developed as part of this work that has been used to help validate the model.
Bulk temperature	The mean temperature of a fluid, averaged over the flow area.
Bulk velocity	The mean velocity of a fluid, averaged over the flow area.
Clearance seal	A small annular gap between a moving object and a bore that restricts the leakage past the moving object.
Cold finger	A component of a Stirling cooler that protrudes from the cold head body. The cooling occurs at the end of the cold finger (and partway along it for a two-stage cooler).
Cold finger tube	The outer tube of the cold finger that withstands the gas pressure.

Cold head	The part of a Stirling cooler that contains the cold finger and the displacer motor. It is connected to the compressor by a transfer line.
Cold head body	The main structure of the cold head, to which the displacer motor and cold finger are attached.
Cold tip	The component at the end of the cold finger that is connected to the item to be cooled. A two-stage cooler has two separate cold tips, with one located partway along the cold finger.
Compressor	The part of a Stirling cooler that expands and compresses the gas at the warm end. It is connected to the cold head by a transfer line. It is also known as a pressure wave generator.
CryoBlue Cooler	A medium-sized, single-stage, long-life Stirling cooler developed at RAL.
Cryocooler	A machine that can provide refrigeration at cryogenic temperatures. Often referred to simply as a cooler.
Dead volume	The space in the working volume of a cooler that is not swept by the displacer or compressor pistons.
Displacer	A component of a Stirling cryocooler that moves back and forth to drive the gas between the warm and cold ends of the cooler.
Displacer bush	A component of a Stirling cryocooler that surrounds the displacer shaft to form a clearance seal between the displacer backshell and the secondary compression chamber.
Displacer inlet	The flow path linking the secondary compression chamber and the regenerator, located at the warm end of the displacer.

Displacer outlet	The flow path linking the regenerator and the expansion chamber (or annular heat exchanger if present). It is located at the cold end of the displacer and at the end of the first stage for a two-stage cooler.
Displacer tube	The outer component of the displacer, often made from plastic. The regenerator is contained within this tube.
Dynamic losses	Loss mechanisms that occur when the displacer is moving but the compressor pistons are stationary. In addition to the static losses, they include shuttle losses, enhanced gas conductivity and regenerator and appendix gap enthalpy transport.
Expansion chamber	The variable volume chamber where the gas is expanded by the motion of the displacer and where the cooling occurs.
Flexure bearing	A bearing consisting of a flexible element. For Stirling coolers, these are used to support the compressor pistons and displacer while only allowing motion in the axial direction.
Gross cooling power	The pressure-volume work done by the gas at the cold end.
Jacobian matrix	A matrix that contains the partial derivative of every solution variable with respect to every other solution variable.
Loss mechanism	An effect that reduces the amount of available cooling power. The net cooling power can be found by subtracting all the loss mechanisms from the gross cooling power.
Net cooling power	The amount of cooling power that is available for cooling the item that is attached to the cold tip. Often referred to simply as cooling power.

Periodic steady state	A state of a model where the solution variables have the same value at the start and end of each cycle.
Pressure swing	The difference between the minimum and maximum pressure at a given location over a cycle.
Primary compression chamber	The variable volume chamber where the gas is compressed and expanded by the compressor pistons.
RAL Third-Order Model	The Stirling cryocooler model developed as part of this work.
Regenerator	A type of heat exchanger that temporarily stores thermal energy. It is used in the Stirling cycle to improve the thermal efficiency.
Sage	A commercially available computer program that can be used for simulating Stirling cryocoolers.
Secondary compression chamber	The variable volume chamber at the warm end of the displacer.
Shuttle loss	A loss mechanism caused by the relative motion between the displacer tube and the cold finger tube. The motion causes their thermal gradients to become offset and heat to flow between them.
Small Scale Cooler	A compact, single-stage, long-life Stirling cooler developed at RAL.
Solution variable	The variables that define the state of the model at each point in time.
Static losses	The loss mechanisms that are present when there is no motion of the displacer or compressor pistons. They include the heat load due to radiation and the heat load due to thermal conduction through the gas and solid components of the cold finger.

Stirling cryocooler	A machine for producing cooling that operates using the Stirling thermodynamic cycle.
Swept volume	The volume through which a piston or displacer moves.
Transfer line	The pipe connecting the compressor to the cold head in a Stirling cooler.
Two-stage cryocooler	A cryocooler that can produce cooling at two separate locations.
Variable volume chamber	A chamber that varies in volume over the course of a cycle. In the model, the variable volume chambers are the primary and secondary compression chambers, the expansion chambers and the compressor and displacer backshells.
Working volume	The region of gas in a Stirling cooler that undergoes the thermodynamic cycle. It does not include the gas in the backshells.

Chapter 1

Introduction

This thesis describes the development, validation and application of the RAL Third-Order Model, a new Stirling cryocooler model that has been developed at the Rutherford Appleton Laboratory (RAL), Oxfordshire, UK. This one-dimensional, finite difference model can simulate single and two-stage cryocoolers and includes a novel simulation of the interactions between the different loss mechanisms. The model uses the latest friction factor and heat transfer correlations from the literature and simulates turbulence generation and thermal penetration depths. It runs fast enough to be useful for optimisation, thanks to a robust artificial convergence technique. The model includes a full representation of the cold finger of Stirling cryocoolers and simulates the displacer motion, the shuttle losses and the flow past the displacer. This enables the optimisation of certain parameters that could not be assessed previously. The model has been validated against single and two-stage coolers and has been used to investigate changing the cold finger geometry of a single-stage cooler.

The model will be used at RAL to aid the development of single and two-stage Stirling coolers that are designed for use in spacecraft. The coolers use flexure bearings and non-contact clearance seals to achieve a long lifetime. The previous RAL model was developed in the 1990s, and it uses several simplifying assumptions due to the limited computing power available at the time [7]. The assumptions in the previous model break down when it is used to simulate coolers outside the frequency and size ranges it has been calibrated for.

The aim of this project is to develop a model that can accurately predict the cooling powers of single and two-stage Stirling cryocoolers for a wider range of cooler sizes than the previous RAL model. It should run fast enough to be useful for design optimisation, be easily configurable to model different cooler

geometries and it should be modifiable so that it can be calibrated using experimental data.

Stirling cryocoolers are difficult to model using commercially available 2D or 3D computational fluid dynamics software. The compressible gas, moving mesh and the variable regenerator temperatures make a 2D or 3D model computationally expensive [8]. The approach commonly used by other researchers is to simulate the machine as a network of one-dimensional flow paths [4][5][9]. Empirical relationships are used to calculate the heat transfer rates and friction factors at different points in the cooler. These models are categorised as third order [10], and this was the approach selected for the new RAL model.

Many of the third-order models in the literature use a modular approach. Each different flow region is contained within a separate module. This has the advantage of making the models flexible but can make it more difficult to simulate complex interactions between the modules. The RAL Third-Order Model takes a different approach. It simulates the cold finger of the cooler as a single system. This allows it to realistically simulate heat transfer between the different gas flow paths and account for the motion of the displacer.

The model was created using the MATLAB programming language. Correlations from the literature are used to simulate heat transfer and pressure drops. The model uses novel methods for simulating the motion of the displacer and the wall heat transfer, and it uses a new method to accelerate convergence.

The model has been validated against single-stage coolers that were previously developed at RAL and against a two-stage cooler that has been developed as part of this work. This two-stage cooler was designed specifically for validating the model and contains cryogenic pressure transducers for measuring the pressure swings at the two cold stages.

The results of the validation show that the model can accurately predict the cooling power of a Stirling cryocooler if the leakage through the clearance seals has been characterised beforehand. It appears that the model tends to underpredict the leakage through these seals if their measured dimensions are used as inputs.

The results of the RAL Third-Order Model show that there is a great deal of interaction between the loss mechanisms that would not be simulated by a model that assesses each flow path separately. The RAL Third-Order Model was also used to simulate changes to cooler geometry that could only be investigated by simulating the cold finger of the cooler as a single system. It was found that some of these geometry adjustments have a significant effect on the predicted cooling power.

This thesis summarises the development, validation and some preliminary applications of the new RAL Third-Order Model. Chapter 2 presents an overview of different types of cryocoolers and looks at the different methods that other researchers have used to simulate Stirling cycle machines; Chapter 3 describes the formulation of the model and the heat transfer and friction factor correlations that it uses; Chapter 4 covers the development of a breadboard cryocooler that has been used to help validate the model; Chapter 5 discusses how the model was validated against performance measurements of Stirling cryocoolers; and Chapter 6 looks at aspects of cooler geometry that can be difficult to investigate with other models but can be simulated using this model.

Chapter 2

Background

Cryocoolers are machines that provide refrigeration at cryogenic temperatures, below approximately 120 K [11]. The term typically refers to devices with a cooling power less than 100 W; larger systems are known as cryogenic refrigerators or cryoplants [12]. The Stirling coolers modelled in this work are one type of cryocooler, but there are other types available which are suited to different applications.

This chapter summarises the different applications of cryocoolers and introduces some of the most used types. The Stirling coolers that are developed at the Rutherford Appleton Laboratory are described, and their key features are summarised. This chapter also provides an overview of the different modelling techniques used to simulate Stirling cycle machines.

2.1 Cryocooler Applications

Cryogenic temperatures are important for many different technologies [13]. Low temperatures can reduce the thermal noise seen by sensors, can be used to change the state of materials and can enable quantum effects such as superconductivity.

A simple way to cool an object to cryogenic temperatures is to use a cryogen that is already at a low temperature such as liquid nitrogen or liquid helium. These cryogens can be produced in large quantities at a liquefaction plant and transported to where they are required. Stored cryogen systems are typically cheaper and simpler than cryocoolers. However, they require regular replenishment and have high mass and volume requirements [14, p. 2]. The key advantages of cryocoolers are that they can produce cooling on demand and do not need the complex infrastructure required for transporting and

storing cryogens. As cryocoolers become cheaper and more reliable, they are being used for a growing number of applications [15].

Cryocoolers are well suited to a variety of applications. Ground based telescopes that are in remote locations, such as the ALMA telescopes in the Atacama Desert [16], often use cryocoolers for cooling their detectors to avoid the logistical challenges of transporting cryogens. Cryocoolers are used in compact systems that require a low mass, such as miniature unmanned aerial vehicles and night vision goggles [17]. Cryocoolers are also becoming more popular in applications that traditionally use cryogens; they are often used to recondense the liquid helium in MRI machines to produce zero boil-off systems [13].

A key area for the use of cryocoolers is in spacecraft. Space missions often have a multi-year lifetime, and it is not practical to have enough stored cryogen to last the mission duration if there is a large cooling power requirement. Since 1991, closed-cycle cryocoolers have been regularly used instead [18]. Cryocoolers are often used for cooling sensitive infrared detectors which require temperatures of around 10-150 K. These infrared detectors can be used for Earth observation or astronomy [18]. Other types of detectors that need cooling include X-ray bolometers (~50 mK) [2], microwave bolometers (~100 mK) [19] and microwave radiometers (~20 K) [19]. Cryocoolers can also be used when transporting liquid propellants to reduce boil-off [20].

2.2 Types of Cryocooler

This section describes some of the common types of cryocoolers that are used for cooling at temperatures above 4 K. All of these cryocoolers use gas in a closed-cycle; by reusing the same gas, they do not require refilling. The gas is typically compressed at room temperature, where it rejects heat, and is expanded at a lower temperature to produce cooling.

The coolers can be split into two types: regenerative and recuperative cryocoolers. Regenerative cryocoolers have an oscillating gas flow between the warm and cold parts of the cooler. The main types are Stirling, Gifford-McMahon and pulse tube coolers. Recuperative coolers have a steady flow of gas between the warm and cold parts of the cooler, with high-pressure gas

travelling towards the cold end and low-pressure gas travelling back towards the warm end. Two common types are Brayton and Joule-Thomson cryocoolers.

2.2.1 Stirling Cryocoolers

Stirling coolers operate using the Stirling thermodynamic cycle. They are closed-cycle systems and typically use helium as their working fluid [14, p. 141]. Single-stage Stirling cryocoolers can cool to around 20 K [14, p. 149] and two-stage Stirling cryocoolers can achieve temperatures below 10 K at the second stage [14, p. 152]. They commonly operate at frequencies between 30 and 70 Hz and at fill pressures of 10 to 35 bar [21]. Their capacity can range from fractions of a watt to hundreds of watts of cooling power [21].

The Stirling Cycle

The Stirling cycle is a thermodynamic cycle that was first used in a heat engine patented by Robert Stirling in 1816 [22, p. 21]. As well as being able to produce mechanical power from a temperature gradient, the cycle can also be used to produce a temperature gradient by using mechanical power [11, p. 95]. This is the principle behind Stirling cryocoolers.

A basic Stirling cryocooler contains two moving components: a compressor piston and a displacer. The compressor piston is located at the warm end of the cooler and the displacer is located between the warm and cold ends of the cooler, as shown in Figure 2.1. When the gas is compressed, work is done on the gas, and it rejects heat to its surroundings; when the gas is expanded, work is done by the gas, and it absorbs heat from its surroundings. The displacer is used to ensure that the gas is at the warm end when it rejects heat and that it is at the cold end when it absorbs heat. This results in cooling at the cold end.

To increase the efficiency of the Stirling cycle, the warm gas can be cooled before it enters the cold end. This is done using a regenerator. A regenerator is a type of heat exchanger that temporarily stores thermal energy. As the warm gas passes through it, the thermal energy of the gas is transferred to the regenerator, cooling the gas. Once the gas has been expanded, it flows back through the regenerator, picking up the thermal energy it deposited earlier in the cycle. A regenerator helps to thermally isolate the warm end from the cold

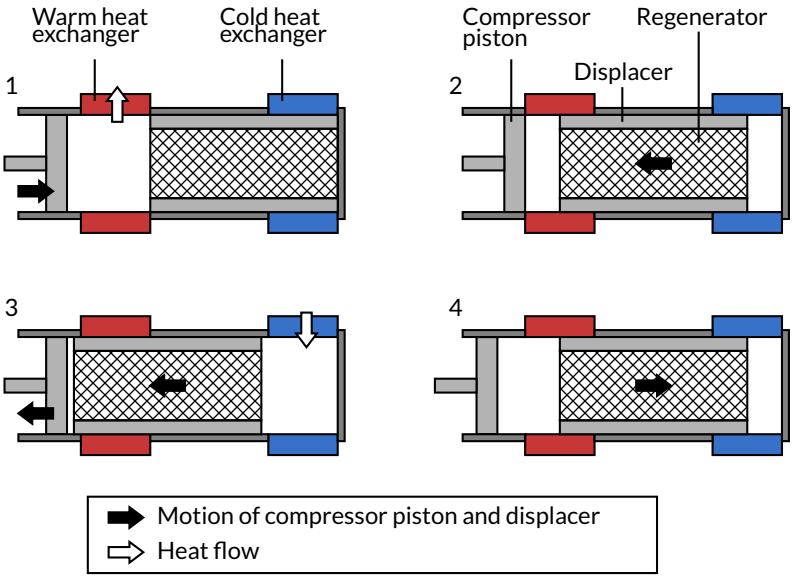

Figure 2.1: A diagram showing the idealised stages of a Stirling cryocooler's thermodynamic cycle.

end. The regenerator in a cryocooler is typically contained within the displacer.

An idealised cycle can be used to make a simple estimate of the cooling power. The ideal cycle consists of four steps [14, p. 136]:

1. **Isothermal compression** — The compressor piston moves forward, changing the volume of the system from V_{max} to V_{min}. The gas is compressed, and its pressure increases. The temperature of the gas is maintained at T_{warm}. Work is done on the gas when it is compressed, and an equal amount of heat is rejected to the warm heat exchanger.

$$W_{comp} = -Q_{warm} = mR_g T_{warm} \ln\left(\frac{V_{max}}{V_{min}}\right) \tag{2.1}$$

2. **Constant-volume regenerative cooling** — The gas is moved to the cold end of the cooler by the motion of the displacer. As it moves, the gas passes through the regenerator which absorbs some of the heat from the gas and cools it from T_{warm} to T_{cold}.

3. **Isothermal expansion** — The compressor piston and displacer move backwards, changing the volume of the system from V_{min} to V_{max}. The gas is expanded, and its pressure decreases. The temperature of the gas

is maintained at T_{cold}. Work is done by the gas when it is expanded, and an equal amount of heat is absorbed from the cold heat exchanger.

$$-W_{exp} = Q_{cold} = mR_g T_{cold} \ln\left(\frac{V_{max}}{V_{min}}\right) \tag{2.2}$$

4. **Constant-volume regenerative heating** — The gas is moved to the warm end of the cooler by the motion of the displacer. The gas warms from T_{cold} to T_{warm} as it passes through the regenerator.

These steps are shown in Figure 2.1 and Figure 2.2. The assumptions made by this ideal cycle are discussed in Section 2.4.1.

The coefficient of performance is the ratio of useful cooling provided to work required.

$$\begin{aligned} CoP &= \frac{Q_{cold}}{W_{comp} + W_{exp}} \\ &= \frac{mR_g T_{cold} \ln\left(\frac{V_{max}}{V_{min}}\right)}{mR_g T_{warm} \ln\left(\frac{V_{max}}{V_{min}}\right) - mR_g T_{cold} \ln\left(\frac{V_{max}}{V_{min}}\right)} \\ &= \frac{T_{cold}}{T_{warm} - T_{cold}} \end{aligned} \tag{2.3}$$

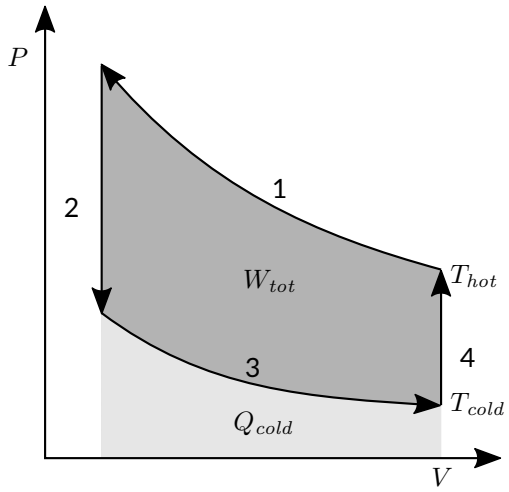

Figure 2.2: A plot of pressure against the total gas volume for the ideal Stirling cycle. The area enclosed by the cycle represents the net work applied to the gas and the area under the curve of Step 3 represents the cooling power.

Because all these steps are reversible, the coefficient of performance of the ideal Stirling cycle is the maximum possible for any refrigeration cycle and is the same as for a Carnot refrigerator [11, p. 47].

Regenerators

The ideal cycle highlights the importance of the regenerator. In this cycle, exactly the same quantity of heat is transferred to the regenerator in Step 2 as is absorbed from the regenerator in Step 4 because the temperature change is reversed and the mass of gas is the same. However, if no regenerator is present, the heat that would be transferred to the regenerator in Step 2 must be rejected to the cold end heat exchanger, greatly reducing the coefficient of performance.

An ideal regenerator must meet the following conflicting requirements:

- There must be a low pressure drop as the gas flows through the regenerator. A high pressure drop reduces the pressure swing at the cold end, which reduces the cooling power.
- There must be good heat exchange between the gas and the regenerator material. If the heat exchange is poor, the gas will not transfer as much thermal energy to the regenerator and will be hot when it flows into the cold end of the cooler.
- The surface of the regenerator must maintain an almost constant temperature to maximise the amount of heat transferred with the gas. This means that the regenerator must have a high heat capacity and that the thermal conductivity must be high to allow enough heat to flow between the regenerator surface and interior.
- There must be low thermal conductance along the regenerator. Thermal conduction applies a heat load, reducing the net cooling power.
- The volume of gas in the regenerator should be low. The space in a cooler that is not swept by the displacer or compressor piston is known as the dead volume. If this is too large, the swept volume of the compressor must be increased to achieve the same pressure swing. This increases the size of the cooler.

Stirling Cooler Configurations

There are two Stirling cooler configurations that are commonly used. These are known as the beta and gamma configurations [22, p. 89] and are shown in Figure 2.3. In the beta configuration, the displacer and compressor piston operate in the same bore. The shaft of the displacer passes through the compressor piston. This configuration can be made very compact and reduces the dead volume in the cooler.

The gamma configuration separates the compressor piston and the displacer. The displacer is contained within the cold head which is connected to the compressor by a transfer line. This enables more flexibility when designing the cooler; the diameters of the displacer and compressor piston can be different, and they can be in different locations. The gamma configuration also allows for two compressor pistons to run in a head-to-head configuration which can reduce the exported vibrations.

Rotary and Linear Stirling Coolers

Stirling coolers can be driven using a rotary motor. The motor is connected to the compressor piston and displacer by crank mechanisms. This allows both

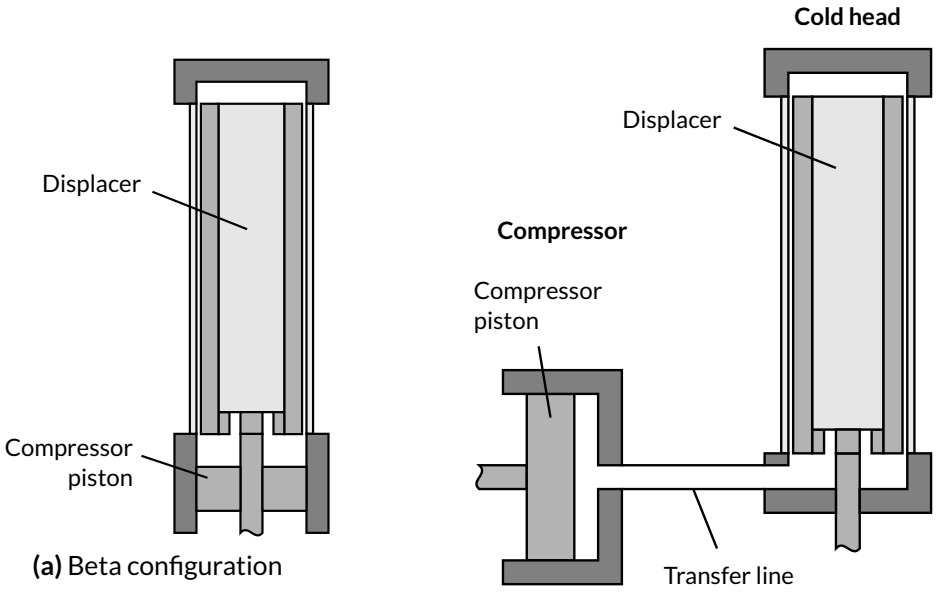

Figure 2.3: Diagrams showing two common Stirling cooler configurations.

the displacer and compressor piston to be driven by a single motor. Rotary motors can be made very cheaply and can be very efficient; however, the joints in the crank mechanism will eventually wear out. Rotary motors are most suitable for small tactical cryocoolers that only need a short lifetime [14, p. 143] or for large cooling plants that can be easily serviced [11, p. 172].

The alternative is to drive the compressor pistons and displacer using electromagnetic linear motors, similar to those found in loudspeakers. Flexure bearings or gas bearings are used to constrain the compressor pistons and displacer radially while allowing them to move axially. Since there is no crank mechanism to wear out, the lifetime can be greatly increased. Linear coolers are often used for applications that require a long lifetime without servicing, such as in spacecraft [14, p. 145]. Linear motors allow the amplitudes and phases of the compressor pistons and displacer to be adjusted. However, the operating frequency of the system must be close to the resonant frequencies of the compressor pistons and displacer for the system to be efficient. This is because running the motors near resonance reduces the motor forces required. The resonant frequencies are dependent on the moving masses and the restoring forces due to the flexure bearings, gas pressure and any magnetic interactions.

It is possible to design coolers that do not have a displacer motor at all. In these coolers, the displacer is driven pneumatically by the gas pressure. The phase and amplitude of the displacer can be tuned by adjusting its mass, spring rate, damping and the area on which the gas pressure acts. Pneumatic displacers are often used in miniature coolers [23].

Two-Stage Stirling Coolers

Stirling coolers can be designed to produce cooling at two different temperatures. The displacer is stepped and there are two expansion chambers, with the coldest temperature occurring at the second stage. A diagram of a two-stage cold finger is shown in Figure 2.4. Two-stage coolers can achieve very low temperatures because losses, such as thermal conduction, are intercepted at the intermediate temperature where more cooling power is available. The cooling at the intermediate temperature can also be useful for cooling radiation shields [24].

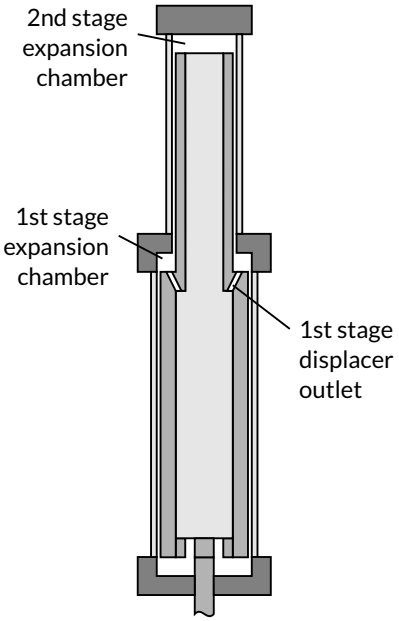

Figure 2.4: A diagram showing the cold head of a two-stage Stirling cryocooler.

2.2.2 Gifford-McMahon Cryocoolers

Gifford-McMahon (GM) cryocoolers operate in a similar way to Stirling coolers; they produce cooling by using a displacer to expand gas. The key difference is that GM compressors produce a constant high pressure instead of an alternating pressure wave. The alternating pressure required to create cooling is generated by valves in the warm part of the cold head that alternately connect the cold head to the high and low-pressure sides of the compressor. The displacer motion is similar to the motion within a Stirling cooler: it moves away from the cold end when the pressure is high and towards the cold end when the pressure is low.

The steady flow produced by the compressor means that long gas lines can be used to connect the compressor to the cold head. This is not possible for Stirling coolers because a long gas line would increase the dead volume and reduce the pressure swing. Using valves to separate the compressor and cold head allows them to operate at different frequencies. The compressors typically operate at 50-60 Hz which allows them to be compact. The switching frequency of the cold head is typically around 1 Hz. This low frequency reduces the flow speed of the gas through the regenerator, reducing the pressure drop and allowing more time for the regenerator to transfer heat

with the gas; the lower losses allow two-stage GM coolers to achieve temperatures of 4 K [21].

The low frequency operation of the cold head brings disadvantages. Clearance seals cannot be used as too much gas would leak past them over a cycle. Instead, contacting seals are used at each stage of the displacer which wear out over time [25]. The low frequency also requires a larger cold head for the same cooling power. The other key disadvantage of this cycle is that it has a low efficiency due to irreversible losses in the valves [13].

GM coolers are popular for use in laboratory applications because of their flexibility and ability to reach low temperatures. They are also relatively cheap because their steady-flow compressors are similar to air conditioning compressors and benefit from the maturity of this technology [21].

2.2.3 Stirling-Type Pulse Tube Cryocoolers

Stirling-type pulse tube cryocoolers operate using a similar thermodynamic cycle to Stirling cryocoolers. In a pulse tube cooler, the mechanical displacer is replaced with a tuned pneumatic circuit. The motion of the gas in the pneumatic circuit causes a phase difference between the mass flow and pressure swing. This phase shift results in the gas rejecting heat at the warm end and absorbing heat at the cold end [21].

Having no moving parts in the cold head brings advantages. It simplifies the assembly of the cooler and reduces the exported vibrations. The major disadvantage is that Stirling-type pulse tube coolers are not as efficient as Stirling coolers [26][27]. The operation of the pneumatic circuit requires a greater flow of gas through the regenerator than an equivalent Stirling cooler. This results in larger losses from imperfect heat transfer and pressure drops. In addition, a pulse tube cooler dissipates the work done by the gas at the cold end as heat at the warm end; whereas a Stirling cooler uses this energy to help compress the gas. The efficiency of low frequency pulse tubes is further reduced if they are not orientated with the cold tip downwards, due to convection in the pneumatic circuit [21].

Stirling-type pulse tube coolers are used in similar applications to Stirling coolers. The compressor pistons can use clearance seals which makes them suitable for applications that require a long lifetime, such as spacecraft. Their

low vibration cold heads make them particularly suitable for cooling vibration sensitive detectors [14, p. 162].

2.2.4 GM-Type Pulse Tube Cryocoolers

GM-type pulse tube cryocoolers combine the tuned pneumatic circuits of Stirling-type pulse tube coolers with the constant pressure compressors of GM coolers. The switching frequency of the cold head is typically around 1 Hz, like a GM cooler, and this low frequency allows them to achieve temperatures of around 4 K [13].

Because they use a pulse tube, they do not have any displacer seals to wear out, although there is still wear in the compressor seals and the valves. The lack of moving parts at the cold end also helps to reduce the levels of exported vibration. Their main disadvantage is their low efficiency due to irreversible expansion in their GM-type valves. Because of their low frequency, their performance is dependent on their orientation, and they need to be operated with the cold end pointing down to achieve maximum cooling power [21]. They are well suited to use in laboratories, particularly for cooling vibration sensitive equipment.

2.2.5 Brayton Cryocoolers

Brayton cryocoolers produce cooling by expanding a steady flow of high-pressure gas. The high-pressure gas enters the expansion chamber and does mechanical work on a piston or turbine. This mechanical work causes the energy of the gas to decrease and its temperature to drop. The cold, low-pressure gas passes through a heat exchanger where it is used to produce cooling. The low-pressure gas then flows back to the warm end where it is recompressed.

To increase the cycle efficiency, Brayton coolers thermally isolate the warm and cold ends of the cooler by using a recuperator. This is a counter-flow heat exchanger that transfers heat between the high-pressure and low-pressure gas. As the high-pressure gas travels towards the cold end, it transfers heat to the low-pressure gas flowing the other way. This ensures that the high-pressure gas is already cold by the time it reaches the expander.

The compressor and expander can be reciprocating, using pistons, or rotary, using turbines. Reciprocating machines are better suited to high pressure ratio, low flow rate applications, whereas rotary machines are better suited to low pressure ratio, high flow rate applications [11, p. 345]. Reciprocating machines can use simpler recuperator designs because the lower mass flows require less heat to be transferred. Rotary machines have the advantage that they do not require valves to control the flow of gas.

Brayton coolers that use turbines are known as turbo-Brayton coolers; these coolers are well suited for use in spacecraft. They can use gas bearings to achieve non-contact operation for a long lifetime and their turbines operate at a high frequency, so their vibrations have little impact on sensitive instruments [28]. The steady flow of gas aids integration as it allows the compressor to be located far from the expander. They are particularly suited for applications where a large amount of cooling power is required because this is when they are the most thermodynamically efficient [29]. The main disadvantage of turbo-Brayton coolers is the extra complexity of having cryogenic moving parts.

2.2.6 Joule-Thomson Cryocoolers

Joule-Thomson coolers also produce cooling from a steady flow of high-pressure gas. Instead of expanding the gas using a piston or turbine, the gas undergoes free expansion by passing through an orifice or porous plug. As the gas expands, its temperature may change. This is known as the Joule-Thomson effect.

The temperature change is caused by a change in the potential energy of the gas as it undergoes free expansion. This effect is caused by the intermolecular forces between the gas particles. Cooling only occurs at certain pressures and temperatures. For example, helium must be below 40 K for Joule-Thomson cooling to occur [11, p. 268]. The cooling power of free expansion is lower than obtained in a Brayton cryocooler because no work is done by the gas.

The simplicity of Joule-Thomson coolers makes them appealing for many applications. They have no moving parts at the cold end, so they are reliable and produce low levels of exported vibrations. The expansion orifice can be located a long way from the compressor which provides flexibility. If long-life, flexure bearing compressors are used, they are suitable for use in spacecraft

[30]. However, they often have a low efficiency and may require precooling of the gas to operate.

2.3 Stirling Cryocoolers Developed at RAL

Stirling cryocoolers for space applications have been developed at RAL since the 1980s [1]. Stirling coolers are a good fit for the requirements of spacecraft: they require low electrical input power because of their high-efficiency thermodynamic cycle; they can be made light and compact because of their high operating frequency; and they can be designed to have a long lifetime by using linear motors and clearance seals. The coolers designed at RAL have been used on several missions, with some built at RAL and some built under licence. RAL Stirling coolers are often used for cooling infrared detectors, but some have been developed for precooling Joule-Thomson coolers [31].

The Stirling cryocoolers developed at RAL use the gamma configuration. For most of the coolers, the compressor and cold head are separate and are linked by a transfer line, as shown in Figure 2.5. Separating the cold head and compressor allows for more flexibility when integrating the cooler. However, for some of the more recent compact cooler developments, the compressor and cold head are integrated into the same body to reduce the system size [32]. The compressor typically consists of two pistons running in a head-to-head configuration into a common bore. This configuration helps to reduce exported vibrations. If the vibration requirements are particularly stringent, the exported vibrations of the displacer can also be reduced by fitting a balancer motor that runs in antiphase to the displacer motor [33].

RAL Stirling coolers use clearance seals at the compressor pistons, the displacer shaft and along the displacer tube. The clearance seals between the compressor pistons and bores and the displacer shaft and bush reduce the leakage of gas into the backshells which would reduce the pressure swing. The clearance seal between the displacer tube and the cold finger tube is known as the appendix gap and this prevents gas from bypassing the regenerator. These clearance seals work by having a very small gap between the moving and stationary components that restricts the flow of gas. They do not wear out because there are no rubbing components, and they enable the lifetime of the coolers to exceed 10 years [13]. The compressor pistons and displacer are driven by linear motors and are suspended on flexure bearings. The flexure

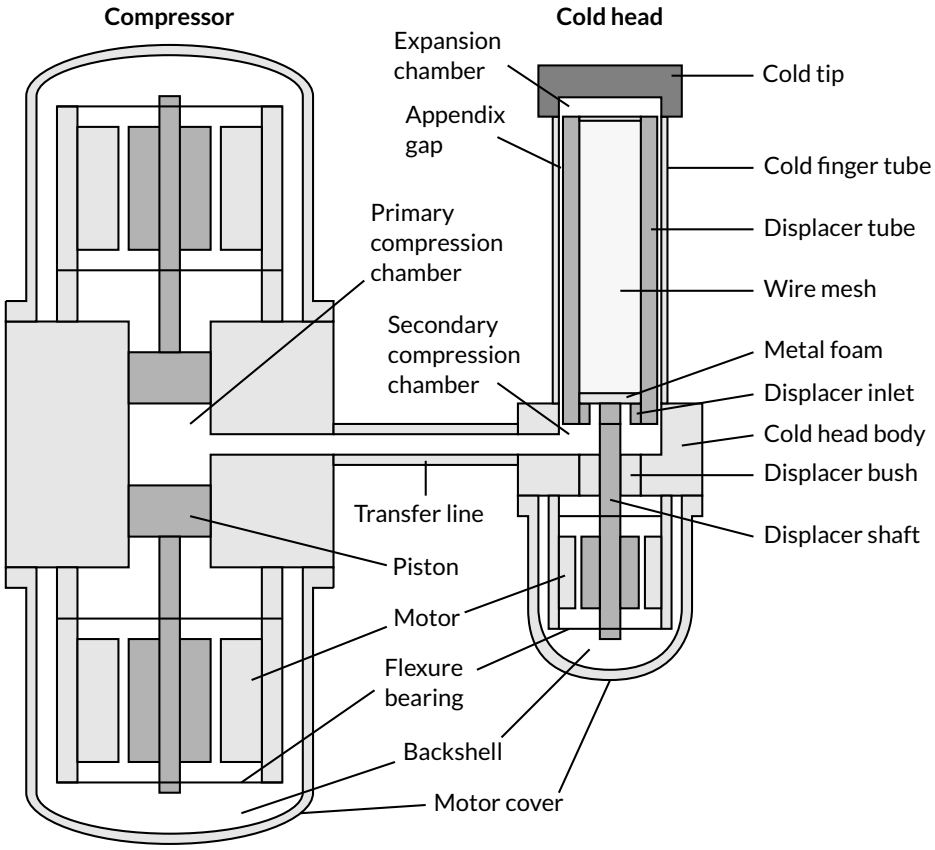

Figure 2.5: A diagram showing a section view of a typical single-stage RAL Stirling cryocooler. Some of the main components are labelled.

bearings are made of a disc of metal with a spiral pattern cut into it, as shown in Figure 2.6. The outer edge of the disc is held stationary, and the centre of the disc is attached to the shaft of the displacer or piston. The flexure bearings are designed so that they are axially compliant but radially stiff. They are made from hardened stainless steel and are designed so that their peak stress is well below the fatigue limit of the material during operation.

The displacer consists of a plastic tube, typically made of Vespel SP-3 [34], that contains the regenerator. Locating the regenerator inside the displacer allows them to be contained in a single cold finger tube which helps to reduce the thermal conduction between the warm and cold parts of the cooler. Vespel has a low thermal conductivity and good wear resistance in case of contact with the cold finger tube. The regenerator is typically composed of stacked discs of fine wire mesh with a wire diameter of 20-50 μm. Stacked discs give a good compromise between heat transfer and pressure drop and have a low

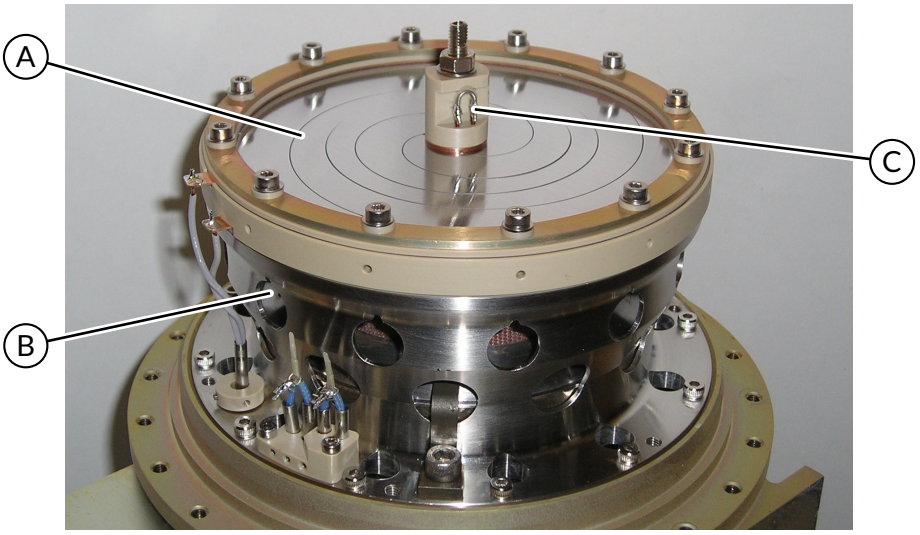

Figure 2.6: A photograph showing one of the compressor motors of the RAL Maxi compressor. Some key parts have been labelled: **A**, the flexure bearing; **B**, the stationary part of the motor; and **C**, the compressor piston shaft.

axial thermal conductance. For temperatures above 20 K, most metals have a much higher heat capacity than the helium gas so work well as a regenerator material. The RAL coolers use stainless steel mesh at these temperatures. At lower temperatures, the heat capacities of most metals fall, and they become ineffective. At these temperatures, the RAL coolers use materials containing rare-earth elements which have peaks in their heat capacity at low temperatures [35]. At the warm end of the regenerator is a disc of metal foam made of Retimet [36] that is used to disperse the jets of gas entering the regenerator so that a larger fraction of the regenerator mesh is used for heat transfer. The displacer is contained within a thin wall Titanium Ti-6Al-4V cold finger tube which has a low thermal conductivity but is strong enough to withstand the gas pressure.

The coolers use helium as a working fluid. In general, lighter gasses enable greater heat transfer rates and lower pressure drops than heavier gasses [11, p. 175]. Both properties are beneficial for Stirling coolers. Hydrogen is the lightest gas, although its other properties mean that it is rarely used in Stirling coolers. It is flammable, can permeate through metals and can cause hydrogen embrittlement. The other disadvantage for use in cryocoolers is that its behaviour can deviate significantly from that of an ideal gas at low temperatures, increasing losses [37, p. 167]. Helium is used instead because it is inert and behaves more like an ideal gas at lower temperatures.

The typical fill pressure is between 10-20 bar and the operating frequency is typically between 20-100 Hz. The simple analysis presented in Section 2.2.1 shows that higher fill pressures and operating frequencies improve the cooling power for a given swept volume. However, increasing either of these increases the mass flow rate of gas through the regenerator, lowering its effectiveness and increasing the losses [11, p. 130]. The optimum fill pressure and frequency depend on the cooler geometry.

The compressor pistons and the displacer are run with a phase difference of 50-90° between their motions to produce cooling. The moving masses, diameters and flexure bearing stiffnesses of the displacer and compressor pistons are tuned so that the resonant frequency of their motion is the same as the operating frequency of the system. Running on resonance reduces the required input power and means that the motors only have to overcome the work done on the gas and the damping; the flexure bearings provide the rest of the force. Through careful selection of the displacer shaft diameter, the gas forces acting on the displacer can be adjusted so that the displacer runs at the correct amplitude and phase with minimal input from the motor. This reduces the force requirements for the displacer motor and allows it to be very compact.

The linear motors that drive the compressor pistons and displacer are designed at RAL. All the different types of motor consist of permanent magnets, iron and a coil, but these components are used in different configurations depending on the system requirements. Moving coil motors are typically used because of their low levels of off-axis vibrations [38]. The magnetic circuit is similar to a loudspeaker motor but has been modified to increase its efficiency. If a higher efficiency is required for the same size of motor, moving magnet motors are used [39].

A range of different sized single-stage Stirling cryocoolers have been developed at RAL: from the Small Scale Cooler [32] (Figure 2.7), which lifts 0.5 W at 77 K and has a mass of 625 g; to the Maxi (Figure 2.8), which lifts 6 W at 77 K and has a mass of 11 kg. Two-stage coolers have also been produced which can reach temperatures as low as 10 K [40].

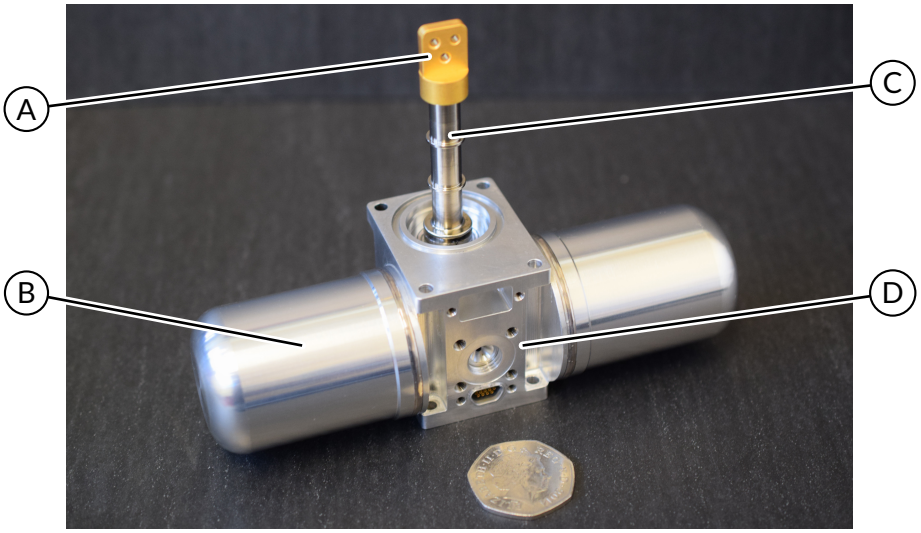

Figure 2.7: A photograph of the RAL Small Scale Cooler. The compressor and cold head of this cooler are integrated into the same body. Some parts of the cooler have been labelled: **A**, the cold tip; **B**, one of the compressor motor covers; **C**, the cold finger tube; and **D**, the body of the cooler (containing the displacer motor).

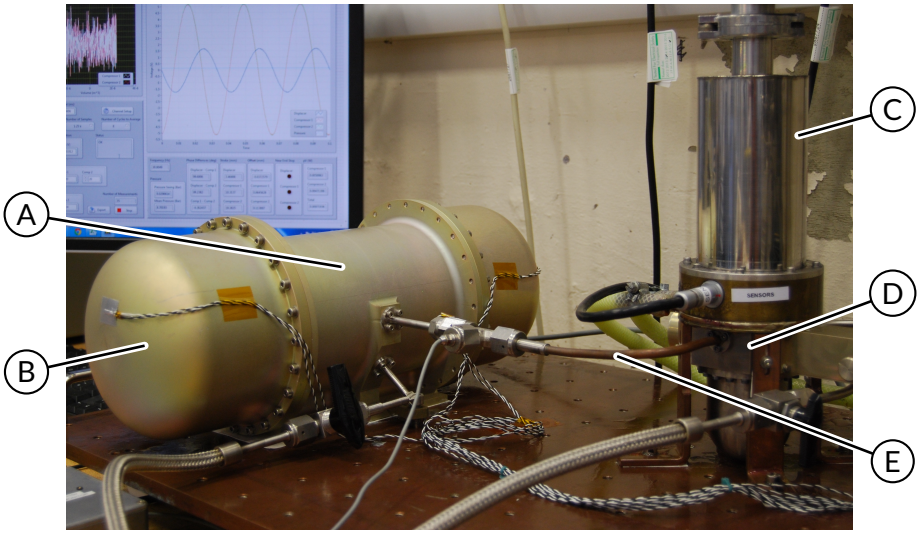

Figure 2.8: A photograph of the RAL Maxi compressor attached to a cold head. The compressor and cold head are connected by a transfer line. Some parts of the cooler have been labelled: **A**, the compressor body; **B**, one of the compressor motor covers; **C**, the vacuum vessel containing the cold finger; **D**, the cold head body; and **E**, the transfer line.

2.4 Stirling Machine Models

A wide range of Stirling machine models have been written about in the literature. Many of these models focus on Stirling engines, but the same techniques are often directly applicable to Stirling coolers; Stirling engines use the same thermodynamic cycle as Stirling coolers, but the cycle is reversed. A common classification, introduced by Martini [10], groups models by their complexity into first-order, second-order and third-order.

2.4.1 First-Order Models

First-order models are the simplest type and assume a simplified thermodynamic cycle without losses. Because of this, they are mostly used for approximate initial sizing of a Stirling machine.

Ideal Stirling Cycle

The ideal Stirling cycle presented in Section 2.2.1 is a form of first-order model. However, it makes several poor assumptions that prevent it from being useful for designing Stirling machines. The assumption of isothermal compression and expansion is inaccurate because Stirling coolers typically operate at a high frequency and there is insufficient time for the gas to thermalise. The model assumes that all the gas will be in the compression or expansion chambers during the isothermal stages; in a real cooler, there will always be gas present in the regenerator which will reduce the pressure swing. In addition, the model assumes that the compressor piston and displacer move sequentially, whereas they move almost sinusoidally in a real cooler.

Schmidt Isothermal Model

A more accurate thermodynamic cycle is the Schmidt isothermal model [14, p. 139]. This model still has a closed-form solution but can account for sinusoidal piston motion and dead volume within the cooler. It assumes that the gas in each region is perfectly thermalised with the region walls, that there are no regenerator losses and that the instantaneous pressure is the same throughout the system.

The Schmidt isothermal model is better at predicting the cooling power for a real machine than the ideal cycle. However, it still assumes that the compression and expansion occur isothermally; therefore, the coefficient of performance is still the same as for a Carnot refrigerator.

2.4.2 Second-Order Models

Second-order models simulate a more realistic thermodynamic cycle, and they account for loss mechanisms such as thermal conduction and imperfect regeneration. The assumption made by second-order models is that the losses do not interact with the thermodynamic cycle. The losses are calculated after the thermodynamic cycle has been computed and are subtracted to find the cooling power.

RAL Second-Order Model

The model that has previously been used at RAL to design Stirling coolers is a second-order model [7]. It is based on the Finkelstein adiabatic model [41]. The model makes the assumption that there is no heat transfer in the compression or expansion chambers. Instead, the heat transfer takes place in separate heat exchangers at either end of the regenerator. The gas in the heat exchangers and the regenerator is at a fixed temperature. The instantaneous pressure is assumed to be the same throughout the system. The system of differential equations cannot be solved analytically, so the equations are integrated over several cycles until a steady state is achieved; this typically takes five cycles.

After the system has converged, the pressure drop can be estimated from the mass flows. The pressure drop waveform is calculated by using empirical correlations for flow through pipes and wire meshes. This waveform is subtracted from the pressure waveform in the cold end expansion chamber. The model is also able to account for the finite speed of sound in the gas. The pressure waveform at the cold end is phase shifted to account for this. After the pressure waveform has been modified, the pressure-volume work done by the gas at the cold end is calculated to find the gross cooling power.

To calculate the net cooling power, the following losses are calculated and subtracted from the gross cooling power:

- **Conduction losses** — The model calculates the thermal conduction along the cold finger tube, displacer tube and the regenerator by using thermal conductivity integrals.
- **Shuttle heat transfer** — This is caused by the relative motion of the displacer tube and the cold finger tube and is described further in Section 3.7. The model uses the analytical equation derived by Zimmerman [42].
- **Regenerator loss** — This accounts for any incomplete cooling of the gas as it travels towards the cold end. The second-order RAL model can estimate the magnitude of these losses from the flow rate of the gas and empirical heat transfer correlations.

The model can simulate the temperature difference between the gas in the cold heat exchanger and the cold tip. The model uses thermal resistances that have been calibrated over a range of displacer strokes and operating frequencies using performance measurements of RAL coolers. This thermal resistance is then used to calculate an increased cold tip temperature.

The RAL Second-Order Model is much more accurate than the isothermal first-order models. The loss mechanisms have a large impact on the cooling power, particularly at lower temperatures. In addition, the adiabatic compression and expansion reduces the coefficient of performance of the cycle and is a much better approximation for typical Stirling coolers because of their high operating frequency. However, it is unable to simulate gas leakage past the clearance seals and, like all second-order models, it makes the assumption that the loss mechanisms do not interact with the thermodynamic cycle or each other.

The model has been found to be sufficiently accurate when simulating single-stage coolers that operate within the correlation ranges, and it can be useful for performing initial optimisations because it is able to run very quickly. However, the cold end heat transfer correlation is only valid over a limited range of operating frequencies and cooler sizes, and the model has difficulties accurately simulating two-stage coolers.

2.4.3 Third-Order Models

Third-order models are the most complex type in Martini's classification and are essentially one-dimensional computational fluid dynamics (CFD) models. They simulate the interactions of the loss mechanisms with the thermodynamic cycle. The machine is divided into a one-dimensional array of cells and the flow of gas between these cells is calculated. Correlations are used to simulate heat transfer and flow friction.

There are several third-order models that have been written about in the literature. Some of the models that have been described in detail are summarised here.

Model by Tew (1983)

Tew's model was developed at the NASA Lewis Research Center to simulate Stirling engines for use in automobiles [43]. It splits the system into control volumes and uses differential equations based on the conservation of mass and energy equations. The momentum equation is simplified to ignore the effects of gas inertia. This allows the pressure drop calculations to be decoupled from the thermodynamic calculations. Because the pressure wave dynamics are not simulated, much larger time steps can be used.

Model by Urieli (1977)

Urieli's model [9] was one of the first to fully model the inertial effects of the gas in a Stirling machine [44]. It models a simplified form of a Stirling engine that uses parallel pipes for its heat exchangers and regenerator; however, the model was designed so that it could be easily modified to include a wire mesh regenerator. The model solves the system of differential equations explicitly using a 4th order Runge-Kutta solver. Because of this, many time steps are required to track the propagation of acoustic waves through the system.

Model by Andersen (2006)

Andersen's model [4] also models the inertial effects of the gas, but it uses a semi-implicit Runge-Kutta scheme to remain stable with larger time steps. It is unusual because it can simulate the shuttle losses due to the relative motion

of the displacer tube and the cold finger tube at the same time as the rest of the thermodynamic cycle. The temperatures of the cells in the displacer and cold finger tubes are interpolated to calculate the heat transfer per unit length along the cold finger; this is integrated to find the rate of heat transfer for each cell.

DeltaEC

The Design Environment for Low-Amplitude Thermoacoustic Energy Conversion (DeltaEC) is a model that has been developed at Los Alamos National Laboratory [45]. It can simulate a wide variety of different systems, including thermoacoustic machines and Stirling coolers.

DeltaEC works by using an acoustic approximation for the gas pressure and flow rates, and it assumes that the pressure and volumetric flow oscillations are sinusoidal. The system is split into segments and the model numerically integrates the differential equations to find the amplitudes and phases of the pressure oscillations at each segment. These approximations enable the model to run very quickly but cause it to have a reduced accuracy at high pressure amplitudes.

Sage

Sage is a commercially available third-order model that is developed by Gedeon [5]. As well as modelling Stirling machines, it can be configured to model different types of periodic systems. Rather than starting with some initial conditions and letting the system converge to a steady state, the model sets periodic boundary conditions so that the start of a cycle is the same as its end. The whole cycle is then solved simultaneously. This allows Sage to solve simple models very quickly, although simulations with fine time or space discretisations can take much longer to solve.

The empirical correlations used by Sage are advanced for a third-order model. It can simulate the effects of oscillating flow in pipes by tracking the build-up of turbulence. It also uses equations for compression and expansion chambers that model the effects of inlet induced turbulence.

Because of its combination of speed, accuracy and versatility, Sage has become a very popular modelling tool for Stirling coolers [46], Stirling engines [47] and pulse tube coolers [48].

2.4.4 2D and 3D CFD Models

Since Martini developed his classification system, 2D and 3D CFD Stirling machine models have also been developed. Some of the models that have been described in the literature are summarised here.

Model by Mahkamov (2005)

One of the first three-dimensional Stirling machine models was developed by Mahkamov at Durham University [49]. This model simulates a Stirling engine powered by biomass and was created using the commercial software Fluent. The model is able to simulate the complicated geometry of the engine and predicts that there are differences in the flow velocity between the individual pipes of the hot heat exchanger.

To simplify the geometry of the regenerator, the model simulates it as a homogeneous object. The momentum and energy equations of the gas are modified to simulate heat transfer and flow resistance. This requires empirical correlations like the ones used in third-order models.

The simulated engine operates at a frequency of 3.3 Hz and the model runs until the temperatures reach a steady state. No artificial convergence method is mentioned (see Section 3.13). Presumably, the model is able to converge naturally in a small number of cycles because the simulated engine operates at a low frequency, allowing more time for heat transfer per cycle.

The model gives good results when compared to experimental data. The pressure-volume work was found to be within 12–18% of the measured value.

Model by Dyson et al. (2008)

A three-dimensional Stirling engine CFD model was developed at the NASA Glenn Research Center to aid the design of Stirling converters for use on spacecraft [8]. It is a highly detailed model: it simulates the motion of the displacer using a moving mesh and includes a full simulation of the appendix

gap and displacer gas seals. This detail requires a large amount of computing power; the full simulation took a few weeks to run on a cluster of 32 computers.

The model was developed using the commercial software Fluent. The simulation performance is highly dependent on the quality of the simulation grid, and it requires a significant amount of manual adjustment. The CFD model is integrated with the magnetic model of the linear motors to investigate the combined effect of the gas and magnetic force on the alternator pistons.

A simplified model of the regenerator is used; the fibres of the regenerator are not modelled, and the gas equations are modified to introduce a pressure drop. The model also makes the assumption that the regenerator and fluid are in thermal equilibrium which should result in the performance being overpredicted. However, the model predicts the motor performance to within the variability of manufactured machines. Dyson notes that this may be caused by the dissipative losses of the first-order accurate numerical solver cancelling out the reduction in regenerator losses.

Model by Della Torre et al. (2014)

This model was developed for the simulation of a beta-type Stirling engine [50]. The software package OpenFOAM was used to create a two-dimensional axisymmetric model of the engine. The model uses the regenerator heat transfer and flow resistance correlations developed by Gedeon and Wood [51]. The model converges naturally in 300-600 cycles when operating at 3.9 Hz and gives good agreement with experimental data.

2.4.5 Sub-System Models

Some models do not simulate an entire Stirling machine but focus on one specific component.

REGEN

The REGEN computer program is developed by the National Institute of Standards and Technology and focuses on modelling cryocooler regenerators

in isolation [52]. The program requires the user to input the mass flows, pressures and the inlet temperatures at either end of the regenerator. It is then able to calculate the pressure drop down the regenerator and the magnitude of the regenerator loss.

The program simulates the gas flow using one-dimensional CFD equations and can model the inertial effects of the gas. The REGEN program can be used as part of a second-order model with the pressures and mass flows calculated from the thermodynamic cycle being used as inputs.

2.4.6 Comparison of Modelling Approaches

A summary of the different types of Stirling system models is presented in Table 2.1.

First-order models do not account for any loss mechanisms. These losses are typically a large fraction of the gross cooling power, so first-order models are not accurate enough to be useful for designing Stirling cryocoolers.

Second-order models can be accurate if they are calibrated using experimental data. The second-order model used at RAL has been adjusted so that it makes good predictions for medium-sized Stirling coolers. However, experience has shown that these calibrations can become invalid if the model is used outside

Table 2.1: A table comparing different types of Stirling system models.

Order	Thermodynamics	Losses	Usage	Example
1st	Idealised thermodynamic cycle that can be solved analytically	Does not account for loss mechanisms	Initial sizing	[14, p. 139]
2nd	More realistic thermodynamics that must be solved numerically	Losses are calculated after the simulation has converged	Fast simulation	[7]
3rd	Accounts for pressure drop and imperfect heat transfer	Losses can interact with the thermodynamic cycle	Detailed simulation	[5]
CFD	Calculates pressure drop and heat transfer by simulating gas motion in multiple dimensions	Losses can interact with the thermodynamic cycle	Complex geometries	[49]

its calibrated regime. Some loss mechanisms, such as clearance seal leakage are difficult to simulate using second-order models, and second-order models do not account for any interactions between the different loss mechanisms.

Third-order models strike a good balance between accuracy and computational complexity. Friction and heat transfer correlations that are valid over a large parameter space can be used to make the model accurate for a wide range of different coolers. Third-order models can be slow to converge and typically require an artificial convergence method so that they can run quickly.

3D CFD models have the potential to produce the most accurate results. They can be much more accurate than third-order models when simulating Stirling machines that have flow paths with small length to diameter ratios [53]. Unfortunately, their complexity means that they take a very long time to run. Their complex simulation grid also makes applying an artificial convergence method challenging. Therefore, they are best suited to machines that operate at a low frequency and converge naturally in only a few cycles. Using a 2D axisymmetric model can speed up the simulation, but this simplification is not suitable for all Stirling machines. Although CFD models can simulate many loss mechanisms from first principles, their regenerators are typically modelled using the same friction and heat transfer correlations that are used in third-order models. These correlations can have a large impact on the predicted performance.

Chapter 3

Model Development

This chapter describes the development of the RAL Third-Order Model, a new Stirling cryocooler model that has been produced as part of this project. In this chapter, the requirements of the model are assessed and are used to justify the selection of the modelling approach. The modelling approach, the assumptions made by the model and the structure of the model are described.

To simulate Stirling coolers, the model divides the system up into cells; the method used to do this and the connections between the cells are explained. The state of the model at each point in time is defined by the solution variables and the rate of change of these solution variables is determined by a set of differential equations. These equations are presented, including the correlations used to represent flow effects in each type of cell. Some key features of the model are highlighted and described in detail. The methods used to interpolate the gas properties are described and the choice of numerical method used to solve the differential equations is explained. Before running, the model needs to calculate the initial state. The model's convergence is then accelerated by using a variety of different techniques. The methods used to initialise and converge the model are described. Finally, the information outputted by the model is listed.

3.1 Model Scope

The primary output of the model is the net cooling power at each stage. This is found by simulating the fluid dynamics, solid temperatures and heat flows within the cooler. The model inputs consist of the following:

- The geometry of the cryocooler
- The materials the cryocooler is made from

- The type of gas the cooler is filled with and the fill pressure and temperature at which it was filled
- The motion of the compressor pistons and displacer (input as the amplitudes, phases and mean value of a Fourier series)
- The temperatures of the thermal interfaces (the cryogenic stages and the heat rejection interfaces)
- The required spatial resolution of the model and the convergence parameters

A complete list of the inputs is given in Section A.3 in Appendix A. From these inputs, the model can calculate the cooling power at each stage and the required mechanical input power. Other outputs are also reported, and these are discussed in Section 3.15.

In this model, the thermal interfaces have a fixed temperature, and the cooling power is an output. The alternative would be to apply a fixed heat load at the stages and let the model calculate the stage temperatures. Modelling with fixed temperatures has the advantage that it is easier to make an accurate initial guess of the temperature distribution. The temperatures are typically the slowest values to converge, so a better initial guess can greatly reduce the time taken to converge. The other advantage of fixed temperatures is that cryocoolers are often designed to maximise cooling at a specific temperature; a fixed temperature model is simpler to use when optimising a design.

The model is designed to be able to simulate a wide range of Stirling cryocooler configurations just by changing the input file. The model can be configured to simulate a single-stage or a two-stage cryocooler. Any number of compressor pistons can be specified. There is the option of annular heat exchangers at the cryogenic stages. The user is also able to split the transfer line and regenerator into sections, with each section having its own geometry. Although there are multiple configuration options, the model is not fully modular like some models in the literature [4][5]. The advantage of not being modular is that the model can be controlled using a simple spreadsheet. In addition, a fully modular model would have difficulty simulating the heat transfer between the displacer tube and cold finger tube when they are moving relative to each other because the interface between these two modules would be very complicated (see Section 3.7).

It would be possible to extend the model to simulate the dynamics of the compressor pistons and displacer or even to include an electromagnetic

simulation of the linear motors. However, this extra complexity can cause issues when trying to design a cooler. It is much simpler to design the cooler with fixed compressor piston and displacer strokes, which allows the fluid dynamics to be modelled in isolation. The initial performance modelling of the cooler can then be conducted without any knowledge of what motors or flexure bearings will be required. Once this initial optimisation has been performed, the results can be used to determine the force requirements of the motors and the required stiffnesses of the flexure bearings.

3.2 Modelling Approach

From analysing the various modelling approaches seen in the literature (Section 2.4), a third-order model seems to be the most suitable for use in the development of RAL cryocoolers. RAL cryocoolers typically have flow paths that have large length to diameter ratios, which makes them well suited to the one-dimensional flow approximations of third-order models. They operate at high frequencies, so an artificial convergence method is required; this is much easier to implement in a third-order model than a 2D or 3D CFD model because of the reduced simulation grid complexity. It is possible to develop a third-order model that is accurate enough to be useful when designing new coolers and can run fast enough to be useful for design optimisation. The simple computational grid makes it easy to modify for different cooler geometries and the empirical correlations used can be easily adjusted to fit experimental data.

The equations of the RAL Third-Order Model form a system of partial differential equations with one space dimension and one time dimension. To solve these numerically, the finite difference method is used [54, p. 27]. The spatial dimension is discretised into cells and the partial differential equations can be solved as ordinary differential equations (ODEs).

The RAL Third-Order Model formulates the system as an initial value problem and lets the temperatures of the solids in the cooler gradually converge over several cycles (see Section 3.13). An alternative is to impose periodic boundary conditions; this technique is used by some of the third-order models in the literature, such as Sage. Periodic boundary conditions ensure that when the equations are solved, the system is in a periodic steady state. This can reduce the computational time required because only a single cycle has to be

simulated. Periodic boundary conditions are not used for the RAL Third-Order Model because the required numerical solver would be much more difficult to implement. Formulating the model as an initial value problem also provides advantages when simulating flow reversals in pipes (see Section 3.6.2).

The model has been written in the MATLAB programming language [55]. MATLAB was selected because it can perform fast calculations on arrays which is useful when evaluating the differential equations. MATLAB contains features that help to simplify the development of the model: the model can use the `parfor` structure that is built into MATLAB to run simulation cases in parallel and the model uses the built-in `ode15s` function to solve the differential equations (see Section 3.11).

3.2.1 Model Structure

The structure of the model is summarised in Figure 3.1. The model starts by loading a case from the input file, which is a Microsoft Excel `.xlsx` file (see Section A.3 in Appendix A). If the model is being validated, each case could represent different measured operating conditions or, if the model is being used to design a new cooler, each case could have a different value of one of the input parameters. The model uses the inputs to calculate the initial states of the solution variables and calculates aspects of the cooler geometry, such as splitting the cooler up into cells and evaluating the flow areas.

The model then simulates the cooler running for a single cycle. At each time step, the model calculates the new positions of the displacer and the compressor pistons from the Fourier components in the input file. The sizes of the variable volume cells are updated to account for these new positions. The model then uses the differential equations to calculate the rates of change of the solution variables and these rates of change are used by the ODE solver to calculate the solution variables for the next time step. An equation of state is used to calculate the thermodynamic properties used in the differential equations from the solution variables.

Once an entire cycle of the cooler has been simulated, the sparsity pattern of the Jacobin matrix is calculated. This is used to speed up the numerical method (see Section 3.11.2). Further cycles of the cooler are simulated, and an artificial convergence method is used to modify the solution variables to

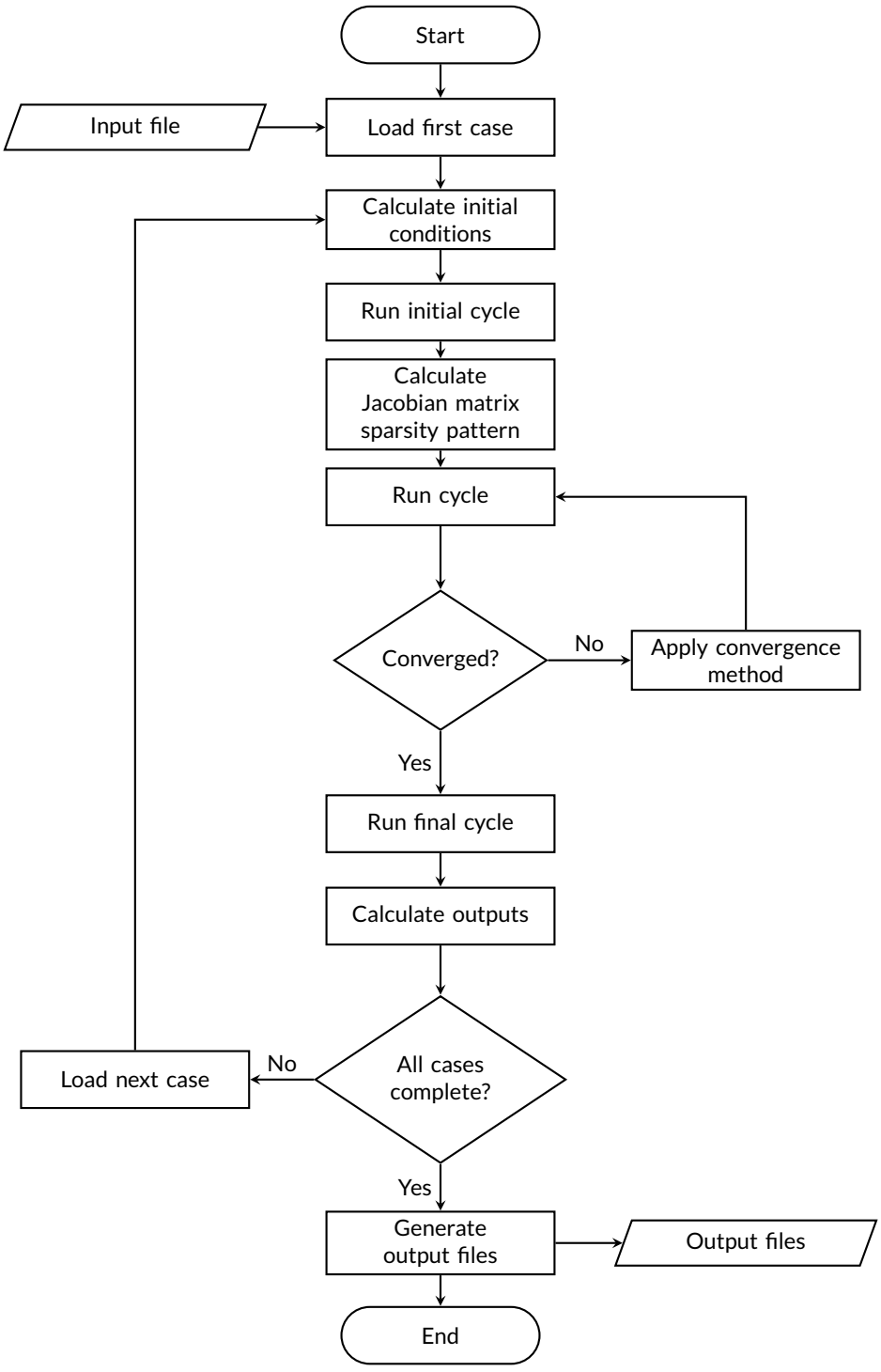

Figure 3.1: A flowchart showing the main steps of the model.

accelerate the rate of convergence. Once the system has converged, a final cycle is simulated, and the results of this cycle are reported in the output file.

3.2.2 Model Assumptions

The selected modelling approach requires the following assumptions to be made:

- The gas properties and solid properties in the model cells are assumed to be uniform within each cell. This can be an issue in the regenerator where the large temperature gradient can cause the material properties to vary significantly along its length. The effects of this assumption can be mitigated by using a finer spatial resolution (see Section 5.1.2).
- The flow regions are modelled using one dimension; the gas in each cell can only travel in one direction, along the length of the cell. This is not the case for a real cooler because effects such as turbulence and changes in flow area cause the flow to move in other dimensions. In addition, the model assumes that the flow velocity profiles and temperature profiles are uniform within each cell and are equal to the bulk velocity and bulk temperature (the mean velocity and temperature over the flow area). This is also not true in a real cooler because friction and heat transfer cause non-uniform profiles to develop. The model estimates the effects of multidimensional flow and non-uniform profiles by using correlations to calculate the pressure drops and rates of heat transfer from the bulk velocities and bulk temperatures.

3.3 Model Discretisation

The model is discretised using an Eulerian grid; this is where the cells are fixed relative to the geometry of the cooler and do not move with the gas. This discretisation method was chosen because different sections of the cooler have different flow friction and heat transfer correlations, so they interact with the gas in different ways. The flow paths are split into cells, as shown in Figure 3.2. The cells are labelled with is and the nodes between the cells are labelled with js. Flow towards the right is in the positive direction.

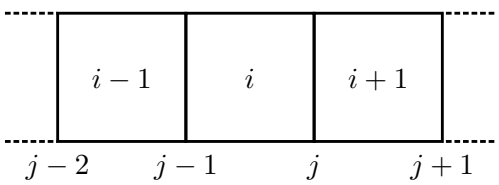

Figure 3.2: A diagram showing the relationship between the cells and nodes in the model.

The flow area of each cell is defined as the volume of gas in the cell divided by the cell length.

$$A_i = \frac{V_i}{x_i} \tag{3.1}$$

The flow areas of the gas cells are fixed, but the lengths of the variable volume cells and the second stage appendix gap cells vary as the compressor pistons and the displacer move. These cell lengths are updated at the beginning of each time step.

The gas cells are assigned types and are linked to other gas cells by flow paths. Figure 3.3 shows how the cells of a two-stage cooler with annular heat exchangers are linked. Cell layouts of other cooler configurations are shown in Appendix A (Section A.1). The primary flow path contains the compression and expansion chambers, the transfer line, the regenerators and the second stage heat exchanger. The secondary flow paths branch off the primary path and are used to simulate the backshells, the first stage displacer outlet and the appendix gaps. The physical regions that the cells correspond to are shown in Figure 3.4. Each gas cell type has its own correlation for flow friction and heat transfer, described in Section 3.6.1.

The solid cells of the model are assumed to have a uniform temperature. They can transfer heat with the gas cells and with the other solid cells via the thermal conduction paths shown in Figure 3.3. The isothermal cells represent the interface between the model and the external environment and heat can enter or exit the system at these cells. The model can simulate the effect of wall surface temperature fluctuations (see Section 3.9). This is achieved by using extra solid cells; the solid components in the cold finger are multiple cells thick and there are extra solid cells between the gas cells and the isothermal regions.

The spatial resolution of the model can be varied by adjusting the number of cells in the transfer line, displacer inlet, first stage expansion chamber inlet

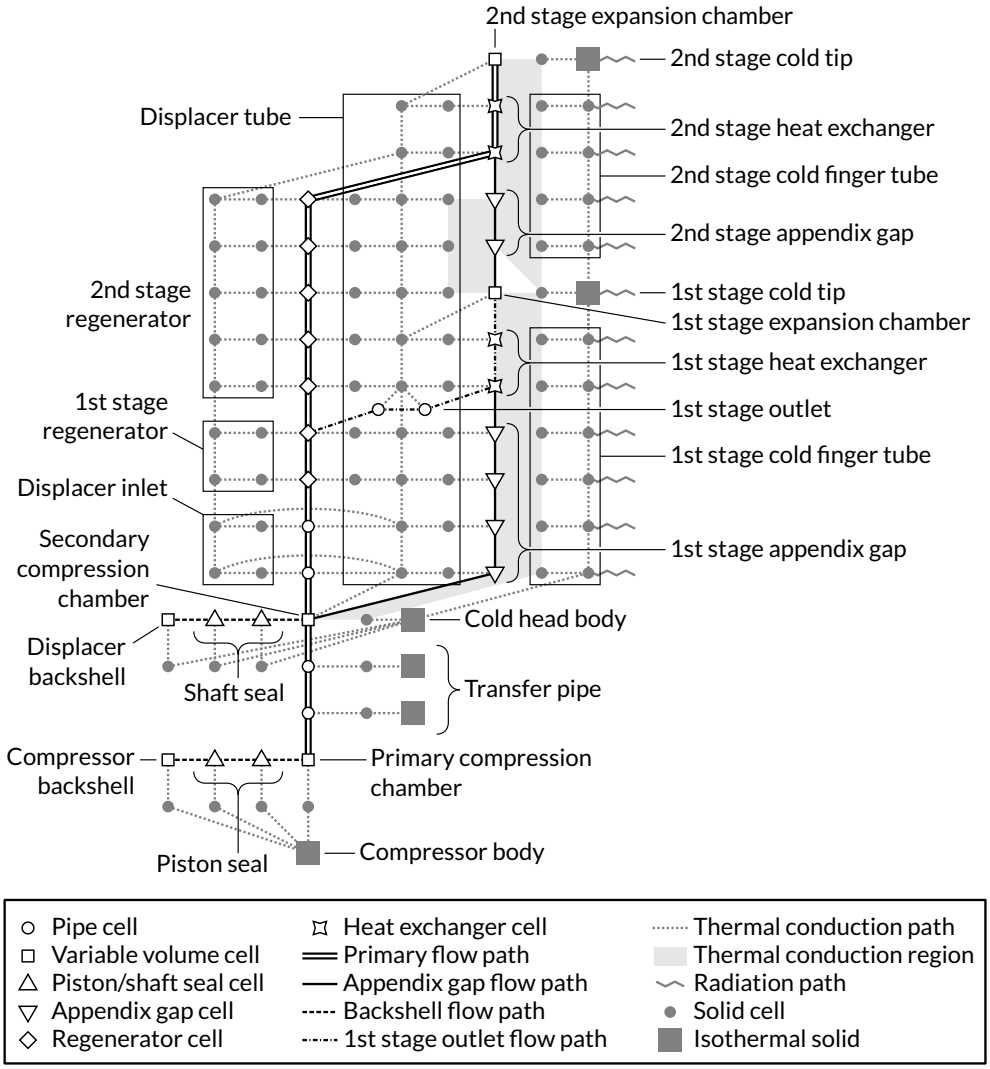

Figure 3.3: A diagram showing the connections between cells when simulating a two-stage cooler with annular heat exchangers. It is possible to adjust the spatial resolution of each section by adjusting the number of cells.

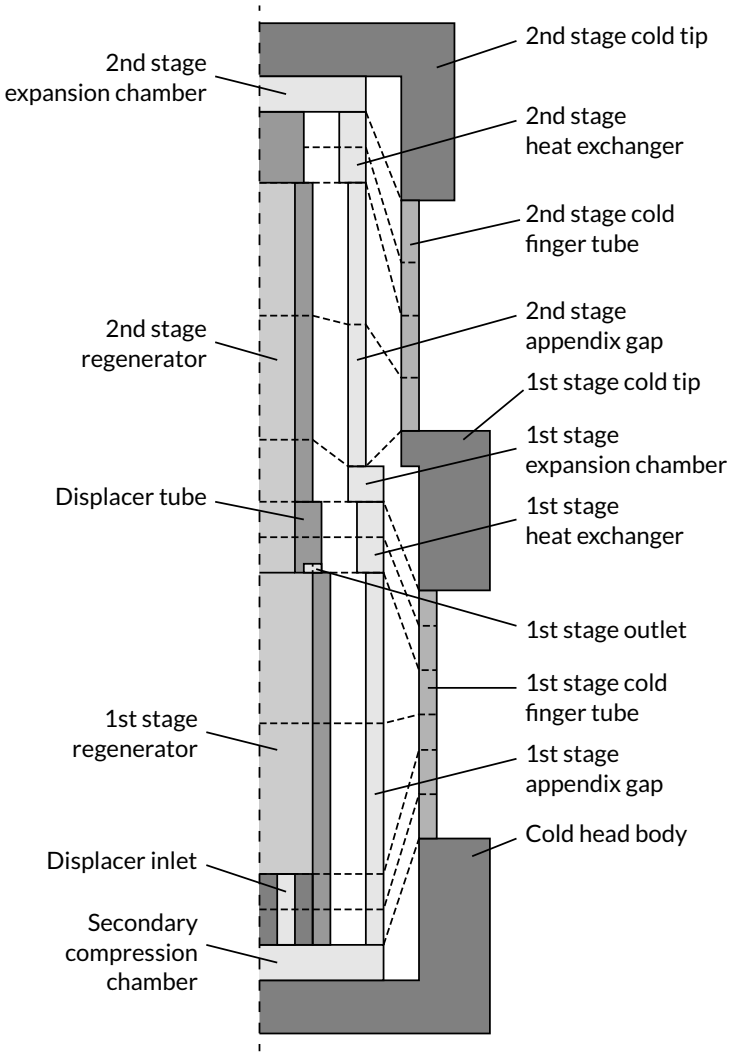

Figure 3.4: A diagram showing the physical locations of the cells of a two-stage cold finger with annular heat exchangers. This section view only shows half of the cold finger; the dashed vertical line represents the axis of symmetry. The cells of this diagram correspond to the cells of Figure 3.3. The dashed lines dividing the regions show the boundaries of the cells. These lines also indicate which cells are on the same rows of Figure 3.3.

and regenerator. It is also possible to model coolers with multiple compressor pistons; the pistons are combined and the model uses a single compression chamber, clearance seal and backshell.

3.4 Solution Variables

The solution variables are the dependent variables of the differential equations, and they define the state of the model at each point in time. Different regions of the model require different solution variables to represent their state.

3.4.1 Gas Domains

The model uses mass, linear momentum and energy as the solution variables for the flow paths. Turbulence kinetic energy is used as an additional solution variable for variable volume cells and turbulent mass is used as an additional solution variable for pipe and heat exchanger cells.

The differential equations are derived from the conservation laws of mass, linear momentum and energy. Selecting mass, momentum and energy as solution variables simplifies the formulation of the differential equations. Some Stirling machine models reformulate the differential equations to use different solution variables. For example, Sage uses density, energy per unit volume and mass flow rate [5, p. 210]. These properties are not affected by the size of the cells and are broadly constant across area discontinuities. This can make the differential equations easier to solve, depending on the type of solver used. However, using these variables can introduce complications when simulating variable volume cells. For example, if the volume of a cell is changed, the density must also be modified otherwise mass will not be conserved. Mass, momentum and energy were selected to avoid these complications and using these solution variables did not have an impact on the performance of the selected solver.

Control Volumes

Each solution variable has an associated control volume. The rates of change of the solution variables can be calculated by considering the interactions of

the gas within each control volume with its surroundings and the quantities of gas moving in and out of the control volume. The model's cells are used as the control volumes for all the solution variables apart from the momentums. The momentums use unique control volumes which are offset from the gas cells, as shown in Figure 3.5. Each momentum control volume corresponds to a node between two cells. Evaluating the momentums at the nodes is known as the staggered grid technique; this technique is commonly used in CFD models [54, p. 113]. Without a staggered grid, the velocity in each cell would be influenced by the pressures in the adjacent cells but would be unaffected by the pressure within its own cell. This can cause an unphysical "zig-zag" pressure distribution to form [9]. A staggered grid ensures that the pressure distribution is calculated correctly.

The momentum control volumes in the primary flow path (see Figure 3.3) extend between the midpoints of the cells. The flow area of each momentum control volume is chosen to be the same as the flow area at the node between the two cells (see Figure 3.5). Using the node flow area rather than expanding the momentum control volumes to fill the cells simplifies the calculation of the pressure forces in the differential equations (see Section 3.5.1). The momentum control volumes in secondary flow paths do not overlap with the main flow path because the model makes the assumption that there is no momentum flow between flow paths (see Section 3.5.1).

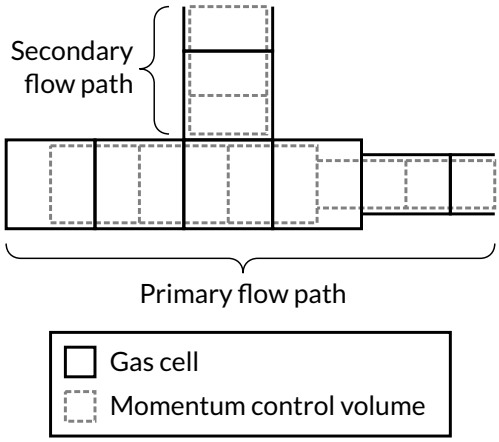

Figure 3.5: A diagram showing the relationship between the gas cells and the momentum control volumes.

Solution Variable Definitions

The mass of gas in each control volume is self-explanatory, but the definitions of the other solution variables are not as straightforward.

The momentum is defined as the product of the mass of gas in the momentum control volume and the bulk velocity of the gas in the flow direction.

$$p_j = m_j v_j \tag{3.2}$$

The mass of gas in the control volume can be calculated by finding the density of the gas in the adjacent cells and multiplying these densities by the volume of the momentum control volume that is within each cell.

$$\rho_i = \frac{m_i}{V_i} \tag{3.3a}$$

$$m_j = \frac{x_i}{2} A_j \rho_i + \frac{x_{i+1}}{2} A_j \rho_{i+1} \tag{3.3b}$$

The energy of the gas in each control volume is the sum of its internal energy and its kinetic energy.

$$E_i = U_i + \frac{1}{2} m_i {v_i}^2 \tag{3.4}$$

The turbulence kinetic energy K, used for the variable volume cells, is the kinetic energy of the turbulent motion of the gas particles. It does not include the kinetic energy due to the bulk motion of the gas. It is the product of the specific turbulence kinetic energy κ and the mass of gas in the cell.

$$K_i = m_i \kappa_i \tag{3.5}$$

The turbulent mass $m_{\mathcal{T}}$, used for the pipe and annular heat exchanger cells, is the product of the turbulence intensity $\mathcal{T}$ and the mass of gas in the cell. The turbulence intensity goes from 0 for laminar flow to 1 for fully turbulent flow.

$$m_{\mathcal{T}i} = m_i \mathcal{T}_i \tag{3.6}$$

Equations of State

An equation of state is used to calculate the pressure and temperature of each gas cell from the values of its solution variables. The model can use the ideal gas equation or simulate a real gas by using a lookup table.

For an ideal gas, the temperature and pressure can be calculated using the following equations:

$$T_i = \frac{E_i - \frac{1}{2} m_i v_i^2}{m_i c_V} \tag{3.7}$$

$$P_i = \rho_i R_g T_i \tag{3.8}$$

To model a real gas, first the densities and internal energies of each cell are calculated. These are then used to calculate the pressures and temperatures by using bilinear interpolation of lookup tables that are generated using REFPROP 9.1 [56] (see Section B.1 in Appendix B). Using a pre-generated lookup table is much faster than using REFPROP to calculate the gas properties as the model is running. The interpolation does not calculate the pressures and temperatures directly. Instead, it calculates a factor that would be constant if the gas was ideal. This helps to reduce the effect of any errors associated with the interpolation. For temperature, the factor f_T is approximately $1/c_V$.

$$T = f_T(u, \rho)\, u \tag{3.9}$$

For pressure, the factor f_P is approximately R_g/c_V.

$$P = f_P(u, \rho)\, \rho u \tag{3.10}$$

Calculating the Gas Properties

The steps used to calculate the properties of the gas cells must be carried out in a specific order, as shown in Figure 3.6. This is because certain gas properties can only be calculated once other ones are known.

Firstly, the gas velocities at each node are calculated from the momentums at the nodes. The masses at the cells are also required for this calculation because they are used to find the mass at each node. Once the node velocities have been found, they can be interpolated to calculate the gas velocities at each cell. The interpolation methods used by the model are discussed in Section 3.10. The remaining gas properties at each cell can then be calculated

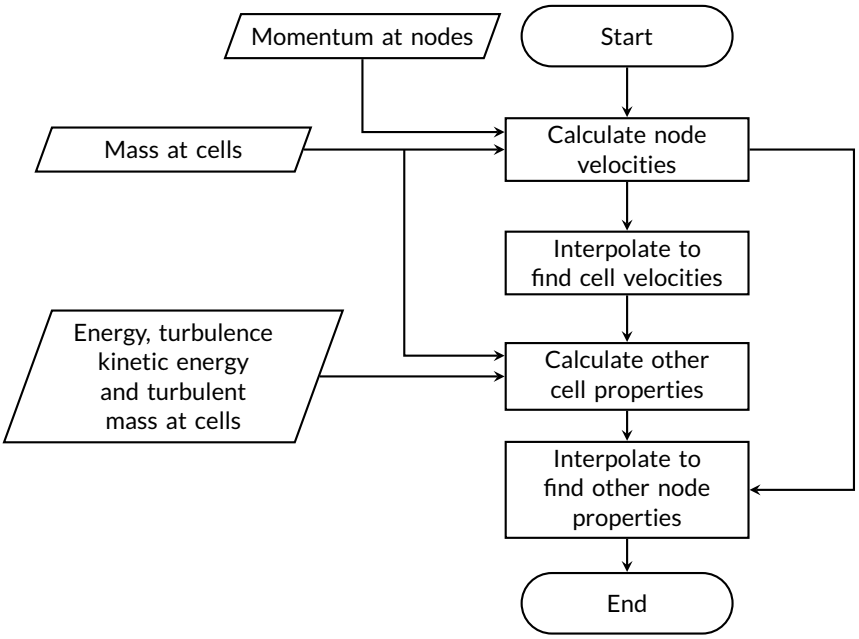

Figure 3.6: A flowchart showing the steps taken to calculate the gas properties at the cells and nodes from the solution variables.

by using the cell velocities and the solution variables. Finally, these properties can be interpolated to calculate the remaining node properties. This interpolation requires information about the gas velocities at the nodes (see Section 3.10).

3.4.2 Solid Cells

The model uses temperature as the solution variable for the solid cells. It would have been possible to use internal energy or specific internal energy as the solution variable instead. However, if internal energy was used as the solution variable, the temperature would need to be calculated from this energy and a function that links the two would have to be derived. It is much easier to find data in the literature that relates the rate of change of internal energy to the rate of change of temperature as this is simply the heat capacity. Using temperature as a solution variable means that its rate of change can be evaluated in the differential equations by using the heat capacity.

3.5 Differential Equations

The differential equations of the model relate the rates of change of the solution variables to the current state of the system.

3.5.1 Gas Domains

The model calculates the rate of change of the flow path solution variables by using the following equations. These equations relate to the gas flow in the primary flow path, shown in Figure 3.3. The secondary flow paths use very similar equations; they can transfer mass and energy with the primary flow path and the pressure of the gas in the primary flow path impacts the flow rate in the secondary flow paths. The exception is that there is no momentum flow between the flow paths; this is equivalent to assuming that the secondary flow path is orthogonal to the primary path.

Some of the cell boundaries in the model move with the displacer and compressor pistons. The effect of this cell motion is often not simulated by Stirling machine models. For example, Sage makes the simplification that the displacer is fixed, and it varies the volume of the cells at either end [5]. This has little impact for most cases but could potentially be an issue if the inertia of the gas becomes significant which could occur at very high frequencies. To avoid this, the motion of the cell boundaries is simulated in the RAL Third-Order Model.

The cell boundaries of the displacer inlet, regenerator, first stage appendix gap and the heat exchangers move with the displacer. The cell boundaries in the compressor piston clearance seals move with the compressor piston. For the second stage appendix gap, there is the complication that the location of the start of the seal is fixed, whereas the end of the seal moves with the end of the displacer (shown in Figure 3.4). To account for this, the boundary of each second stage appendix gap cell has a unique velocity, linearly interpolated from zero, at the start of the appendix gap, to the displacer velocity, at the end.

The relative gas velocity at the cells and nodes (indicated by †) is found by subtracting the velocity of the boundaries.

$$v_i^\dagger = v_i - \frac{v_{boundj-1} + v_{boundj}}{2} \tag{3.11a}$$

$$v_j^\dagger = v_j - v_{boundj} \tag{3.11b}$$

The model uses this relative velocity when calculating the forces acting on the gas and the amount of gas flowing between the cells. However, the absolute velocity is used when calculating the kinetic energy of the gas.

Mass

The equation for the rate of change of mass for each gas cell is derived from the law of conservation of mass. The rate of change is the difference between the mass flow rates into and out of the cell.

$$\frac{dm_i}{dt} = \dot{m}^{\dagger}_{j-1} - \dot{m}^{\dagger}_{j} \tag{3.12}$$

Momentum

The equation for the rate of change of momentum for each node is derived from the law of conservation of linear momentum. The rate of change is given by the sum of the momentum flow rate, the pressure force, the friction force and the minor loss force (which accounts for changes in flow area).

$$\dot{p}_j = \dot{p}_{flow_j} + F_{pres_j} + F_{fric_j} + F_{minor\,j} \tag{3.13}$$

In the model, it is possible for adjacent cells to have different flow areas. The momentum control volume spanning this area change must account for any forces in the flow direction that are due to the changing flow area. If the momentum control volume is defined so that it has a changing flow area (Figure 3.7a), the force on the gas due to the changing flow area F_2 must be accounted for. To calculate the force at the area change, the pressures of the adjacent cells can be interpolated, and this is the method used by Andersen [4, p. 27]. However, interpolating the pressure was found to cause instabilities when used in the RAL Third-Order Model, so a different approach was implemented to cope with area changes.

The method used in this model is depicted in Figure 3.7b. The pressure forces are calculated as if the flow area was constant and equal to the flow area of the node between them. This removes the need to calculate F_2. Unfortunately, artificially reducing the flow area introduces a further complication. For steady flow in a region of constant flow area, the momentum flow rate into the region should be equal to the momentum flow

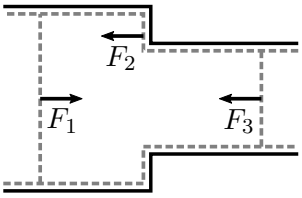

(a) The pressure forces if the flow area of the momentum control volume changes.

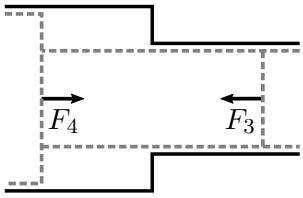

(b) The pressure forces if the flow area of the momentum control volume is constant.

Figure 3.7: A diagram showing different options for calculating pressure forces when there is a change in flow area.

rate out of the region. For steady flow in Figure 3.7b, the gas velocity at the left side of the region would be lower than the gas velocity at the right side, which would result in the momentum flows being unbalanced. This can be corrected by modifying the gas velocities to suit the artificially reduced flow area A_j. The modified velocities are indicated by $*$.

$$v_i^* = \frac{A_i}{A_j} v_i \tag{3.14a}$$

$$v_{i+1}^* = \frac{A_{i+1}}{A_j} v_{i+1} \tag{3.14b}$$

The net momentum flow rate is given by the momentum flow rate at the centre of the left cell minus the momentum flow rate at the centre of the right cell. The modified velocities are used for this calculation.

$$\dot{p}_{flow_j} = \dot{m}_i^\dagger \, v_i^* - \dot{m}_{i+1}^\dagger \, v_{i+1}^* \tag{3.15}$$

The pressure force is calculated using modified pressures. If the modified velocity is greater than the real velocity, the modified pressure will be lower due to Bernoulli's principle.

$$P_i^* = \left(P_i + \frac{1}{2} \rho_i v_i^2 \right) - \frac{1}{2} \rho_i v_i^{*2} \tag{3.16}$$

The pressure force is then found by subtracting the modified pressure in the centre of the left cell from the modified pressure in the centre of the right cell. The pressure acts on the flow area at the node to produce the force.

$$F_{pres_j} = A_j \, \left(P_i^* - P_{i+1}^* \right) \tag{3.17}$$

The friction force is calculated by summing the pressure drops due to friction ΔP in the two adjacent half cells and then multiplying by the flow area at the node. The correlations used to calculate the pressure drops are described in Section 3.6.

$$F_{fric_j} = -A_j \left(\frac{\Delta P_i}{2} + \frac{\Delta P_{i+1}}{2} \right) \tag{3.18}$$

When a fluid flows through a region with a sudden change in flow area, the fluid loses kinetic energy. To recover the kinetic energy, energy is taken from the pressure energy of the gas, resulting in a pressure drop. The amount of kinetic energy lost depends on the type of feature and is represented by the minor loss coefficient K_L. The minor loss is modelled as a force acting on the gas, given by Equation 3.19.

$$F_{minorj} = -A_j \, K_{Lj} \, \frac{\rho_j \, v_j^\dagger \, |v_j^\dagger|}{2} \tag{3.19}$$

- **Increase of Flow Area** — When the flow area increases, such as when the gas enters a variable volume space from a pipe, the model assumes that all kinetic energy is lost. Therefore, $K_L = 1$ [57, p. 2-11].
- **Decrease of Flow Area** — When the flow area decreases, such as when the gas enters a pipe, the model assumes that the velocity of approach is negligible and the pipe is sharp edged. Half of the kinetic energy is lost and $K_L = 0.5$ [57, p. 2-11].
- **Orifice** — For flow through an orifice, where the flow area at the node is smaller than in the cells either side, the model assumes that a vena contracta is formed, and all kinetic energy is lost. Therefore, $K_L = 1/0.61^2 \approx 2.69$ [58].
- **Regenerator** — Minor losses are not simulated when the gas enters or exits the regenerator because the minor loss pressure drop is accounted for by the flow friction correlation in the regenerator [59, p. 110].

Energy

The equation for the rate of change of energy for each gas cell is derived from the first law of thermodynamics. The rate of change of energy is given by the sum of the energy flow rate, the flow work rate, the gas conduction, the rate of

heat transfer with the adjacent solid cells and the mechanical work rate.

$$\frac{dE_i}{dt} = \dot{E}_{flow_i} + \dot{W}_{flow_i} + \dot{Q}_{cond_i} + \dot{Q}_{trans_i} + \dot{W}_{mech_i} \tag{3.20}$$

The energy flow rate accounts for the advection of energy into the cell. It is the sum of the flow rate of internal energy and kinetic energy into the cell minus the flow rate of internal energy and kinetic energy out of the cell.

$$\dot{E}_{flow_i} = \dot{m}^{\dagger}_{j-1}\left(u_{j-1} + \frac{v^2_{j-1}}{2}\right) - \dot{m}^{\dagger}_{j}\left(u_j + \frac{v^2_j}{2}\right) \tag{3.21}$$

The flow work rate is the power required to push gas across the boundaries between the cells. The cell gains energy when gas is pushed into it and loses energy when it pushes gas out. The flow work rate is given by

$$\dot{W}_{flow_i} = P_{j-1}\,\dot{V}^{\dagger}_{j-1} - P_j\,\dot{V}^{\dagger}_{j} \tag{3.22}$$

where $\dot{V}_j$ is the volumetric flow rate at the node.

$$\dot{V}_j = v_j A_j \tag{3.23}$$

The gas conduction rate is found by dividing the temperature difference between the current cell and its adjacent cell by the thermal resistance between the cell centres. This is done for both adjacent cells. The thermal resistance calculation uses the enhanced conductivity k_e to account for the effects of thermal dispersion (described in Section 3.6.1).

$$\dot{Q}_{cond_i} = \frac{T_{i-1} - T_i}{R_{i-1} + R_i} - \frac{T_i - T_{i+1}}{R_i + R_{i+1}} \tag{3.24a}$$

$$R_i = \frac{x_i}{2\,k_{ei}\,A_i} \tag{3.24b}$$

The formula used to calculate the rate of energy transfer with the solid cells $\dot{Q}_{trans_i}$ depends on the cell type. The formulas used are listed in Section 3.6.

The mechanical work rate is the product of the force applied to the gas cell by a moving component and the velocity of the component. The moving component could be the compressor piston, the displacer or a cell boundary. Energy is gained by the gas if the force and velocity are in the same direction

and is lost if they are in opposition.

$$\dot{W}_{mech\,i} = F_{mech\,i}\, v_{mech\,i} \tag{3.25}$$

The force applied to a gas cell by a moving component is the sum of a minor loss force, a flow friction force and a pressure force.

$$F_{mech\,i} = F_{minorMech\,i} + F_{fricMech_i} + F_{presMech_i} \tag{3.26}$$

The minor loss forces are calculated using Equation 3.19. In the appendix gaps and the piston and shaft clearance seals, some of the minor loss force is applied by the moving component, but some is applied by the stationary wall so does not need to be included in the energy calculation. To account for this, the force is scaled by the ratio between the surface area per unit length of the moving component $s_{mech\,j}$ and the total surface area per unit length of the node s_j. The force is assumed to be applied by the downwind cell so that the energy is deposited downwind of the node.

$$F_{minorMech\,i} = F_{minorLeft_i} + F_{minorRight_i} \tag{3.27a}$$

$$F_{minorLeft_i} = \begin{cases} F_{minor\,j-1} \frac{s_{mech\,j}}{s_j} & \text{if } \dot{V}_{j-1} > 0 \\ 0 & \text{otherwise} \end{cases} \tag{3.27b}$$

$$F_{minorRight_i} = \begin{cases} F_{minor\,j} \frac{s_{mech\,j}}{s_j} & \text{if } \dot{V}_j < 0 \\ 0 & \text{otherwise} \end{cases} \tag{3.27c}$$

The friction forces applied to the gas by the moving components are a superposition of two forces: a Poiseuille flow force and a Couette flow force. The Poiseuille flow force is caused by the motion of the gas relative to the mean velocity of the walls and is calculated from the frictional pressure drops used in Equation 3.18. This force is scaled in a similar way to the minor loss forces to account for cells where some of the wall is stationary. The Couette flow force is caused by the relative motion between the moving component (with surface area $S_{mech\,i}$) and the stationary wall. It is derived from Newton's law of viscosity. It is only present in the cells where there are fixed and moving walls, such as the clearance seals. The superposition of the two forces is only valid for laminar flow; the flow in the clearance seals is typically laminar, so

this is a reasonable assumption.

$$F_{fricMech_i} = F_{Poiseuillei} + F_{Couettei} \tag{3.28a}$$

$$F_{Poiseuillei} = -\Delta P_i A_i \frac{s_{mechi}}{s_i} \tag{3.28b}$$

$$F_{Couettei} = \frac{\mu S_{mechi} v_{mech}}{a_i} \tag{3.28c}$$

where a is the radial gap size.

The pressure force applied by the moving components is the product of the pressure at the cell boundary and the gas flow area. The force on the left of the cell is positive and the force on the right is negative. This force is only calculated for cell boundaries that are moving with the compressor piston or displacer.

$$F_{presMech_i} = (P_{j-1} - P_j)\, A_i \tag{3.29}$$

The pressure force is calculated for the entire gas flow area and not just the solid area of the compressor piston or displacer. This ensures that Equation 3.25 correctly accounts for the work done by the moving cell boundary. If two cells share a boundary and have the same flow area, equal and opposite forces will be applied to the two cells and there will be no net change in energy due to the motion of the boundary.

Turbulence Kinetic Energy

The level of turbulence kinetic energy in the variable volume spaces is used for calculating the rate of heat transfer (see Section 3.6.4). The rate of change of turbulence kinetic energy is based on the method used by Sage [5, p. 233] and is given by the sum of the flow rate and the rate of decay.

$$\frac{dK_i}{dt} = \dot{K}_{flow_i} + \dot{K}_{decay_i} \tag{3.30}$$

The turbulence kinetic energy flow rate is the net flow rate of turbulence kinetic energy into the cell.

$$\dot{K}_{flow_i} = \dot{m}^{\dagger}_{j-1}\, \kappa_{j-1} - \dot{m}^{\dagger}_{j}\, \kappa_j \tag{3.31}$$

The method used to calculate κ at each node is discussed in Section 3.10.3.

The rate of decay is a function of κ. The empirical correlation that is used is given in Section 3.6.4.

Turbulent Mass

The level of turbulence in pipe and heat exchanger cells can affect the flow friction and the rate of heat transfer with the walls. The turbulence in pipe and heat exchanger cells is calculated in a different way to the turbulence in variable volume cells. The RAL Third-Order Model uses the same turbulence model as Sage [5, p. 225]. The rate of change of turbulent mass for each pipe and heat exchanger cell is given by the sum of the flow rate, the rate of generation and the rate of decay.

$$\frac{dm_{\mathcal{T}_i}}{dt} = \dot{m}_{\mathcal{T}_{flow_i}} + \dot{m}_{\mathcal{T}_{generation_i}} + \dot{m}_{\mathcal{T}_{decay_i}} \tag{3.32}$$

The turbulent mass flow rate is the net flow rate of turbulent mass into the cell.

$$\dot{m}_{\mathcal{T}_{flow_i}} = \dot{m}^{\dagger}_{j-1}\,\mathcal{T}_{j-1} - \dot{m}^{\dagger}_{j}\,\mathcal{T}_{j} \tag{3.33}$$

The method used to calculate $\mathcal{T}$ at each node is discussed in Section 3.10.3.

A generation term is present in the equation to account for the fact that turbulence in a pipe can occur spontaneously if the flow is fast enough. The equations used for determining the rate of turbulence generation and decay are given in Section 3.6.2.

3.5.2 Solid Cells

For the solid cells, the rate of change of temperature is evaluated at each time step. These rates of change are then used to calculate the temperatures at the next time step.

The equation for the rate of change of temperature of the solid cells is derived from the law of conservation of energy. The rate of change of temperature can be calculated from the rate of internal energy change. The specific heat capacity c_s is calculated using the temperature of the cell at the previous time

step (see Section B.2.2 in Appendix B).

$$\frac{dT_{si}}{dt} = \frac{1}{m_{si}c_{si}}\frac{dU_{si}}{dt} \tag{3.34}$$

The rate of change of energy is given by the sum of the axial and radial conduction rates with neighbouring solid cells, the rate of heat transfer with the gas and the radiation load from the environment.

$$\frac{dU_{si}}{dt} = \dot{Q}_{s\,axial\,i} + \dot{Q}_{s\,radial\,i} + \dot{Q}_{s\,transi} + \dot{Q}_{s\,radi} \tag{3.35}$$

The axial conduction rate is found by dividing the temperature difference between the current cell and its adjacent cell by the thermal resistance between the cell centres. This is done for both adjacent cells to find the net conduction rate.

$$\dot{Q}_{s\,axial\,i} = \frac{T_{si-1} - T_{si}}{R_{i-1} + R_i} - \frac{T_{si} - T_{si+1}}{R_i + R_{i+1}} \tag{3.36a}$$

$$R_i = \frac{x_i}{2\,k_{si}\,A_{si}} \tag{3.36b}$$

where k_s is the thermal conductivity of the solid and A_s is the cross-sectional area of the solid. For regenerator cells, the tortuosity τ and porosity ϕ are accounted for (see Section 3.6.1).

$$R_i = \frac{x_i}{2k_{si}A_{si}\tau_i\,(1-\phi_i)} \tag{3.36c}$$

This axial thermal conduction is only calculated between the interior cells of the solid components and not the wall cells (see Section 3.9). The entire cross-sectional area is used when calculating the thermal resistance.

A similar formula is used to calculate the radial conduction between each cell (cell i) and the cells that are radially adjacent (either inside or outside of cell i). $T_{s\,inner}$ and $T_{s\,outer}$ are the inner and outer cell temperatures and R_{inner} and R_{outer} are the thermal resistances between those cells and cell i. The calculation of the thermal resistances is described in Section 3.9.

$$\dot{Q}_{s\,radial\,i} = \frac{T_{s\,outer} - T_{si}}{R_{outer}} - \frac{T_{si} - T_{s\,inner}}{R_{inner}} \tag{3.37}$$

The rate of energy transfer to the solid from the gas is the same as the rate of energy transfer to the gas from the solid but with the opposite sign. The correlations used are listed in Section 3.6.1.

$$\dot{Q}_{s\,trans\,i} = -\dot{Q}_{trans\,i} \tag{3.38}$$

The radiation load acts on the outermost cold finger cells. The formula used depends on whether the cold finger is wrapped in multi-layer insulation. The equations for the radiation loads are given in Section 3.8.

3.6 Cell Correlations

The one-dimensional approach of simulating the gas flow means that correlations specific to each cell type are required to calculate the pressure drops, the rates of heat transfer and the increased thermal conduction due to the mixing of the gas. Each type of gas cell uses different correlations for simulating these effects. The regenerator solid cells use correlations to simulate the reduction in axial thermal conduction due to their complex geometry.

3.6.1 Cell Correlation Equations

The model uses cell correlations to calculate dimensionless factors. These factors are then used to calculate physical quantities used by the differential equations. Friction factors are used for calculating the pressure drops, Nusselt numbers are used for calculating heat transfer and conduction enhancement factors are used to simulate the increased thermal conduction in the gas. The tortuosity is used to calculate the reduction in thermal conductivity in the regenerator cells.

The correlations used to determine these factors often use dimensionless numbers that represent a ratio between two flow properties.

- The Reynolds number is the ratio of inertial forces to viscous forces within a fluid [60, p. 271]. It is used to determine the onset of turbulent flow in the fluid.

$$Re = \frac{\rho\, v\, d_h}{\mu} \tag{3.39}$$

where d_h is the hydraulic diameter which is equivalent to the pipe diameter if the pipe has a circular cross-section and can be calculated using the volume V and surface area S for other duct geometries [60, p. 369].

$$d_h = \frac{4V}{S} \tag{3.40}$$

- The Prandtl number is the ratio of momentum diffusivity to thermal diffusivity [60, p. 611]. It is used in heat transfer correlations.

$$Pr = \frac{c_P \, \mu}{k} \tag{3.41}$$

- The Valensi number is related to the ratio of hydraulic diameter to viscous penetration depth [5, p. 206] and can be thought of as a dimensionless frequency. It is used in oscillating flow correlations.

$$Va = \frac{\rho \, \omega \, d_h^2}{4\mu} \tag{3.42}$$

- The turbulent Reynolds number is similar to the conventional Reynolds number, but the bulk flow velocity is replaced by the square root of the specific turbulence kinetic energy κ (from Equation 3.5). This dimensionless number is used for correlations in variable volume cells.

$$Re_{\mathcal{T}} = \frac{\rho \, d_h \, \kappa^{0.5}}{\mu} \tag{3.43}$$

Some the correlations that have been developed for oscillating flow simulate frictional forces or heat transfer that is out of phase with the oscillation of bulk velocity or bulk temperature. The model does this by using complex numbers. The velocities and temperatures are split into a real component and an imaginary component. This can be thought of as similar to how a complex sinusoid has a real and imaginary component.

$$e^{i\omega t} = \cos(\omega t) + i \sin(\omega t) \tag{3.44}$$

The real component is the current value of the gas property, and the imaginary component is a quarter cycle behind. If this complex representation of the gas property is then multiplied by a complex factor to calculate the force or rate of

heat transfer, the calculated value will be phase shifted relative to the gas property.

To convert the temperatures and velocities into this complex form, they are first split into their steady and oscillating components, $\bar{y}$ and $\boldsymbol{y}(t)$, where only the oscillating component is complex. The steady component is calculated by finding the mean value of the variable over the previous cycles $\bar{y}_{last}$. The real part of the oscillating component is calculated by subtracting $\bar{y}_{last}$ from the current value. The imaginary part of the oscillating component is found by phase shifting the previous cycle's variable by a quarter of a cycle and subtracting $\bar{y}_{last}$.

$$\bar{y} = \bar{y}_{last} \tag{3.45}$$

$$\Re\left[\boldsymbol{y}(t)\right] = y(t) - \bar{y}_{last} \tag{3.46a}$$

$$\Im\left[\boldsymbol{y}(t)\right] = y_{last}(t - \tfrac{1}{4f}) - \bar{y}_{last} \tag{3.46b}$$

The evaluation of y_{last} is performed by using a weighted mean of the previous three cycles to improve the convergence stability.

$$y_{last} = \frac{3y_{k-1} + 2y_{k-2} + y_{k-3}}{6} \tag{3.47}$$

where k represents the current cycle.

Friction

The frictional force opposing the motion of a fluid is a combination of viscous shear (skin friction) and pressure force (form drag) [59, p. 8]. Because the model simulates the flow as one-dimensional, there is no simulation of viscous shear or changes in flow direction, and an additional equation must be used to model the frictional effects.

The pressure drop due to friction is modelled using the Darcy-Weisbach equation [60, p. 127]. This relates the pressure drop to the Darcy friction factor f_D.

$$\frac{\Delta P}{x} = \frac{f_D\, \rho\, {v^\dagger}^2}{2\, d_h} \tag{3.48}$$

where $v^\dagger$ is the relative velocity between the gas and the solid components. In the clearance seals, the walls can move relative to each other. In this case, the relative gas velocity is calculated by subtracting the mean wall velocity from the gas velocity. The pressure drop is used in the differential equations to evaluate the rate of change of momentum (Equation 3.18).

The friction factor correlations used for some cells can tend to infinity when the gas is stationary relative to its surroundings. This causes the model calculations to fail. To overcome this, the model calculates $f_D Re$ instead of f_D and uses this to evaluate the pressure drop. This is the method proposed by Urieli [9].

$$\Delta P = \frac{(f_D Re)\, v^\dagger\, \mu\, x}{2\, d_h^2} \tag{3.49}$$

In the regenerator and clearance seal cells, the flow velocity profile is assumed to be fully developed throughout the cycle because the hydraulic diameters are typically very small. This means that the pressure drop is only dependent on the bulk flow velocity and the friction factor is a real number. However, in the pipe and annular heat exchanger cells, this assumption is no longer valid, and the model accounts for pressure drops that are out of phase with the velocity due to the oscillating flow. These cells use the complex velocity $\boldsymbol{v}^\dagger$ and a complex friction factor $\boldsymbol{f_D Re}$ to achieve the required pressure drop phase shift. This is added to the steady component of the pressure drop which is calculated using the cycle-averaged velocity $\bar{v}^\dagger$ and a steady-state friction factor $(f_D Re)_0$.

$$\Delta P = \frac{(f_D Re)_0\, \bar{v}^\dagger\, \mu\, x}{2\, d_h^2} + \frac{\Re\left[(\boldsymbol{f_D Re})\, \boldsymbol{v}^\dagger\right]\, \mu\, x}{2\, d_h^2} \tag{3.50}$$

Heat Transfer

Most of the cell types calculate the rate of heat transfer using the Nusselt number Nu, which is the ratio of convective to conductive heat transfer [61, p. 402]. The rate of heat transfer is proportional to the Nusselt number [60, p. 274], and the Nusselt number is greatly increased when the flow becomes turbulent. Each cell type has its own correlation for the Nusselt number; the exception is for laminar flow in the appendix gaps, which uses a unique equation to cope with situations where the walls differ in temperature.

For the regenerator and clearance seal cells, the model assumes that heat transfer is proportional to the difference between the solid temperature and the bulk gas temperature because the hydraulic diameters are typically very small. The rate of heat transfer is calculated using Equation 3.51.

$$\dot{Q}_{trans} = \frac{Nu\, k\, S}{d_h} \left(T_s - T\right) \tag{3.51}$$

where k is the thermal conductivity of the gas, S is the surface area of the solid in contact with the gas, T is the bulk gas temperature and T_s is the wall temperature. In the regenerator cells, the heat transfer with the inner wall of the displacer tube is modelled using the same Nusselt number as the heat transfer with the regenerator.

For the variable volume, pipe and annular heat exchanger cells, the heat transfer can be out of phase with the temperature difference due to the oscillating flow. For these cells, complex Nusselt numbers and complex formulations of the temperatures are used. The heat transfer in variable volume cells is given by the following equation:

$$\dot{Q}_{trans} = \frac{S\, k}{d_h} \left(Nu_0 \left(T_s - \bar{T}\right) - \Re\left[\boldsymbol{Nu}\, \boldsymbol{T}\right]\right) \tag{3.52}$$

For the pipe and annular heat exchanger cells, the complex temperatures are split into compression and advection components. This is because heat transfer for laminar oscillating flow occurs at a different rate depending on whether the temperature change is due to advection or compression [5, p. 213].

$$\dot{Q}_{trans} = \frac{S\, k}{d_h} \left(Nu_0 \left(T_s - \bar{T}\right) - \Re\left[\boldsymbol{Nu_c}\, \boldsymbol{T_c}\right] - \Re\left[\boldsymbol{Nu_a}\, \boldsymbol{T_a}\right]\right) \tag{3.53}$$

The model only calculates the total oscillating temperature $\boldsymbol{T}$ so the relative contribution of the compression and advection components must be estimated. The model assumes that the compression component $\boldsymbol{T_c}$ consists of any temperature oscillation that is in phase with the pressure oscillation because the compression component is caused by the pressure variation. It is calculated by scaling the oscillating pressure of the previous cycle by a real factor λ until it matches the oscillating temperature of the previous cycle as closely as possible, using a least-squares fit. This scale factor is then used to

calculate $\boldsymbol{T_c}$ at each time step of the current cycle from the oscillating pressure $\boldsymbol{P}$. The remaining oscillating temperature is assumed to be $\boldsymbol{T_a}$.

$$\boldsymbol{T_c} = \lambda\, \boldsymbol{P} \tag{3.54a}$$

$$\boldsymbol{T_a} = \boldsymbol{T} - \boldsymbol{T_c} \tag{3.54b}$$

Conduction Enhancement

As the gas flows, any turbulence can cause mixing of the gas. This mixing results in thermal dispersion which enhances the effective thermal conductivity of the gas. This effect is modelled by multiplying the thermal conductivity of the gas by a conduction enhancement factor N_k, which the model calculates with different correlations for each cell type. The enhanced thermal conductivity k_e is used in the differential equations to calculate the rate of change of energy (Equation 3.24).

$$k_e = N_k\, k \tag{3.55}$$

Tortuosity

The solid cells in the regenerator have correlations that are used for modelling thermal conduction. The thermal conduction through a regenerator is dependent on the shape of the matrix. For wire meshes, the thermal energy must take a longer path to reach the cold end than it would if the wires ran straight from the warm to the cold end. This can be represented by the tortuosity τ which is defined as the effective thermal conduction cross-sectional area divided by the mean cross-sectional area of the solid.

$$\tau = \frac{A_{effective}}{A_s} \tag{3.56}$$

It is used in Equation 3.36 of the differential equations.

3.6.2 Pipes

The same friction factors and heat transfer correlations are used for the transfer line, the displacer inlet and the displacer outlet (at the first stage of two-stage coolers). The pressure drop and heat transfer in pipes depends on the frequency of oscillation [62]. When the flow is laminar and oscillating, the

friction factor and Nusselt number are different than would be expected for steady flow with the same bulk velocity. This is because the velocity of the fluid near the wall can be out of phase with the bulk velocity. However, when the flow is turbulent and oscillating, the steady-state correlations correctly predict the friction factor and Nusselt number [5, p. 252].

Turbulence

The transition from the laminar to the turbulent regime for oscillating flow occurs at a higher Reynolds number than for steady-state flow. However, once the gas becomes turbulent, it stays turbulent until the Reynolds number drops to the steady-flow laminar range [5, p. 230]. Empirical correlations are used to determine when turbulence generation should occur and the magnitude of turbulence generation and decay. These rates of generation and decay are used in Equation 3.32.

The turbulence model is based on the model developed for the Sage software [5, p. 225] which assumes that the onset of turbulence is delayed because the boundary layer takes time to grow. The boundary layer starts growing when the flow reverses. In the RAL Third-Order Model, turbulence generation starts when the following condition is met:

$$Re > \max\left[\frac{200\sqrt{Va}}{0.075 + 0.112\omega\,(t - t_0)}, 2300\right] \tag{3.57}$$

In this expression $(t - t_0)$ is the time since flow reversal and ω is the angular frequency. Turbulence generation ends when the Reynolds number drops below 2300, and turbulence decay occurs whenever generation is turned off.

The RAL Third-Order Model calculates the times that turbulence generation and decay occur by analysing the results of the previous cycle. Because the model gradually converges to a periodic steady state, it is reasonable to assume that the turbulence generation times will be the same from one cycle to the next. Firstly, the times of flow reversal are calculated for each cell and then the turbulence generation and decay switching times are calculated by using the Reynolds numbers.

The equation for the rate of turbulence generation in each cell is the same as the one used in the Sage model:

$$\dot{m}_{\mathcal{T}\,generation} = 0.008\,\frac{\omega\, m\, Re\ (1-\mathcal{T})}{Va} \tag{3.58}$$

where $\mathcal{T}$ is the turbulence intensity, defined in Section 3.4.1. The factor of $(1-\mathcal{T})$ prevents $\mathcal{T}$ from exceeding 1.

The equation for the rate of turbulence decay is also the same as the one used in the Sage model:

$$\dot{m}_{\mathcal{T}\,decay} = -0.25\,\frac{2300\,\omega\, m\, \mathcal{T}^{\frac{2}{3}}}{Va} \tag{3.59}$$

Sage uses a smoothing term to aid model stability. The RAL Third-Order Model does not use a smoothing term as it was found to have little impact on the speed or stability of the model.

Friction

Two separate friction factor correlations are used for flow in pipes: a complex factor for the oscillating flow $\boldsymbol{f_D Re}$ and a real factor for the steady-state flow $(f_D Re)_0$. These are used in Equation 3.50 to calculate the pressure drop.

The complex factor uses different correlations for simulating laminar and turbulent flow. The laminar friction forces can be out of phase with the bulk velocity for oscillating flow. The exact functions are complex Bessel functions which would be difficult for the model to compute [5, p. 252]. Instead, the model uses the same approximations as the Sage model.

$$\Re\left[(\boldsymbol{f_D Re})_{\boldsymbol{L}}\right] = \begin{cases} 64 & \text{if } Va \leq 32 \\ \sqrt{128\,Va} & \text{otherwise} \end{cases} \tag{3.60a}$$

$$\Im\left[(\boldsymbol{f_D Re})_{\boldsymbol{L}}\right] = \begin{cases} \frac{8\,Va}{3} & \text{if } Va \leq 18 \\ \sqrt{128\,Va} & \text{otherwise} \end{cases} \tag{3.60b}$$

The turbulent frictional forces are in phase with the bulk velocity and the Haaland correlation is used for turbulent flow [63]. This equation was developed for steady-state flow and is not valid for turbulence at low Reynolds numbers which can occur in the model if the flow slows down before the turbulence has decayed. This issue is mitigated by preventing the

Reynolds number used in this equation from dropping below 2300.

$$(f_D Re)_T = Re^* \left(-1.8 \log_{10} \left(\left(\frac{\epsilon/d_h}{3.7} \right)^{1.11} + \frac{6.9}{Re^*} \right) \right)^{-2} \tag{3.60c}$$

where

$$Re^* = \begin{cases} 2300 & \text{if } Re < 2300 \\ Re & \text{otherwise} \end{cases} \tag{3.60d}$$

These are then weighted with the turbulence intensity $\mathcal{T}$ and summed to give $\boldsymbol{f_D Re}$, which is used in Equation 3.50.

$$\boldsymbol{f_D Re} = \boldsymbol{(f_D Re)_L} (1 - \mathcal{T}) + (f_D Re)_T \mathcal{T} \tag{3.60e}$$

The steady-state factor $(f_D Re)_0$ is calculated using Equation 3.60 with Va set to 0.

Heat Transfer

The model uses separate Nusselt number correlations for the steady, compression and advection components of the temperature in pipes. These are then used in Equation 3.53 to calculate the rate of heat transfer.

The steady component of the Nusselt number Nu_0 uses the same correlation as the Sage model for laminar flow [5, p. 253] and uses the Gnielinski correlation [60, p. 360] for turbulent flow. This equation is not valid for Reynolds numbers below 2300, so the Reynolds number used in the equation is prevented from dropping below this value by using Equation 3.60d.

$$Nu_{0L} = 6 \tag{3.61a}$$

$$Nu_T = \frac{(f_D/8)(Re^* - 1000)Pr}{1 + 12.7(f_D/8)^{1/2} \left(Pr^{2/3} - 1 \right)} \tag{3.61b}$$

where

$$f_D = \left(-1.8 \log_{10} \left(\left(\frac{\epsilon/d_h}{3.7} \right)^{1.11} + \frac{6.9}{Re^*} \right) \right)^{-2} \tag{3.61c}$$

The laminar and turbulent Nusselt numbers are weighted using the turbulence intensity $\mathcal{T}$ and summed to give Nu_0.

$$Nu_0 = Nu_{0L} (1 - \mathcal{T}) + Nu_T \mathcal{T} \tag{3.61d}$$

The Nusselt numbers for the compression and advection components of temperature, $\boldsymbol{Nu_c}$ and $\boldsymbol{Nu_a}$, use complex numbers to simulate the heat transfer for laminar flow which can be out of phase with the temperature difference. The real and imaginary components are calculated by using the same correlations as the Sage model [5, p. 253]. For the compression component of temperature, these are

$$\Re\left[\boldsymbol{Nu_{cL}}\right] = \begin{cases} 6 & \text{if } \sqrt{2\,VaPr} \leq 6 \\ \sqrt{2\,VaPr} & \text{otherwise} \end{cases} \tag{3.62a}$$

$$\Im\left[\boldsymbol{Nu_{cL}}\right] = \begin{cases} \frac{1}{5}\,VaPr & \text{if } VaPr \leq 5\sqrt{2\,VaPr} \\ \sqrt{2\,VaPr} & \text{otherwise} \end{cases} \tag{3.62b}$$

and for the advection component, these are

$$\Re\left[\boldsymbol{Nu_{aL}}\right] = \begin{cases} 4.2 & \text{if } \sqrt{2\,VaPr} \leq 8.4 \\ \frac{1}{2}\sqrt{2\,VaPr} & \text{otherwise} \end{cases} \tag{3.62c}$$

$$\Im\left[\boldsymbol{Nu_{aL}}\right] = \begin{cases} \frac{1}{10}\,VaPr & \text{if } VaPr \leq 5\sqrt{2\,VaPr} \\ \frac{1}{2}\sqrt{2\,VaPr} & \text{otherwise} \end{cases} \tag{3.62d}$$

The turbulent correlation is the same as used for Nu_0 (Equation 3.61b). The laminar and turbulent components are weighted using the turbulence intensity $\mathcal{T}$ and summed.

$$\boldsymbol{Nu_c} = \boldsymbol{Nu_{cL}}\,(1-\mathcal{T}) + Nu_T\mathcal{T} \tag{3.62e}$$

$$\boldsymbol{Nu_a} = \boldsymbol{Nu_{aL}}\,(1-\mathcal{T}) + Nu_T\mathcal{T} \tag{3.62f}$$

Conduction Enhancement

The conduction enhancement factor for pipes was developed by Gedeon [5, p. 253]. The conduction is only enhanced if turbulence is present.

$$N_k = (1-\mathcal{T}) + 0.022\;Pr\;Re^{0.75}\mathcal{T} \tag{3.63}$$

3.6.3 Annular Heat Exchangers

The annular heat exchangers that may be present at the first or second stage use similar correlations to pipes. However, the friction factor and Nusselt

number correlations are slightly different for laminar flow due to the different geometry.

Turbulence

The turbulence is calculated in the same way as for pipes.

Friction

Annular heat exchangers use a complex friction factor for the oscillating flow $\boldsymbol{f_D Re}$ and a real factor for the steady-state flow $(f_D Re)_0$. Like pipe cells, they use Equation 3.50 to calculate the pressure drop.

The laminar friction factors assume that the flow in an annular heat exchanger behaves the same as the flow between two parallel plates. This is a reasonable assumption because the gap of an annular heat exchanger is typically much smaller than its diameter. The laminar correlations are the same as used by the Sage model for flow between parallel plates [5, p. 254].

$$\Re\left[(\boldsymbol{f_D Re})_{\boldsymbol{L}}\right] = \begin{cases} 96 & \text{if } Va \leq 72 \\ \sqrt{128\,Va} & \text{otherwise} \end{cases} \tag{3.64a}$$

$$\Im\left[(\boldsymbol{f_D Re})_{\boldsymbol{L}}\right] = \begin{cases} \frac{16\,Va}{9} & \text{if } Va \leq 40.5 \\ \sqrt{128\,Va} & \text{otherwise} \end{cases} \tag{3.64b}$$

The turbulent friction factor $(f_D Re)_T$ is calculated using the same correlation used for pipes (Equation 3.60c). These are then weighted by the turbulence intensity $\mathcal{T}$ and summed.

$$(\boldsymbol{f_D Re}) = (\boldsymbol{f_D Re})_{\boldsymbol{L}}\,(1 - \mathcal{T}) + (f_D Re)_T \mathcal{T} \tag{3.64c}$$

Heat Transfer

The Nusselt number correlations are also calculated in a similar way to pipes. Separate correlations are used for the steady, compression and advection components of the temperature and these Nusselt numbers are used in Equation 3.53 to calculate the rate of heat transfer.

The correlations for the laminar Nusselt numbers are the same as used in the Sage model for flow between parallel plates [5, p. 255].

$$Nu_{0L} = 10 \tag{3.65a}$$

$$\Re\left[\boldsymbol{Nu_{cL}}\right] = \begin{cases} 10 & \text{if } \sqrt{2\,VaPr} \leq 10 \\ \sqrt{2\,VaPr} & \text{otherwise} \end{cases} \tag{3.65b}$$

$$\Im\left[\boldsymbol{Nu_{cL}}\right] = \begin{cases} \frac{1}{5}\,VaPr & \text{if } VaPr \leq 5\sqrt{2\,VaPr} \\ \sqrt{2\,VaPr} & \text{otherwise} \end{cases} \tag{3.65c}$$

$$\Re\left[\boldsymbol{Nu_{aL}}\right] = \begin{cases} 8.1 & \text{if } \sqrt{2\,VaPr} \leq 16.2 \\ \frac{1}{2}\sqrt{2\,VaPr} & \text{otherwise} \end{cases} \tag{3.65d}$$

$$\Im\left[\boldsymbol{Nu_{aL}}\right] = \begin{cases} \frac{1}{10}\,VaPr & \text{if } VaPr \leq 5\sqrt{2\,VaPr} \\ \frac{1}{2}\sqrt{2\,VaPr} & \text{otherwise} \end{cases} \tag{3.65e}$$

The turbulent Nusselt number Nu_T is calculated using the same correlation used for pipes (Equation 3.61b). The laminar and turbulent components are weighted using the turbulence intensity $\mathcal{T}$ and summed.

$$\boldsymbol{Nu_c} = \boldsymbol{Nu_{cL}}\,(1 - \mathcal{T}) + Nu_T\mathcal{T} \tag{3.65f}$$

$$\boldsymbol{Nu_a} = \boldsymbol{Nu_{aL}}\,(1 - \mathcal{T}) + Nu_T\mathcal{T} \tag{3.65g}$$

Conduction Enhancement

The conduction enhancement factor used for annular heat exchangers is the same as for pipes (Equation 3.63).

3.6.4 Variable Volume Cells

The variable volume cells of the model are the primary and secondary compression chambers, the expansion chambers and the compressor and displacer backshells. All these cells use the same correlations.

Turbulence

The variable volume cells have an associated turbulence kinetic energy (see Section 3.5.1). The turbulence kinetic energy decays over time as the kinetic

energy is converted to thermal energy. The correlation used to model the rate of decay has been developed by Gedeon [5, p. 234] to match measurements taken by Cantelmi [64].

$$\dot{K}_{decay} = -5.8\frac{\kappa^{\frac{2}{3}}\rho V}{d_h} \tag{3.66}$$

Friction

The frictional effects in the variable volume spaces are assumed to be negligible. This is because these spaces have a large cross-sectional area, so the gas is moving slowly and the frictional force is low.

Heat Transfer

The heat transfer in variable volume spaces is modelled using Equation 3.52. This equation uses a complex Nusselt number with a real and imaginary component; the imaginary component causes some of the heat transfer to be out of phase with the variation in bulk fluid temperature. This is most important when there is no turbulence in the variable volume space to disrupt the boundary layer of the gas near the wall. This is the assumption made by Lee for his model of heat transfer in a gas spring [65].

To improve heat transfer, it is desirable to have turbulent gas in the variable volume spaces. Therefore, the coolers developed at RAL try to maximise turbulence in these volumes and Lee's model is not suitable. Some models, such as the one by Cantelmi [64], consider the effects of this inflow-induced turbulence. Gedeon used Cantelmi's data to produce an empirical correlation for the heat transfer [5, p. 257] and this correlation is used in the RAL Third-Order Model. The Nusselt numbers that are used in Equation 3.52 are calculated using the following correlations:

$$Nu_0 = 6 + 0.084 Re_{\mathcal{T}} \tag{3.67}$$

$$\Re\left[\boldsymbol{Nu}\right] = \begin{cases} \sqrt{2\,VaPr} & \text{if } Re_{\mathcal{T}} \leq 7.7\sqrt{2\,VaPr} \\ \dfrac{0.13 Re_{\mathcal{T}}}{\ln\left(\dfrac{0.35 Re_{\mathcal{T}}}{\sqrt{2\,VaPr}}\right)} & \text{otherwise} \end{cases} \tag{3.68a}$$

$$\Im\left[\boldsymbol{Nu}\right] = \frac{\tanh\left(\frac{0.4}{\eta}\right)}{1+3\eta}\Re\left[\boldsymbol{Nu}\right] \tag{3.68b}$$

where

$$\eta = \sqrt{\frac{Re_{\mathcal{T}}}{7.8\,VaPr}} \tag{3.68c}$$

Displacer End Conduction

The model accounts for the thermal conduction from the solid cells at the ends of the displacer into the variable volume cells at either end. Equation 3.52 is not used to calculate the heat transfer because it does not account for the thermal resistance of the solid cell which may be significant in the axial direction. The equation is modified by summing the thermal resistance along half of the solid cell length and the effective gas resistance to find the total steady-state thermal resistance.

$$R_{tot} = R_s + R_g = \frac{x_s}{2\,k_s\,S} + \frac{d_h}{Nu_0\,S\,k} \tag{3.69a}$$

$$\dot{Q}_{trans} = \frac{\left(T_s - \bar{T}\right)}{R_{tot}} - \frac{S\,k}{d_h}\Re\left[\boldsymbol{Nu}\,\boldsymbol{T}\right] \tag{3.69b}$$

Conduction Enhancement

The conduction enhancement factor for variable volume cells was developed by Gedeon to account for the increased mixing due to turbulence [5, p. 258].

$$N_k = 1 + 0.014\,Re_{\mathcal{T}} \tag{3.70}$$

3.6.5 Regenerator — Wire Mesh

The regenerators of the Stirling cryocoolers developed at RAL consist of stacked discs of wire mesh. The empirical correlations for this region are some of the most important in the model because the properties of the regenerator have such a large impact on the cooler performance (see Section 5.1.4).

Some commonly used correlations for flow through wire mesh are the ones developed by Kays and London [59]. These correlations were used in the

previous iteration of the RAL model [7]. The correlations were generated using steady-state flow measurements. More recently, there have been several papers claiming that correlations developed using steady flow data may be invalid for oscillating flow [66][67]. However, Gedeon and Wood [51] performed a series of measurements at the frequencies and Reynolds numbers commonly found in cryocoolers and did not find any difference between the flow friction and heat transfer for steady-state and for oscillating flow at the same Reynolds numbers. They explain that this is because the small flow paths within the mesh mean that the flow becomes fully developed very quickly. Because Gedeon and Wood's test setup was designed to be representative of the conditions found in a cryocooler, their correlations have been used for this model.

Turbulence

The gas in wire mesh cells is assumed to always be turbulent. This is because the wires disrupt the flow of the gas and cause turbulent mixing.

Friction

The friction factor correlation is taken from the paper by Gedeon and Wood [51], and the friction factor is used in Equation 3.49.

$$f_D Re = 129 + 2.91 Re^{0.897} \tag{3.71}$$

Heat Transfer

The heat transfer correlation is also taken from the paper by Gedeon and Wood [51], and the Nusselt number is used in Equation 3.51.

$$Nu = \left(1 + 0.99\,(Re\,Pr)^{0.66}\right)\phi^{1.79} \tag{3.72}$$

where ϕ is the porosity of the mesh (the void volume divided by the total volume).

Conduction Enhancement

The conduction enhancement factor is taken from the same paper [51].

$$N_k = 1 + 0.5\,(Pr\,Re)^{0.66}\,\phi^{-2.91} \tag{3.73}$$

Tortuosity

The model uses the tortuosity correlation developed by Gedeon [5, p. 244]:

$$\tau = \left(\frac{k_s}{k_g}\right)^{-0.835} \left[\frac{3(k_s/k_g - \phi) + (2 + k_s/k_g)\phi}{3(1-\phi) + (2 + k_s/k_g)\phi}\right] \tag{3.74}$$

where k_s and k_g are the conductivity of the solid and gas (without enhancement).

3.6.6 Regenerator — Metal Foam

There is little information in the literature about metal foams in the oscillating flow regimes found in regenerators. However, some correlations have been developed for metal foams in steady flows. Friction factor correlations have been summarised by Edouard [68] and heat transfer correlations have been summarised by Mahjoob [69]. Because of the uncertainty about whether these correlations would be applicable for flows in regenerators, the model uses the random fibre regenerator matrix correlations that have been developed by Gedeon [5, p. 246]. These correlations do not depend on the operating frequency. It is hoped that a random fibre matrix with the same porosity and surface area as a metal foam will have similar flow properties.

The surface area is calculated using the equation developed by Lacroix et al. [70]:

$$S = \frac{4}{d_{strut}}(1-\phi) \tag{3.75}$$

where the strut diameter d_{strut} is calculated from the distance between the pores x_{pore} and the porosity ϕ.

$$d_{strut} = \frac{x_{pore}\left[\frac{4}{3\pi}\,(1-\phi)\right]^{\frac{1}{2}}}{1 - \left[\frac{4}{3\pi}\,(1-\phi)\right]^{\frac{1}{2}}} \tag{3.76}$$

Turbulence

The gas in metal foam cells is assumed to always be turbulent, for the same reasons as for wire mesh cells.

Friction

The friction factor is calculated by using Gedeon's correlation for a random fibre matrix [5, p. 247] and is used in Equation 3.49.

$$f_D Re = a_1 + a_2 \, Re^{a_3} \tag{3.77a}$$

where

$$a_1 = 25.7 \frac{\phi}{1-\phi} + 79.8 \tag{3.77b}$$

$$a_2 = 0.146 \frac{\phi}{1-\phi} + 3.76 \tag{3.77c}$$

$$a_3 = -0.00283 \frac{\phi}{1-\phi} + 0.9252 \tag{3.77d}$$

Heat Transfer

The Nusselt number is calculated by using Gedeon's correlation for a random fibre matrix [5, p. 247] and is used in Equation 3.51.

$$Nu = 1 + 0.186 \frac{\phi}{1-\phi} \left(Pr \, Re\right)^{0.55} \tag{3.78}$$

Conduction Enhancement

The conduction enhancement for a metal foam is assumed to be the same as for a random fibre matrix [5, p. 247].

$$N_k = 1 + \left(Pr \, Re\right)^{0.55} \tag{3.79}$$

Tortuosity

For metal foams, the tortuosity is calculated by assuming the foam has a cubic lattice structure. If this is the case, only a third of the struts within the foam can be aligned along the thermal gradient at once. Therefore, the tortuosity is

given by

$$\tau_{foam} = \frac{1}{3} \tag{3.80}$$

3.6.7 Piston and Shaft Clearance Seals

The flow in the compressor piston and displacer shaft clearance seals is modelled as flow between two parallel plates. This is because the gap width is much smaller than diameter of the compressor piston or the displacer shaft. The velocity and temperature profiles of the flow are assumed to be fully developed throughout the cycle because the gap width is so small. This allows steady-state correlations to be used.

Turbulence

Because the flow is assumed to always be fully developed, the turbulence intensity is only dependent on the Reynolds number. The flow is assumed to be fully laminar below 2300 [61, p. 491]. When the Reynolds number is above 4000, the flow is assumed to be fully turbulent because the turbulent friction factor and Nusselt number correlations are valid for Reynolds numbers greater than this. Linear interpolation is used to calculate the turbulence intensity between these values.

$$\mathcal{T} = \begin{cases} 0 & \text{if } Re \leq 2300 \\ \frac{Re-2300}{4000-2300} & \text{if } 2300 < Re < 4000 \\ 1 & \text{if } Re \geq 4000 \end{cases} \tag{3.81}$$

Friction

The laminar friction factor depends on the eccentricity ε of the piston or shaft in the bore, where ε is the ratio of the offset to the mean radial clearance [71, p. 616]. This is discussed in more detail in Section 5.4. The turbulent friction factor does not need to account for the eccentricity as the turbulent friction factor is independent of the pipe geometry [59, p. 116]. The same turbulent correlation as for flow in pipes is used.

$$(f_D Re)_L = \frac{96}{(1 + 1.5\varepsilon^2)} \tag{3.82a}$$

$$(f_D Re)_T = Re\left(-1.8\log_{10}\left(\left(\frac{\epsilon/d_h}{3.7}\right)^{1.11} + \frac{6.9}{Re}\right)\right)^{-2} \tag{3.82b}$$

$$f_D Re = (f_D Re)_L\,(1-\mathcal{T}) + (f_D Re)_T \mathcal{T} \tag{3.82c}$$

Heat Transfer

The laminar heat transfer correlation assumes a constant wall temperature [59] and the turbulent correlation is the same as for pipes.

$$Nu_L = 7.54 \tag{3.83a}$$

$$Nu_T = \frac{(f_D/8)(Re-1000)Pr}{1+12.7(f_D/8)^{1/2}\left(Pr^{2/3}-1\right)} \tag{3.83b}$$

where

$$f_D = \left(-1.8\log_{10}\left(\left(\frac{\epsilon/d_h}{3.7}\right)^{1.11} + \frac{6.9}{Re}\right)\right)^{-2} \tag{3.83c}$$

The laminar and turbulent Nusselt numbers are weighted using the turbulence intensity $\mathcal{T}$ and summed to give Nu.

$$Nu = Nu_L\,(1-\mathcal{T}) + Nu_T \mathcal{T} \tag{3.83d}$$

Conduction Enhancement

The conduction enhancement factor used for the piston and shaft clearance seals is the same as for pipes (Equation 3.63).

3.6.8 Appendix Gaps

The appendix gap cells in the model are a form of clearance seal, so they use similar correlations to the piston and shaft clearance seal cells. The exception is the method used to calculate heat transfer.

Turbulence

The turbulence intensity is modelled in the same way as for the piston and shaft clearance seal cells (Equation 3.81).

Friction

The friction factor correlations are the same as for the piston and shaft clearance seal cells (Equation 3.82).

Heat Transfer

The heat transfer correlation used for the appendix gap must be able to model cases where the inner and outer walls are at significantly different temperatures. This is important for accurately modelling the shuttle losses (see Section 3.7). The constant wall temperature correlation for laminar flow is not valid as the correlation assumes that the walls are the same temperature.

The RAL Third-Order Model uses the correlation developed by Andersen [4] to calculate the rate of heat transfer for laminar flow. This correlation approximates the radial temperature in the gap using a quadratic polynomial. The mean value of the polynomial is the same as the bulk gas temperature T and the temperatures at the ends of the polynomial are the same as the wall temperatures. The rate of heat transfer can be calculated from the gradient of the polynomial near the walls. The calculation is performed separately for the displacer tube and the static components of the cold finger. Subscript $s1$ refers to the wall that the heat transfer is calculated for and $s2$ refers to the opposite wall.

$$\dot{Q}_L = \frac{S_{s1}k}{a}\left(4T_{s1} + 2T_{s2} - 6T\right) \tag{3.84a}$$

where a is the size of the appendix gap. The turbulent heat transfer correlation is the same as for pipes.

$$\dot{Q}_T = \frac{S_{s1}k}{d_h} Nu_T \left(T_{s1} - T\right) \tag{3.84b}$$

$$Nu_T = \frac{(f_D/8)(Re - 1000)Pr}{1 + 12.7(f_D/8)^{1/2}\left(Pr^{2/3} - 1\right)} \tag{3.84c}$$

where

$$f_D = \left(-1.8\log_{10}\left(\left(\frac{\epsilon/d_h}{3.7}\right)^{1.11} + \frac{6.9}{Re}\right)\right)^{-2} \tag{3.84d}$$

The laminar and turbulent heat transfer rates are weighted using the turbulence intensity $\mathcal{T}$ and summed to give $\dot{Q}$.

$$\dot{Q} = \dot{Q}_L \left(1 - \mathcal{T}\right) + \dot{Q}_T \mathcal{T} \tag{3.84e}$$

Conduction Enhancement

The conduction enhancement factor used for appendix gaps is the same as for pipes (Equation 3.63).

3.7 Heat Transfer to Moving Cells

The displacer cells can move relative to the other cold finger cells. This poses a problem when simulating the heat transfer to the displacer cells; the contact area between the displacer cells and the static cold finger cells is constantly changing, and which cells are in contact with each other is not fixed. It is important that this heat transfer is simulated accurately because it causes a significant loss mechanism, known as shuttle loss. As the displacer tube and cold finger tube move past each other, their thermal gradients become offset. When the displacer is at the warm end, thermal energy conducts across the appendix gap from the cold finger tube to the displacer tube. When the displacer moves towards the cold end, this thermal energy conducts back across the appendix gap from the displacer tube to the cold finger tube. This has the net effect of "shuttling" the thermal energy towards the cold end.

To simulate the heat transfer between the static and moving cells, the model splits the cells in the displacer tube, cold finger tube and nearby gas and solid cells into subcells, as shown in Figure 3.8. The method used to create the subcells ensures that the subcells do not overlap the boundaries of their parent cells and that the subcells in the different components share the same axial locations. How the cells are divided depends on the position of the displacer and is recalculated for each time step.

The properties of the subcells must be found before the rates of heat transfer can be calculated. For subcells within the displacer tube, appendix gap, heat exchangers and cold finger tubes, the temperatures are linearly interpolated from the temperatures of the cells. Subcells within variable volume cells or

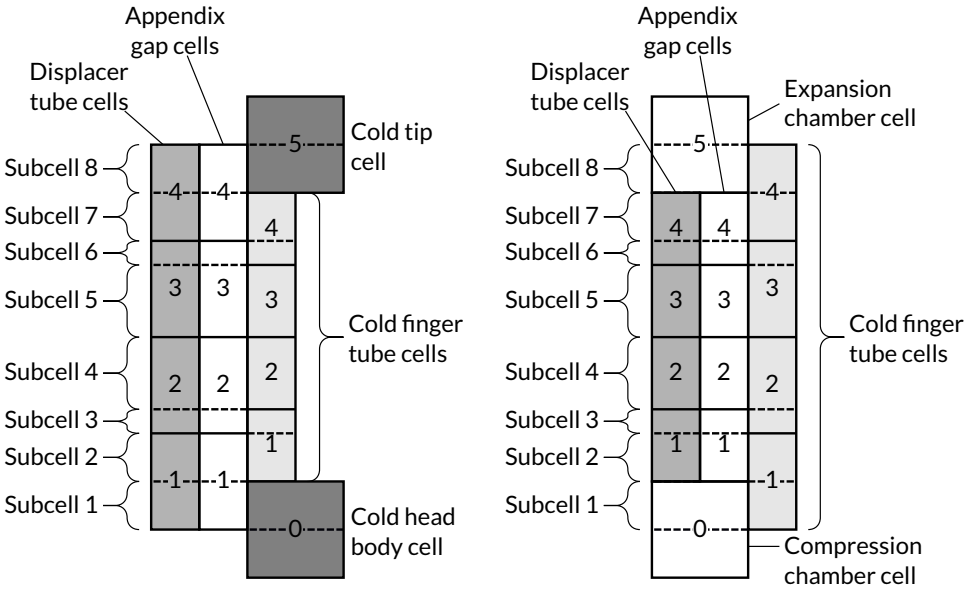

(a) Example subcells for a displacer tube that overlaps the cold finger tube at both ends.

(b) Example subcells for a cold finger tube that overlaps the displacer tube at both ends.

Figure 3.8: Diagrams showing how the cells of a single-stage cold finger are divided into subcells. The solid lines represent the boundaries of the parent cells. The lengths of the subcells are set so that they do not overlap any cell boundaries.

their walls take the temperature of the parent cell. Reynolds numbers and turbulence intensities are always taken from the parent cell.

Each gas subcell is connected to a maximum of one displacer tube subcell and one static cold finger subcell because the subcells of the different components have the same axial locations. The rates of heat transfer to the gas subcell are calculated using the correlations described in Section 3.6. The rates of heat transfer to each subcell of a parent cell are summed to find the total rate of heat transfer to that parent cell.

3.8 Radiation Loads on the Cold Finger Tube

Radiation loads are applied to the outermost cells of the cold finger tube as the model runs. The radiation loads acting on the stages are calculated after the model has converged (see Section 3.14).

The cold finger tube can be covered in multi-layer insulation (MLI) or left bare. If no MLI is present, the heat load is calculated by using the Stefan-Boltzmann

law.

$$\dot{Q}_{rad} = S_{rad}\,\epsilon_0\,\sigma\left(T_{env}^4 - T_s^4\right) \tag{3.85}$$

where σ is the Stefan–Boltzmann constant, S_{rad} is the surface area exposed to the radiation, ϵ_0 is the surface emissivity, T_s is the temperature of the surface and T_{env} is the temperature of the surrounding environment.

The emissivity of the cold finger tube cells is dependent on temperature and is calculated by linearly interpolating the data in Table 3.1. In practice, the emissivity is also dependent on the type of material, the surface finish and the amount of oxidation, but the model assumes the cold finger tube is unpolished and unoxidised and is made from stainless steel or titanium, which have similar emissivities [73, p. 1486].

MLI can be used to reduce heat transfer by radiation in a vacuum environment [74]. It is typically composed of many layers of metallised plastic film that are separated by plastic scrim. The metal coating reflects incident radiation, and this effect is enhanced by having multiple layers. The scrim separating each layer reduces thermal conduction. The cold finger tube of a cryocooler can be wrapped in MLI to reduce the radiative heat load. The insulation is not perfect, so any heat load passing through the insulation must be accounted for by the model. This heat load consists of a radiative and a conductive component. The model uses a correlation that was developed in a study conducted by Lockheed for NASA [75].

$$\dot{q} = \dot{q}_c + \dot{q}_r = \frac{C_c\,N^{2.56}\,T_m}{n+1}\,(T_h - T_c) + \frac{C_r\,\epsilon_0}{n}\left(T_h^{4.67} - T_c^{4.67}\right) \tag{3.86}$$

where $\dot{q}$ is the total heat flux density (W m^{-2}), $\dot{q}_c$ is the conductive heat flux density, $\dot{q}_r$ is the radiative heat flux density, C_c is the conduction constant (8.95×10^{-8}), C_r is the radiation constant (5.39×10^{-10}), T_h is the hot side temperature (K), T_c is the cold side temperature (K), T_m is the mean MLI

Table 3.1: A table listing the points that are interpolated to calculate the emissivity of the cold finger tube. This data is based on the unpolished stainless steel data in [72, p. 424] and [73, p. 1219].

Temperature (K)	Emissivity
4.2	0.12
77	0.34
400	0.34

temperature ($(T_h + T_c)/2$), ϵ_0 is the MLI shield-layer emissivity at 300 K (0.031), N is the MLI layer density (layers/cm) and n is the number of MLI layers.

The model provides the option to simulate a radiation shield for two-stage coolers. This shield is attached to the first stage cold tip and surrounds the second stage of the cooler. If a radiation shield is present, the radiation environment of the second stage is assumed to be at the same temperature as the first stage cold tip.

3.9 Wall Surface Temperature Fluctuations

When heat is applied to the surface of a solid, the temperature of the surface will increase at a faster rate than the interior of the solid because it takes time for the heat to propagate through the material. This means that when a sinusoidal heat flow is applied to the surface, the temperature fluctuations in the interior will be smaller than the temperature fluctuation at the surface, and they will be phase shifted relative to the surface fluctuation. The thermal penetration depth δ is the depth at which the amplitude of the temperature fluctuation will have decreased to $1/e$ of the amplitude at the surface.

$$\delta = \sqrt{\frac{2k_s}{\omega \rho_s c_s}} \tag{3.87}$$

where ω is the angular frequency of the cycle, k_s is the thermal conductivity of the solid, ρ_s is the density and c_s is the specific heat capacity.

These surface temperature fluctuations can significantly reduce the temperature difference between the gas and the wall surface, reducing the rate of heat transfer. This is particularly true when the wall is a poor thermal conductor. To ensure the model is accurate for a wide range of possible input parameters, the wall surface temperature fluctuations are simulated for all the solids in the model.

It would be possible to simulate the temperature fluctuations of each solid component by splitting up each cell into many layers at different depths and computing the heat flow between the layers. This would give an accurate prediction but would be computationally expensive. This method can be simplified because it is not necessary to accurately simulate the temperature

fluctuations within the interior of the solids. Only the temperature fluctuation at the surface needs to be simulated accurately because this affects the heat transfer with the gas.

Some of the solids have a variable interior temperature, whereas some have an interior temperature that is fixed. These two types are simulated using different methods.

3.9.1 Variable Interior Temperature

Solids such as the regenerator mesh, displacer tube and cold finger tube do not have a fixed temperature and change temperature as the model converges. It is possible to simulate the surface temperature fluctuation of these regions by splitting each solid cell into two, a wall cell and an interior cell, as shown in Figure 3.9. The model uses the temperature of the wall cell as the solid surface temperature when calculating heat transfer with the gas.

Carslaw and Jaeger give an equation for the wall temperature of a solid that is subject to a sinusoidal heat flow rate [76, p. 110]. For a solid of thickness r, insulated on one side and subject to a sinusoidal heat flow rate of amplitude $\dot{Q}_A$ on the other, the oscillating component of the wall temperature $\boldsymbol{T_W}$ divided by the heat flow rate $\dot{\boldsymbol{Q}}$ is given by

$$\frac{\boldsymbol{T_W}}{\dot{\boldsymbol{Q}}} = \frac{\delta}{k_s S\,(1+i)} \frac{1}{\tanh\left(\frac{r}{\delta}\,(1+i)\right)} \tag{3.88a}$$

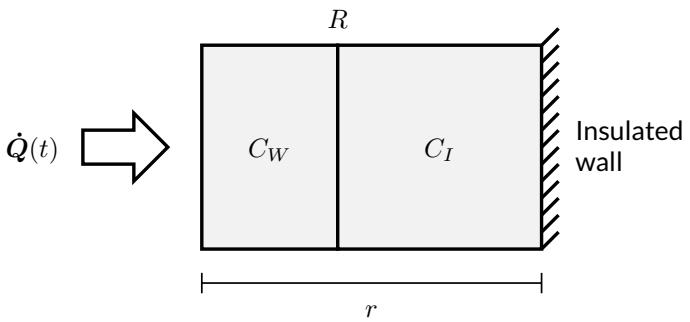

Figure 3.9: A diagram showing the arrangement of the solid cells used by the model to simulate the wall surface temperature fluctuation when the interior temperature is variable.

where $\dot{\boldsymbol{Q}}$ and $\boldsymbol{T_W}$ are complex sinusoids (see Section 3.6.1) and $\dot{\boldsymbol{Q}}$ is given by

$$\dot{\boldsymbol{Q}} = \dot{Q}_A e^{i\omega t} \tag{3.88b}$$

By tuning the heat capacities and thermal resistance between these cells, the wall temperature response to a sinusoidal heat flow rate can be matched to Equation 3.88. The two solid cells can be thought of as being part of a thermal circuit, where temperature takes the place of voltage and heat flow rate takes the place of current. The thermal resistance between the two cells is represented by a resistor and their heat capacities are represented by capacitors, as shown in Figure 3.10.

By using the mesh analysis method on this circuit [77, p. 290], the oscillating component of the wall temperature divided by the heat flow rate is found to be given by

$$\frac{\boldsymbol{T_W}}{\dot{\boldsymbol{Q}}} = \frac{\left(R + \frac{1}{i\omega C_I}\right)\frac{1}{i\omega C_W}}{R + \frac{1}{i\omega C_I} + \frac{1}{i\omega C_W}} \tag{3.89}$$

By equating the real and imaginary components of Equations 3.88a and 3.89, and by knowing that the heat capacities must sum to equal the physical heat capacity, the values of R, C_W and C_I can be found.

$$R = \frac{\left(\Re\left(\frac{\boldsymbol{T_W}}{\dot{\boldsymbol{Q}}}\right)^2 C\omega + \Im\left(\frac{\boldsymbol{T_W}}{\dot{\boldsymbol{Q}}}\right)^2 C\omega + \Im\left(\frac{\boldsymbol{T_W}}{\dot{\boldsymbol{Q}}}\right)\right)^2}{\Re\left(\frac{\boldsymbol{T_W}}{\dot{\boldsymbol{Q}}}\right)\left(\Re\left(\frac{\boldsymbol{T_W}}{\dot{\boldsymbol{Q}}}\right)^2 C^2\omega^2 + \Im\left(\frac{\boldsymbol{T_W}}{\dot{\boldsymbol{Q}}}\right)^2 C^2\omega^2 + 2\Im\left(\frac{\boldsymbol{T_W}}{\dot{\boldsymbol{Q}}}\right) C\omega + 1\right)} \tag{3.90a}$$

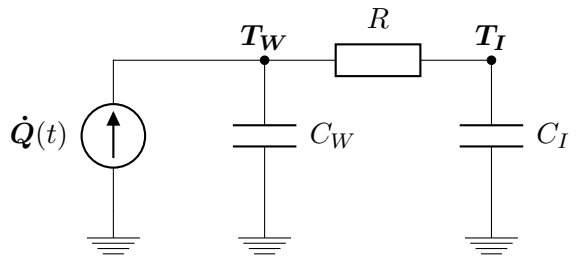

Figure 3.10: A diagram showing the thermal circuit that represents the interactions between the solid cells of the model when the interior temperature is variable.

$$C_W = -\frac{\Im\left(\frac{\boldsymbol{T_W}}{\dot{\boldsymbol{Q}}}\right) C\omega + 1}{\omega\left(\Re\left(\frac{\boldsymbol{T_W}}{\dot{\boldsymbol{Q}}}\right)^2 C\omega + \Im\left(\frac{\boldsymbol{T_W}}{\dot{\boldsymbol{Q}}}\right)^2 C\omega + \Im\left(\frac{\boldsymbol{T_W}}{\dot{\boldsymbol{Q}}}\right)\right)} \tag{3.90b}$$

$$C_I = C - C_W \tag{3.90c}$$

where

$$\Re\left(\frac{\boldsymbol{T_W}}{\dot{\boldsymbol{Q}}}\right) = \frac{\delta}{k_s S}\,\frac{\sin\frac{2r}{\delta} - \sinh\frac{2r}{\delta}}{2\left(\cos\frac{2r}{\delta} - \cosh\frac{2r}{\delta}\right)} \tag{3.90d}$$

$$\Im\left(\frac{\boldsymbol{T_W}}{\dot{\boldsymbol{Q}}}\right) = \frac{\delta}{k_s S}\,\frac{\sin\frac{2r}{\delta} + \sinh\frac{2r}{\delta}}{2\left(\cos\frac{2r}{\delta} - \cosh\frac{2r}{\delta}\right)} \tag{3.90e}$$

$$C = C_W + C_I = c_W m_W + c_I m_I \tag{3.90f}$$

Figure 3.11 compares the results of this two-cell method to a high-resolution method where the solid is divided into many cells. It can be seen that the surface temperature predicted by the high-resolution method is almost identical to the temperature of the wall cell in the two-cell method. This indicates that the two-cell method is giving the desired temperature response.

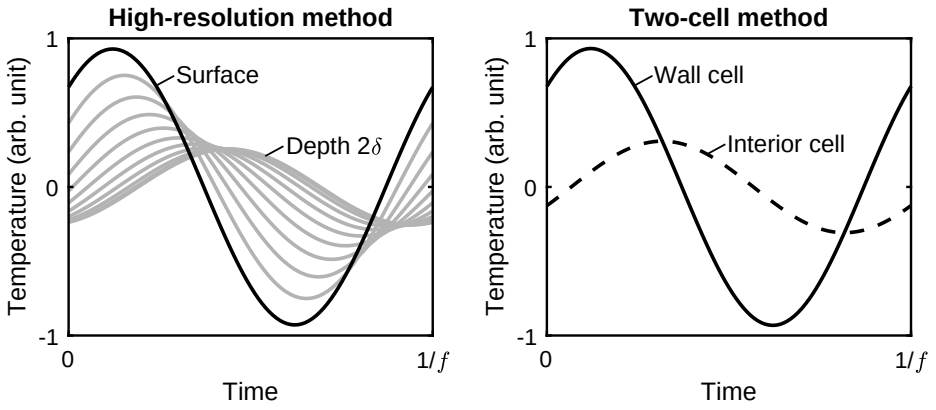

Figure 3.11: Plots showing the temperature fluctuations predicted for a solid 2δ deep with a sinusoidal heat flow rate on one side and zero heat flow rate on the other. The plot on the left shows the results of the high-resolution method where the solid was divided into 300 equal cells. The black line shows the temperature fluctuation at the surface where the heat flow rate is being applied. The grey lines show the temperature fluctuations at 10 other points, equally spaced through the depth of the solid. The plot on the right shows the results of the two-cell method discussed in this section. The solid was split into a wall cell and an interior cell, with their heat capacities and thermal resistance calculated using Equation 3.90.

The two-cell method is only exactly true for a sinusoidal heat flow rate and constant material properties. The material properties are approximately constant for typical temperature fluctuations, but the non-linear effects of the method can cause the heat flow rate to be non-sinusoidal and contain higher harmonics. Simulations have been run to investigate how the two-cell method behaves at these higher frequencies. Figure 3.12 compares the surface temperature responses of the two methods at the fifth harmonic. The plot shows that the surface temperature amplitude predicted by the two-cell method is slightly lower than for the high-resolution method and that there is a small phase shift. However, the two-cell method still gives a reasonably accurate response at these higher frequencies. At the lower harmonics, the responses of the methods are even closer.

A special case occurs for the displacer tube because it can exchange heat with two gas flow paths: the flow through the regenerator, on the inside of the displacer tube; and the flow through the appendix gap, on the outside. To cope with this, the model splits the displacer tube cells into three: a wall cell on each

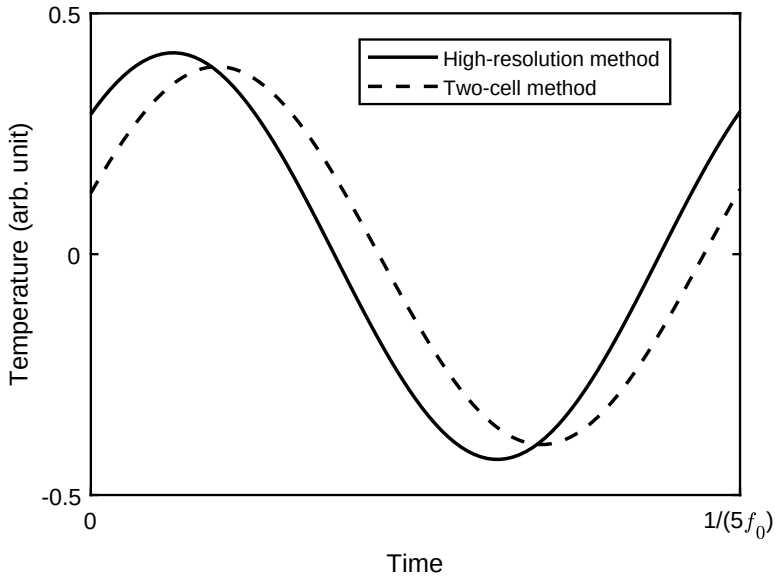

Figure 3.12: A plot showing how the surface temperature fluctuations plotted in Figure 3.11 are affected by increasing the sinusoidal heat flow rate frequency by a factor of five. The other parameters of the methods, such as the thickness, material properties and heat flow rate amplitude, were kept the same. The parameter f_0 is equal to f in Figure 3.11. The arbitrary temperature units in this plot are the same as in Figure 3.11.

side and an interior cell. The thicknesses of the wall cells are calculated separately, and the remaining mass makes up the interior cell.

3.9.2 Fixed Interior Temperature

The solids such as the walls of the compression chambers, expansion chambers and transfer line have their interior temperature held constant. The wall surface temperature fluctuation can be simulated using a single cell, as shown in 3.13. The equivalent thermal circuit is shown in Figure 3.14.

To calculate the values of C_W and R that will give the required temperature response, this type of solid can be thought of as a special case of the two-cell method where C_I and r approach infinity. Equation 3.88 becomes

$$\frac{\boldsymbol{T_W}}{\dot{\boldsymbol{Q}}} = \frac{\delta}{k_s S\,(1+i)} \tag{3.91}$$

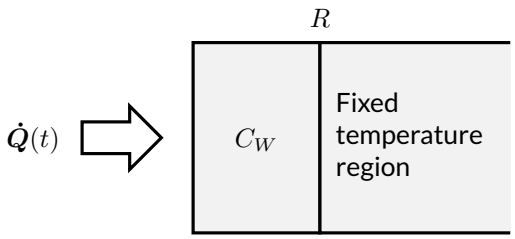

Figure 3.13: A diagram showing the arrangement of the solid cells used by the model to simulate the wall surface temperature fluctuation when the interior temperature is fixed.

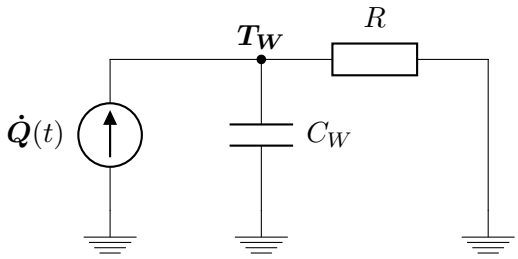

Figure 3.14: A diagram showing the thermal circuit that represents the interactions between the solid cells of the model when the interior temperature is fixed.

and Equation 3.89 becomes

$$\frac{\boldsymbol{T_W}}{\dot{\boldsymbol{Q}}} = \frac{R\,\frac{1}{i\omega C_W}}{R + \frac{1}{i\omega C_W}} \tag{3.92}$$

By equating the real and imaginary components, R and C_W can be found.

$$R = \frac{\delta}{k_s S} \tag{3.93a}$$

$$C_W = \frac{k_s S}{\omega \delta} \tag{3.93b}$$

This method for simulating surface temperature fluctuations for regions with fixed interior temperatures has previously been used in the model developed by Kühl [78].

3.10 Interpolation of Gas Properties

The differential equations for the gas, presented in Section 3.5.1, require knowledge of the state of the gas at both the cells and at the nodes between the cells. For example, the model uses the state of the gas at the nodes to calculate the advection of energy between cells. Most of the solution variables relate to the state of the gas at the cells, so these cell values must be interpolated to find the gas state at the nodes. Similarly, the momentums are evaluated at each node, and these must be interpolated to find the gas velocity within each cell.

The choice of which gas properties to interpolate and which interpolation methods to use can affect the accuracy and stability of the model. This section discusses the advantages and disadvantages of using different gas properties and interpolation methods and summarises the techniques used by the model.

3.10.1 Interpolated Properties

The solution variables cannot be interpolated directly, they must first be converted into intensive properties that are unaffected by the cell sizes. The interpolated properties should also be unaffected by changes in the flow area. This improves accuracy when interpolating between cells of different sizes.

Thermodynamic Properties

The cell temperatures and pressures seem like obvious gas properties to interpolate because the temperatures and pressures at the nodes are used in many of the differential equations. However, the temperature and pressure of the gas may change sharply at a node if there is a difference in the flow area. A smaller flow area will increase the gas velocity which will cause the pressure and temperature to decrease. Therefore, pressure and temperature are not suitable properties for interpolation. Instead, the model interpolates the stagnation pressure and stagnation temperature. These stagnation properties represent the temperature and pressure that would be measured if the gas was brought to rest. They are constant when the flow area changes so are suitable for interpolation.

The stagnation temperatures and pressures are calculated for each cell using Equation 3.94 and 3.95. These use the gas velocities at the cells, the calculation of which is described in Section 3.10.3.

$$T_{stag_i} = T_i + \frac{v_i^2}{2c_P} \tag{3.94}$$

$$P_{stag_i} = P_i + \frac{1}{2}\rho_i v_i^2 \tag{3.95}$$

Equation 3.95 is only valid at low Mach numbers, but this should be the case for most Stirling coolers.

Once the stagnation temperatures and stagnation pressures have been interpolated at the nodes using the methods listed in Section 3.10.3, the temperatures and pressures at the nodes can be calculated.

$$T_j = T_{stag_j} - \frac{v_j^2}{2c_P} \tag{3.96}$$

$$P_j = \frac{P_{stag_j}}{1 + \frac{v_j^2}{2R_g T_j}} \tag{3.97}$$

Equation 3.96 is a simple rearrangement of Equation 3.94. Equation 3.97 is a rearrangement of Equation 3.95, but the density at the node is not known. Instead, the ideal gas equation is used to estimate the density ($\rho = P/(R_g T)$) and this is substituted into Equation 3.95. This is a reasonable approximation,

even for a real gas, because the difference between P_j and P_{stag_j} is typically very small.

The density ρ and the energy density E/V could be used as interpolation properties instead of the stagnation temperatures and pressures. These properties are also constant with changing flow areas and are the ones used by Sage [5, p. 215]. However, using these properties for interpolation was found to give unphysical node temperatures. For example, for two cells at the same temperature with a large pressure difference between them, the node temperature calculated from these interpolation properties was found to be significantly different from the cell temperatures. These unphysical node temperatures can be avoided by interpolating the stagnation temperature instead.

Velocity

The model interpolates the volumetric flow rate to calculate the gas velocities at the cells. The volumetric flow rate $\dot{V} = vA$ can be interpolated as it is unaffected by changes in flow area if the temperature and pressure are constant.

Turbulence

The turbulence state of the gas is interpolated using the specific turbulence kinetic energy κ for variable volume cells and the turbulence intensity $\mathcal{T}$ for pipe and heat exchanger cells.

3.10.2 Interpolation Methods

A variety of different interpolation methods are described in the literature, each suited to different fluid dynamics applications. For each application, it is important to pick a method that gives a stable solution with a good accuracy. An interpolation method with a poor accuracy can introduce an artificial energy transport mechanism called numerical diffusion [4, p. 30]. In a Stirling cooler model, this has the effect of increasing the heat flow along the regenerator, resulting in a poor prediction of cooling power. This section summarises some of the commonly used methods and describes how they can

be used to interpolate node properties from cell properties; each method can also be used to interpolate cell properties from node properties instead.

Central Differencing Scheme

The most obvious way to interpolate the gas properties at a node is to take the average of the properties of the adjacent cells (y_i and y_{i+1}). This is known as the central differencing scheme [54, p. 82]. This interpolation can be volume weighted to take into account how close the node is to the centre of the adjacent cells.

$$y_{j\,CD} = \frac{y_{i+1}V_i + y_i V_{i+1}}{V_i + V_{i+1}} \tag{3.98}$$

The central differencing method has a good accuracy and produces low amounts of numerical diffusion because its Taylor series truncation error is second order [79, p. 447]. However, it can introduce unphysical spatial oscillations of the gas properties in regions of strong convection and low diffusion [79, p. 145]. When convection dominates, the flow from the upwind direction should have a greater influence on the value at the node; using the central differencing scheme allows the information to propagate against the flow.

Upwind Differencing Scheme

To reduce the oscillations, the interpolation can be weighted towards the upwind direction. This ensures that information travels with the flow. The simplest way to do this is to set the node value to be the same as the upwind cell value. This is known as the upwind differencing scheme [79, p. 146].

$$y_{j\,UD} = \begin{cases} y_i & \text{if } \dot{V}_j > 0 \\ y_{i+1} & \text{if } \dot{V}_j \leq 0 \end{cases} \tag{3.99}$$

This is stable but can introduce a large amount of numerical diffusion because it is only first-order accurate. A high spatial resolution is required to get an accurate result.

Linear Upwind Differencing Scheme

The upwind differencing scheme can be extended to be second-order accurate by extrapolating the node value from the values of the two upwind cells. This is known as the linear upwind differencing scheme [79, p. 165].

$$y_{j\,LUD} = \begin{cases} y_i + \dfrac{V_i}{2}\dfrac{y_i - y_{i-1}}{\frac{V_i}{2} + \frac{V_{i-1}}{2}} & \text{if } \dot{V}_j > 0 \\ y_{i+1} + \dfrac{V_{i+1}}{2}\dfrac{y_{i+1} - y_{i+2}}{\frac{V_{i+1}}{2} + \frac{V_{i+2}}{2}} & \text{if } \dot{V}_j \leq 0 \end{cases} \tag{3.100}$$

This scheme is more accurate than the upwind differencing scheme and does not introduce the oscillations of the central differencing scheme.

QUICK Scheme

The linear upwind differencing scheme and the central differencing scheme can be combined using a weighted average to produce a scheme that is accurate and stable. This approach was recommended by Kühl [78].

$$y_{j\,weighted} = w\, y_{j\,CD} + (1 - w) y_{j\,LUD} \tag{3.101}$$

Kühl recommends a weighting factor of $w = 0.7$. If a weighting factor of $w = 0.75$ is used, the scheme becomes equivalent to the QUICK scheme [79, p. 156]. The QUICK scheme calculates the node value using a quadratic fit between the two adjacent upwind cells and the one adjacent downwind cell. It is third-order accurate.

$$y_{j\,QUICK} = \frac{3}{4} y_{j\,CD} + \frac{1}{4} y_{j\,LUD} \tag{3.102}$$

Total Variation Diminishing Schemes

The QUICK scheme can still introduce oscillations in the gas properties under some circumstances [79, p. 165]. To remove the oscillations completely, the scheme must be total variation diminishing (TVD). TVD schemes do not create new undershoots and overshoots in the solution and do not accentuate existing extremes [79, p. 168].

TVD schemes combine the central differencing scheme and the upwind differencing scheme to produce an interpolation method that is second-order accurate and produces no oscillations. The central differencing scheme and the upwind differencing scheme are weighted using a slope limiter ψ.

$$y_j = \psi_j \, y_{j\,CD} + (1 - \psi_j) y_{j\,UD} \tag{3.103}$$

When the gas property is changing linearly, the central differencing scheme is used. In locations where the spatial gradient of the gas property is changing rapidly, the upwind differencing scheme is used. For situations between these two extremes, a weighted average of the two interpolation methods is used.

The slope limiter is a function of the gradient ratio θ [4, p. 33].

$$\theta_j = \begin{cases} \text{sign}\left[(y_i - y_{i-1})(y_{i+1} - y_i)\right] \dfrac{\left(\dfrac{\max\left[\varepsilon_0, |y_i - y_{i-1}|\right]}{\frac{V_i}{2} + \frac{V_{i-1}}{2}}\right)}{\left(\dfrac{\max\left[\varepsilon_0, |y_{i+1} - y_i|\right]}{\frac{V_{i+1}}{2} + \frac{V_i}{2}}\right)} & \text{if } \dot{V}_j > 0 \\ \text{sign}\left[(y_{i+1} - y_{i+2})(y_i - y_{i+1})\right] \dfrac{\left(\dfrac{\max\left[\varepsilon_0, |y_{i+1} - y_{i+2}|\right]}{\frac{V_{i+1}}{2} + \frac{V_{i+2}}{2}}\right)}{\left(\dfrac{\max\left[\varepsilon_0, |y_i - y_{i+1}|\right]}{\frac{V_i}{2} + \frac{V_{i+1}}{2}}\right)} & \text{if } \dot{V}_j \leq 0 \end{cases} \tag{3.104}$$

where ε_0 is an arbitrarily small, positive constant. The gradient ratio describes how quickly the gradient of y is changing. It is equal to 1 if the gradient across the upwind cells is equal to the gradient across the adjacent cells.

The slope limiter recommended by Andersen is the van Leer slope limiter [4, p. 33][80, p. 115].

$$\psi_{j\,vanLeer} = \frac{\theta_j + |\theta_j|}{1 + |\theta_j|} \tag{3.105}$$

Another option is the superbee slope limiter [81]. This limiter was designed to preserve sudden changes in the spatial gradient of the gas properties.

$$\psi_{j\,superbee} = \max[0, \min[2\theta_j, 1], \min[\theta_j, 2]] \tag{3.106}$$

Summary

Figure 3.15 shows a visual representation of the node values that these different interpolation methods produce. From the plot, some of the key properties of the methods can be seen. For example, the node values calculated using the central differencing method are independent of the flow direction; the upwind differencing method has a poor accuracy when the gas property is changing; and the superbee method preserves sudden changes in the gas property.

3.10.3 Selected Interpolation Methods

The model uses different interpolation methods for different gas properties. This is because the different gas properties have unique stability and accuracy requirements.

Stagnation Temperature

The most important interpolation method is the one used for the stagnation temperatures because it can have a significant impact on the accuracy and stability of the model.

The choice of interpolation method for the stagnation temperatures affects the number of cells required to accurately predict the cooling power. This is particularly important within the regenerator; small differences in interpolation can strongly influence the regenerator losses because of the high mass flows and large temperature gradient.

The relationship between cooling power and spatial resolution was investigated for different stagnation temperature interpolation methods. The results are plotted in Figure 3.16. A lower number of cells is desirable as the simulation time is approximately proportional to the number of cells.

All the interpolation methods asymptotically approach the same value as the number of cells is increased. In this case, the central differencing scheme is most accurate for a given number of cells. The central differencing scheme requires the fewest cells because the interpolated node value is independent of the flow direction. This is particularly beneficial in the regenerator because the regenerator losses are caused by the gas having different temperatures

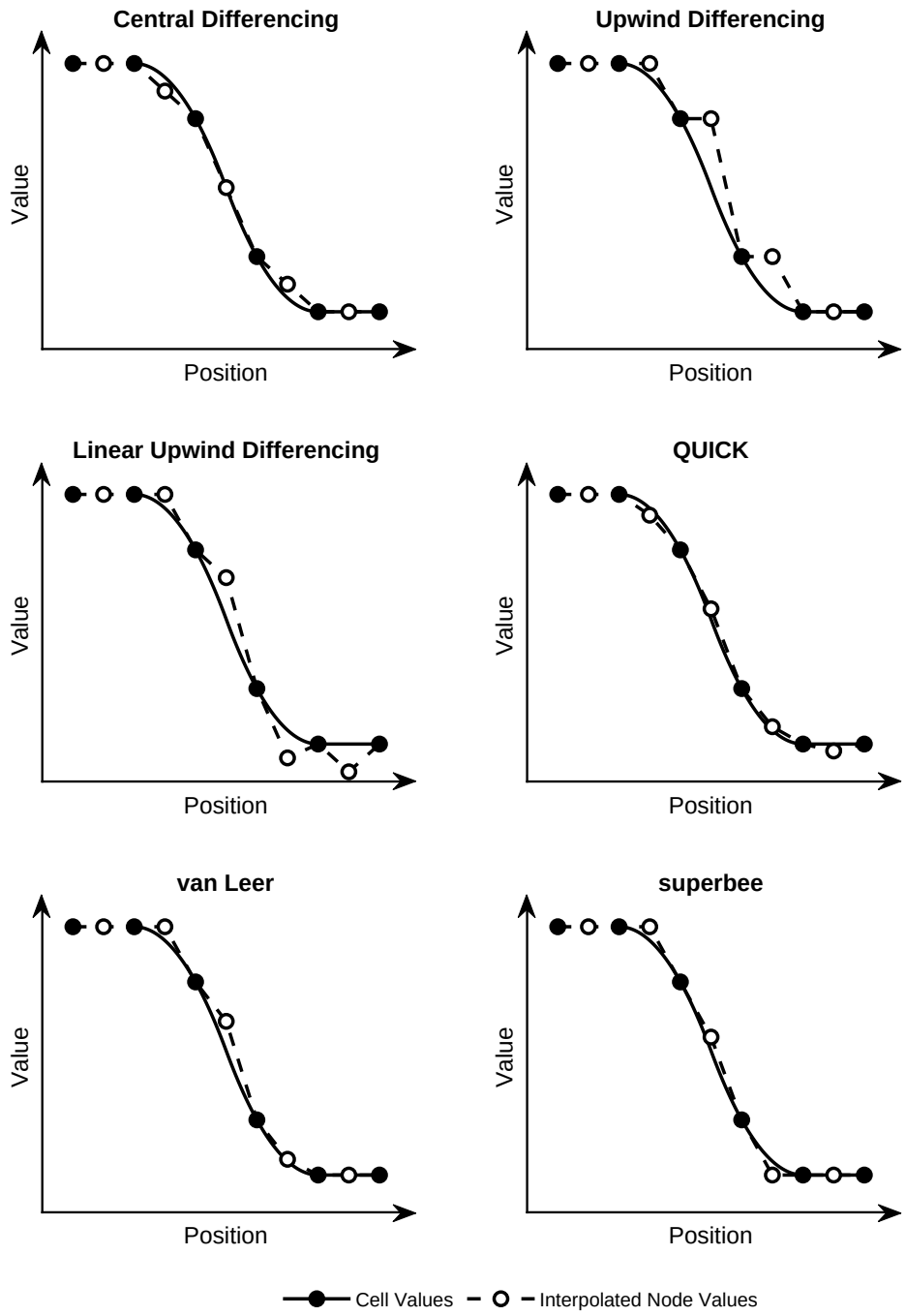

Figure 3.15: Plots showing how the schemes discussed in Section 3.10.2 interpolate the values at the nodes from the cell values. The flow is in the positive direction.

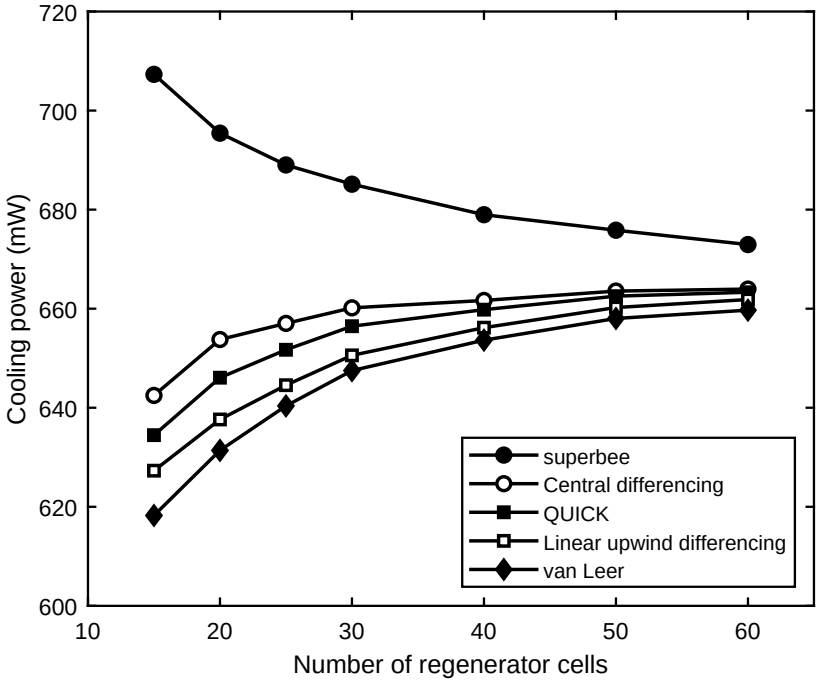

Figure 3.16: A plot comparing the relationship between the number of regenerator cells and cooling power for different stagnation temperature interpolation methods. The upwind differencing method was also simulated but is not shown because the cooling powers it predicted were significantly lower than the powers predicted by the other methods. The model was used to simulate a measurement taken using the Small Scale Cooler (see Section 5.1).

when flowing in different directions. The disadvantage of the central differencing scheme is that it can produce unphysical oscillations of the gas properties. This can be seen in Figure 3.17. These oscillations are most prominent in the transfer line because of the poor thermal contact with the surroundings. These oscillations do not appear to significantly affect the predicted cooling power for the Small Scale Cooler, but it is possible that they could have more significant effects when simulating other coolers.

The QUICK scheme is the next most accurate, and it does not introduce unphysical oscillations, so this scheme was selected for interpolating the stagnation temperatures. The QUICK scheme is only used in regions of constant flow area and cell type. This ensures that the node temperatures are only interpolated using information from the same type of region, which helps to prevent artificially smoothing out the stagnation temperatures. Different

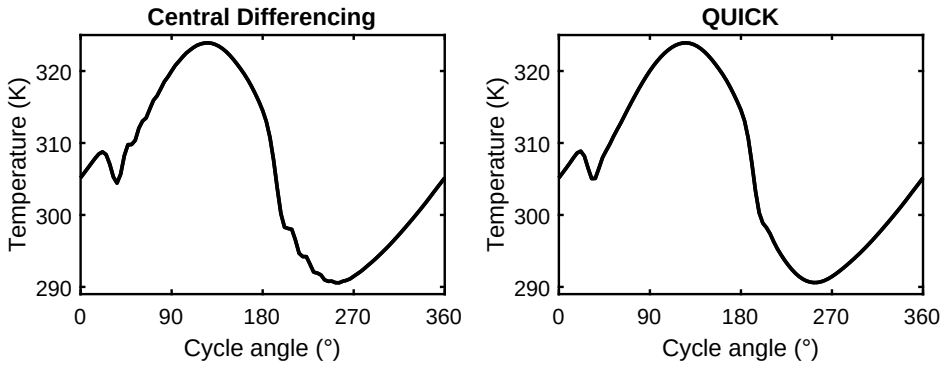

Figure 3.17: Plots showing the temperature variation of a cell over a cycle for the central differencing and QUICK interpolation schemes. This cell is located in the middle of the transfer line and the model is simulating the Small Scale Cooler (see Section 5.1). Oscillations can be seen at 60° and 220° for the central differencing scheme.

interpolation methods are used for nodes that are at the interface between different regions, as shown in Table 3.2.

Stagnation Pressure

The stagnation pressures are interpolated using the central differencing scheme. It is not necessary to weight the interpolation towards the upwind direction to prevent unphysical oscillations. This is because Stirling machines typically operate at low Mach numbers, so the pressure information travels much faster than the flow speed. For nodes adjacent to variable volume cells, the stagnation pressure of the gas in the variable volume cell is used because there is no pressure drop in the cell. The central differencing scheme is used for all other nodes.

Table 3.2: A table showing how the schemes used for interpolating the stagnation temperatures are selected based on the position of the node relative to the interfaces between different regions.

Node type		Interpolation scheme
Interpolation node	**Upwind node**	
Interface	Interface	Upwind differencing
Interface	Not an interface	Linear upwind differencing
Not an interface	Interface	Central differencing
Not an interface	Not an interface	QUICK

Volumetric Flow Rate

The volumetric flow rates at the centres of the cells are calculated by using the central differencing scheme. Using this scheme for the volumetric flow rates does not appear to introduce any unphysical oscillations of the gas properties.

Specific Turbulence Kinetic Energy

The specific turbulence kinetic energy in variable volume cells is generated by incoming flow. Therefore, the method used for calculating the specific turbulence kinetic energy at the nodes depends on whether the flow is outgoing or incoming.

For outgoing flow, the specific turbulence kinetic energy at the node κ_j is calculated using the upwind differencing method and is equal to the specific turbulence kinetic energy at the cell centre. This is because the variable volume cells are assumed to be well mixed. For incoming flow, κ_j is calculated using Equation 3.107 which assumes that all the flow kinetic energy is converted to turbulence kinetic energy.

$$\kappa_j = \frac{1}{2} v_j^2 \tag{3.107}$$

Turbulence Intensity

The turbulence intensity in pipe and heat exchanger cells is primarily interpolated using the upwind differencing method. Upwind differencing provides good stability and prevents the interpolated value from exceeding 1 or dropping below 0. The empirical cell correlations that use the turbulence intensity already have a significant uncertainty, so the reduced accuracy of upwind differencing is not an issue.

The exception is when the cells on either side of the node are different types or have different flow areas. In these cases, the incoming flow is assumed to always be fully turbulent and $\mathcal{T}_j$ is set to 1.

3.11 Differential Equation Solver

The choice of ordinary differential equation solver influences the speed of the model and the accuracy of the solution. It is important to select a solver that is suited to the system of differential equations.

The model equations presented in Section 3.5 are stiff. A system of differential equations is stiff if an explicit method requires very short time steps to remain stable, even when the solution variables are changing slowly [82, p. 72]. This is the case when simulating the subsonic flow and compressible gas found in Stirling coolers because the pressure waves in the gas travel much faster than the gas itself. To remain stable, the time step of an explicit method must be shorter than the length of time it takes for an acoustic wave to cross a cell; this is the Courant–Friedrichs–Lewy (CFL) condition [83]. For a time step Δt and a cell length x, the CFL condition can be written as

$$\Delta t \leq \frac{x}{v_{sound}} \tag{3.108}$$

where v_{sound} is the speed of sound, given by

$$v_{sound} = \sqrt{\gamma \, R_g \, T} \tag{3.109}$$

To avoid this limitation on the time step, the model uses an implicit method. Whereas explicit methods calculate the future state of a system from the state of the system at the current time, implicit methods find the future state by solving an equation involving both the future state of the system and the current state. Implicit methods take longer to calculate each step, but they often take less time overall for stiff problems because they can take longer time steps. This was the case for the differential equations of this model.

The method selected for use in this model is the backward differentiation formula (BDF), implemented by using the `ode15s` function that is part of the MATLAB ODE suite [82, p. 39]. The `ode15s` function was the fastest of the methods of the MATLAB ODE suite for this system of differential equations. It was found that its speed could be further improved by limiting its maximum order of accuracy to 2 and setting it to use backward differentiation formulas instead of numerical differentiation formulas [84].

3.11.1 Error Tolerances

The `ode15s` function uses a variable time step to provide the required accuracy. It estimates the accuracy of the solution by calculating the local truncation error [82, p. 74]. If the error becomes too large, the function reduces the step size.

When the model is started, acoustic pressure waves form as the gas velocities stabilise. The model must take small steps to properly track these waves. However, after a little while, these acoustic waves will "ring out" and the solver can take much longer time steps.

The required accuracy of the solution is specified by two variables: the relative and absolute tolerances. The `ode15s` function adjusts the step size so that the error in the calculation of each solution variable is always less than either the relative tolerance multiplied by the solution variable or the absolute tolerance.

$$|Error| \leq \max\left(RelTol\,|y|\,, AbsTol\right) \tag{3.110}$$

The `ode15s` function uses the same relative tolerance for all solution variables and the model uses an initial relative tolerance of 1×10^{-3}. As the solution converges, the relative tolerance is updated at the end of each cycle to be a factor of 100 lower than the largest convergence error for the solid and gas temperatures (see Section 3.13.4). A factor of 100 appears to give sufficient accuracy for the model to converge reliably, but it can be adjusted in the input file if necessary (see Section A.3 in Appendix A).

A different absolute tolerance can be set for each variable. This tolerance is particularly important for solution variables that approach zero; setting an absolute tolerance prevents the required error from also approaching zero. This is the case for the gas momentum, turbulent mass and turbulence kinetic energy. Before running the first cycle, the model calculates the absolute tolerances for these variables at every cell or node by using Equations 3.111, 3.112 and 3.113.

$$AbsTol_{p_j} = 1 \times 10^{-3}\, v_{soundj}\, m_j \tag{3.111}$$

$$AbsTol_{m_{\mathcal{T}}i} = 1 \times 10^{-3}\, m_i \tag{3.112}$$

$$AbsTol_{Ki} = \frac{1}{2}\left(1 \times 10^{-3}\, v_{soundi}\right)^2 m_i \tag{3.113}$$

The speed of sound is calculated using Equation 3.109.

With these error tolerances, the solver typically takes a few hundred steps per cycle. The smallest time steps occur when the flow reverses direction.

3.11.2 Jacobian Matrix

The `ode15s` function uses a Jacobian matrix to calculate the solution variables for the next step [82, p. 70]. The Jacobian matrix contains the partial derivatives of the solution variables with respect to all the other solution variables. This provides the `ode15s` function with information about how changing one variable will affect the other solution variables.

The `ode15s` function numerically recomputes the Jacobian matrix if it is unable to find the solution variables for the next step. To speed up this process, the model provides the `ode15s` function with the sparsity pattern of the Jacobian matrix. The sparsity pattern is found by analysing the Jacobian matrix at various times over the first cycle and identifying any elements that are non-zero. A typical sparsity pattern is shown in Figure 3.18.

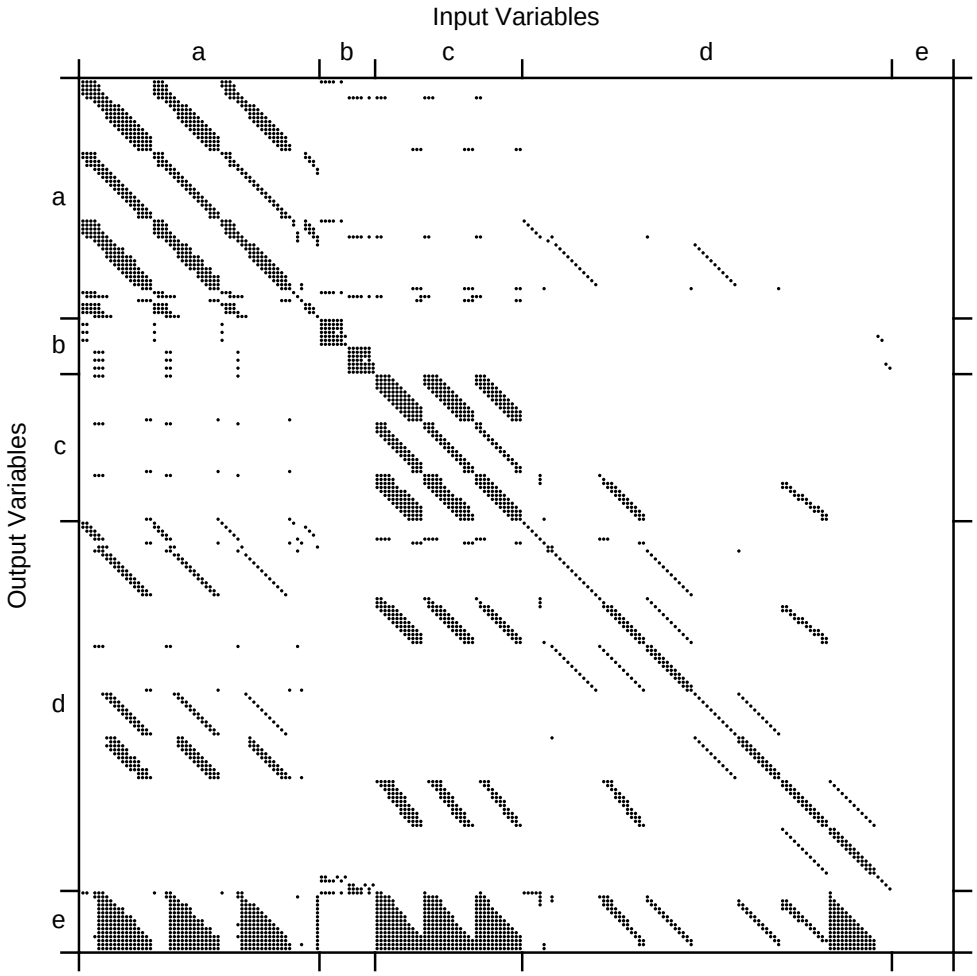

Figure 3.18: A typical Jacobian matrix sparsity pattern calculated by the model. This sparsity pattern is for a single-stage cooler with 10 regenerator cells. Each dot represents a non-zero value of the Jacobian matrix, where a change in the associated input causes a change in the associated output. The input and output variables are sorted into groups: **a**, gas properties in the main flow path; **b**, gas properties in the piston and shaft clearance seals and backshells; **c**, gas properties in the appendix gap; **d**, solid cell temperatures; and **e**, energy flow along the cold finger. The energy flow along the cold finger does not affect the other variables, but it is tracked for use by the artificial convergence routine (see Section 3.13.1).

3.12 Initial State

The initial states of the solution variables are calculated from the input file parameters (see Section A.3 in Appendix A). The model aims to set an initial state that is close to what the final state will be once the model has converged; this helps to reduce the time taken for convergence.

The input parameters define the temperatures of the compressor body, the cold head body, the transfer line and the cold tips. Linear interpolation is used to calculate the initial temperature profile along the cold finger tube, displacer tube, regenerator and the gas cells of the regenerator and appendix gaps. The input parameters also specify the fill pressure of the cooler and temperature of the cooler when it was filled. This pressure and temperature are used to calculate the total mass of gas in the system by using either the ideal gas equation of state or a real gas lookup table.

The solid cells use temperature as their solution variable, so the model can set these solution variables directly. In contrast, the thermodynamic state of the gas cells is defined by the mass and energy which need to be calculated. The model knows the temperatures of the gas cells and the total mass of gas from the input parameters and uses this information to calculate the mass and energy of each cell.

To calculate the initial mass and energy of each cell, the model first works out the initial pressure distribution in the system. The pressure of the working volume (the main flow path and the appendix gaps) and the pressures of the backshells (which contain the linear motors) can differ significantly over the thermodynamic cycle as the compressor pistons and displacer move; therefore, the model must estimate individual initial pressures for each of these regions. Firstly, the model estimates the cycle-averaged system pressure $\bar{P}$ by using the cycle-averaged cell volumes.

$$\bar{P} = \frac{m_{tot}\, R_g}{\sum_i \frac{\bar{V}_{wi}}{T_{wi}} + \sum_i \frac{\bar{V}_{bi}}{T_{bi}}} \tag{3.114}$$

where $\bar{V}_{wi}$ and $\bar{V}_{bi}$ are the mean volumes of the working volume cells and the backshell cells and T_{wi} and T_{bi} are the initial cell temperatures. The total mass

of gas in the working volume $m_{w\,tot}$ can then be calculated.

$$m_{w\,tot} = \frac{\bar{P} \sum_i \frac{\bar{V}_{wi}}{T_{wi}}}{R_g} \tag{3.115}$$

Then the initial pressure in the working volume P_w can be calculated by using the initial volumes of the cells in the working volume V_{wi}.

$$P_w = \frac{m_{w\,tot}\, R_g}{\sum_i \frac{V_{wi}}{T_{wi}}} \tag{3.116}$$

Finally, the initial mass and energy solution variables for each cell in the working volume can be calculated.

$$m_{wi} = \frac{P_w\, V_{wi}}{R_g\, T_{wi}} \tag{3.117}$$

$$E_{wi} = c_V\, m_{wi}\, T_{wi} \tag{3.118}$$

The model uses a lookup table instead of Equations 3.117 and 3.118 when simulating a real gas. A similar process is used for calculating the masses and energies of the gas cells in the backshells.

The model sets the initial values of the momentum, turbulence kinetic energy and turbulent mass to be zero. This does not delay the model convergence significantly because these properties converge quickly.

3.13 Convergence Acceleration

The solution variables of the Stirling model described in the previous sections will converge towards a periodic steady state in the same way that a real Stirling machine will. A periodic steady state is where the solution variables have the same value at the start and end of each cycle. The input and cooling powers of the modelled cooler can only be evaluated accurately when this periodic steady state has been reached.

Some model properties take longer to converge than others. For example, the pressure swings and gas velocities in the primary flow path reach a periodic steady state in around three cycles of the mechanism. However, the

temperatures of the regenerator mesh cells may take thousands of cycles to converge to a steady state. This is because the heat capacity of the mesh cells is large compared to the heat capacity of the gas. The flow through the compressor piston and displacer shaft clearance seals can also take a long time to converge if the seals are effective.

Each cycle takes around a minute to run, so it can take a very long time for the model to converge naturally. Artificial convergence acceleration methods are used by the model to speed up the convergence.

3.13.1 Temperature Convergence

Accelerating the temperature convergence is challenging because of the high heat capacity of the solid cells compared to the gas cells and the complicated relationships between the cell temperatures and heat flows. The artificial convergence methods discussed in the literature were reviewed to help select the convergence method for this model.

Methods Discussed in the Literature

One of the simplest artificial convergence methods is to determine how the temperature of each cell is changing and then extrapolate this change. The procedure suggested by Urieli [9] is to calculate the change in temperature of each regenerator cell between the start and the end of the cycle. This temperature change is then multiplied by a factor and the result is added to the temperature of the cell at the end of the cycle. This approach was unsuccessful when used to accelerate the temperature convergence in the RAL Third-Order Model. The approach works best if each cell is in an unchanging environment; however, the flow of gas in the regenerator causes the temperature of each regenerator cell to strongly affect the temperatures of the neighbouring cells. This results in the convergence becoming unstable if the multiplication factor is too large. A smaller factor can be used, but the model takes a very long time to converge when the factor is small enough to be stable.

A similar method to Urieli's is the epsilon algorithm [85]. Andersen suggested that this method could be used for accelerating the convergence of Stirling machine models [4]. The algorithm assumes that the temperatures will settle

by exponential decay and uses this information to extrapolate to the periodic steady-state temperatures. This is slightly more effective than Urieli's method but still takes a long time to converge for similar reasons.

A method suggested by Schock [86] is to set the specific heat capacity of the regenerator cells to a very low value at the start of the simulation and then to gradually increase it after each cycle up to its physical value. This method did not work successfully when used in the RAL Third-Order Model. The model did converge quickly when the heat capacities were low but the temperatures it converged to were very different from the periodic steady-state temperatures when the full heat capacities were used.

The method used by Kühl [78] and Harvey [87] is based on the principle that heat can only enter or leave the regenerator at either end. When the model is converged, the net energy flowing along the regenerator per cycle will be the same for all the nodes along the length of the regenerator. If there is more energy flowing across some nodes than others, the regenerator mesh temperatures can be adjusted to correct this. This method is most effective when the temperatures of the regenerator cells strongly affect the temperature of the gas leaving each cell. This occurs when the heat capacity of the regenerator cells is high and there is good thermal contact between the gas and the regenerator. These conditions apply for most Stirling coolers.

An alternative approach is to find the periodic steady-state solution numerically rather than by trying to artificially speed up the natural convergence process. For example, Andersen [4] uses a shooting method to guess the required solution variables. This method trials different sets of initial solution variables by running a cycle with each set of variables. It adjusts the initial variables until a periodic steady state is found. This numerical method can be fast for low resolution models but can take much longer to solve higher resolution models [4].

The Sage model [5] also finds the periodic steady state using a numerical method. It creates a system of equations where the solution variables at the end of a cycle are defined as being equal to the solution variables at the start of the cycle. This ensures that the solution to the equations will be the periodic steady state. This system of equations is then solved by using a nonlinear solver.

Selected Method

None of the methods found in the literature were determined to be suitable for the RAL Third-Order Model. Urieli's method and the epsilon algorithm do not work well for converging the regenerator cells, whereas the method used by Kühl works well for the regenerator cells but struggles when the displacer tube and cold finger tube are included in the model. The shooting method used by Andersen was not attempted because it was thought that it would take a very long time to find a solution due to the large number of cells in the model. The method used by Sage would require the development of a periodic differential equation solver which was out of the scope of this project.

The selected approach for the RAL Third-Order Model combines two methods: energy flow equalisation, based on the method used by Kühl, and cell temperature adjustment, based on the method used by Urieli. These two methods are effective in different situations. The energy flow equalisation method is suitable if the cells are well-connected thermally because a temperature change of one cell will strongly affect the energy flows to neighbouring cells. This occurs if the regenerator is effective because the temperature of a regenerator mesh cell strongly affects the temperature of the gas flowing through it. If the regenerator is ineffective, temperature changes of cells have little impact on their neighbours and the cell temperature adjustment method works better.

Another advantage of using two convergence methods is that they apply their temperature adjustments in different ways. The energy flow equalisation method applies its temperature adjustments to groups of cells. If this is the only method used, it can take a long time for the individual cells to reach their periodic steady-state temperatures. The cell temperature adjustment method applies a different temperature adjustment to each cell, so it can help the individual cells converge faster. Combining both techniques produces a convergence acceleration method that is fast and robust for a range of different coolers.

Energy Flow Equalisation

The energy flow equalisation method used in this model is similar to the method used by Kühl but with a significant modification. Kühl's model uses the method to converge the cell temperatures of the regenerator mesh; the RAL

Third-Order Model extends the method to help converge the temperatures of all the solid and gas cells in the cold finger and the gas in the transfer line and compression chambers.

The method uses the principle that convergence is achieved when the heat flowing into each region over a cycle is equal to the heat flowing out. If this is the case, the region temperature will be the same at the start and end of the cycle. The cold finger is divided along its length into regions, with each region consisting of a row of cells in Figure 3.3. A typical cold finger region would contain a regenerator mesh cell, a displacer tube cell, a cold finger tube cell and the associated gas cells. The gas cells in the compression chambers and transfer line are grouped into a region and the gas in the expansion chamber is in its own region. The method achieves convergence by applying temperature adjustments to the cells in each region. The cells in a region can have different temperatures, but the method applies the same temperature adjustment to all the cells in each region.

The convergence method calculates the required temperature adjustments by making the approximation that the regions are part of a thermal circuit and are connected by thermal resistances. The thermal circuit of a single-stage cooler is shown in Figure 3.19. This thermal circuit is used to predict how a temperature adjustment to one region will affect the energy flows to other regions. Temperature adjustments are applied to regions $comp$, exp, $CF1$ and $CF2$ until the heat flow rates are balanced, as defined by Equation 3.119.

$$\dot{Q}_{warm} + \dot{Q}_{PVwarm} = \dot{Q}_{CF0} = \dot{Q}_{CF1} = \dot{Q}_{CF2} = \dot{Q}_{cold} + \dot{Q}_{PVcold} \qquad (3.119)$$

In order to calculate the required temperature adjustments, the average heat flow rates of the previous cycle and the thermal resistances between regions must be found.

The average heat flow rates are calculated by finding the integral of the heat flow rates between regions over the previous cycle and then dividing by the cycle period. In Figure 3.19, $\dot{Q}_{warm}$ and $\dot{Q}_{cold}$ represent the heat flow rate from the isothermal walls to the gas in the warm and cold regions of the cooler; $\dot{Q}_{PVwarm}$ and $\dot{Q}_{PVcold}$ represent the rate of work done on the gas by the motion of the compressor pistons and the displacer; and $\dot{Q}_{CF0}$, $\dot{Q}_{CF1}$ and $\dot{Q}_{CF2}$ represent the heat flow along the cold finger which consists of the motion of the gas and the conduction through the gas or solids. There are

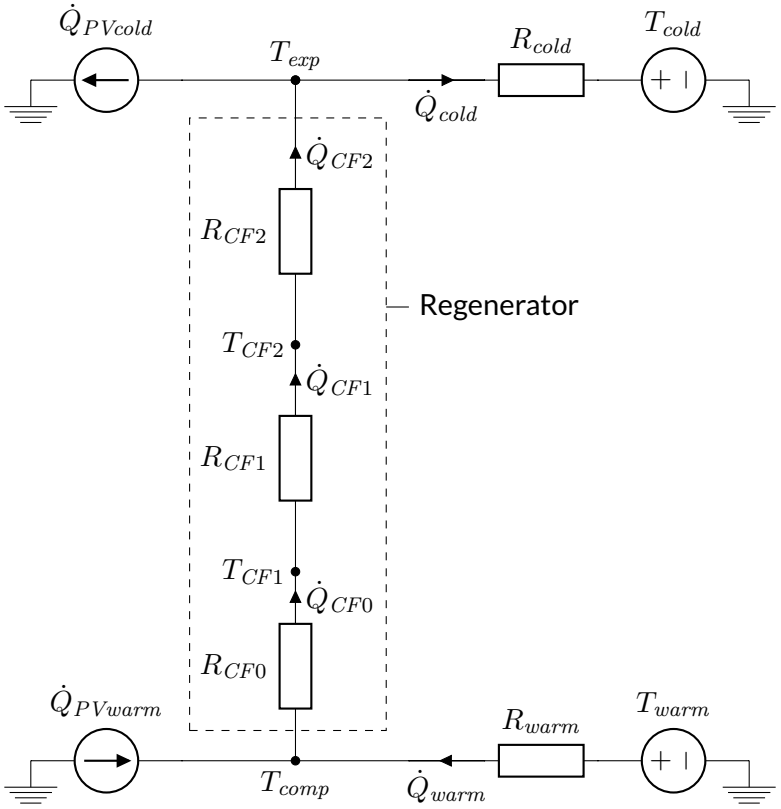

Figure 3.19: A diagram showing the thermal circuit approximation for a single-stage cooler used by the energy flow equalisation method. The temperatures, heat flow rates and thermal resistances are equivalent to the voltages, currents and electrical resistances of an electrical circuit. When the model is converged, the heat flow rates will satisfy the relationships shown in this diagram. All temperatures, heat flow rates and thermal resistances are the average over a cycle. The temperatures represent the region temperatures; these are not well defined, but this is not an issue as they are not required by the convergence method. Models typically have many more cold finger regions than the two shown in this diagram.

some additional aspects that must be considered when calculating $\dot{Q}_{CF0}$, $\dot{Q}_{CF1}$ and $\dot{Q}_{CF2}$:

- Heat transfer in the appendix gap is not always between cells in the same region (see Section 3.7). The model tracks the heat transferred in the appendix gap between different regions and includes it in the calculation of the average heat flow rates.
- The model can simulate the external radiation loads on the cold finger. The heat from these radiation loads is then transported towards the cold end. To account for these loads in the energy balance, any radiation loads at cells nearer the warm end of the cold finger are subtracted from the measured heat flows. For example, any radiation loads at $CF1$ and $CF2$ in Figure 3.19 would be subtracted from $\dot{Q}_{CF2}$.

The thermal resistances between the gas and the walls at the warm and cold ends of the cooler (R_{warm} and R_{cold}) are calculated using the heat transfer correlations presented in Section 3.6. The resistances are calculated with Equation 3.120, which uses the surface areas S, gas conductivities k, hydraulic diameters d_h and Nusselt numbers Nu, averaged over the previous cycle. The calculation of R_{warm} accounts for the thermal resistance between the walls and gas in both compression chambers and in the transfer line cells.

$$\frac{1}{R} = \sum_i \frac{\overline{S_i}\,\overline{k_i}}{\overline{d_{hi}}}\overline{Nu_i} \tag{3.120}$$

The thermal resistances between the cold finger regions (R_{CF0}, R_{CF1} and R_{CF2}) account for the advection of energy and the thermal conduction; they are calculated using Equation 3.121. The gas leaving each regenerator cell is assumed to be the same temperature as the mesh, so an increase in mesh temperature increases the energy flowing out of the cell. Only half the mass flow $\dot{m}$ is accounted for because the gas is flowing out of the cell for approximately half of the cycle. The thermal conduction accounts for the conduction through all the gas cells and solid cells, although Equation 3.121 has been simplified to only include a single conduction path. The conductance depends on the cell length x; the flow or cross-sectional area A; and the cycle-averaged conductivity k, which may be enhanced for gas cells (see Section 3.6).

$$\frac{1}{R_j} = \frac{\overline{|\dot{m}_j|}}{2} c_P + \frac{1}{\frac{x_i}{2\overline{k_i} A_i} + \frac{x_{i+1}}{2\overline{k_{i+1}} A_{i+1}}} \tag{3.121}$$

Once the heat flow rates and thermal resistances from the previous cycle have been calculated, they can be used to calculate the required temperature adjustments. They are used in a system of linear equations which relate the required temperature adjustments to the required changes in heat flow rates. For the thermal circuit shown in Figure 3.19, the system of equations is as follows:

$$\frac{-\Delta T_{comp}}{R_{warm}} = \dot{Q}_{target} - \dot{Q}_{warm} - \dot{Q}_{PVwarm} \tag{3.122a}$$

$$\frac{\Delta T_{comp} - \Delta T_{CF1}}{R_{CF0}} = \dot{Q}_{target} - \dot{Q}_{CF0} \tag{3.122b}$$

$$\frac{\Delta T_{CF1} - \Delta T_{CF2}}{R_{CF1}} = \dot{Q}_{target} - \dot{Q}_{CF1} \tag{3.122c}$$

$$\frac{\Delta T_{CF2} - \Delta T_{exp}}{R_{CF2}} = \dot{Q}_{target} - \dot{Q}_{CF2} \tag{3.122d}$$

$$\frac{\Delta T_{exp}}{R_{cold}} = \dot{Q}_{target} - \dot{Q}_{cold} - \dot{Q}_{PVcold} \tag{3.122e}$$

where ΔT represents the required temperature adjustment for a region and $\dot{Q}_{target}$ is the target heat flow rate that is constant along the cold finger. The unknown variables of this system of equations are ΔT_{comp}, ΔT_{CF1}, ΔT_{CF2}, ΔT_{exp} and $\dot{Q}_{target}$ and they are found by solving the equations using MATLAB's `mldivide` function [55].

The thermal circuit approximation of the artificial convergence method can be extended to work with two-stage coolers, as shown in Figure 3.20. For this thermal circuit, the unknown variables are ΔT_{comp}, ΔT_{CF1}, ΔT_{CF2}, ΔT_{CF3}, ΔT_{CF4}, ΔT_{exp2}, $\dot{Q}_{target1}$, $\dot{Q}_{target2}$ and the system of equations is as follows:

$$\frac{-\Delta T_{comp}}{R_{warm}} = \dot{Q}_{target1} - \dot{Q}_{warm} - \dot{Q}_{PVwarm} \tag{3.123a}$$

$$\frac{\Delta T_{comp} - \Delta T_{CF1}}{R_{CF0}} = \dot{Q}_{target1} - \dot{Q}_{CF0} \tag{3.123b}$$

$$\frac{\Delta T_{CF1} - \Delta T_{CF2}}{R_{CF1}} = \dot{Q}_{target1} - \dot{Q}_{CF1} \tag{3.123c}$$

$$\frac{\Delta T_{CF2} - \Delta T_{CF3}}{R_{CF2}} = \dot{Q}_{target1} - \dot{Q}_{CF2} \tag{3.123d}$$

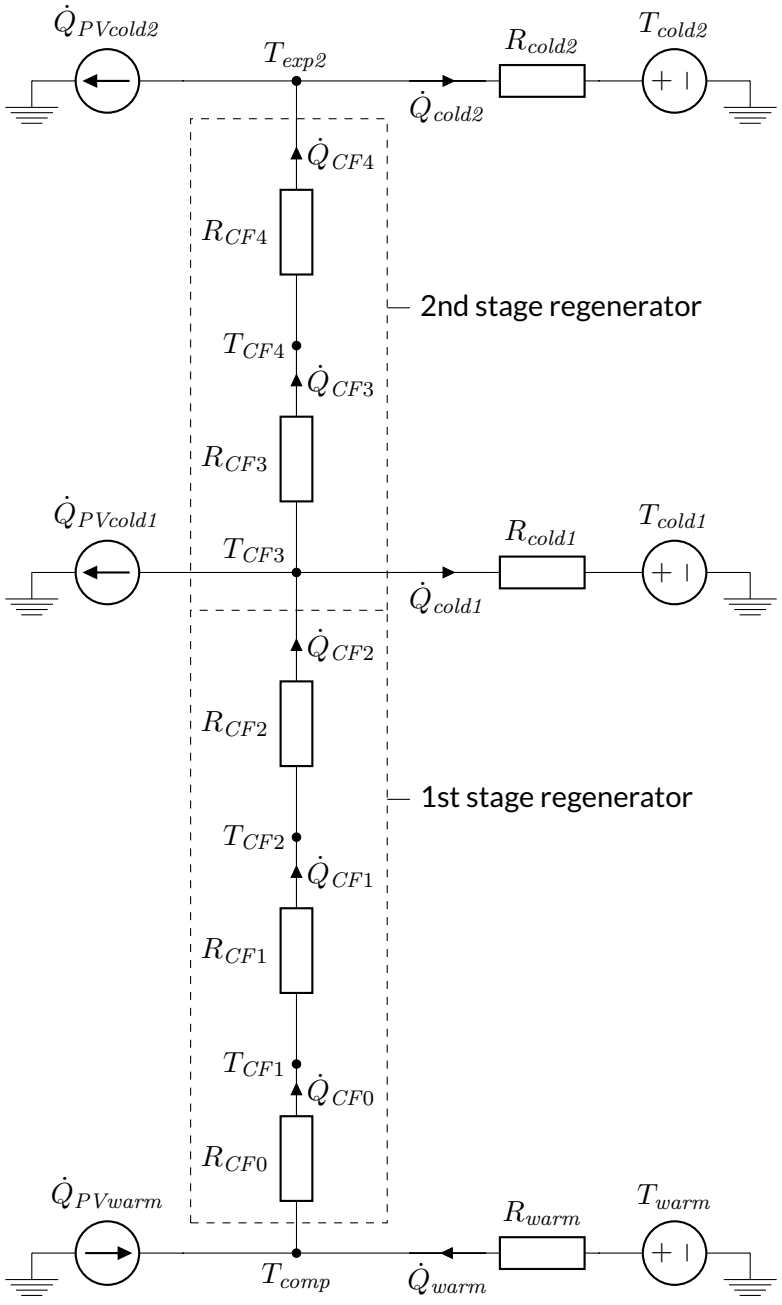

Figure 3.20: A diagram showing the extension of the thermal circuit approximation of Figure 3.19 for two-stage coolers.

$$\frac{\Delta T_{CF3}}{R_{cold1}} = (\dot{Q}_{target1} - \dot{Q}_{target2}) - (\dot{Q}_{CF1} - \dot{Q}_{CF2}) \tag{3.123e}$$

$$\frac{\Delta T_{CF3} - \Delta T_{CF4}}{R_{CF3}} = \dot{Q}_{target2} - \dot{Q}_{CF3} \tag{3.123f}$$

$$\frac{\Delta T_{CF4} - \Delta T_{exp2}}{R_{CF4}} = \dot{Q}_{target2} - \dot{Q}_{CF4} \tag{3.123g}$$

$$\frac{\Delta T_{exp2}}{R_{cold2}} = \dot{Q}_{target2} - \dot{Q}_{cold2} - \dot{Q}_{PVcold2} \tag{3.123h}$$

Cell Temperature Adjustment

The other technique that the model uses to accelerate the temperature convergence is the cell temperature adjustment method. This method calculates the required temperature adjustments by extrapolating the natural temperature change over each cycle. These temperature adjustments are combined with the adjustments calculated by the energy flow equalisation method. The combined temperature adjustments are calculated using the following steps:

1. The natural temperature change over the previous cycle is calculated for the regenerator mesh, displacer tube and cold finger tube cells.
2. These temperature changes are then normalised by dividing each change by the largest absolute value of temperature change over the previous cycle for that type of cell. For example, each regenerator mesh cell temperature change is normalised by dividing by the largest absolute regenerator mesh cell temperature change.
3. The normalised temperature changes are then multiplied by half the largest absolute value of the energy flow equalisation temperature adjustment. Capping the maximum temperature in this way helps to keep the convergence stable.
4. The temperature adjustments calculated by the two methods are then added together.

Ensuring Stable Convergence

The temperature adjustments are calculated and applied every two cycles. This allows the gas pressures to stabilise for one cycle before the model measures the energy flow rates and the natural temperature changes.

Applying the calculated temperature adjustments may result in the model overshooting and starting to diverge. To prevent this, the required temperature adjustments are multiplied by a scale factor. This scale factor starts at 1 and is modified as the model converges:

- If the magnitude of any of the required temperature changes exceeds a temperature adjustment cap (typically 5 K), then the scale factor is reduced so that the magnitude of the largest temperature adjustment is the same as the temperature adjustment cap. For the first five convergence iterations, the scale factor is reset to 1 after each iteration. Keeping the scale factor high for the first five convergence attempts prevents the scale factor from getting too small too quickly. After five iterations, the reduced scale factor is retained for future convergence iterations.
- The convergence method occasionally ends up in a situation where the signs of the applied temperature changes oscillate from one application to the next and the model does not diverge or converge. This situation can be identified by checking for oscillations in $\Delta\dot{Q}$, which is the difference between the rates of energy flow at either end of the cold finger. For the single-stage cooler represented by the thermal circuit in Figure 3.19, $\Delta\dot{Q}$ is calculated using the following equation:

$$\Delta\dot{Q} = \dot{Q}_{CF2} - \dot{Q}_{CF0} \tag{3.124}$$

  The model records $\Delta\dot{Q}$ each time temperature adjustments are applied. The system is determined to be oscillating if the most recent local maximum and minimum values of $\Delta\dot{Q}$ are both similar in magnitude to the current value of $\Delta\dot{Q}$, as defined by Equations 3.125a and 3.125b.

$$\left|\left|\Delta\dot{Q}_{max}\right| - \left|\Delta\dot{Q}_{current}\right|\right| < 0.5\left|\Delta\dot{Q}_{current}\right| \tag{3.125a}$$

$$\left|\left|\Delta\dot{Q}_{min}\right| - \left|\Delta\dot{Q}_{current}\right|\right| < 0.5\left|\Delta\dot{Q}_{current}\right| \tag{3.125b}$$

  The scale factor is reduced by 10% if the system is oscillating.

Separate scale factors are used for each stage of a two-stage cooler. This was found to improve the speed of convergence.

3.13.2 Pressure Convergence

The flow through the piston and shaft clearance seals can take a long time to reach a periodic steady state if the seals are effective. The convergence of the flow is accelerated by artificially adjusting the pressure in the backshells. The model does this by finding the average mass flow rates through the seals over the cycle and then calculating the pressure changes required to counteract this, using Equation 3.49 in Section 3.6. These pressure changes are applied to the backshells every two cycles (at the same time as the temperature adjustments).

3.13.3 Applying the Temperature and Pressure Adjustments

The solid cells use temperature as their solution variable, so it is trivial to apply the calculated temperature adjustments. For gas cells, the model modifies the masses and energies of the cells to make the required temperature and pressure adjustments while conserving the total mass of gas in the system.

The gas cell temperature adjustments are applied while keeping the cell pressures constant. The required mass adjustment is calculated by using the ideal gas equation; the change in mass is typically small relative to the total cell mass, so it is not necessary to include real gas effects. The internal energy is unaffected by a temperature change, so only the kinetic energy component is modified.

$$\Delta m = \frac{PV}{R_g\left(T + \Delta T\right)} - \frac{PV}{R_g T} \tag{3.126a}$$

$$m_{adj} = m + \Delta m \tag{3.126b}$$

$$E_{adj} = E + \frac{1}{2}\Delta m v^2 \tag{3.126c}$$

The pressure adjustments are applied while keeping the temperature constant. The gas is assumed to be ideal for this adjustment so both the mass

and energy are proportional to pressure.

$$m_{adj} = m\frac{P + \Delta P}{P} \tag{3.127a}$$

$$E_{adj} = E\frac{P + \Delta P}{P} \tag{3.127b}$$

After applying the temperature and pressure adjustments, the mass and energy of each cell are corrected to ensure that the total mass of gas in the system m_{tot} is unchanged. This is done by adjusting all the cell pressures in proportion while keeping the cell temperatures constant.

$$m_{corrected\,i} = m_{adj_i}\frac{m_{tot}}{\sum_i m_{adj_i}} \tag{3.128a}$$

$$E_{corrected\,i} = E_{adj_i}\frac{m_{tot}}{\sum_i m_{adj_i}} \tag{3.128b}$$

3.13.4 Convergence Criteria

The model continues to run until it is sufficiently close to a periodic steady state. Convergence is achieved when the relative changes of all solid cell temperatures are below a specified value and the relative changes of the mass flows in the piston and shaft clearance seals are also below a specified value.

$$\frac{|T_{end} - T_{start}|}{T_{end}} < \text{Convergence criterion} \tag{3.129}$$

$$\frac{|\dot{m}_{end} - \dot{m}_{start}|}{\dot{m}_{end}} < \text{Convergence criterion} \tag{3.130}$$

For the model, both values are typically set to 1×10^{-6} as this was found to give solutions with very similar cooling power predictions when different initial conditions were used. The model usually converges in less than 300 cycles, which takes approximately four hours on a desktop computer.

3.14 Non-Interacting Losses

The model assumes that some of the loss mechanisms do not interact with the fluid dynamics. These losses are computed after the cycle has converged and are subtracted from the cooling power.

3.14.1 MLI In-Plane Conduction

If multi-layer insulation is wrapped around a cold finger tube, the model calculates the in-plane conduction through the MLI as a non-interacting loss. Most of this conduction is through the aluminium that is deposited on the plastic film of the MLI. Although it is a very thin layer (around 40 nm), the high purity aluminium used has a very high thermal conductivity.

When calculating the heat load due to in-plane conduction, the model assumes that the inner layer will have the same temperature difference along it as the cold finger tube and the outermost layer is assumed to be at the radiation background temperature along its length. The temperature differences along the length of the middle layers are calculated by a linear interpolation between these two extremes.

The model calculates the conduction separately for each layer by assuming it is thermally insulated along its length and the heat flow is constant. The heat flow is calculated by using a thermal conductivity integral [88, p. 50].

$$\dot{Q} = \frac{A_s}{x_{tot}} \int_{T_{start}}^{T_{end}} k_s(T)\, dT \tag{3.131}$$

where A_s is the cross-sectional area of the aluminium or plastic film, x_{tot} is the total length and k_s is the conductivity. This integral is evaluated numerically.

It should be reasonable to model this loss as non-interacting because it is typically small and there should be poor thermal contact between the cold finger tube and the MLI. Simulating the MLI conduction loss as the model runs would require an array of cells for each sheet of MLI which would greatly increase the model complexity.

3.14.2 Radiation Loads

The thermal radiation loads on the first and second stage cold tips are also calculated after the cycle has converged. These heat loads are transmitted directly to the cold tip cells which are modelled as being isothermal. Therefore, it is not necessary to consider these heat loads while the fluid dynamics are being simulated.

If a radiation shield is present, the radiation load on the shield is added to the radiation load on the first stage cold tip. This radiation load accounts for the

radiation from the environment and the radiative heat transfer between the shield and the second stage.

The cold tips and radiation shield are assumed to be surrounded with multi-layer insulation. The radiation loads are calculated in the same way as the radiation loads on the cold finger tube cells when MLI is present (using Equation 3.86).

3.15 Model Outputs

After the model has converged, it runs one final cycle in which it records the forces on the moving components, the work done on every gas cell and the heat transferred between cells. The results of this final cycle are then used to produce the model outputs.

3.15.1 Numerical Outputs

The model calculates key quantities from the final cycle which are saved to a Microsoft Excel `.xlsx` file (see Section A.3 in Appendix A). The spreadsheet includes the following results:

- The heat input at the stages and warm end
- The mechanical power applied to the gas (the pressure-volume power)
- The approximate contribution of each loss mechanism
- The forces acting on the compressor pistons and the displacer
- The amplitudes and phases of the pressure waveform harmonics at different points in the cryocooler
- The mean temperatures at different points in the cryocooler
- Model diagnostic information, such as convergence speed

These results are calculated using the following methods.

Heat Input

The model outputs the average rate of heat transfer to the gas at the cold stages and at the warm end of the cooler. This is the total heat transferred from each isothermal solid over a cycle, divided by the cycle period. The heat transferred to the gas at the warm end includes the heat from the cold head body, the transfer line and the compressor body.

Mechanical Power

The mechanical power applied to the gas is found by dividing the cycle-averaged mechanical work by the cycle period. It is calculated for the warm end and for each stage. The warm end power includes the power of the compressor piston and the warm end of the displacer. The mechanical power of each stage includes the powers along the stage of the displacer and the power at the expansion chamber of that stage.

Loss Mechanisms

The model estimates how much each loss mechanism contributes to the difference between the gross cooling power (the mechanical power) and the net cooling power (heat transferred) at each stage. The sizes of the losses can indicate where performance improvements could be made. Because these losses interact with each other, it is not possible to reduce one without affecting the others; however, splitting up the loss mechanisms can still produce useful insights.

The magnitude of each loss can be different at different points along the cold finger. An average value along the length of the cold finger is calculated for each loss, weighted by the length of each cell. To calculate the size of the losses, they need to be integrated over a cycle. This is done by adding them as solution variables for the final cycle.

The following loss mechanisms are reported by the model:

- **Enthalpy transport** — These losses represent the net enthalpy transport of the gas in the regenerator and the appendix gap. If the gas travelling to the cold end is warmer than the gas returning, there is an associated loss of cooling power.
- **Shuttle loss** — This loss represents the net heat flow down the cold finger due to the conduction between the static cold finger components and the gas in the appendix gap. The model records how much heat is conducted from each static cold finger cell to each appendix gap gas cell over the cycle. If the cells are on different rows (see Figure 3.3), this heat transfer is counted as conduction along the cold finger. The heat flows are summed to calculate the net heat flow along the cold finger at each node.

- **Gas conduction** — These losses represent the heat conducted through the gas in the regenerator and the appendix gap.
- **Solid conduction** — These losses represent the heat conducted through the regenerator, the displacer tube and the cold finger tube.
- **Radiation Loads** — The model reports the total radiation load on each stage. This includes the radiation that heats the stage directly and the radiation that heats the respective cold finger tube.

Forces

The model reports the mean forces acting on the compressor pistons and the displacer as well as the amplitudes and phases of the first 10 harmonics of the force waveforms. The harmonic content is found by performing a Fourier transform.

Pressures

The model reports the mean pressures at all variable volume cells and also reports the amplitudes and phases of the first 10 harmonics of the pressure waveforms.

Temperatures

The model reports the mean gas temperatures at the expansion and compression chambers.

3.15.2 Output Waveforms

In addition to these outputs, the model can export a MATLAB `.mat` file which contains the value of the solution variables and other key properties at specified intervals during the final cycle.

Chapter 4

Breadboard Cooler Development

A breadboard two-stage Stirling cryocooler has been developed to help validate the RAL Third-Order Model. This cooler is much larger than the two-stage coolers that have previously been developed at RAL and allows the model to be validated over a new parameter range. This chapter describes the requirements, design, assembly and operation of the cooler. The performance of the cooler is compared with the model predictions in Chapter 5.

4.1 Breadboard Cooler Requirements

A breadboard is a low-fidelity unit that demonstrates the function of the system, without respecting the form or fit of the final hardware [89, p. 49]. The Breadboard Cooler uses clearance seals and linear motors to ensure that its thermodynamic performance is broadly representative of a flight-like cooler. However, the requirements on mass, size and reliability that would typically apply to a flight-like cooler have been relaxed.

A range of different sensors are needed to help validate the model. RAL coolers typically have temperature, motor position and warm end pressure sensors. In addition to these sensors, the Breadboard Cooler has been designed so that the pressure at the expansion chambers can be measured. This allows for the gross cooling power to be calculated, which is a key output of the model.

The Breadboard Cooler is also envisioned as being useful for prototyping future RAL two-stage coolers. The Breadboard Cooler has been designed to be easily reconfigurable. It can be modified to match new cooler designs to verify the cooling powers predicted by modelling. The Breadboard Cooler is large enough to accommodate the required cold finger geometry of foreseeable future two-stage coolers.

4.2 Breadboard Cooler Design

The cooler was designed before the model development was complete, so the model was not available for optimising the design to improve its performance. The geometry was selected by a simple scaling of previous RAL two-stage cooler designs. A high thermodynamic performance was not required because the only aim was to produce results that could be used to validate the model.

The Breadboard Cooler is shown in Figure 4.1. It uses a gamma configuration, with the compressor and cold head separated by the transfer line. This increases the system flexibility and allows the compressor to be swapped.

The temperatures of the warm regions of the Breadboard Cooler are measured using platinum resistance thermometers. These are located on the compressor, the transfer line, the displacer motor and near the secondary compression chamber. Lake Shore Cryotronics Cernox temperature sensors are used for measuring the temperatures of the cold stages. Heat loads are applied by using resistors that are bolted to each stage. An Endevco 8510B-200 piezo-resistive pressure sensor is installed in the transfer line to measure the pressure swing and mean pressure. The pressure swings at the first and second stage expansion chambers are measured using PCB Model 112A03

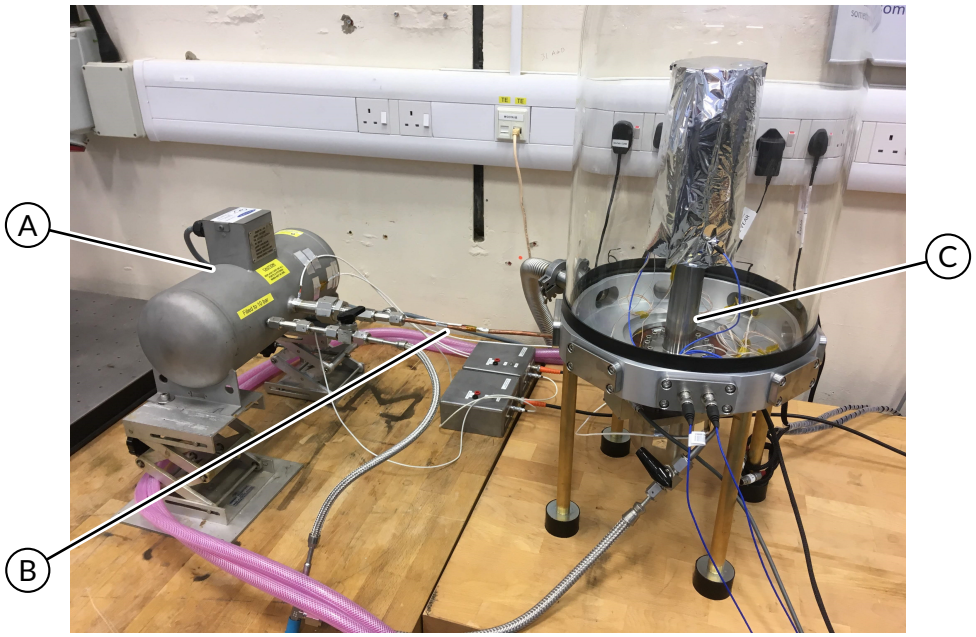

Figure 4.1: A photograph of the Breadboard Cooler. The key components have been labelled: **A**, the compressor; **B**, the transfer line; and **C**, the cold head.

charge output pressure sensors. These sensors can operate at low temperatures but can only measure dynamic pressures; the mean pressure is assumed to be the same as the mean pressure in the transfer line.

4.2.1 Compressor

An off-the-shelf compressor, the Qdrive 2S132W pressure wave generator, is used to drive the cooler to reduce the development costs. This is a linear compressor that uses two pistons with clearance seals running in a head-to-head configuration. It can deliver up to 450 W of pressure-volume output power for 600 W of electrical input power [90]. The compressor is air cooled using fans.

The compressor motors do not have built-in position sensors. The position is measured using the manufacturer's recommended method: a pressure sensor is connected to the backshell volume, and the measured pressure waveform is used to calculate the piston motion [90].

4.2.2 Cold Head

The cold head is shown in Figure 4.2 and a section view is shown in Figure 4.3. Each stage of the cold head uses a separate cold finger tube and displacer tube. This allows the geometry of each stage to be modified independently. It also simplifies manufacture as the tight tolerance parts are simple cylinders and are not stepped. The cold finger tubes are joined to an interface piece using indium seals, as shown in Figure 4.4. This gives a gas-tight seal that functions at cryogenic temperatures.

The cold finger tubes are constructed from stainless steel with a 0.5 mm wall thickness. The thin walls help to reduce thermal conduction. The cold finger tubes used in RAL coolers are typically made from titanium with an even thinner wall thickness, but thicker stainless steel tubes were selected to simplify manufacture.

The displacer is shown in Figure 4.5. The displacer tube is made from molybdenum disulphide filled nylon-6 which is cheaper than the Vespel SP-3 that is typically used in flight coolers. The molybdenum disulphide acts as a lubricant if the displacer tube rubs on the cold finger tube and helps to prevent

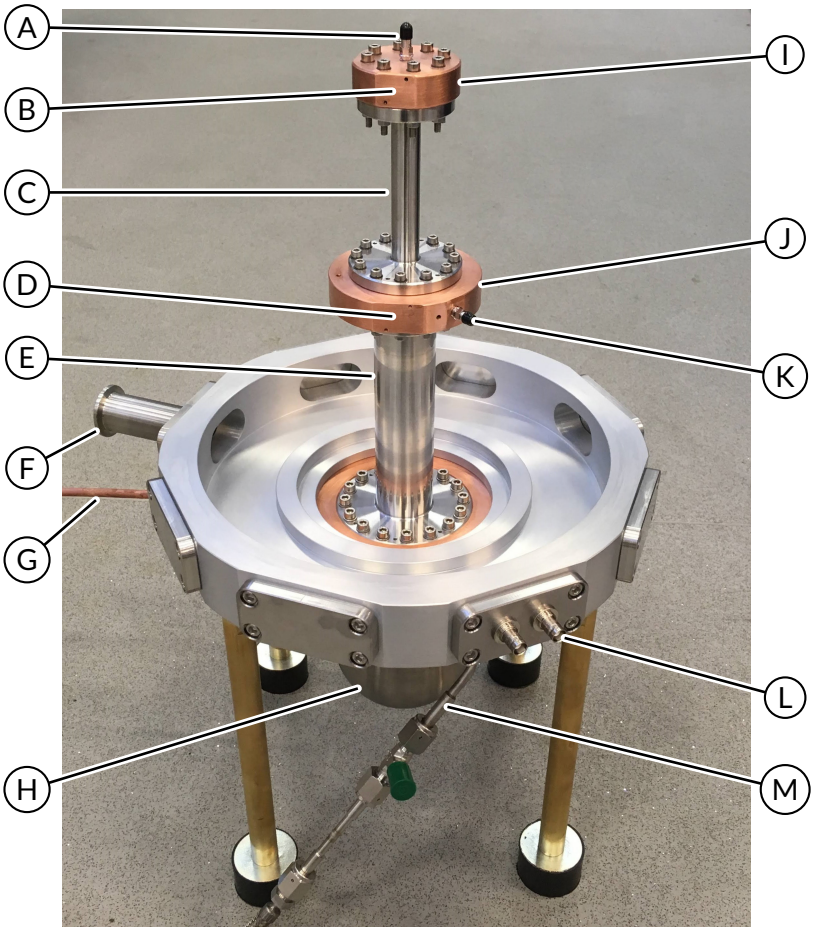

Figure 4.2: A photograph of the cold head of the Breadboard Cooler. Some of the key components have been labelled: **A**, the second stage cryogenic pressure sensor; **B**, the second stage heater mounting location; **C**, the second stage cold finger tube; **D**, the first stage heater mounting location; **E**, the first stage cold finger tube; **F**, the vacuum port; **G**, the transfer line; **H**, the displacer motor cover; **I**, the second stage cold tip; **J**, the first stage cold tip; **K**, the first stage cryogenic pressure sensor; **L**, the electrical feedthroughs for the cryogenic pressure sensors; and **M**, the fill line.

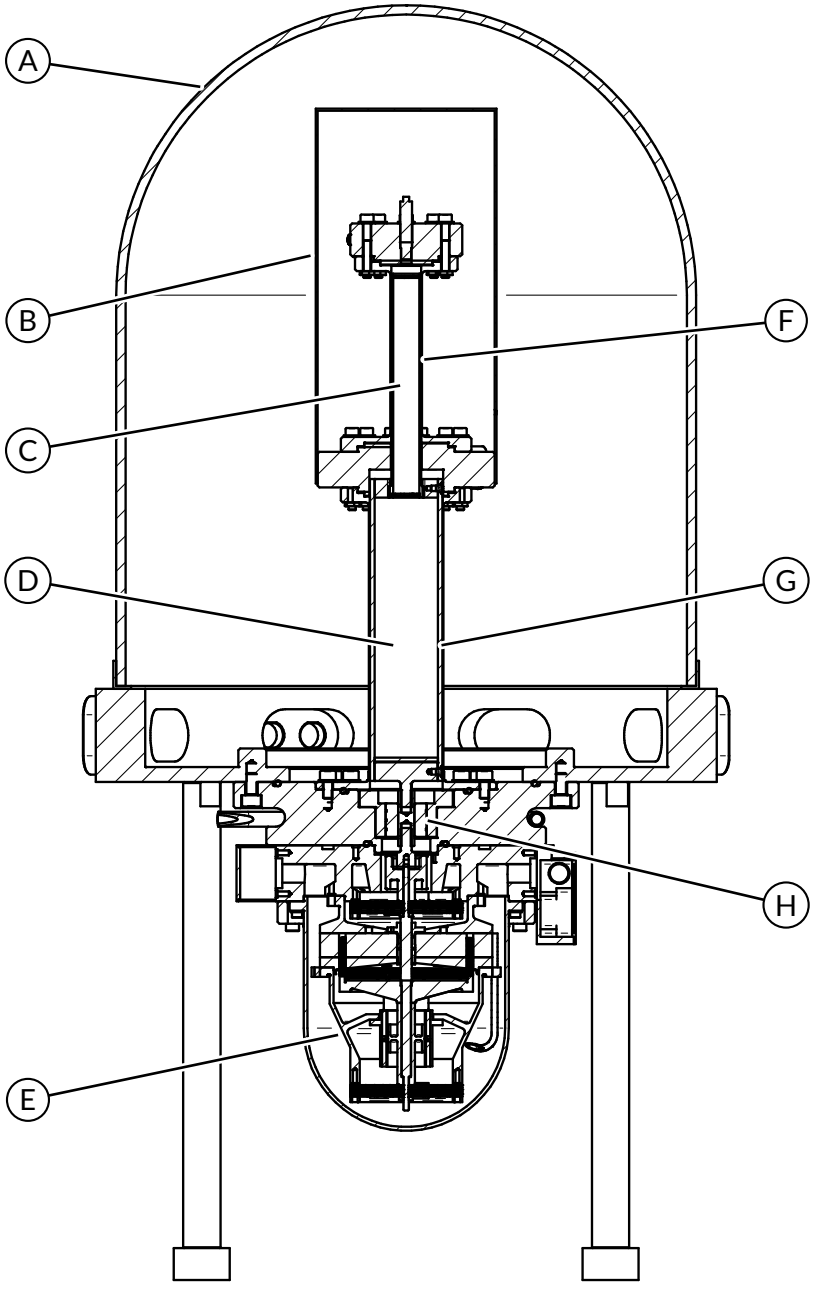

Figure 4.3: A section view of the cold head of the Breadboard Cooler. Some of the key components have been labelled: **A**, the vacuum bell jar; **B**, the radiation shield; **C**, the second stage regenerator; **D**, the first stage regenerator; **E**, the displacer motor; **F**, the second stage displacer tube; **G**, the first stage displacer tube; and **H**, the displacer bush.

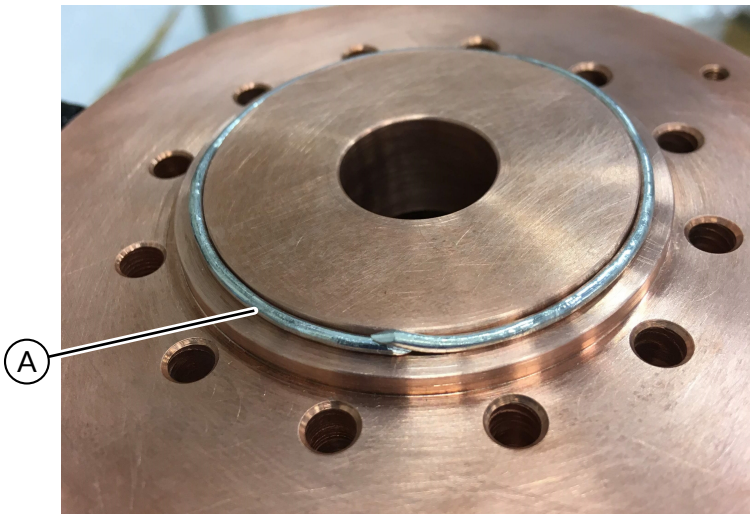

Figure 4.4: A photograph of one of the indium seals of the Breadboard Cooler. **A** is the indium wire.

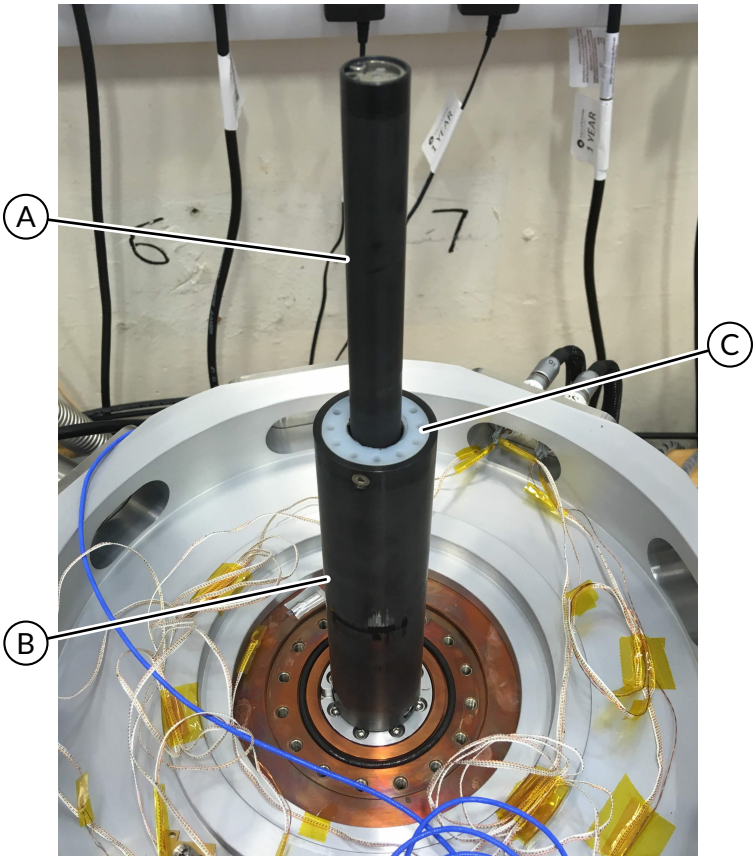

Figure 4.5: A photograph of the displacer of the Breadboard Cooler. Some of the key components have been labelled: **A**, the second stage displacer tube; **B**, the first stage displacer tube; and **C**, the displacer outlet.

it from seizing. The displacer bush is made of Vespel SP-3 which also contains molybdenum disulphide.

A stainless steel wire mesh regenerator is used. Lower temperatures could have been targeted by using a regenerator coated with material that has a high heat capacity at low temperatures (see Section 2.3); however, this was deemed unnecessary for the initial model validation. The regenerator material can be easily changed for future testing if required. A sheet of Retimet metal foam is located at the displacer inlet to disperse the gas entering the regenerator.

The cooler is filled with helium. The fill pressure was varied from 5 to 15 bar during testing to provide data that could be used to validate the model over a wide parameter range.

The cold finger is surrounded by a bell jar, as shown in Figure 4.3 and this chamber is evacuated before running the cooler. The vacuum reduces the thermal conduction and convection. An aluminium radiation shield is attached to the cold tip of the first stage and the shield is covered with multi-layer insulation. This shield surrounds the second stage of the cooler to reduce the radiation load on this stage. The second stage cold tip is also surrounded with multi-layer insulation.

The displacer is driven using a repurposed motor from a RAL Standard Compressor. These motors were historically used as compressor motors for Stirling coolers, but it is used as a displacer motor here to drive the large displacer. The displacer motor is cooled using a chilled water circuit. The displacer position waveform is measured using a bespoke capacitive position sensor that is part of the motor. The sensor is calibrated by removing the pressure cover and physically measuring the displacement of the motor.

Alignment Procedures

Three components in the cold head require alignment to allow the displacer to move freely: the displacer shaft in the bush and the two displacer tubes in the cold finger tubes. The alignments do not need to be as precise as for a flight-like cooler, since the reliability requirements are less demanding; however, alignment procedures are still used to reduce the friction to a low level.

The alignment procedures are similar for all the components and take advantage of the differences in the thermal expansion coefficients of the plastic and metal components.

The displacer shaft and the bush are aligned before the displacer is attached. The shaft and bush are shown in Figure 4.6. The displacer shaft is a separate component to the motor shaft; they are joined by a screw thread where the male thread is undersized. This allows the displacer shaft to move relative to the motor shaft. To perform the alignment, glue is applied to the screw thread and the parts are screwed together before the glue has set. The plastic bush is heated, but its expansion is constrained by the metal bush holder. This causes the inner diameter of the bush to shrink and grip the displacer shaft, centring the displacer shaft within the bush. The predicted changes in diameter are shown in Figure 4.7. Once the glue sets and the bush cools back down, there is a small radial gap between the displacer shaft and the bush.

The alignment of the displacer is carried out in a similar way to the shaft. There are two joints that require alignment: the joint between the displacer

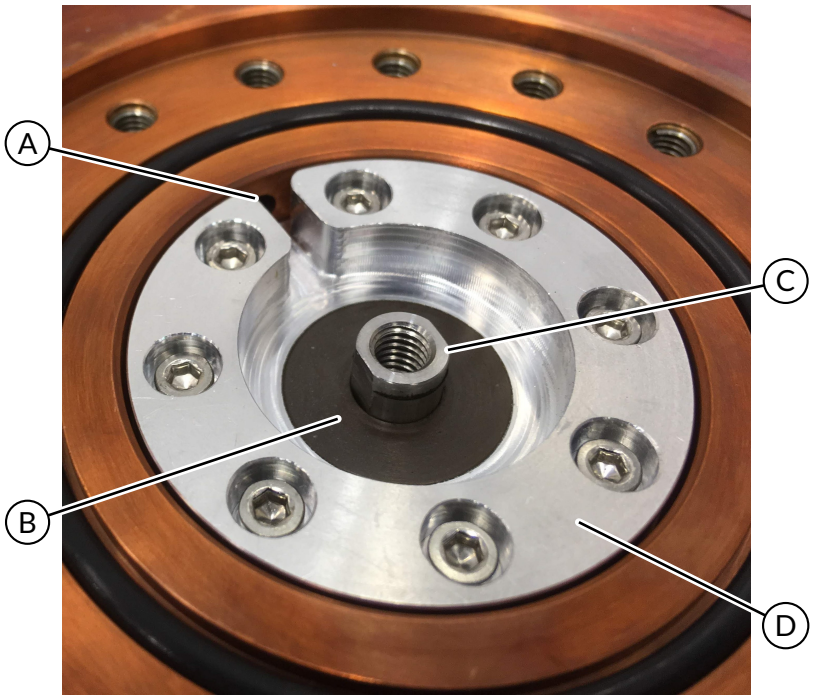

Figure 4.6: A photograph of the displacer shaft seal of the Breadboard Cooler. Some of the key components have been labelled: **A**, the transfer line outlet; **B**, the bush; **C**, the displacer shaft; and **D**, the bush holder.

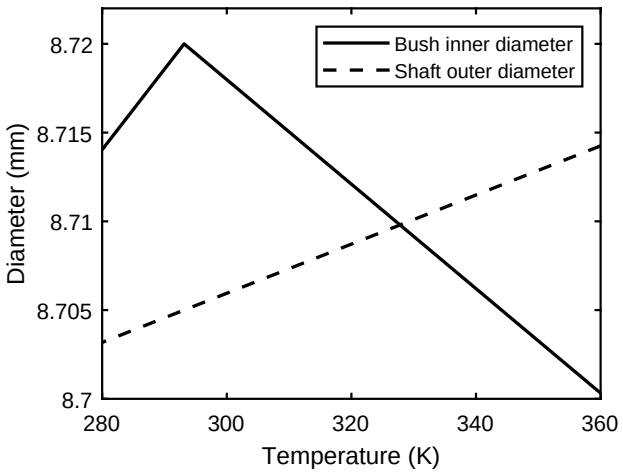

Figure 4.7: A plot showing the predicted change in diameter of the bush and displacer shaft with temperature. The bush would start to grip the shaft above approximately 328 K, but the components are modelled in isolation and the contact is not simulated.

shaft and the first stage of the displacer and the joint between the two displacer stages. Both joints are loose screw threads that are glued. To align the displacer, the cold finger tubes are slid over the displacer tubes before the glue has set, and then the whole assembly is heated. The heat causes the plastic displacer tubes to expand until they grip the inside of the cold finger tubes. The predicted expansion of the cold finger tubes and displacer tubes are shown in Figure 4.8. The glue in the two joints sets when the displacer is hot, and this keeps the displacer sections aligned. The heat is applied using a water bath, as shown in Figure 4.9. When the displacer cools down, there are small radial gaps between the displacer tubes and the cold finger tubes.

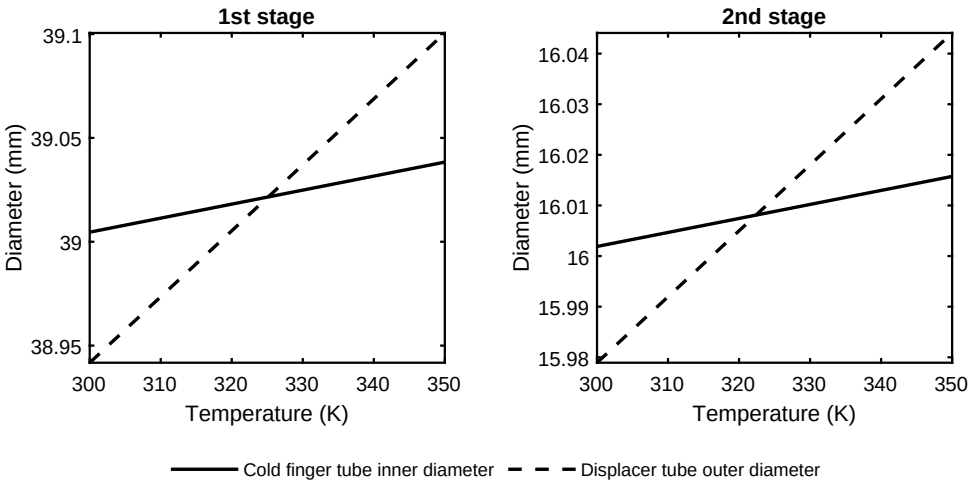

Figure 4.8: Plots showing the predicted thermal expansion of the cold finger tube and displacer tube for both stages of the Breadboard Cooler. The cold finger tubes would start to grip the displacer tubes above approximately 325 K and 322 K, but the components are modelled in isolation and the contact is not simulated.

Figure 4.9: A photograph showing the displacer alignment procedure of the Breadboard Cooler. The cold head has been placed upside-down in a hot water bath.

4.3 Breadboard Cooler Operation

The alignment procedures were successful, and the cooler was able to run without issues. However, when the cold finger tubes were removed, some wear was visible on the first stage displacer tube (this can be seen in Figure 4.5). It is thought that this is because the shaft joint used in the Breadboard Cooler is not as stiff as would be used in a flight-like cooler.

For the initial testing of the Breadboard Cooler, no effort was made to modify the suspension systems of the compressor and displacer motors to match their resonant frequencies. The compressor resonant frequency was much higher than that of the displacer. Because of this, the cooler was run with the compressor and displacer motors off-resonance which limited their stroke due to the high currents required. If measurements at longer strokes are required in future, it would be relatively simple to add stiffer flexure bearings to the displacer motor to increase its resonant frequency.

The Breadboard Cooler was used to produce a large range of performance measurements that have been used to validate the model. The results are presented and compared to the model predictions in Section 5.3.

Chapter 5

Model Validation

The RAL Third-Order Model, described in Chapter 3, has been validated against single and two-stage Stirling coolers that have been tested at RAL. The aim of the model validation was to estimate the accuracy of the model by assessing how well the model predicts the measured performance of the coolers. The model has been validated against measurements of cooling powers, loss mechanisms, displacer forces and pressure waveforms. In addition, the sensitivity of the model to changes in the input parameters and gas cell correlations has been assessed.

Two single-stage coolers were used for the validation: the compact Small Scale Cooler and the larger CryoBlue Cooler. In addition, validation was performed against the large two-stage Breadboard Cooler that was developed during this project. Using a range of different sized coolers for the validation helps to assess the accuracy of the model over a wide parameter space.

5.1 Validation Against the Small Scale Cooler

Performance measurements of the Small Scale Cooler were used to validate the model. The Small Scale Cooler is the most recent single-stage Stirling cooler developed at RAL that has undergone a complete testing program.

The Small Scale Cooler is a miniature cooler, with a mass of only 625 g, which is designed for use on small Earth observation satellites. It operates at a high frequency (90 Hz) and produces around 0.5 W of cooling at 77 K. The compressor and cold head are integrated into the same body to keep the cooler as compact as possible. The first version of the Small Scale Cooler was produced in 2014. A new version was developed in 2018 that features improvements that make it easier to integrate into spacecraft, such as adding

extra thermal interfaces and improving the thermal conductivity of the body. The 2018 version is shown in Figure 2.7 in Section 2.3.

A range of performance measurements and loss characterisation tests were performed on the original Small Scale Cooler between 2014 and 2017 by the author and others at RAL. The performance of the 2018 model was also measured, but a full characterisation was not carried out as the internal geometry was identical to the previous cooler. The RAL Third-Order Model was used to reproduce these tests and the model results have been compared to the measured data.

5.1.1 Input Parameters

The input parameters used for modelling the Small Scale Cooler were derived from multiple sources: from measurements taken during the build process; from characterisation tests on key subsystems; and from measurements taken during the performance testing.

Geometry

The geometries of the Small Scale Coolers that were used for validating the model are well known because metrology was performed on the critical dimensions during their build process. For example, the wall thickness of the cold finger tube was measured using a coordinate measuring machine (CMM) and the wire diameter of the regenerator mesh was measured optically using a microscope. The temperatures and fill pressures are also known accurately. The temperatures were measured using platinum resistance thermometers and the pressures were measured using a calibrated gauge while the cooler was being filled.

Position Waveforms

There are no position sensors for the compressor pistons or the displacer for either iteration of the Small Scale Cooler. This means that the position waveforms used by the model had to be derived from the measured current and voltage waveforms of the compressor and displacer motors. A simple electrical model was used to estimate the back electromotive force across each motor coil. This back electromotive force is caused by electromagnetic

induction as the motor moves, so could be used to estimate the motor velocity. This velocity was then integrated to find the position waveform.

Clearance Seals

The geometries of the clearance seals were calculated using different methods. The clearance seal gaps for the compressor pistons and appendix gap were calculated from the measured geometry. The sizes of the compressor pistons were measured using a micrometer and the bores were measured using a CMM. The displacer tube and inside of the cold finger tube were also measured using a CMM. The clearance seal gaps were then calculated using the least-squares diameter of the CMM measurements. The eccentricity was not measured, but an eccentricity of 1 was assumed as the worst case for the alignment.

The leakage of the displacer shaft clearance seal was measured directly using a helium flow test and the measurements were used to derive the clearance seal gap used by the model that would give an equivalent leakage. This is a more useful way of estimating the clearance seal for the purposes of modelling the cooler performance because it means that the seal leakage predicted by the model should be a better representation of the seal leakage in the cooler. The method used to calculate the clearance seal gap used as a model input is described in Section 5.4.1. There was no need to account for the eccentricity of the seal because the gap was derived from the flow measurements with the assumption of no eccentricity.

It is important to account for thermal expansion and contraction when calculating the clearance seal gaps. For example, the compressor pistons of the Small Scale Cooler are made of plastic and expand more than the metal bore if they are running at a high temperature. This reduces the size of the clearance seal. For the cases used to validate the model, the body temperature of the cooler was slightly above room temperature, so the input gap sizes of the piston clearance seals and the shaft clearance seal were reduced. In the appendix gap, the plastic displacer tube shrinks away from the cold finger tube; the cold end gap used in the model was increased to account for this. The displacer tube is packed with regenerator mesh which is metal and does not shrink as much as the plastic displacer tube. However, it was assumed that

this did not prevent the contraction of the displacer tube as the mesh is porous and not very rigid.

5.1.2 Spatial Resolution

Before the model results could be compared to the measured data, it was necessary to determine the required spatial resolution of the model. If the spatial resolution is too low, it can have a significant impact on the predicted cooling power. The spatial resolution is most important in the regenerator because the large temperature gradient means there are large differences in the properties of neighbouring cells.

The effect of adjusting the number of regenerator cells on the cooling power at 78 K is shown in Figure 5.1. The 78 K case was selected because this is the operating point the cooler design was optimised for. It can be seen that, if more than 15 cells are used, the cooling power asymptotically approaches a value as the resolution is increased. This is a useful indicator to check that the model is functioning correctly. The difference in cooling power between using

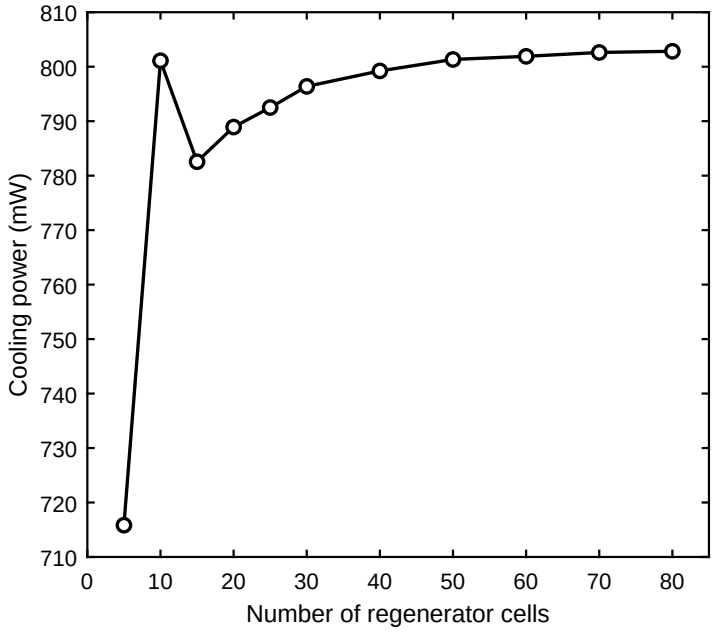

Figure 5.1: A plot showing how the modelled cooling power predicted by the RAL Third-Order Model is affected by the number of regenerator cells for the 78 K case of the 2018 Small Scale Cooler.

50 and 60 regenerator cells is only around 0.5 mW so increasing the resolution further was deemed unnecessary. All further modelling was carried out using 60 regenerator cells.

Adjusting the number of cells in the transfer line and clearance seals had a negligible effect on the predicted cooling power. For all further modelling, six cells were used for the transfer line and one cell was used for both the compressor piston and displacer shaft clearance seals.

5.1.3 Performance Modelling

The primary function of the model is to predict the cooling power of a cooler for given operating conditions. The predictions of the model have been compared to the measured performance of the Small Scale Cooler.

A load line was taken for the 2018 Small Scale Cooler by applying a range of heat loads and recording the cold tip temperature. The amplitudes and phases of the compressor pistons and the displacer were adjusted to maximise the cooling power at each point for 22 W of electrical input power. The test setup is shown in Figure 5.2.

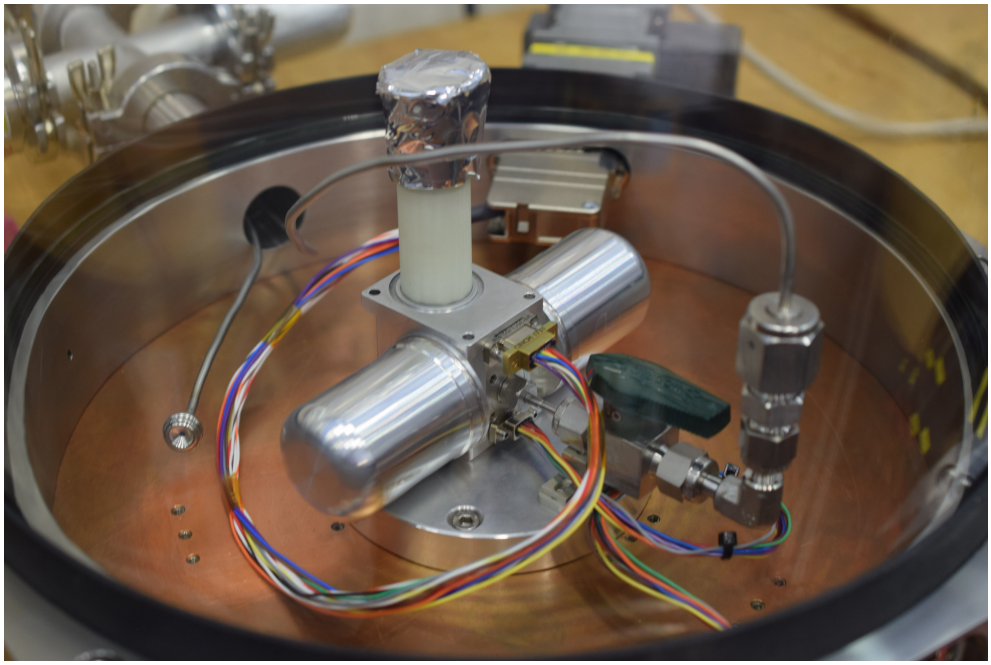

Figure 5.2: A photograph of the 2018 Small Scale Cooler undergoing performance testing.

To compare the results to the model, the measured displacer and compressor position waveforms and the measured temperatures were used as inputs. The model was run to find the cooling power it predicts. The results are plotted in Figure 5.3.

The cooler was also modelled using Sage (see Section 2.4.3), with the same inputs where possible. The main differences in the inputs were related to the compressor piston clearance seals and the appendix gap. Sage is not able to account for the eccentricity of the clearance seals, so the compressor seal gap used in the Sage model was a factor of $2.5^{\frac{1}{3}}$ larger than the gap in the RAL Third-Order Model to ensure that the flow resistance was identical for both models. This factor comes from the fact that a full eccentricity increases the flow rate by a factor of 2.5 (see Equation 3.82) and that the flow rate is proportional to the cube of the gap size (see Equation 5.7). Sage is unable to simulate tapered appendix gaps (see Section 6.1), so the appendix gap size used in the Sage model was the mean gap size of the RAL Third-Order Model.

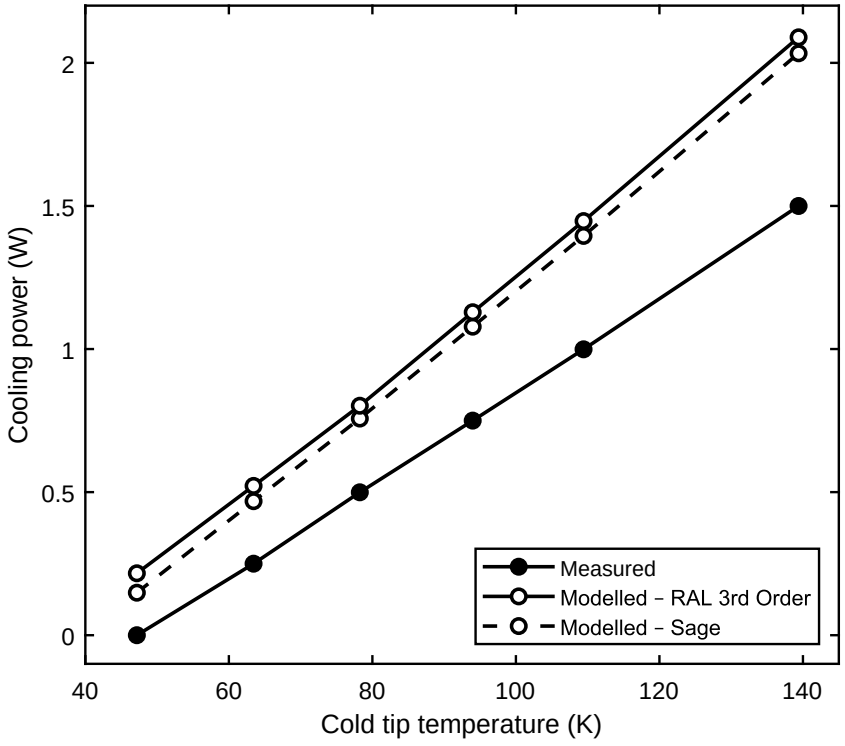

Figure 5.3: A plot comparing the measured cooling powers of the 2018 Small Scale Cooler at different cold tip temperatures with the cooling powers predicted by the RAL Third-Order Model and Sage.

Although the appendix gap was assumed to be eccentric in the RAL model, the gap was not increased in the Sage model because this would alter the shuttle losses. The results of the Sage model are also plotted in Figure 5.3.

It can be seen that both the RAL Third-Order Model and Sage overpredict the cooling power by a similar amount across the entire load line. This suggests that either both models incorrectly simulate some aspect of the cooler or that there is an issue with the input parameters. Possible causes of this discrepancy are discussed in Section 5.1.6.

Operational Losses

Models can be used to analyse the individual loss mechanisms of a Stirling cooler. Looking at the loss mechanisms can provide a clearer picture of why a cooler performs the way it does compared to looking only at the net cooling power (the cooling power available at the cold tip). Comparing the loss mechanisms of different models can also be useful for determining why they give different predictions of the net cooling power.

The net cooling power can be thought of as the difference between the gross cooling power and the sum of the loss mechanisms. The gross cooling power is the rate of pressure-volume work done by the gas on the displacer in the expansion chamber. When the gas does work, it cools and absorbs heat from its surroundings. Only some of this is useful cooling; the remainder of the heat absorbed by the gas comes from the loss mechanisms described in Section 3.15.1.

The pressure-volume relationship at the expansion chamber predicted by the two models is plotted in Figure 5.4. The gross cooling power can be calculated by multiplying the area of the pressure-volume loop by the operating frequency. The plot shows that there is good agreement between the models, although the gross cooling power is slightly higher for the RAL Third-Order Model because its pressure swing is larger.

Figure 5.5 compares the gross cooling power, net cooling power and total losses predicted by the two models. The total losses are calculated by subtracting the net cooling power from the gross cooling power. It shows that there is good agreement between the models for all three of these quantities. Both the gross cooling power and net cooling power are larger for the RAL

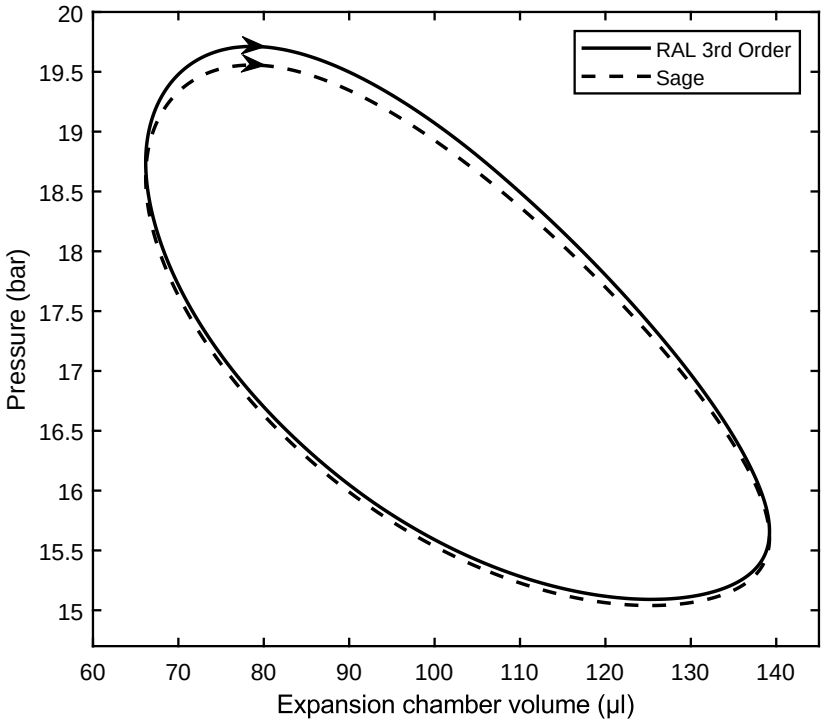

Figure 5.4: A plot of the expansion chamber pressure-volume loops predicted by the RAL Third-Order Model and Sage for the 78 K case of the 2018 Small Scale Cooler (shown in Figure 5.3). The area of the loop represents the gross cooling energy per cycle. The paths have a clockwise direction because work is being done by the gas on the cold end of the displacer.

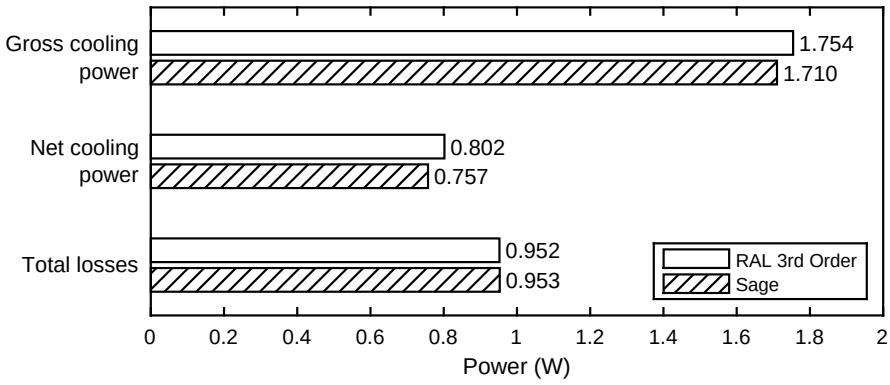

Figure 5.5: A plot of the gross cooling power, net cooling power and total losses predicted by the RAL Third-Order Model and Sage for the 78 K case of the 2018 Small Scale Cooler.

Third-Order Model by a similar amount; because of this, the total losses of the two models are almost identical. This plot also highlights the difficulties involved in predicting the performance of Stirling cryocoolers. Because the net cooling power is small compared to the gross cooling power and the total losses, any errors in the estimation of these two quantities will result in a larger relative error in the net cooling power, which is the difference between them.

The differences between the two models can be seen by comparing the contributions of each individual loss mechanism. The RAL Third-Order Model calculates the contribution of each loss mechanism by using the length-averaging method described in Section 3.15.1. The sum of these loss mechanisms differs from the total losses given in Figure 5.5 by 0.02%, showing that the length-averaging gives accurate results.

A similar length-averaging method was used to calculate the individual loss mechanisms for the Sage model. Sage reports the size of most of the loss mechanisms along the length of the cold finger; however, the sizes of the regenerator and appendix gap enthalpy transport are only reported at either end. The size of the enthalpy transport along the length of the cold finger was calculated by averaging the product of the volume specific total energy and the volumetric flow rate over a cycle. This was then scaled so that it matched the reported enthalpy transport at either end. Summing all the length-averaged losses gave a total loss that was 3.3% lower than given in Figure 5.5. The largest uncertainty was in the calculation of the enthalpy transport losses, so these were scaled to make the total losses match.

The contribution of the individual loss mechanisms predicted by the two models is shown in Figure 5.6. The plot shows that the models give significantly different predictions for enthalpy transport and shuttle loss. This may be due to the different ways that these losses are calculated. Sage uses an analytical formula to calculate the shuttle losses, and this is done separately from the rest of the simulation. The RAL Third-Order Model calculates the shuttle losses as the simulation is running and allows the shuttle losses to be affected by the flow of gas in the cooler. It appears that this interaction reduces the appendix gap enthalpy losses at the expense of increasing the shuttle losses.

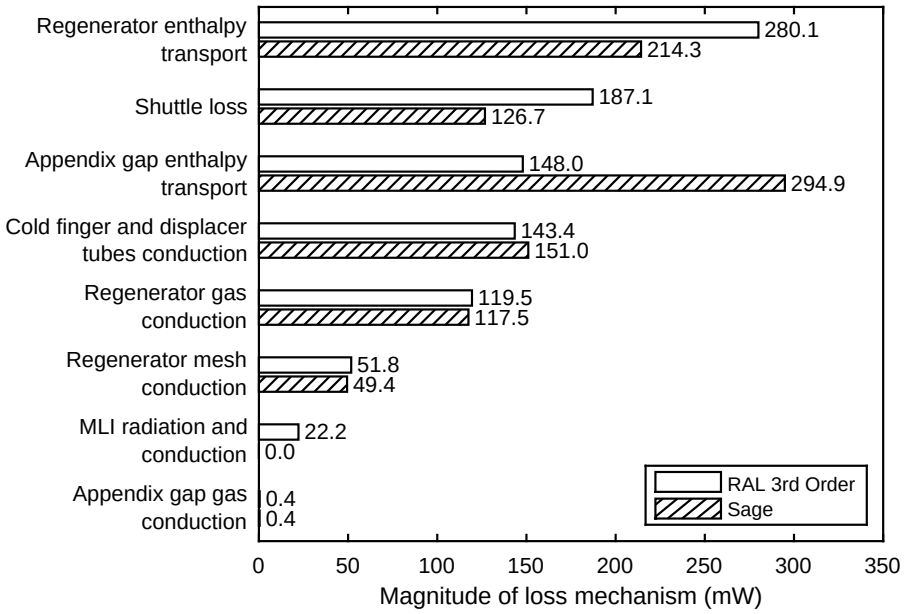

Figure 5.6: A plot comparing the losses predicted by the RAL Third-Order Model with the losses predicted by Sage for the 78 K case of the 2018 Small Scale Cooler.

The other factor to consider is that Sage simulates the appendix gap as being a constant size along its length, whereas the RAL Third-Order Model can simulate it as being tapered. This may help explain why the appendix gap enthalpy transport is lower for the RAL Third-Order Model; the small gap at the warm end reduces the flow of gas. This is discussed in more detail in Section 6.1.

The gas and solid conduction losses are similar for both models. This is unsurprising as both models simulate these effects in a similar manner. Sage reports the cold finger and displacer conduction as a combined loss, so these losses from the RAL Third-Order Model have also been combined. Sage does not account for radiation losses and conduction along the MLI, but the RAL Third-Order Model indicates that these losses are small.

5.1.4 Uncertainty and Sensitivity Analysis

Uncertainty analysis and sensitivity analysis are useful tools for assessing the relative importance of the model inputs and empirical correlations. They can provide guidance on how accurately the model will be able to predict the

performance of a cooler. This analysis was performed on the 78 K case of the 2018 Small Scale Cooler.

Input Parameters

Uncertainty analysis was performed on the model inputs. The goal of this analysis was to determine how the accuracy of the model is affected by uncertainty in its inputs.

The first step was to determine the level of uncertainty of each input. These uncertainties were estimated in different ways. For physical dimensions, the uncertainty was estimated from the tolerance on the engineering drawings or from the measurement technique used if metrology was performed on the part. The uncertainty in the regenerator mesh wire diameter was determined from the measured variation in wire diameter over a sheet of mesh and the uncertainty in the mesh porosity was derived from the uncertainty in the wire density. For the position waveforms of the compressor pistons and displacer, the uncertainties were estimated from the accuracies of the electrical models used to calculate the position. For the temperatures, a thermal model was used to estimate the temperature differences between the sensor locations and the surfaces in contact with the gas.

A one-at-a-time approach was used to perform the uncertainty analysis. Each input parameter was increased in turn to the upper limit of its uncertainty. The cooling power of each case was then compared with the nominal cooling power to find the error that this uncertainty produced.

The results are plotted in Figure 5.7. The most significant source of error is due to the uncertainty in the gap size of the compressor piston clearance seals. The gap size uncertainty was derived from the uncertainty of the alignment of the pistons in the bore; a gap size uncertainty of 3 μm was used as this gave a change in flow that was equivalent to changing the alignment from centred to fully eccentric. The measurements of the pistons and bore themselves had a sub-micron level of accuracy, so they were not a significant source of uncertainty. The uncertainty in the gap size produced a very significant change in the cooling power. The larger gap allowed more gas to leak past the piston, reducing the pressure swing and the gross cooling power.

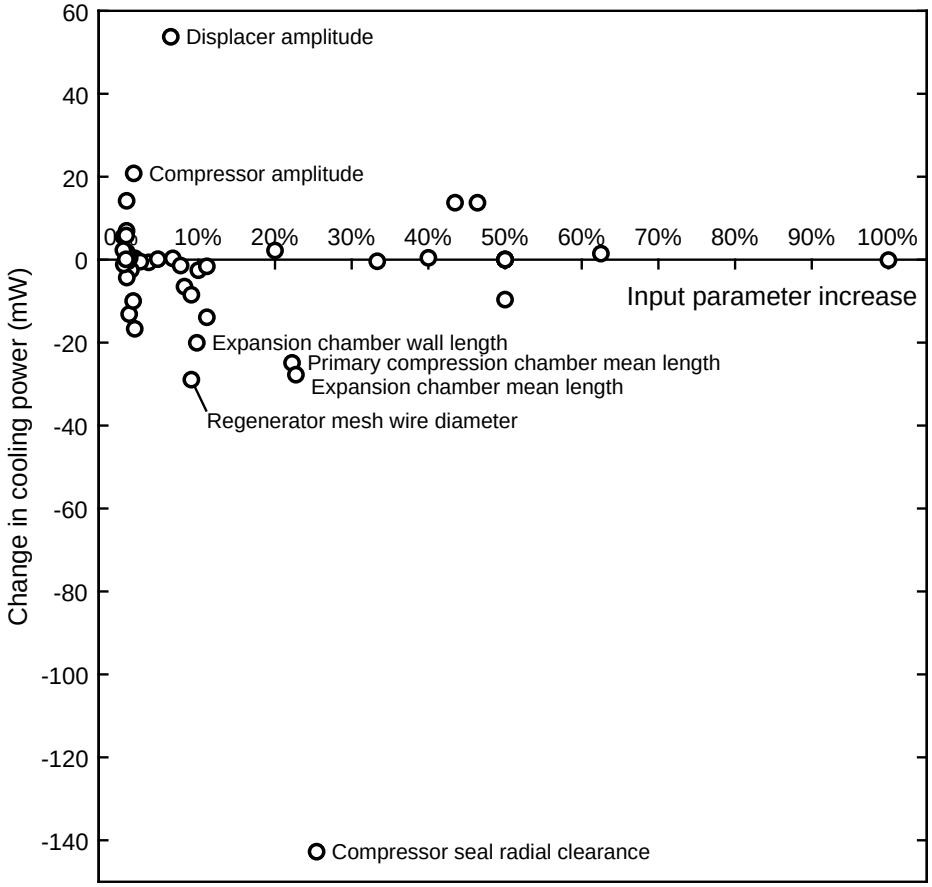

Figure 5.7: A plot of the variation in cooling power for the 78 K case of the 2018 Small Scale Cooler predicted by the RAL Third-Order Model when each of the inputs is increased to the upper limit of its uncertainty. The inputs that resulted in an error larger than 20 mW are labelled.

The other significant sources of error are due to uncertainties in the position waveforms of the compressor pistons and displacer. The errors of the electrical models used to calculate the amplitudes and phases of the motion were assessed by correlating them against measurements taken with a laser position sensor. An uncertainty of 30 μm was used for the compressor pistons and 50 μm was used for the displacer. The electrical models could not be used to determine the mean position of the compressor pistons and displacer, so the uncertainties were estimated from typical offsets seen in other coolers. These uncertainties were used for the mean lengths of the compression and expansion chambers.

Adding all the cooling power errors in quadrature gives a total error of 167 mW. This is a significant fraction of the total cooling power at this operating point. The large error shows the importance of obtaining accurate inputs for the model. The position waveform accuracy could be improved by directly measuring the position waveforms of the mechanisms, although installing position sensors would increase the size of the cooler. Taking measurements of the gas flow through the clearance seals would remove the uncertainty in the piston alignment as it would enable a gap size to be calculated that gives a leakage equivalent to the measured value. However, installing the gas ports necessary to perform this flow test would increase the size of the cooler.

Heat Transfer

The sensitivity of the model to changes in the heat transfer correlations was assessed. The rates of heat transfer in each region were increased by 10% using a one-at-a-time approach.

The results are plotted in Figure 5.8. Modifying the heat transfer correlations only has a small impact in most of the regions. The largest impact is in the regenerator where an increase in the rate of heat transfer increases the regenerator efficiency and increases the cooling power. Increasing the heat transfer in the appendix gap reduces the cooling power because it increases the magnitude of the shuttle losses. It is interesting to note that increasing the heat transfer in the primary and secondary compression chambers reduces the cooling power. The improved heat transfer slightly reduces the pressure swing which reduces the gross cooling power.

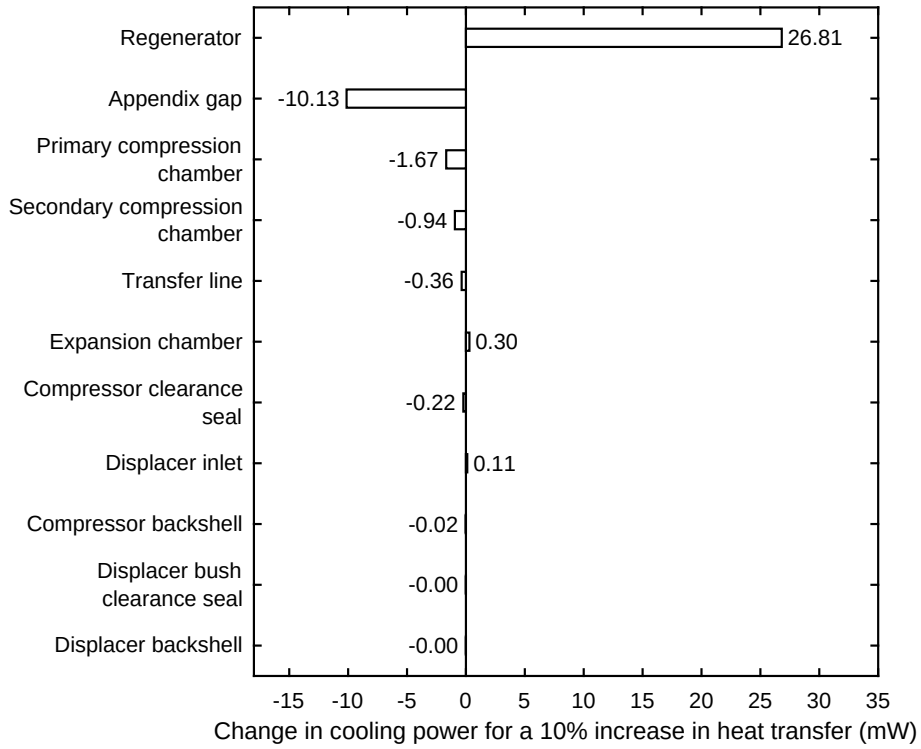

Figure 5.8: A plot of the variation in cooling power for the 78 K case of the 2018 Small Scale Cooler predicted by the RAL Third-Order Model when the rates of heat transfer in each region are increased by 10%.

The relative error in the regenerator heat transfer correlations is estimated to be about 10% for high peak Reynolds numbers (>1000) and about 50% for low (<5) [51]. The typical peak Reynolds number for the Small Scale Cooler regenerator is around 50, so the error will be between these two values. The error of the heat transfer correlation in the appendix gap is unknown because it is theoretical and not derived from experimental data. It may be large if the assumptions are incorrect (see Section 3.6.8).

Friction

The friction factor in each region was increased by 10% in a similar way to the rates of heat transfer. The results are potted in Figure 5.9. Unsurprisingly, increasing the friction factor in the clearance seals improves the effectiveness of the seals and improves the performance of the cooler. Increasing the friction factor in the regenerator reduces the cooling power because it

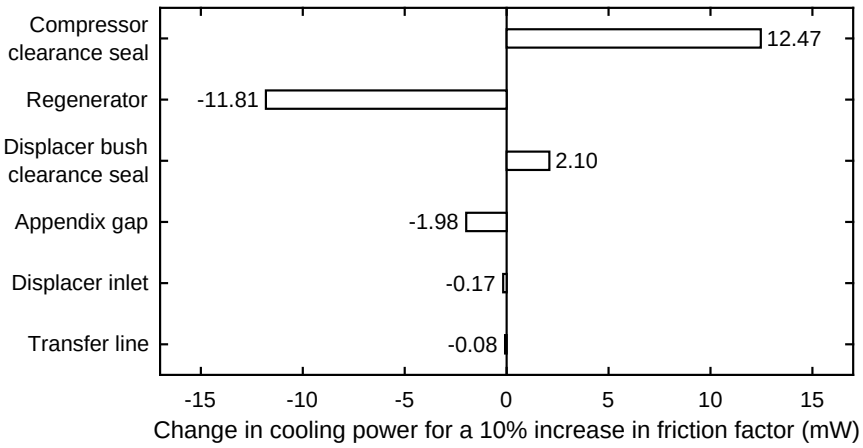

Figure 5.9: A plot of the variation in cooling power for the 78 K case of the 2018 Small Scale Cooler predicted by the RAL Third-Order Model when the friction factors in each region are increased by 10%.

increases the pressure drop along its length and reduces the pressure swing in the expansion chamber.

The friction factor correlation in the clearance seals is theoretically exact. Its accuracy depends on the validity of the assumptions, such as the flow being fully developed (see Section 3.6.7). The uncertainty of the friction factor correlation in the regenerator is estimated to be around 10% [51].

5.1.5 Loss Mechanisms

It is possible to investigate some aspects of the modelling in isolation by simulating tests that aim to isolate individual loss mechanisms [91]. Static loss and dynamic loss tests were performed on the 2014 Small Scale Cooler and these tests have been simulated using the model.

Static Losses

The static losses include the heat load due to thermal conduction through the gas and solid components of the cold finger and the heat load due to radiation. To measure these losses, the cooler is first run until the cold tip temperature is below the temperature of interest. The cooler is then turned off, and the warm-up rate is measured. This is repeated with a range of electrical heat loads being applied to the cold tip. By comparing the warm-up rates with

different electrical heat loads, the heat load due to the static losses can be calculated. To increase the accuracy of the measurement, the warm-up rate is slowed by attaching a large thermal mass to the cold tip (as shown in Figure 5.10).

A comparison of measured and modelled static losses for the 2014 Small Scale Cooler is shown in Figure 5.11. There is good agreement between the measured and modelled static losses across a large temperature range, which indicates that the model is accurately predicting the conductive and radiative heat loads.

Dynamic Losses

The dynamic losses are measured in a similar way to the static losses, but only the compressor pistons are stopped. The motion of the displacer results in the total heat load being higher than in the static loss case. The displacer motion

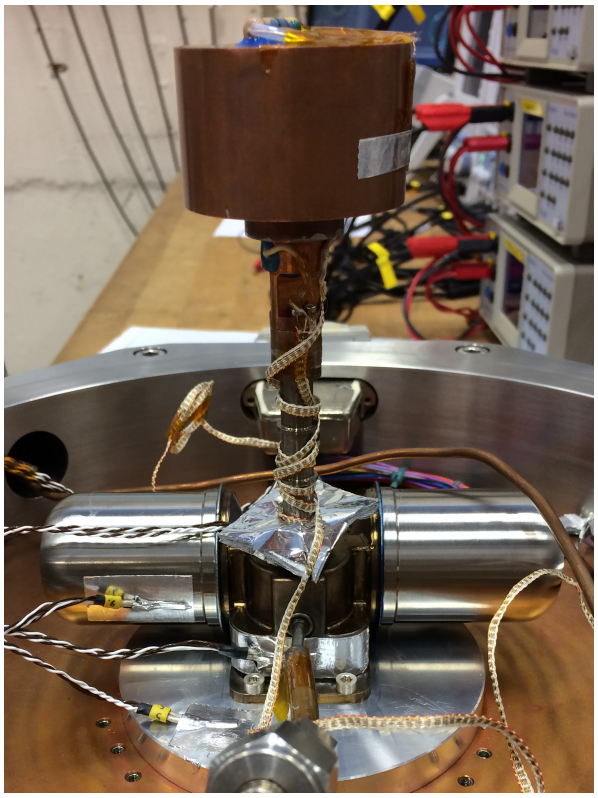

Figure 5.10: A photograph of the 2014 Small Scale Cooler undergoing loss mechanism testing.

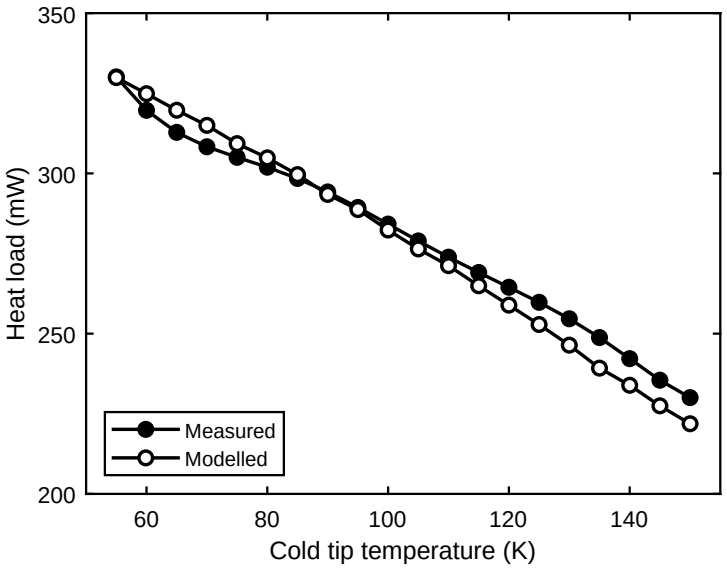

Figure 5.11: A plot comparing the measured static losses of the 2014 Small Scale Cooler at different cold tip temperatures with the static losses predicted by the RAL Third-Order Model.

introduces new loss mechanisms: shuttle losses; enhanced gas conductivity; and regenerator and appendix gap enthalpy transport.

A comparison of the measured and modelled dynamic losses for the 2014 Small Scale Cooler is shown in Figure 5.12. The model gives a good prediction of the dynamic losses of the Small Scale Cooler over the full range of strokes. This indicates that the model is accurately simulating the shuttle losses, enhanced conductivity and enthalpy transport.

5.1.6 Model Calibration

The results from the sensitivity analyses and loss mechanism modelling can be used to help understand why the model overpredicts the cooling power when simulating a load line (as shown in Figure 5.3).

The results of the sensitivity analyses indicate that errors in the heat transfer and friction factor correlations of the regenerator and in the heat transfer correlation of the appendix gap could have a significant impact on the cooling power. However, the static and dynamic loss test results suggest that the model is correctly simulating the regenerator losses and shuttle losses which depend on these correlations. The only other correlation that has a significant

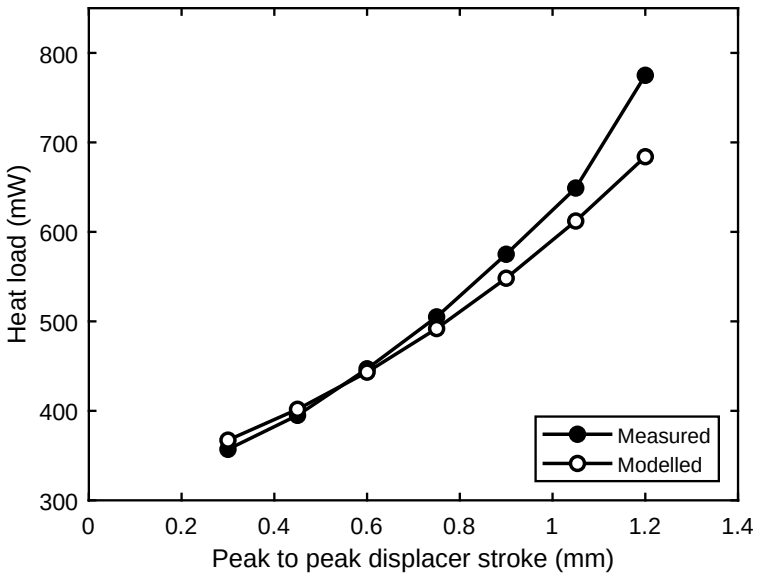

Figure 5.12: A plot comparing the measured dynamic losses of the 2014 Small Scale Cooler at different displacer strokes with the dynamic losses predicted by the RAL Third-Order Model. The cold tip was at 75 K for all cases.

impact on the cooling power is the friction factor of the compressor piston clearance seals; this may be causing the overprediction of the cooling powers.

The uncertainty analysis of the input parameters also highlights the importance of correctly modelling the compressor piston clearance seals. An error in the radial clearance could account for the overprediction in cooling power, although this is unlikely because the uncertainty in the radial clearance is mostly from the uncertainty in the eccentricity and the piston was already assumed to be fully eccentric. Errors in the thermal expansion coefficients would only have a small impact on the gap size because the compressor was only just above room temperature. It appears to be more likely that the friction factor correlation is incorrect.

Measurements have been taken at RAL that indicate that the measured flow rate of gas past a clearance seal is often higher than is calculated theoretically from measuring the dimensions of the piston and bore. These measurements are presented in Section 5.4. This provides further evidence that the friction factor correlation is underpredicting the leakage.

These results suggest that the accuracy of the model could be improved by increasing the clearance seal leakage predicted by the model. This could be

done by either adjusting the friction factor correlation or increasing the gap sizes of the clearance seals in the input file. Increasing the gap size was chosen because it made it easier to adjust individual seals. This method of calibration has been previously used in the Joule-Thomson compressor model developed at RAL and has given good results. For the Small Scale Cooler, this calibration was only applied to the compressor piston seal gaps and the appendix gap as these were calculated from the dimensions of the components; the displacer shaft seal gap was calculated from flow test data so did not need to be adjusted.

The gap of the compressor clearance seals and the appendix gap were adjusted to see what impact increasing the gaps had on the cooling power. The sensitivity analysis indicates that increasing the compressor piston clearance seal gap has a much greater impact on the cooling power than increasing the appendix gap; however, both gaps were increased by the same amount because it is not clear why the correlation would be needed for one clearance seal and not the other.

Figure 5.13 shows the effect that increasing the size of both gaps by 50% and 100% has on the predicted cooling power. The plot shows that the best agreement between measured and modelled cooling power is found if both gaps are increased by around 50%. Applying this calibration results in the load line to agreeing across the whole temperature range; this gives confidence that this is an effective method for calibrating the model.

Losses with the Calibration Applied

The impact of this calibration on the powers and losses has been investigated. A comparison of the gross cooling power and net cooling power with and without the calibration applied is plotted in Figure 5.14. Increasing the gaps causes a significant reduction in gross cooling power, resulting in a reduction in net cooling power. The reduction in gross cooling power occurs because more gas can leak past the compressor piston, reducing the pressure swing.

The changes in the individual loss mechanisms have also been analysed. The contributions of the loss mechanisms for both cases are plotted in Figure 5.15. The three largest changes are in the regenerator enthalpy transport, appendix gap enthalpy transport and regenerator gas conduction. The reduction in regenerator enthalpy transport and gas conduction is probably partly due to

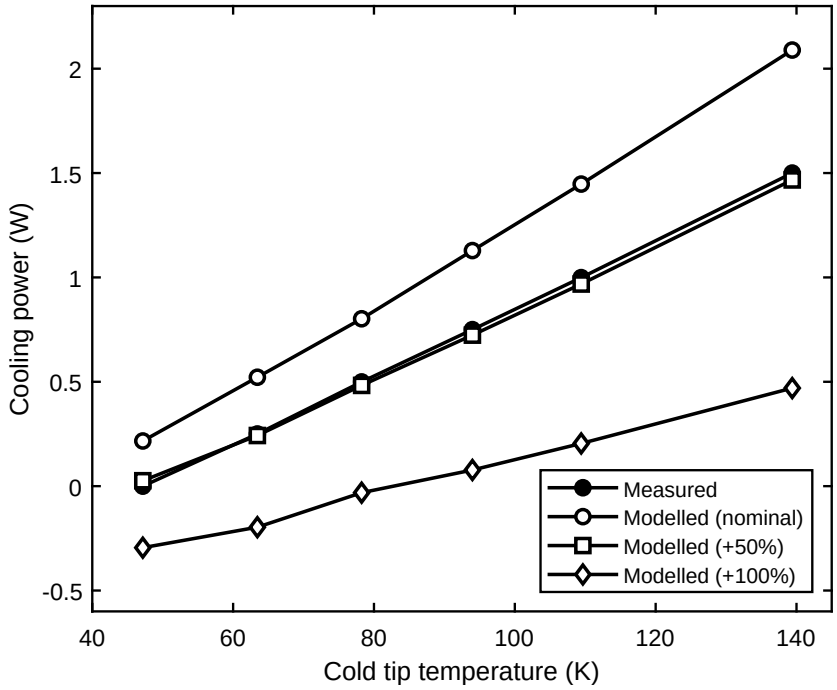

Figure 5.13: A plot showing the effect that increasing the compressor seal radial clearance by 50% and 100% has on the net cooling power predicted by the RAL Third-Order Model for the 2018 Small Scale Cooler. These results are compared to the measured cooling power.

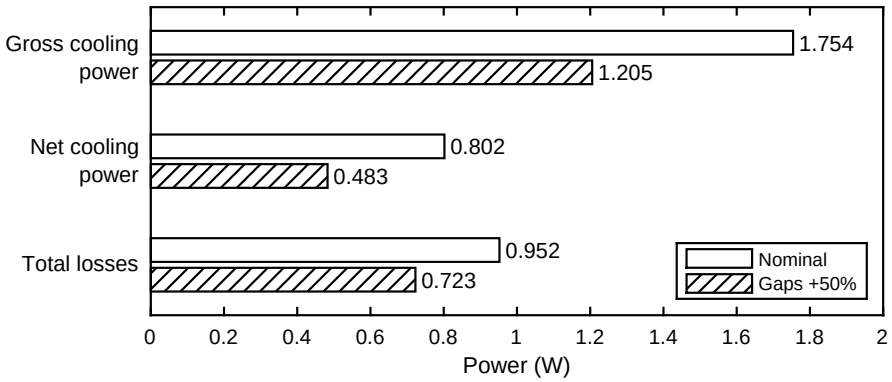

Figure 5.14: A plot showing the change in the gross cooling power, net cooling power and total losses predicted by the RAL Third-Order Model for the 78 K case of the 2018 Small Scale Cooler when the sizes of the compressor clearance seal gaps and appendix gap are increased. The total losses are calculated by subtracting the net cooling power from the gross cooling power.

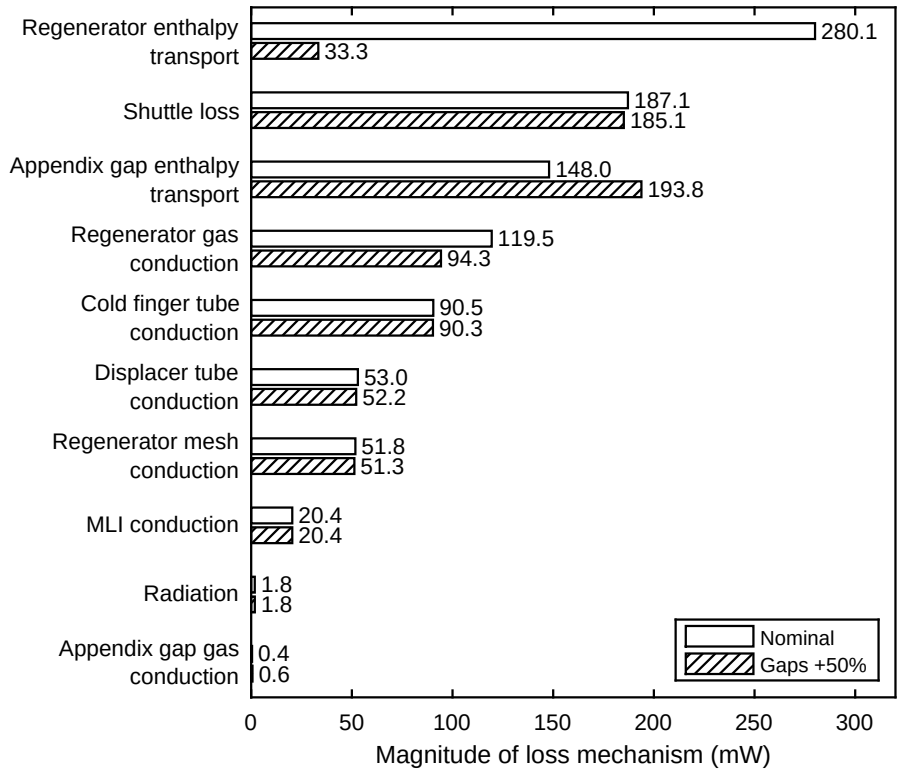

Figure 5.15: A plot showing the change in the losses predicted by the RAL Third-Order Model for the 78 K case of the 2018 Small Scale Cooler when the sizes of the compressor clearance seal gaps and appendix gap are increased.

the increase in the compressor clearance seals. This reduces the pressure swing, reducing the mass flow of gas through the regenerator and reducing both of these losses. The increase in appendix gap enthalpy transport is probably caused by increasing the appendix gap. This increases the flow of gas through the appendix gap which deposits more energy at the cold end. It was found that the increased flow in the appendix gap also influences the regenerator enthalpy transport by the transfer of heat through the displacer tube. This is discussed further in Section 6.1.

The shuttle losses are almost unchanged when the clearance seal gaps are increased. If the shuttle losses were simulated in isolation, they would be expected to decrease when the appendix gap size is increased because the thermal conductance across the appendix gap would be reduced. However, it appears that this effect is being counteracted by the increased flow in the

appendix gap, which is acting to enhance the conduction to the gas and increase the shuttle losses.

5.2 Validation Against the CryoBlue Cooler

The latest single-stage Stirling cryocooler that has been developed at RAL is the CryoBlue Stirling Cooler, shown in Figure 5.16 [33]. This is a more powerful cooler than the Small Scale Cooler and can produce more cooling power at lower temperatures.

The cooler is still under development and has not yet undergone a full test campaign. However, some initial results have been taken which have been used to validate the model.

5.2.1 Input Parameters

The geometry input parameters for the CryoBlue Cooler were calculated in a similar way as for the Small Scale Cooler. However, an advantage of validating the model against the CryoBlue Cooler is that the seal leakages of the compressor pistons and displacer shaft were measured using flow tests before

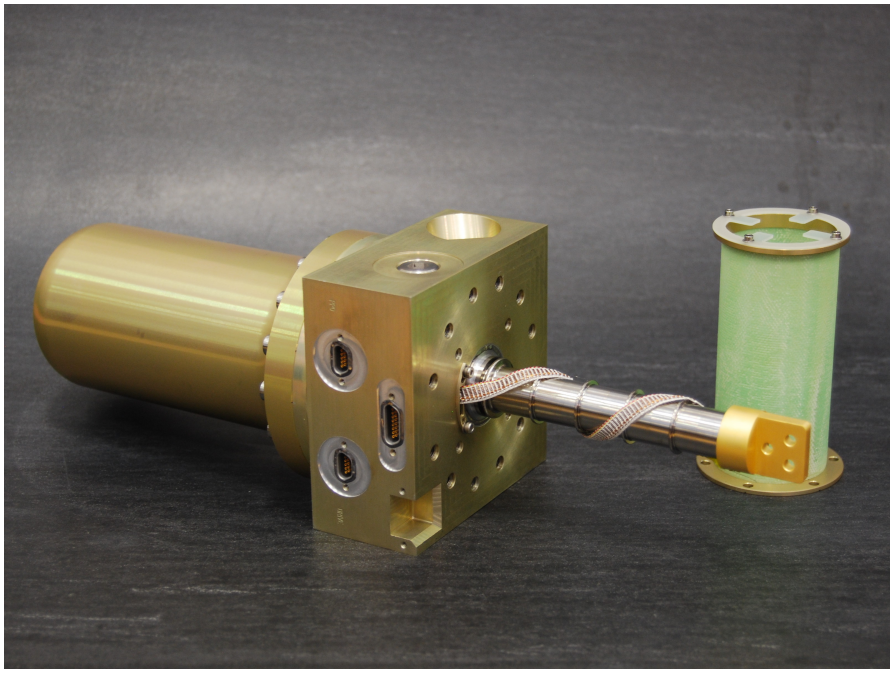

Figure 5.16: A photograph of the cold head of the CryoBlue Cooler.

the cooler was assembled. For the Small Scale Cooler, only the shaft seal gap was calculated in this way. The CryoBlue Cooler flow test results were used to calculate the gaps used by the model, as described in Section 5.4.1, and should provide an accurate seal leakage when used in the RAL Third-Order Model. The flow past the appendix gap was not measured, so this gap was calculated from measurements of the displacer tube and bore. The displacer was assumed to be fully eccentric in the cold finger tube. All of the clearance seal gaps were adjusted to account for thermal expansion or contraction.

Another advantage is that the position waveforms were measured directly using a laser position sensor for the compressor pistons and a capacitive position sensor for the displacer. This greatly reduces the uncertainty in these inputs.

Unlike the Small Scale Cooler, the CryoBlue Cooler contains a pressure transducer in the transfer line. The model's fill pressure input parameter was adjusted so that the mean pressure predicted by the model matched the mean pressure recorded by this sensor.

5.2.2 Spatial Resolution

The regenerator resolution required by the model was assessed in the same way as for the Small Scale Cooler. The regenerator resolution of the 57 K case was varied. This case was selected because this is the operating point the cooler design was optimised for. The results are plotted in Figure 5.17. The results are similar to the Small Scale Cooler, and this is not surprising because both are single-stage coolers operating at similar temperatures. A resolution of 60 regenerator cells was selected for the further modelling.

5.2.3 Performance Modelling

The results of the RAL Third-Order Model are compared to the measured performance data in Figure 5.18. It can be seen that there is good agreement between the model predictions and the measured data for all three load cases. Because the flow past the appendix gap was not measured, the modelling was repeated with the gap increased by 50% — the calibration factor required by the RAL Third-Order Model when modelling the Small Scale Cooler

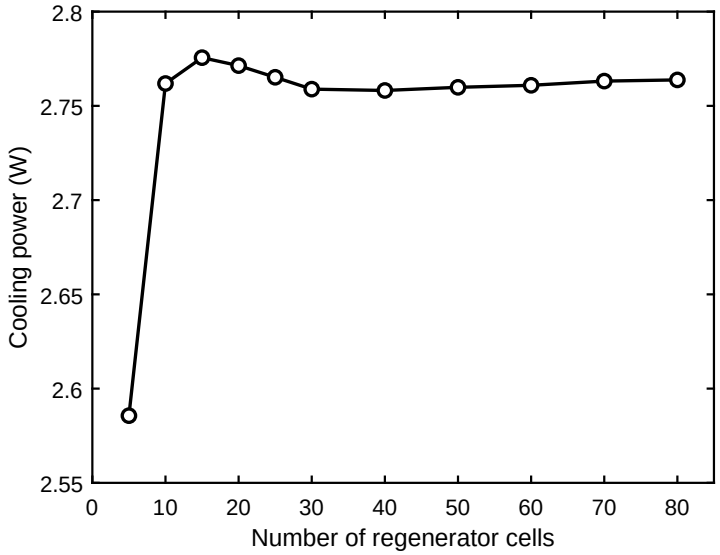

Figure 5.17: A plot showing how the cooling power predicted by the RAL Third-Order Model is affected by the number of regenerator cells for the 57 K case of the CryoBlue Cooler.

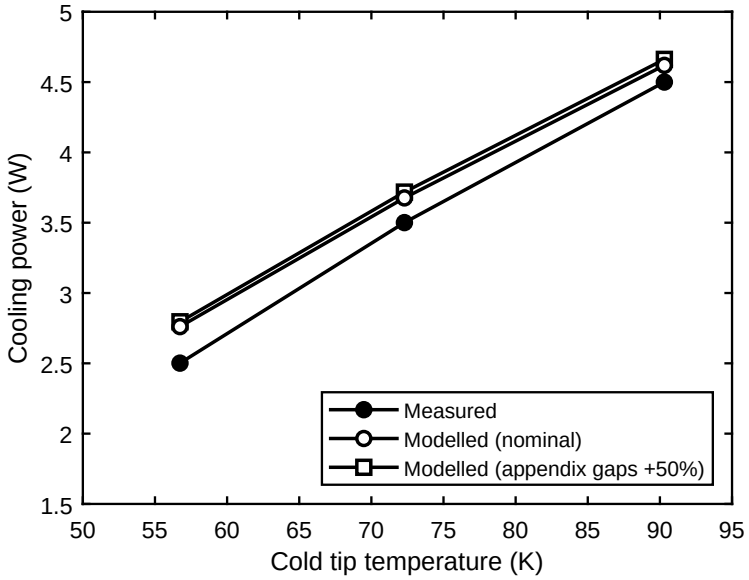

Figure 5.18: A plot comparing a measured load line of the CryoBlue Cooler to the performance predicted by the RAL Third-Order Model. The model was run with the measured appendix gap and with the gap increased by 50%. It should be noted that the measured load line was taken with a low compressor input power and is not representative of the maximum cooler performance.

performance (Section 5.1.6). However, it was found that this had little effect on the modelled performance in this case.

It is reassuring to see that there is good agreement between the model predictions and the measured data when simulating a cooler where the compressor piston seal leakages were measured experimentally. The predicted performance is still slightly higher than the measured performance by approximately 6% for the 72 K case. However, this is a large improvement when compared to the 61% error of the uncalibrated model for the 78 K case of the 2018 Small Scale Cooler. The model's accuracy when using measured clearance seal leakages provides further evidence that the overprediction of the cooling power of the Small Scale Cooler was due to problems with the clearance seal friction factor correlation.

Operational Losses

The predicted gross cooling power, net cooling power and total losses are plotted in Figure 5.19. The plot shows that applying the calibration to the appendix gap has little impact on any of these results.

In contrast, applying the calibration to the appendix gap has a significant effect on the individual loss mechanisms, as shown in Figure 5.20. The impact on the loss mechanisms is similar to what was seen when the calibration was

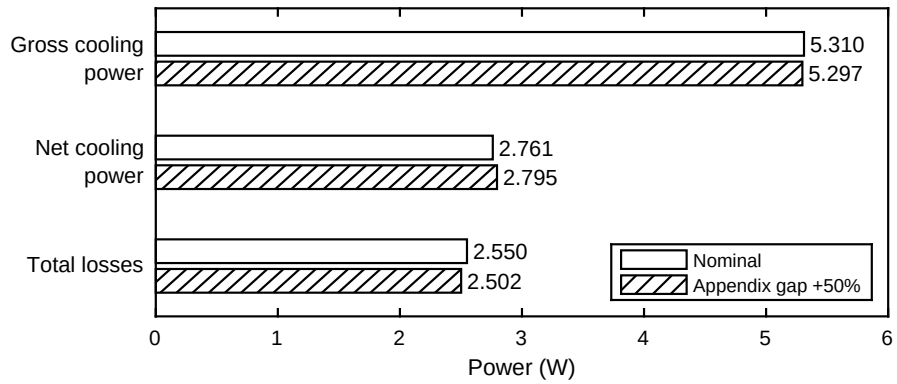

Figure 5.19: A plot of the gross cooling power, net cooling power and total losses predicted by the RAL Third-Order Model for the 57 K case of the CryoBlue Cooler. The model was run with the measured appendix gap and with the gap increased by 50%. The total losses are calculated by subtracting the net cooling power from the gross cooling power.

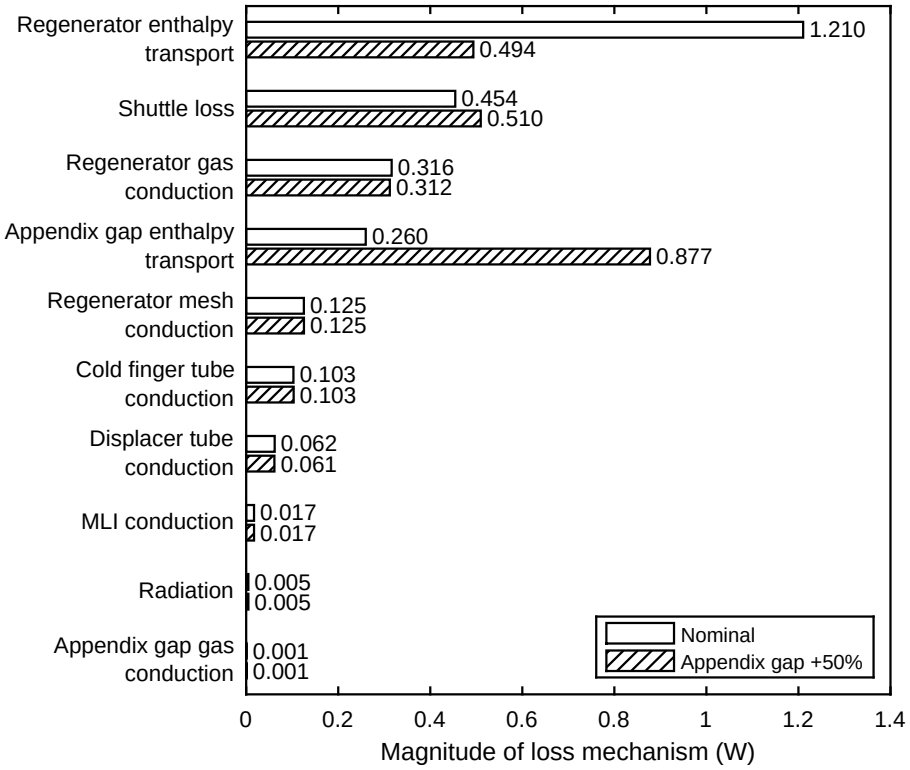

Figure 5.20: A plot showing the losses predicted by the RAL Third-Order Model for the 57 K case of the CryoBlue Cooler. The model was run with the measured appendix gap and with the gap increased by 50%.

applied to the Small Scale Cooler in Section 5.1.6. There is a large increase in the appendix gap enthalpy transport, a reduction in the regenerator enthalpy transport and the shuttle losses are almost unaffected.

Pressure Waveform

The pressure swing predicted by the model can be validated against data taken from the pressure transducer in the transfer line of the CryoBlue Cooler. Accurately predicting the pressure waveform is useful because it can be combined with results from an electromagnetic model of the motors to predict the electrical input power required by the compressor motors. The modelled and measured pressure waveforms are plotted in Figure 5.21. There is very good agreement between the waveforms; the shape, amplitude and

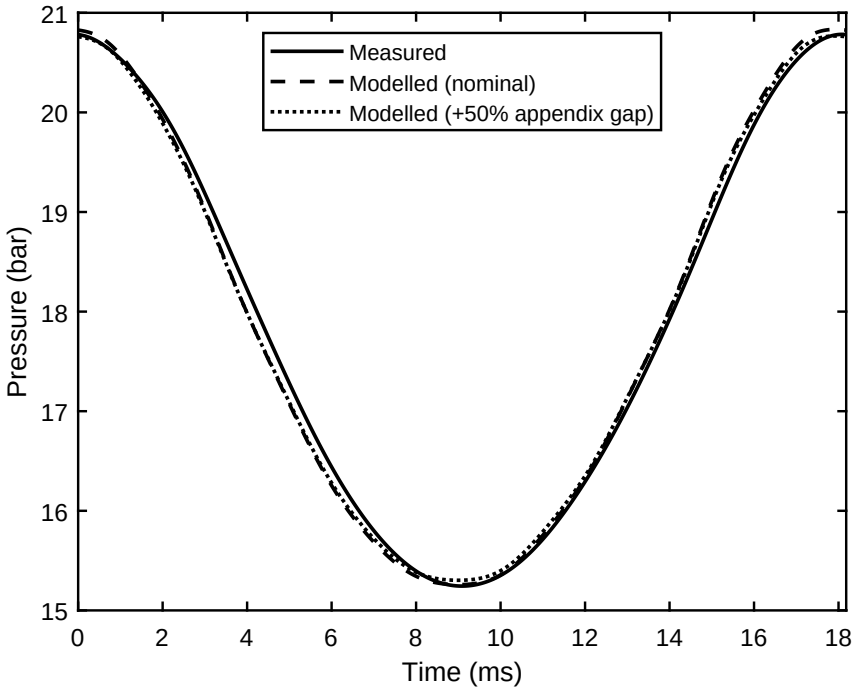

Figure 5.21: A plot showing the pressure waveform measured in the transfer line for the 57 K case of the CryoBlue Cooler. This is compared to the results of the RAL Third-Order Model which was run with the measured appendix gap and with the gap increased by 50%.

phase are very similar. Applying the calibration to the appendix gap has very little impact on the pressure waveform.

5.2.4 Displacer Forces

The RAL Third-Order Model can be used to predict the gas forces acting on the compressor pistons and displacer (see Section 3.1). It is useful to know the gas forces when designing a Stirling cooler because they affect the dynamics of the system. If the gas forces are known, it is possible to optimise the geometry, moving masses and spring rates of the cooler so that the required position amplitudes and phases can be achieved with minimal motor power. For example, the diameter of the displacer shaft can be adjusted to affect the pressure forces acting on the displacer. If the gas forces on the displacer can be predicted with sufficient accuracy, it is possible to design a cooler that will not require a displacer motor at all and can be driven pneumatically (see Section 2.2.1).

The accuracy of the displacer gas force prediction was assessed for the CryoBlue Cooler. The gas force is difficult to measure directly while the cooler is operating, but it is possible to derive it. This can be done by subtracting the other known forces from the force required to produce the motion of the displacer. The resultant force is the gas force.

$$F_{gas} = F_{motion} - F_{motor} - F_{spring} - F_{damping} \tag{5.1}$$

These forces are plotted in Figure 5.22. The motion force is calculated from the position waveform of the displacer x, which was measured with a capacitive position sensor, and the moving mass of the displacer m.

$$F_{motion} = m\,\ddot{x} \tag{5.2}$$

The other forces are calculated using the motor constant k_{motor}, spring rate k_{spring} and damping constant $c_{damping}$, which are determined from separate motor characterisation tests. The displacer motor current I is measured during operation using a current probe.

$$F_{motor} = k_{motor}\,I \tag{5.3}$$

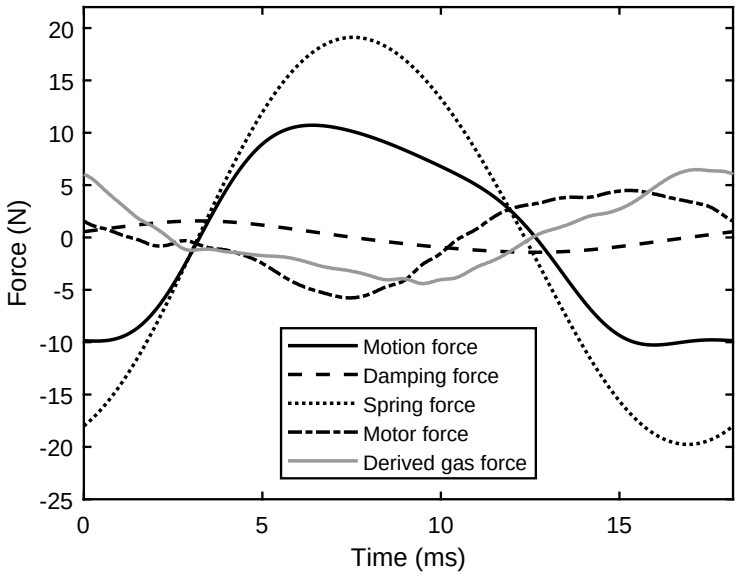

Figure 5.22: A plot showing the measured and derived forces acting on the displacer for the 57 K case of the CryoBlue Cooler.

$$F_{spring} = -k_{spring}\, x \tag{5.4}$$

$$F_{damping} = -c_{damping}\, \dot{x} \tag{5.5}$$

Figure 5.23 compares the gas force derived from these measurements with the displacer gas force predicted by the model.

There is good agreement between the amplitude, shape and phase of the force waveforms. The gas force appears to be unaffected by applying the calibration to the appendix gap.

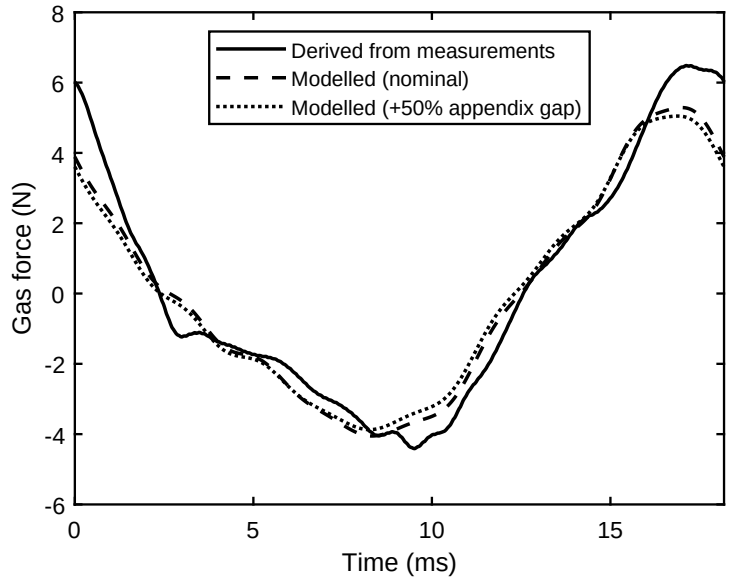

Figure 5.23: A plot comparing the gas forces calculated by the RAL Third-Order Model for the 57 K case of the CryoBlue Cooler with the gas force derived from measurements, shown in Figure 5.22. The model was run with the measured appendix gap and with the gap increased by 50%.

5.3 Validation Against the Breadboard Cooler

The Breadboard Cooler, described in Chapter 4, was tested under a range of different conditions in order to validate the model over a wide parameter space. The cooler was tested with fill pressures of 5, 10 and 15 bar and a range of heat loads were applied to the two stages. Each of these tests were repeated with and without cryogenic pressure sensors. The cryogenic pressure sensors are useful for verifying the modelled pressure waveforms but add a significant heat load to the stages.

The resonant frequencies of the compressor and displacer motors were not matched, so it was not possible to run both the mechanisms at full stroke at the same frequency (see Section 4.2). As a compromise, the cooler was run at 20 Hz, which is between the resonant frequencies of the displacer and the compressor motors, and the motors were driven so that they were near their electric current limit. The phasing between the compressor and displacer drive waveforms was chosen so that the gross cooling power at the second stage expansion chamber was maximised; this gross cooling power was calculated from the motion of the displacer and the pressure waveform at the expansion chamber. The amplitude and phase of the drive waveforms was set for each fill pressure when there was no heat load and with the cryogenic pressure sensors attached. The drive waveforms were then kept constant for all the other measurements at that fill pressure (for the different heat loads and with and without cryogenic pressure sensors).

5.3.1 Measured Performance

Figure 5.24 shows the load maps of the cooler at the three fill pressures without cryogenic pressure sensors.

The load maps show that the best performance was achieved at the 10 bar fill pressure. The performance is much worse for the 5 bar case, although the second stage base temperature is similar. It can be seen that the temperature of the second stage is not much lower than the temperature of the first stage for any of the 10 and 15 bar load cases. The model has been used to investigate why this is the case and this is discussed in Section 5.3.4.

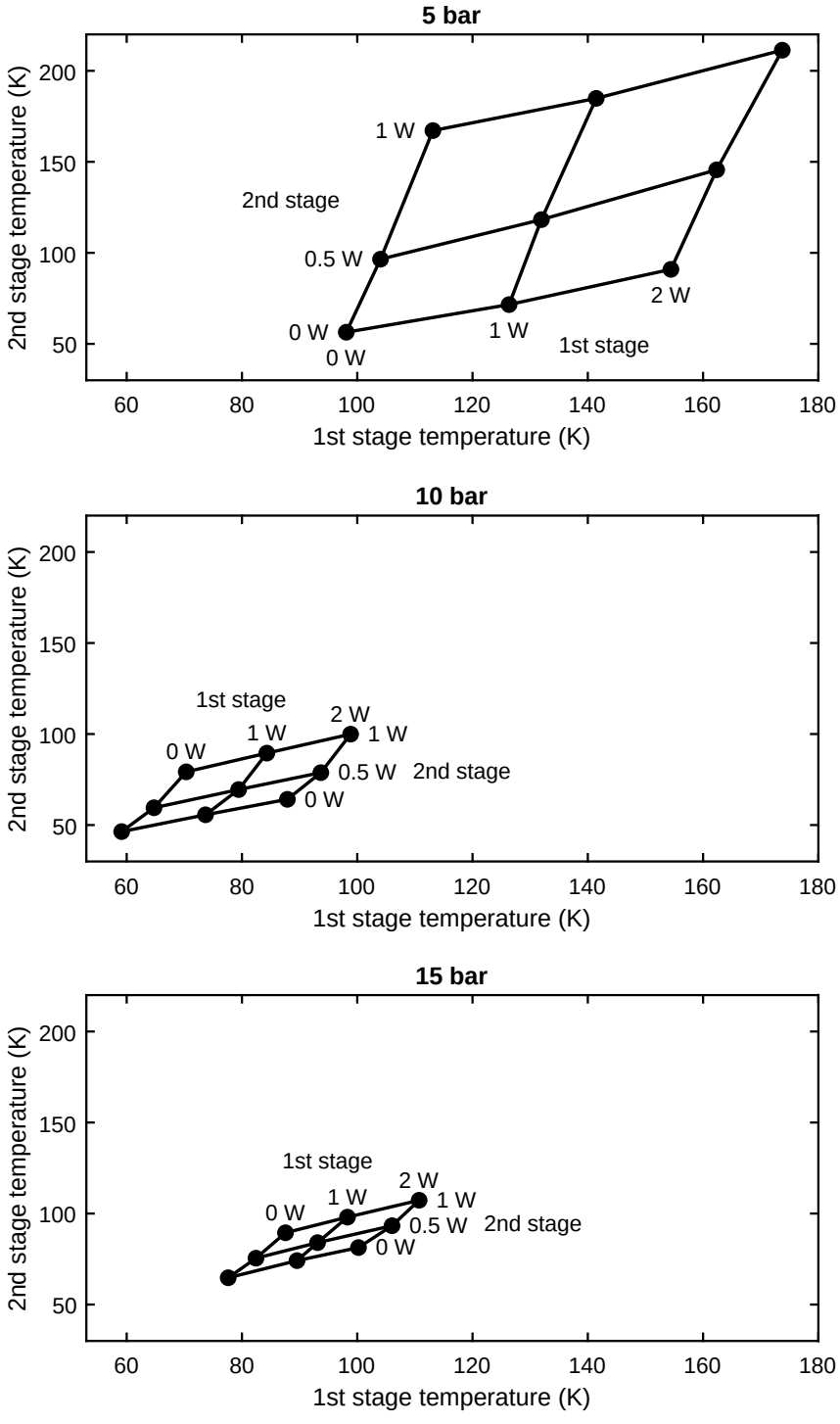

Figure 5.24: Plots showing the performance of the Breadboard Cooler at three different fill pressures without the cryogenic pressure sensors. The annotations show the heater power that was applied to the stages for each point.

5.3.2 Input Parameters

The critical geometry of the two-stage cooler was measured prior to assembly so that the measurements could be used to calculate the model inputs. For example, the wall thicknesses of the cold finger tubes were measured using a coordinate measuring machine. The sensors used to measure the pressures, temperatures and position waveforms are described in Section 4.2. The model's fill pressure input parameters were adjusted so that the mean pressures predicted by the model matched the mean pressures recorded by the pressure sensor in the transfer line.

The clearance seal gaps of the compressor pistons and the displacer shaft were derived from helium flow test measurements, using the method described in Section 5.4.1. The calculated gaps should provide an accurate seal leakage when used in the RAL Third-Order Model. It was not possible to carry out flow tests on the appendix gaps, so their sizes were calculated from the dimensions of the displacer tubes and cold finger tubes. Full eccentricity was assumed because there was some rubbing between the displacer tube and the cold finger tube. All the clearance seal gaps were adjusted to account for thermal expansion.

5.3.3 Spatial Resolution

The impact of the spatial resolution of the regenerators was assessed for the 10 bar case, with 1 W of heat load on the first stage, 0.5 W on the second and without cryogenic pressure sensors. This case was selected because it was the middle of the fill pressure and heat load ranges. The number of cells in each stage were varied together so that both stages contained the same number of cells.

The results are shown in Figure 5.25. The cooling power does not change significantly when the number of cells in the regenerators is increased past 40. For the further modelling, a resolution of 40 regenerator cells was selected for both stages.

5.3.4 Performance Modelling

The load cases plotted in Figure 5.24 were simulated using the model. The initial results are plotted in the first column of Figure 5.26. There is good

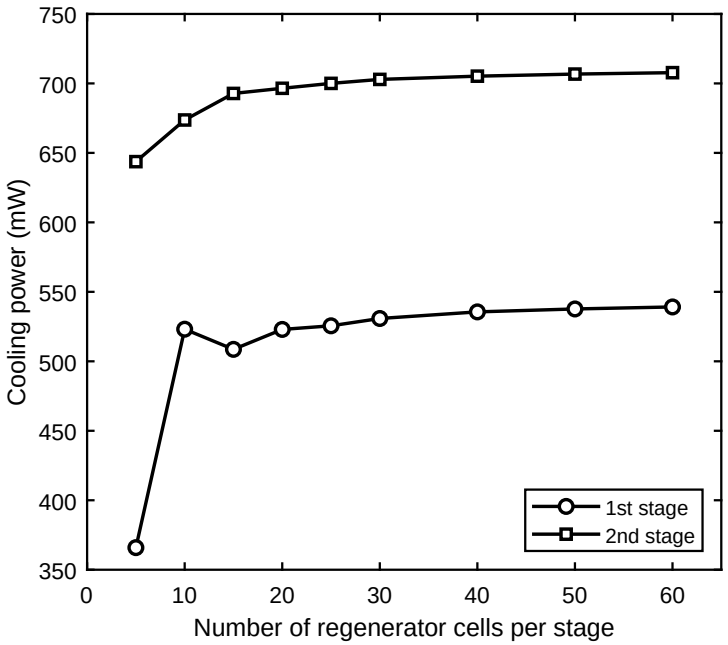

Figure 5.25: A plot showing how the cooling power predicted by the RAL Third-Order Model is affected by the number of regenerator cells for the Breadboard Cooler. The modelled case was the 10 bar, 1 W, 0.5 W case without cryogenic pressure sensors.

agreement for the 5 bar cases. However, for some of the 10 and 15 bar cases, the model overpredicts the cooling power at the second stage. The error in the cooling power does not seem to be constant. This is shown by the distortion of the grids of predicted cooling power for the 10 and 15 bar cases. Is in unlikely that the errors are caused by incorrectly predicting the gross cooling power because this would result in an almost constant offset, as was seen with the Small Scale Cooler. Instead, the errors may be due to a loss mechanism that varies in magnitude for the different cases.

The calibration method used for the Small Scale Cooler was attempted for the Breadboard Cooler. Because the compressor piston and displacer shaft clearance seal gaps were calculated from flow tests, they were not increased but the appendix gap size was. It was found that increasing the appendix gap size for both stages had a significant impact on the predicted cooling power. Both gaps were initially increased by 50%, but it was found that a better match between the measured and modelled results was obtained when both gaps were increased by 40%.

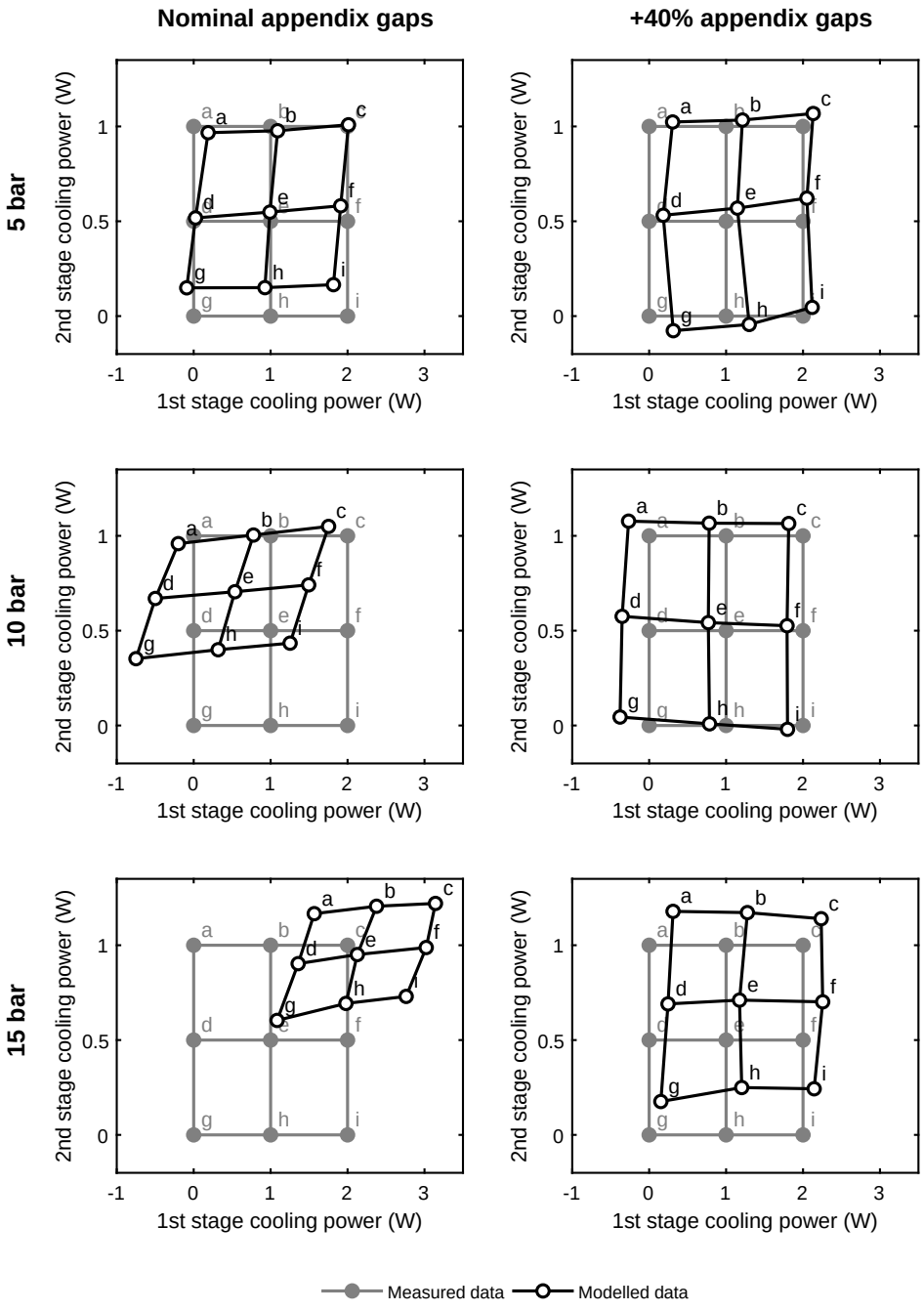

Figure 5.26: Plots comparing the measured cooling powers of the Breadboard Cooler with the cooling powers predicted by the RAL Third-Order Model. The cases are the same as the ones plotted in Figure 5.24. The letter of each modelled case indicates which measured case the input parameters were taken from. Measured and modelled cases with the same letter have the same temperatures and compressor and displacer amplitudes and phases.

The results with the calibration applied are plotted in the second column of Figure 5.26. Increasing the size of the first and second stage appendix gaps by 40% had a dramatic impact on the cooling powers for the 10 and 15 bar cases. The grids of modelled cooling powers with the calibrated appendix gaps have similar spacings to the measured cooling powers. This suggests that the model is correctly simulating the relationships between the stage temperatures and the cooling powers. The small offsets between the grids of measured and modelled cooling could be caused by effects that are independent of the stage temperatures. The errors may be due to inaccuracies in the input parameters, and this has been investigated further by performing a sensitivity analysis (see Section 5.3.5).

Operational Losses

The gross cooling powers and loss mechanisms have been examined to investigate what causes the large change in cooling power when the appendix gaps are increased. The predicted gross cooling power, net cooling power and total losses for one of the cases is shown in Figure 5.27. The contribution of each loss mechanism is shown in Figure 5.28. The selected case was the 10 bar, no cryogenic pressure transducer case where 1 W was applied to the first stage and 0.5 W was applied to the second stage (the 10 bar case “e” in Figure 5.26).

Figure 5.27 shows that the gross cooling power is almost unchanged by increasing the size of the appendix gap. The change in the net cooling power is mostly due to a change in the total losses for each stage. This plot also highlights the difficulty in predicting the net cooling power at the first stage for this case, as the net cooling power is only a small fraction of the gross cooling power.

Figure 5.28 shows that increasing the size of the appendix gaps has a similar effect on the individual loss mechanisms as was seen when modelling the Small Scale Cooler and the CryoBlue Cooler. There is a dramatic increase in the appendix gap enthalpy transport, a reduction in the regenerator enthalpy transport and little impact on the shuttle losses.

If increasing the appendix gaps by 40% makes the simulation more realistic, it may explain the poor second stage cooling performance for the 10 and 15 bar cases. The increased flow through the appendix gap meant the regenerator

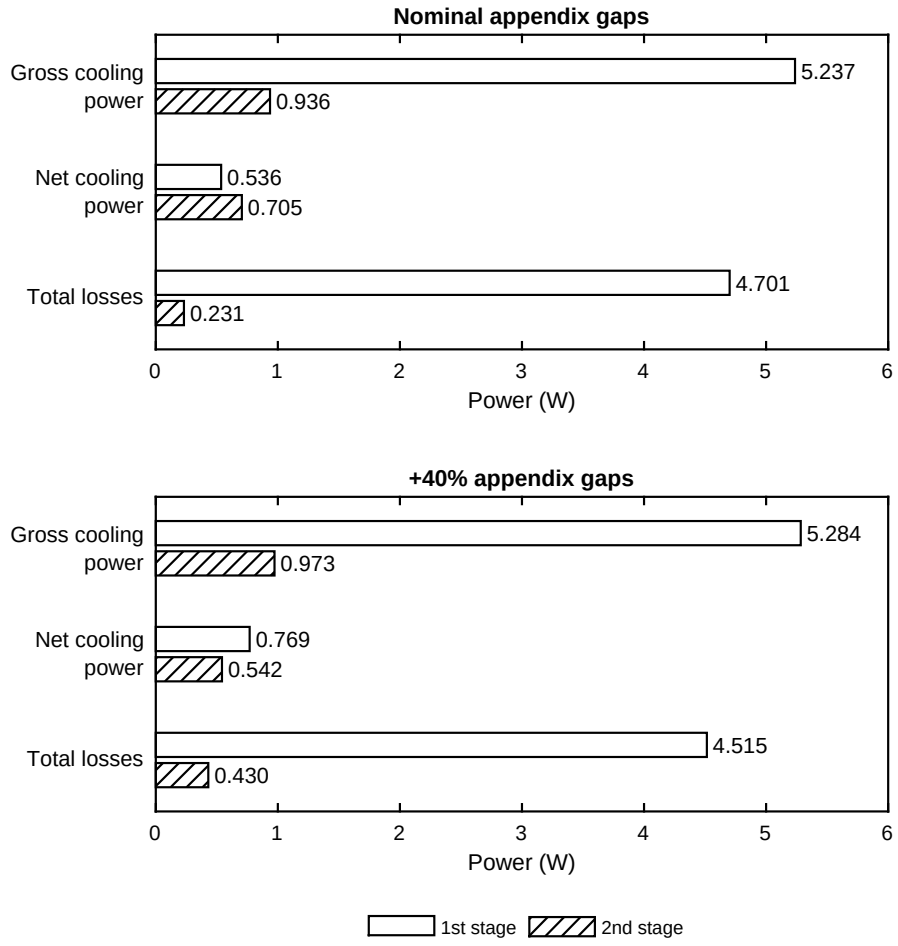

Figure 5.27: Plots showing the gross cooling power, net cooling power and total losses predicted by the RAL Third-Order Model for the no pressure transducer, 10 bar, 1 W, 0.5 W case of the Breadboard Cooler. The results with the measured appendix gap and with the gap increased by 40% are shown. The total losses for each stage are calculated by subtracting the net cooling power from the gross cooling power.

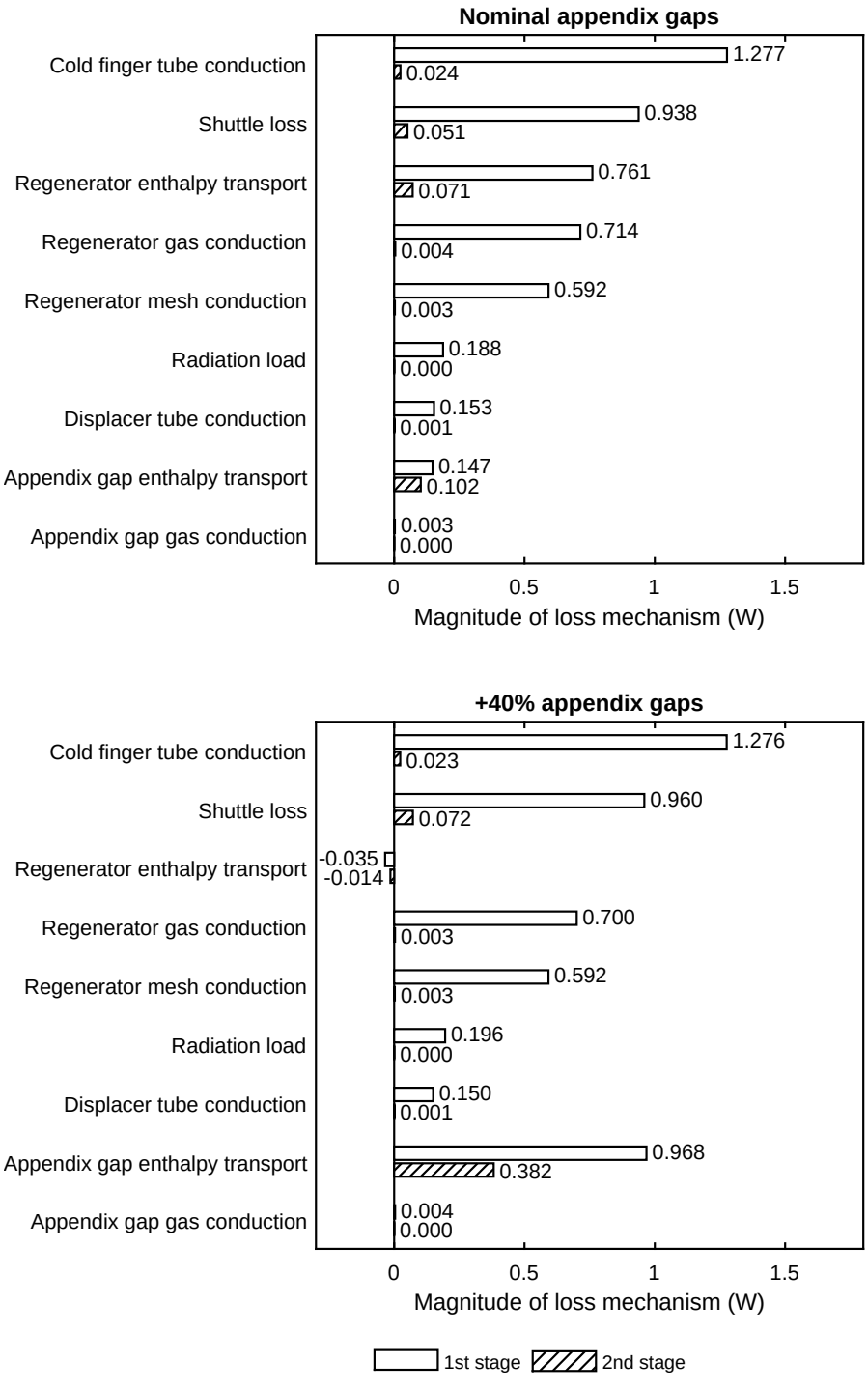

Figure 5.28: Plots showing the losses predicted by the RAL Third-Order Model for the no pressure transducer, 10 bar, 1 W, 0.5 W case of the Breadboard Cooler. The results with the measured appendix gap and with the gap increased by 40% are shown.

was being bypassed, and the warm gas was flowing straight to the second stage. This was less of a problem for the 5 bar cases because the lower pressure gas transports less enthalpy. This allowed the second stage to reach a much lower temperature than the first stage.

Pressure Waveforms

The measured pressure waveforms in the transfer line and expansion chambers have been compared to the waveforms predicted by the model. Comparing the pressure waveforms in the expansion chambers is particularly useful because these determine the gross cooling powers. The measured and modelled pressure waveforms of the 10 bar, 1 W, 0.5 W case are plotted in Figure 5.29.

Figure 5.29 shows that the model accurately predicts the amplitudes and phases of the pressure waveforms at the three locations. Increasing the appendix gap causes very little change in the modelled pressure waveforms. The model correctly predicts that most of the pressure drop along the cold finger occurs in the first stage; there is very little difference in the pressure waveforms of the two expansion chambers for either the measured or modelled data. The measured and modelled pressures were also similar for all the other fill pressures and heat loads.

Mean Pressures

A potential issue with linear compressors is that the mean position of the piston can drift when they are in operation [92]. When the gas in the primary compression chamber is compressed, the high pressure gas leaks through the compressor piston clearance seal into the compressor backshell; when the gas is expanded, lower pressure gas leaks from the backshell into the compression chamber. Because the high pressure gas has a higher density, there is a net flow of gas into the backshell. This results in the mean backshell pressure being higher than the mean pressure in the working volume. This pressure differential applies a force to the piston, pushing it forwards.

The Breadboard Cooler has piezo-resistive pressure transducers in the transfer line and compressor backshell that are able to measure the mean pressures in these regions. The pressure in the transfer line is likely to be very

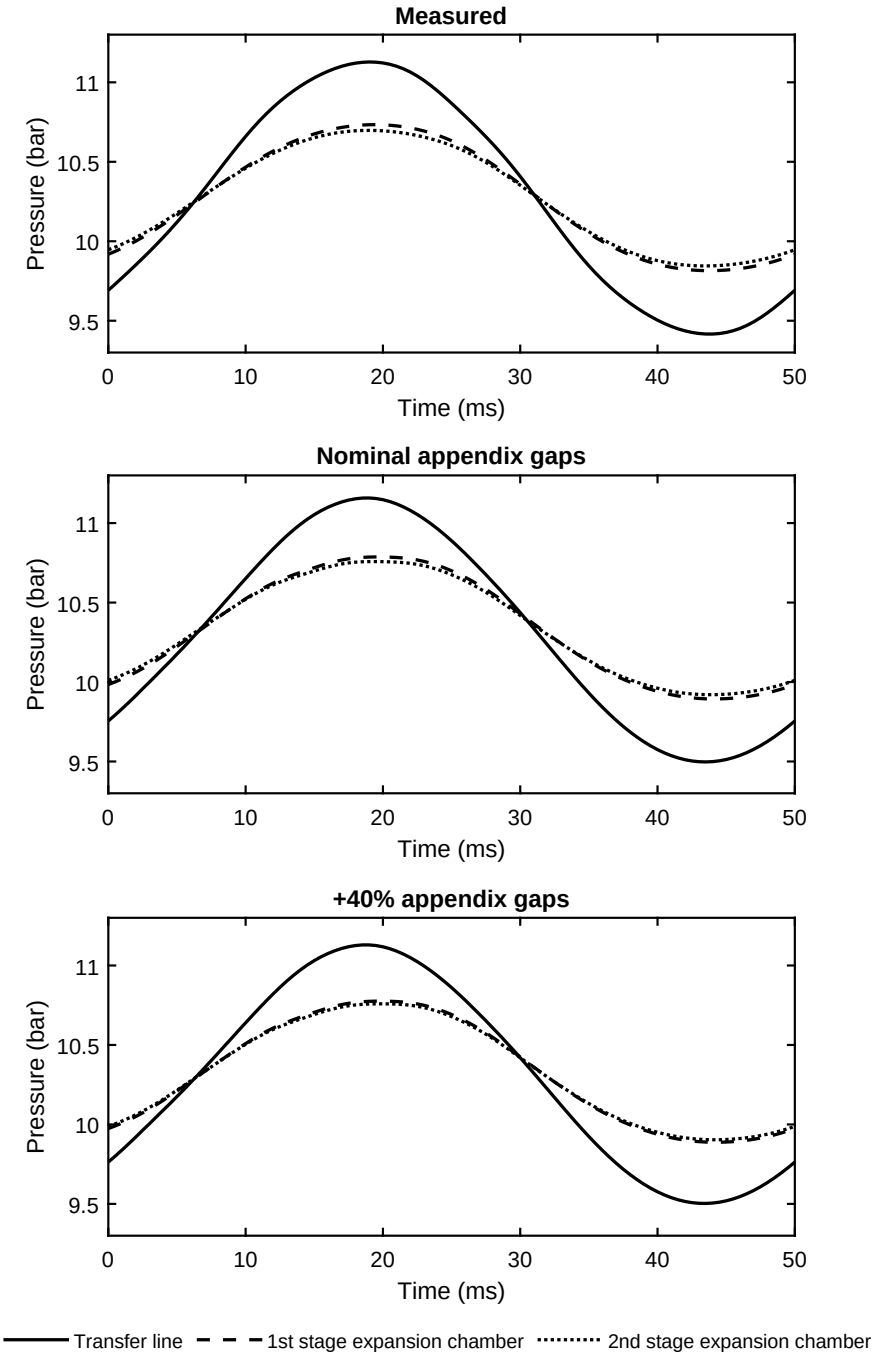

Figure 5.29: Plots comparing the measured and modelled pressure waveforms for the 10 bar, 1 W, 0.5 W case with cryogenic pressure sensors installed. These cryogenic pressure sensors at the first and second stage expansion chambers can only measure the pressure fluctuations and are unable to measure the mean pressure. It has been assumed that the mean pressure at the expansion chambers is the same as in the transfer line.

similar to the pressure in the primary compression chamber due to their proximity. Therefore, the measurements of the pressure transducers can be used to investigate the pressure differential caused by the motion of the pistons.

The measured and modelled mean pressures of the 10 bar, 1 W, 0.5 W case are presented in Table 5.1. The table shows that the model correctly predicts that the mean backshell pressure is higher than the mean transfer line pressure but that it incorrectly predicts the magnitude of this effect.

The table also shows the predicted piston offset, calculated from the pressure difference, piston area and spring stiffness. The predicted offsets for both the measured and modelled pressure differences are small compared to the maximum stroke amplitude of 7 mm. The mean position drift does not appear to be a significant issue for this type of cooler as it could be easily corrected by applying a small DC bias to the drive current waveform. If the piston offset is found to be an issue when developing coolers in the future, it would be worthwhile investigating this effect further to determine the cause of the discrepancy between the measured and modelled pressure differences.

5.3.5 Uncertainty and Sensitivity Analysis

Uncertainty and sensitivity analyses was performed for the 10 bar, 1 W, 0.5 W case without cryogenic pressure sensors. The appendix gap calibration was applied for the nominal case (both gaps increased by 40%).

Table 5.1: A table showing the measured and modelled pressures of the compressor backshell and transfer line of the Breadboard Cooler for the 10 bar, 1 W, 0.5 W case. The table also shows the differences between the two pressures and the mean piston offsets calculated from these pressure differences. The modelled data is with the appendix gaps increased by 40%.

	Mean pressure (bar)		Pressure difference (mbar)	Predicted offset (μm)
	Compressor backshell	Transfer line		
Measured	10.36	10.27	93.69	413.7
Modelled	10.33	10.30	27.36	120.8

Input Parameters

The approximate uncertainties of each input variable were estimated in a similar way to uncertainties of the Small Scale Cooler inputs (Section 5.1.4). The most significant difference was in the errors of the displacer and compressor position measurements. The displacer of the Breadboard Cooler has a capacitive position sensor, so the uncertainty in its position is low. The compressor piston position uncertainty is high because it is estimated from the pressure swing in the compressor backshell. The amplitude of the pressure swing is dependent on the volume of the backshell, which was estimated by taking the value from the compressor's data sheet and adding the approximate volume of the pressure sensor. Because this volume was not measured directly, its uncertainty is quite high.

The uncertainty analysis was carried out using the one-at-a-time method discussed in Section 5.1.4. The results of the uncertainty analysis are plotted in Figure 5.30. They show that the uncertainty in the compressor amplitude is a significant source of cooling power error for both stages. Increasing the compressor amplitude to the upper limit of its uncertainty increased the cooling power at both stages. This result highlights the importance of accurately measuring the compressor piston positions when validating the model; it would have been better to use a capacitive position sensor, as was used on the displacer.

The other significant source of error is due to the uncertainty in the size of the appendix gaps. The uncertainties in the appendix gap sizes were calculated by combining two sources of uncertainty. Firstly, the alignment between the displacer tube and the cold finger tube can affect the flow resistance and this effect was represented as an uncertainty in gap size. Secondly, there was uncertainty in the coefficient of thermal expansion of the displacer tube which influences the appendix gap size in the cold region of the cooler. Increasing the size of the appendix gap at the warm end of the first stage to the upper limit of its uncertainty caused more gas to flow through the gap and resulted in a large increase in the enthalpy transport loss at the first stage. Similarly, increasing the size of the second stage appendix gap increased the level of enthalpy transport from the first stage to the second stage. This increases the cooling power at the first stage at the expense of cooling power at the second stage.

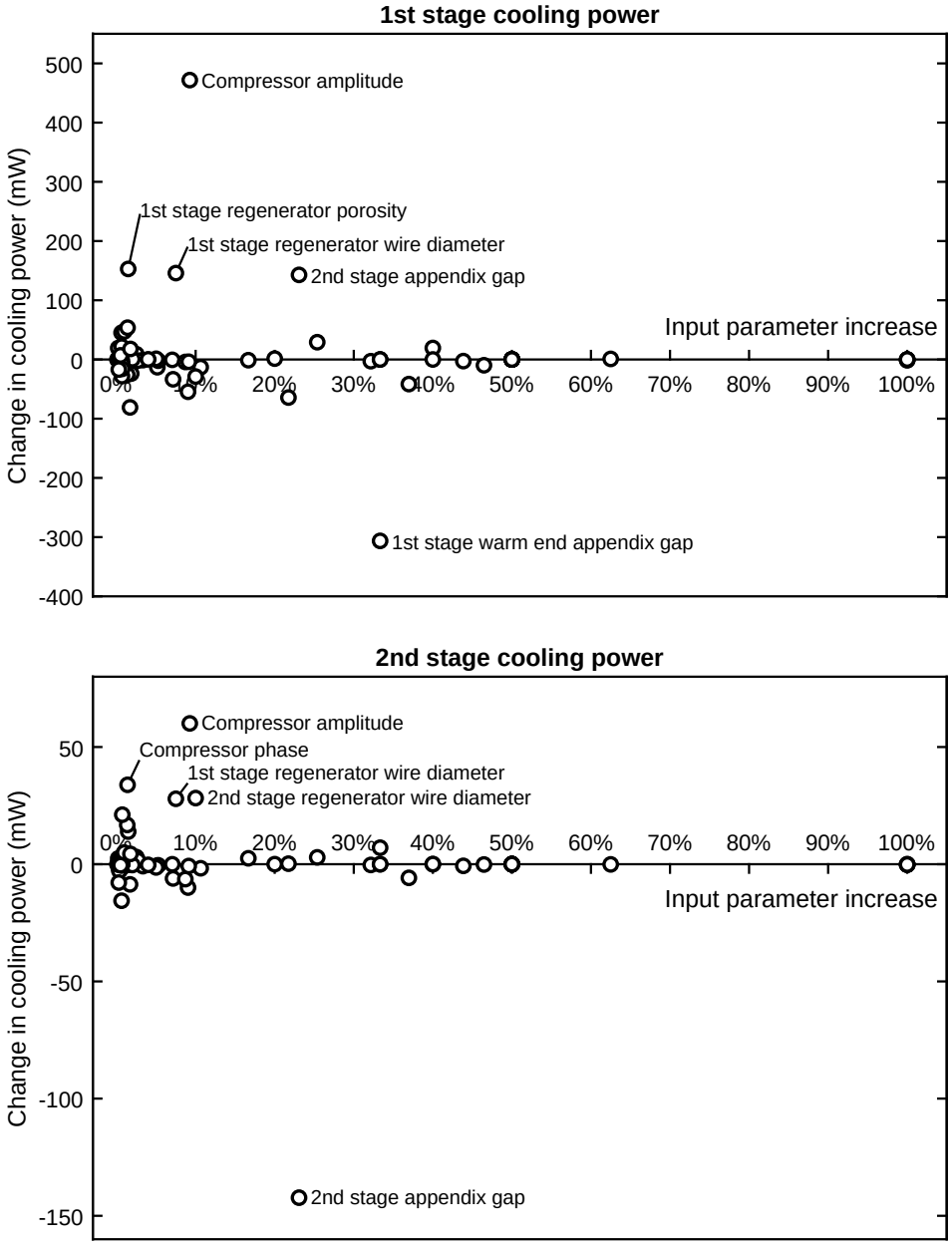

Figure 5.30: Plots of the variations in cooling powers of the Breadboard Cooler predicted by the RAL Third-Order Model when each of the inputs is increased to the upper limit of its uncertainty. The no pressure transducer, 10 bar, 1 W, 0.5 W case with both appendix gaps increased by 40% was used for the nominal inputs. The inputs that resulted in an error larger than 100 mW for the 1st stage and 25 mW for the 2nd stage are labelled.

Adding all errors in quadrature gives a total error of 642 mW for the first stage and 168 mW for the second stage. The uncertainties in the input parameters may be the cause of the errors in cooling power seen in the second column of Figure 5.26 because the errors are similar in magnitude.

Heat Transfer

A heat transfer sensitivity analysis was performed using the one-at-a-time method discussed in Section 5.1.4. The impact on the cooling power at the two stages is plotted in Figure 5.31.

It can be seen that the largest change in the first stage cooling power is caused by increasing the heat transfer in the first stage regenerator. Improved heat transfer improves the effectiveness of the regenerator. The peak Reynolds number in this region was around 25, so the error is between 10% and 50% (see Section 5.1.4). The uncertainty of the heat transfer in this region could have a large impact on the cooling power.

Modifying the heat transfer in the first stage appendix gap also results in significant change in the first stage cooling power. Increasing the heat transfer in this location increases the magnitude of the shuttle losses. As stated in Section 5.1.4, the heat transfer correlation in this region is theoretical, and the uncertainties may be large if the assumptions are incorrect.

Increasing the heat transfer in the second stage appendix gap has an impact on the cooling power at both stages. It decreases the cooling power for the first stage but increases it for the second stage. The increase in the second stage cooling power appears to be because the increased heat transfer reduces the enthalpy transport loss in the second stage appendix gap. Because this reduces the enthalpy transport between the two stages, there is a corresponding decrease in the first stage cooling power.

Friction

A friction factor sensitivity analysis was performed using the one-at-a-time method discussed in Section 5.1.4. The results are plotted in Figure 5.32.

Increasing the friction factor of the first stage regenerator has the largest impact on the cooling power for both stages. This is due to the large pressure

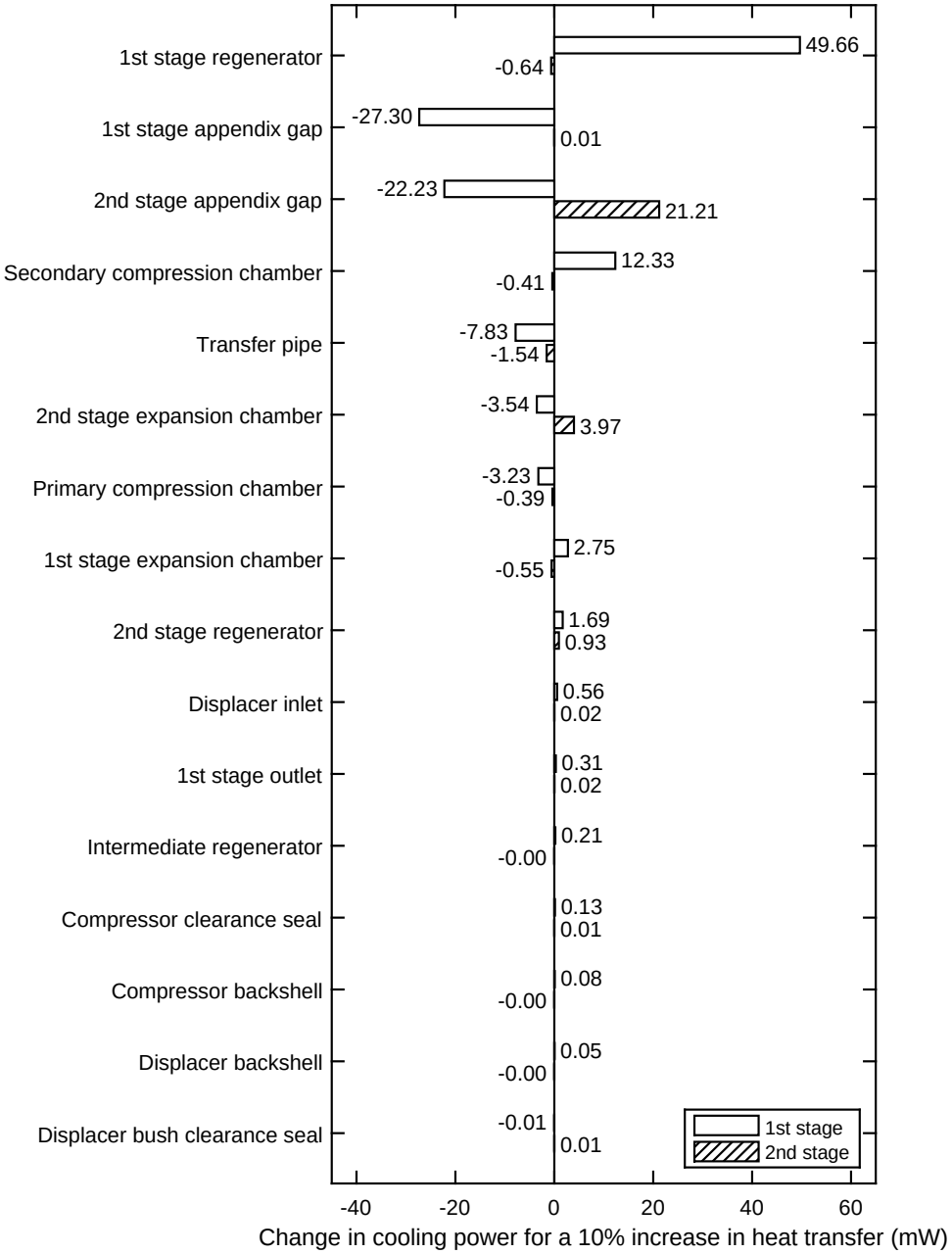

Figure 5.31: A plot of the variations in cooling powers predicted by the RAL Third-Order Model for the Breadboard Cooler when the heat transfer coefficients in each region are increased by 10%. The simulated case is the no pressure transducer, 10 bar, 1 W, 0.5 W case with both appendix gaps increased by 40%.

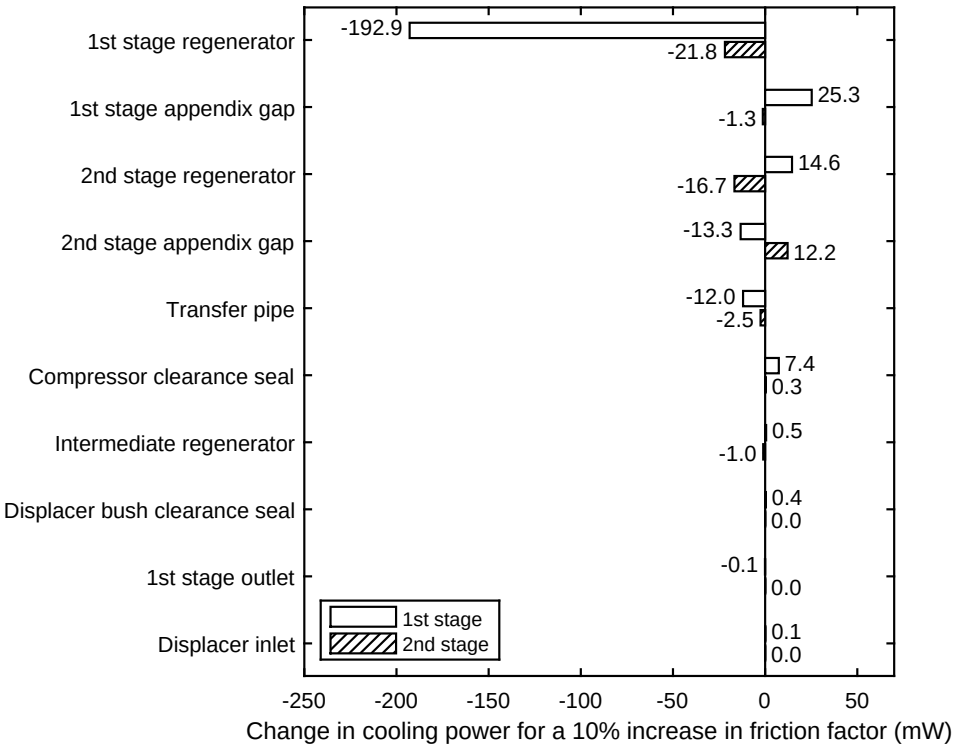

Figure 5.32: A plot of the variations in cooling powers predicted by the RAL Third-Order Model for the Breadboard Cooler when the friction factors in each region are increased by 10%. The simulated case is the no pressure transducer, 10 bar, 1 W, 0.5 W case with both appendix gaps increased by 40%.

drop in this region, as shown in Figure 5.29. The uncertainty of the friction factor correlation in this region is estimated to be around 10% (see Section 5.1.4); however, errors in this correlation would manifest themselves as errors in the pressure drops, which are not apparent in Figure 5.29.

5.4 Clearance Seal Measurements

The validation of the model against measurements of the Small Scale Cooler and the Breadboard Cooler suggest that the accuracy of the model can be improved by applying a calibration factor to any clearance seal gap sizes that have been measured directly. It is hypothesised that the calibration factor is required because the real flow through clearance seals is larger than is predicted by theory if the measured gap size is used.

Measurements of clearance seal geometries and flow through the seals have been taken by other researchers at RAL; this data has been used to explore the hypothesis that the flow through clearance seals is larger than predicted by the equations used in the RAL Third-Order Model.

5.4.1 Theoretical Clearance Seal Flow

The flow through a clearance seal can be calculated theoretically by assuming that the flow can be approximated as laminar flow between two parallel plates. It is reasonable to assume that the walls of the seal are parallel rather than forming an annulus because the gap between them is around 1000 times smaller than the diameter. The flow is laminar in all the seals studied in this work; the Reynolds number is low because the hydraulic diameter of the seal is so small.

The volumetric flow $\dot{V}$ per unit width z between two parallel plates of length x and separation a depends on the pressure differential ΔP and the dynamic viscosity of the fluid μ [93, p. 10-1].

$$\frac{\dot{V}}{z} = \frac{\Delta P\, a^3}{12 \mu x} \tag{5.6}$$

For a clearance seal of a piston with diameter d, the volumetric flow can be found by substituting the perimeter of the piston πd for z.

$$\dot{V} = \frac{\Delta P\, \pi d a^3}{12 \mu x} \tag{5.7}$$

Equation 5.7 assumes that the size of the clearance seal gap is uniform. If the piston is not perfectly aligned in the bore, the gap size will be different at different locations around the piston, as shown in Figure 5.33. The eccentricity ε of the piston in the bore is defined by Equation 5.8.

$$\varepsilon = \frac{a_{max} - a_0}{a_0} \tag{5.8}$$

If the eccentricity is greater than 0, the gap size is a function of θ.

$$a(\theta) = a_0 \left(1 + \varepsilon \cos\theta\right) \tag{5.9}$$

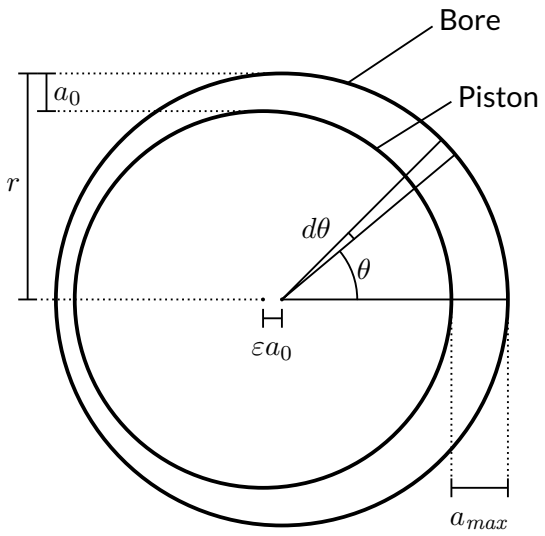

Figure 5.33: A diagram showing a clearance seal consisting of an eccentric piston in a bore.

The total flow through a clearance seal with an eccentric piston can be found by integrating the flow around the seal. By starting with Equation 5.6, substituting the arc length $r\,d\theta$ for z and using Equation 5.9 for the gap size, the total volumetric flow can be calculated.

$$\dot{V} = \int_0^{2\pi} \frac{\Delta P}{12\mu x} a(\theta)^3 r\,d\theta \tag{5.10a}$$

$$= \frac{\Delta P\, r}{12\mu x} \int_0^{2\pi} \left(a_0\left(1+\varepsilon\cos\theta\right)\right)^3\,d\theta \tag{5.10b}$$

$$= \frac{\Delta P\, r}{12\mu x} 2\pi a_0^3 (1.5\varepsilon^2+1) \tag{5.10c}$$

$$= \frac{\Delta P\, \pi d a_0^3}{12\mu x} (1.5\varepsilon^2+1) \tag{5.10d}$$

The clearance seal friction factor correlation used by the RAL Third-Order Model (Equation 3.82) results in the same relationship between flow rate and pressure drop as given by Equation 5.10. Therefore, Equation 5.10 can be rearranged to find the clearance seal gap required by the model so that the modelled seal leakage will match the leakage measured by a flow test. The same eccentricity that is used when calculating the gap size must be used as a model input. This approach was used for the displacer shaft seal of the Small Scale Cooler, the compressor piston and displacer shaft seals of the CryoBlue Cooler and the compressor piston and displacer shaft seals of the Breadboard Cooler.

5.4.2 Ariel Clearance Seal Measurements

Characterisation measurements have been performed on the piston seals of the Ariel compressor by other researchers at RAL. This compressor is a prototype of the one that will be used to circulate neon in the Joule-Thomson cooler of the ESA Ariel space mission [94]. The compressor has two compression stages, each using a piston of a different diameter. The Joule-Thomson compressors developed at RAL use the same flexure bearing and clearance seal technology as the RAL Stirling compressors.

Measurements of the pistons and the bores were taken using a coordinate measuring machine before they were assembled. The mean clearance seal gap was calculated from these measurements by fitting theoretical cylinders to the piston and bore by using the least-squares method and then subtracting the radii of these cylinders. These measured gaps are presented in Table 5.2.

Flow measurements were taken for both clearance seals. Helium gas at above atmospheric pressure was applied to one side of the seal with the other side at atmospheric pressure. The gas flow was measured using a thermal mass flow meter. The flow rate was measured at three different pressures in both directions for each seal. The mass flow was converted to a mean volumetric flow for comparison with the theoretical model. This was done by dividing the mass flow by the average of the gas density at either side of the seal, calculated from pressure and temperature measurements. The results are plotted in Figure 5.34.

The eccentricity of the pistons in the bores is difficult to quantify. The plastic pistons had been aligned by heating them until the thermal expansion caused them to grip the bore. They were then glued to the shaft so that they remained centred when they cooled back down. It was not possible to measure the alignment directly, but, by applying a sinusoidal current to the motor and

Table 5.2: A table showing the measured gap sizes of the Ariel compressor piston clearance seals and the gap increases required to fit the modelled flow resistances to the measured values.

	Measured mean gap (μm)	Assumed Eccentricity	Required gap increase
Piston 1	10.8	0	41.8%
Piston 2	11.4	0	41.7%

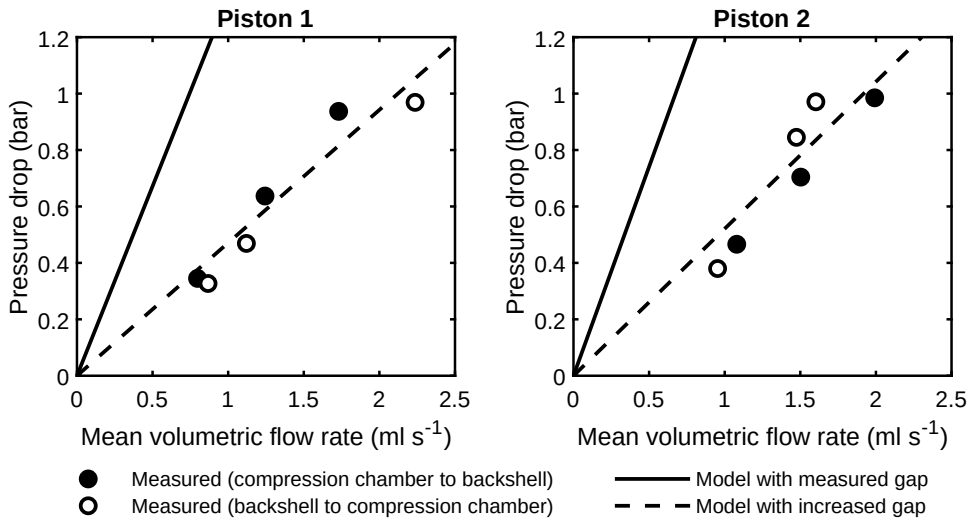

Figure 5.34: Plots showing the flow resistance measurements of the Ariel compressor piston clearance seals. The modelled relationships between pressure drop and flow rate are also plotted for the measured and increased gap sizes.

looking for hysteresis in the position waveform, the friction between the pistons and the bore could be quantified. No friction was measured at any point in the strokes of the two motors, so it was assumed that the pistons were centred in the bores with 0 eccentricity.

The flow measurements can be compared to the flow predicted by Equation 5.10. The predicted relationship between pressure drop and flow rate is shown by the solid line in Figure 5.34. It can be seen that this greatly overestimates the pressure drop. The gaps were increased by a scale factor to fit the theoretical flow resistance to the measured values, as shown by the dashed line in Figure 5.34. The required increases in the gaps are presented in Table 5.2. It is not clear why the theoretical model does not accurately predict the relationship between pressure drop and flow rate; this is discussed further in Section 5.5.1.

5.5 Summary of the Model Validation

The results presented in this section show that the RAL Third-Order Model can accurately simulate many aspects of Stirling coolers. There is good agreement between the modelled and measured data for the static losses and dynamic losses of the Small Scale Cooler; the cooling powers, pressure

waveforms and displacer forces of the CryoBlue Cooler; and the pressure waveforms of the Breadboard Cooler.

5.5.1 Clearance Seal Correlations

It appears that the clearance seal flow correlation used by the model is wrong. The cooling power predictions of the model can be improved by using clearance seal gap sizes that are larger than the measured gaps. Using a calibration factor of 50% gave the closest results for the Small Scale Cooler and a factor of 40% gave the closest results for the Breadboard Cooler.

The calibration factors required by the model to match the cooling powers are very similar to the calibration factors required by the Ariel compressor pistons to match the theoretical prediction to the measured values, as can be seen in Table 5.3. This provides evidence that the flow resistance of clearance seals is lower than is predicted theoretically.

One significant difference between the clearance seals simulated by the model and the clearance seals of the Ariel compressor pistons is the assumed eccentricity. For the Ariel pistons, no rubbing between the pistons and bores was observed, so the eccentricity was assumed to be 0. For all the seals

Table 5.3: A table showing the measured dimensions of the clearance seals simulated by the model where the flow resistance had not been measured. The table also shows the gap increase required to fit the modelled cooling power to the measured value for cases where the cooling power was strongly influenced by the gap size. These clearance seals are compared to the piston clearance seals of the Ariel compressor, presented in Table 5.2.

Cooler	Location	Measured gap (μm)	Assumed eccentricity	Required gap increase
Ariel	Piston 1	10.8	0	41.8%*
	Piston 2	11.4	0	41.7%*
Small Scale	Compressor	11.8	1	50%†
	Appendix	11.5–43.1	1	Unknown
CryoBlue	Appendix	12–65	1	Unknown
Breadboard	1st appendix	15–230	1	40%†
	2nd appendix	93.0	1	40%†

* To fit the theoretical clearance seal model to the measured flow data.
† To fit the RAL Third-Order Model to the measured cooling power.

simulated by the model where the gaps had not been calculated using flow measurements, rubbing had been detected during their characterisation tests and an eccentricity of 1 was assumed. The eccentricity has a large impact on the flow resistance. If an eccentricity of 1 is assumed for the Ariel pistons, the required gap increases drop to around 5%. It is probably fair to assume that the eccentricity of the Ariel pistons is significantly less than 1 because no rubbing was observed at any point during the characterisation tests.

It is unclear what is causing the increased flow compared to the theoretical flow. For the Small Scale Cooler compressor piston seals and the Breadboard Cooler appendix gap seals, it could be caused by inaccurate thermal expansion coefficients for the plastic pistons and displacer. If these coefficients were incorrect, the gap sizes calculated for use in the model would be wrong. However, any inaccuracies in thermal expansion coefficients would not impact the Ariel results because the geometry measurements and flow tests for these pistons were performed at the same temperature.

Another possible cause is that the pistons, displacer tubes and the bores are not perfectly cylindrical: their cross sections will not be perfectly circular, their diameters will vary along their length, their axes will not be perfectly straight and their surfaces will not be perfectly smooth. This deviation from a perfect cylinder is often significant when compared to the radial gap size. The mean diameters of the cylinders were used by the RAL Third-Order Model and the theoretical flow model, but this may be an unfair approximation. The deviation from a true cylinder will result in variations in the clearance seal gap size and this may have a significant impact on the flow rate.

Dynamic effects may also have an impact on the flow rate. The axis of motion of a piston or displacer may not be aligned with the bore which would cause a variation in the eccentricity over the stroke. However, this would not explain the increased flow in the Small Scale Cooler and the Breadboard Cooler because the model already assumed full eccentricity for these cases. It would also not explain the increased flow seen in the Ariel measurements because the pistons were stationary. A dynamic effect that could explain the increased flow is off-axis vibration of the piston or displacer in the bore caused by the flow of gas past it. This could potentially affect the rate of gas flow, although it is not clear whether this type of vibration occurs and, if it does, whether it would cause the flow to increase or decrease.

If the leakage of a clearance seal has been measured by using a flow test, this measured leakage can be used to calibrate the clearance seal gap used by the model. This technique was used for compressor piston and displacer shaft seals of the CryoBlue Cooler and resulted in accurate cooling power predictions (6% error for the 72 K case). This suggests that, although the simulation of the flow through clearance seals requires improvement, the rest of the model performs well.

5.5.2 Comparison with Sage

The RAL Third-Order Model predicts the cooling power for the Small Scale Cooler with a similar accuracy to Sage. Sage also overpredicts the cooling power by a similar amount when the nominal clearance seals are used. The sum of the losses is broadly the same for the two models, although the magnitudes of some of the individual losses are different. The results of the RAL Third-Order Model indicate that there is significant coupling between some of the loss mechanisms, particularly the regenerator enthalpy transport and the appendix gap enthalpy transport. This occurs because both flow paths can transfer heat with the displacer tube. Sage cannot accurately simulate heat transfer with the displacer tube because it models the displacer tube and cold finger tube as a single object [5, p. 124].

5.5.3 Uncertainty and Sensitivity Analyses

The uncertainty and sensitivity analyses performed for the Small Scale Cooler and the Breadboard Cooler highlight how the accuracy of the input parameters and the empirical correlations affect the results. For both coolers, it was found that accurately knowing the amplitudes of the compressor pistons is very important when simulating the coolers. Installing position sensors on future RAL coolers would be very useful for further validating the model. The sensitivity analyses also showed the importance of the heat transfer and friction factor correlations for the regenerator. It is important that these are known accurately so that the pressure drop and regenerator effectiveness can be simulated correctly.

The uncertainty and sensitivity analyses for the Small Scale Cooler and Breadboard Cooler did not give similar results for all the parameters and correlations. The results show that the uncertainty in the compressor piston

clearance seal gap sizes has a much larger impact on the cooling power in the Small Scale Cooler than the Breadboard Cooler. This may be because the Small Scale Cooler has a much smaller working volume, so any leakage has a larger effect on the pressure swing. The uncertainty in the appendix gap sizes has a larger impact on the cooling power for the Breadboard Cooler than for the Small Scale Cooler. This is because the appendix gap enthalpy transport was the dominant loss mechanism for the second stage of the Breadboard Cooler. The uncertainty in these input parameters could be reduced by performing flow measurements on the seals rather than just measuring their geometry.

The results of the uncertainty analyses showed that it may be possible to significantly increase cooling powers by minimising the leakage through clearance seals. In the current generation of RAL coolers, the compressor pistons are made of plastic and the bores are made of metal. This means that there must be a significant gap between the piston and bore so that it does not seize when the compressor gets hot and the piston expands. The appendix gap size is mainly affected by the amount that the plastic displacer tube shrinks when it cools down. This is not a significant issue for the first stage of a Stirling cooler because there will still be a good gas seal at the warm end. However, it becomes an issue for second stages because the displacer tube is cool along its entire length. The gap sizes of the compressor pistons seals and appendix gaps could potentially be reduced by using piston and displacer tube materials that have similar coefficients of thermal expansion to the bore and cold finger tube; however, this would make it difficult to align the piston or displacer by using heat (as described in Section 4.2.2).

Chapter 6

Model Applications

The key advantage of the RAL Third-Order Model over other third-order models, such as Sage, is that it simulates the geometry of the cold finger in a way that is more representative of the cold finger of a real cooler. The RAL Third-Order Model simulates the interactions between all the solid and gas regions of the cold finger and also simulates the motion of the displacer. In this chapter, the impact of three aspects of cold finger geometry are investigated: tapering of the appendix gap, overlap between the regenerator and the cold tip and overlap between the regenerator and the cold head body. All these aspects are difficult to simulate accurately with Sage but have all been found to have an impact on the predicted cooling power.

6.1 Appendix Gap Geometry

The RAL Third-Order Model can simulate coolers with a tapered appendix gap, where the size of the appendix gap varies along the length of the cold finger (as shown in Figure 6.1). This is often the case for coolers built at RAL; the displacer tube is typically made from plastic which shrinks more than the metal cold finger tube when cooled, increasing the gap at the cold end. Sage is only able to simulate appendix gaps of a constant size; it is possible to link multiple appendix gaps of different sizes together, but a smooth taper cannot be achieved.

Another key advantage of the RAL Third-Order Model is that it can simulate the interaction of the loss mechanisms within the appendix gap. This is because the model simulates the shuttle losses as part of the thermodynamic simulation (see Section 3.7). Sage calculates the shuttle losses separately from the thermodynamic cycle, so they do not interact with the other loss mechanisms.

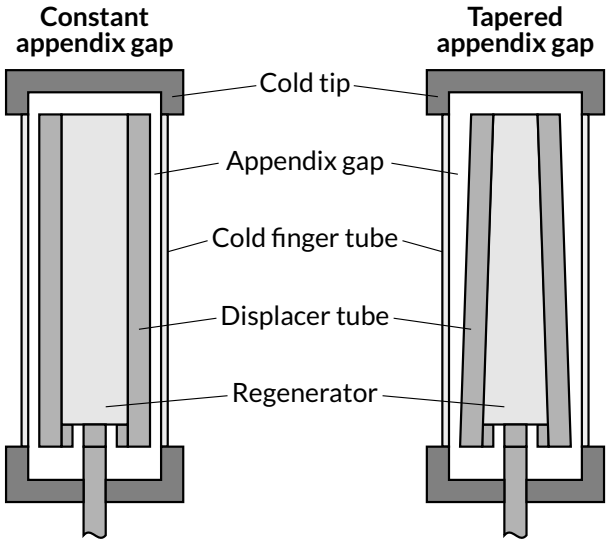

Figure 6.1: Diagrams depicting an appendix gap of a constant size and a tapered appendix gap. The size of the appendix gap is exaggerated.

6.1.1 Modelled Cases

The RAL Third-Order Model was used to investigate the relationship between cooling power and appendix gap size for constant and tapered appendix gaps. The nominal case that was selected was the 78 K case of the 2018 Small Scale Cooler. The calibration discussed in Section 5.1.6 was applied, increasing the size of the compressor clearance seals and the size of the appendix gap at both ends by 50%. In this nominal configuration, the appendix gap is tapered with a radial clearance of 17.3 µm at the warm end and 64.7 µm at the cold end. The displacer was assumed to be fully eccentric in the cold finger tube. For the tapered appendix gap cases, the gradient of the taper was fixed and the gap at both ends was changed by the same amount. These cases were then repeated with a constant appendix gap that was set to be the mean gap of the tapered cases.

6.1.2 Results

The results are plotted in Figure 6.2. At the nominal mean appendix gap size, the model predicts that a tapered appendix gap gives 88 mW more cooling power than a constant appendix gap. The peak cooling power of the tapered gap occurs at a greater mean gap width than for the constant appendix gap.

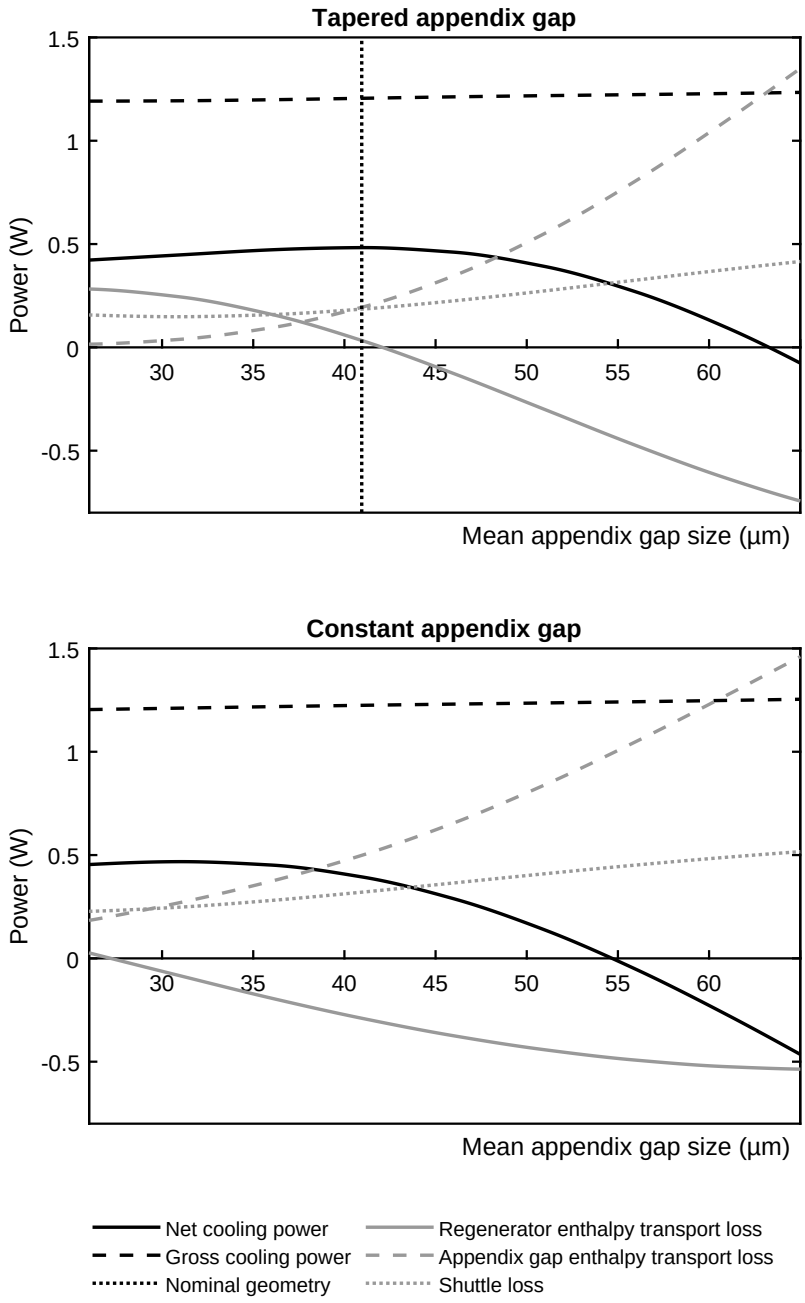

Figure 6.2: Plots of the cooling power predicted by the RAL Third-Order Model for tapered and constant appendix gaps of different mean sizes. The nominal case is the 78 K case of the 2018 Small Scale Cooler with the clearance seal calibration applied. The vertical dotted line in the tapered appendix gap plot represents the nominal geometry. The plots also show how the gross cooling power and three of the loss mechanisms are affected by changing the mean gap size. The other loss mechanisms are not plotted as they do not vary significantly when the appendix gap is adjusted.

These differences in cooling power can be explained by looking at the individual loss mechanisms. The plots show that the tapered appendix gap keeps the appendix gap enthalpy transport losses lower than when the appendix gap is constant. This is because the tapered gap reduces the flow along the appendix gap by creating a restriction at the warm end. This reduced flow causes the peak cooling power to occur at a larger gap size. As the appendix gap gets wider, the appendix gap enthalpy transport becomes the dominant loss mechanism for both appendix gap geometries.

Plotting the individual loss mechanisms provides further evidence of the interactions between them that were seen in Chapter 5. As the gap size is increased, the enthalpy transport in the appendix gap increases and the enthalpy transport in the regenerator decreases. This decrease can partly be explained by the increased volumetric flow in the appendix gap, as shown in Figure 6.3. However, this cannot be the only reason for the change in regenerator enthalpy transport. For the 56 µm tapered gap case, the

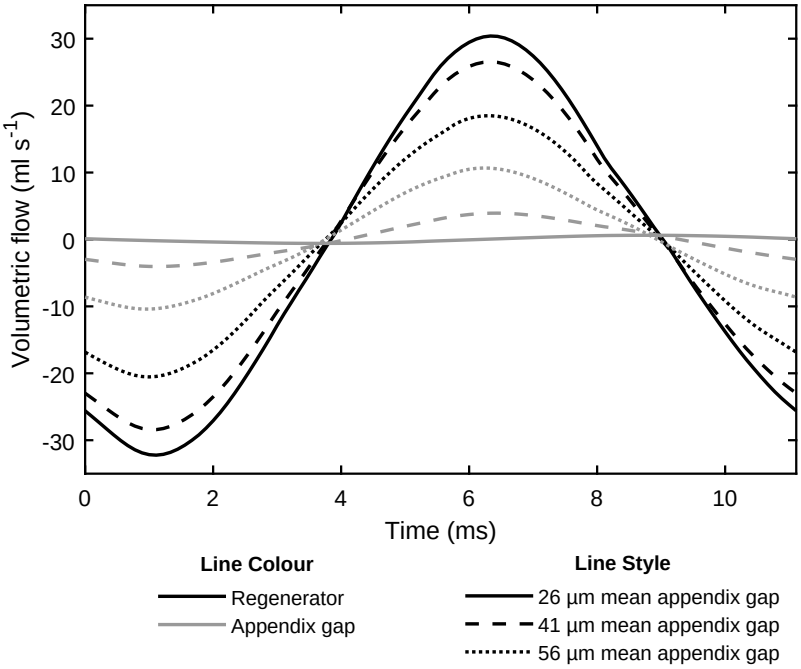

Figure 6.3: A plot showing the volumetric flow predicted by the RAL Third-Order Model for three different sizes of tapered appendix gap. The 41 µm case is the 78 K case of the 2018 Small Scale Cooler with the clearance seal calibration applied. The plotted volumetric flows are at the midpoint of the regenerator and the midpoint of the appendix gap (the 30th cell of 60).

regenerator enthalpy transport loss is negative even though there is still significant flow through the regenerator. This can occur because the model simulates the conduction of heat through the displacer tube, between the gas in the regenerator and the appendix gap.

Increasing the gap size also results in an increase in the shuttle losses. This is surprising as the analytical equation derived by Zimmerman [42] predicts that the shuttle losses would decrease with increasing gap size because the conduction path across the gap is longer. The increase in the shuttle losses appears to be caused by the increased flow of the gas in the appendix gap.

6.2 Cold Tip and Regenerator Overlap

The RAL Third-Order Model simulates the motion of the displacer by using a moving mesh. The moving mesh allows the model to simulate the flow of heat from the gas in the regenerator, across the displacer tube and appendix gap to the static parts of the cold finger. Depending on the position of each displacer cell, the heat may be transferred to the body of the cold head, to a cold finger tube or to a cold tip (see Section 3.7).

Simulating the displacer motion in this way allows the model to predict how changing the geometry of the static parts of the cold finger will affect the cooling power. For example, if the cold tip is made longer, it can be made to overlap the mean position of the cold end of the regenerator, as shown in Figure 6.4. Increasing the overlap provides more surface area for the heat

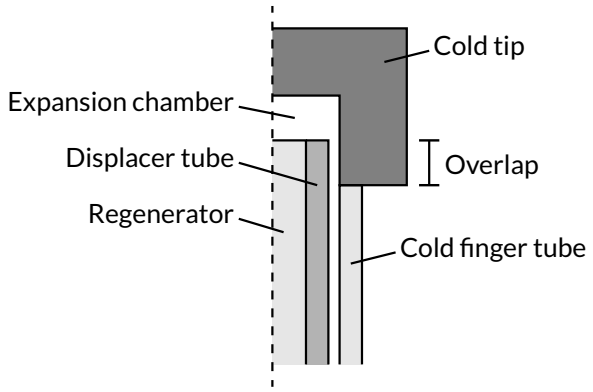

Figure 6.4: A diagram showing the cold tip and regenerator overlap. The dashed vertical line represents the axis of symmetry. The mean overlap is when the displacer is at the midpoint of its motion.

transfer to occur, which should reduce the temperature difference between the gas and the cold tip, improving the cooling power. However, changing the overlap can also affect the alignment of the thermal gradients along the displacer and the static parts of the cold finger. The shuttle losses are increased if the gradients are not aligned. The effect of changing this overlap cannot be assessed by using a model such as Sage because it does not simulate the relative motion of the displacer and the static parts of the cold finger.

6.2.1 Modelled Cases

The RAL Third-Order Model was used to assess the impact of adjusting the cold tip mean overlap for the Small Scale Cooler. The nominal case was the 78 K case of the 2018 Small Scale Cooler with the calibration discussed in Section 5.1.6 applied. The length of the cold tip was varied to change the overlap, and the length of the cold finger tube was also varied to maintain a constant total cold finger length. The length of the displacer and the length of the expansion chamber were not changed.

6.2.2 Results

The results are plotted in Figure 6.5. They indicate that an improvement in cooling power of around 40 mW can be made by adjusting the mean overlap between the cold tip and the regenerator. For the Small Scale Cooler, the cooling power is maximised when the overlap is approximately zero. This is because the temperature profile of the regenerator and the cold finger tube would both be approximately linear if they did not interact with each other. Setting the overlap to zero aligns these temperature profiles and minimises the shuttle losses.

Figure 6.6 shows the temperature profile of the regenerator for two different overlaps and helps to explain the change in the shuttle losses. It can be seen that the regenerator temperature profile is very non-linear when there is an 8 mm overlap. This is because the heat in the gas at the cold end of the regenerator is being conducted through the displacer wall and across the appendix gap to the cold tip. This appears as a shuttle loss in the model, even though it is not caused by the displacer motion, because the displacer cells are on different rows to the cold tip (see Section 3.15.1).

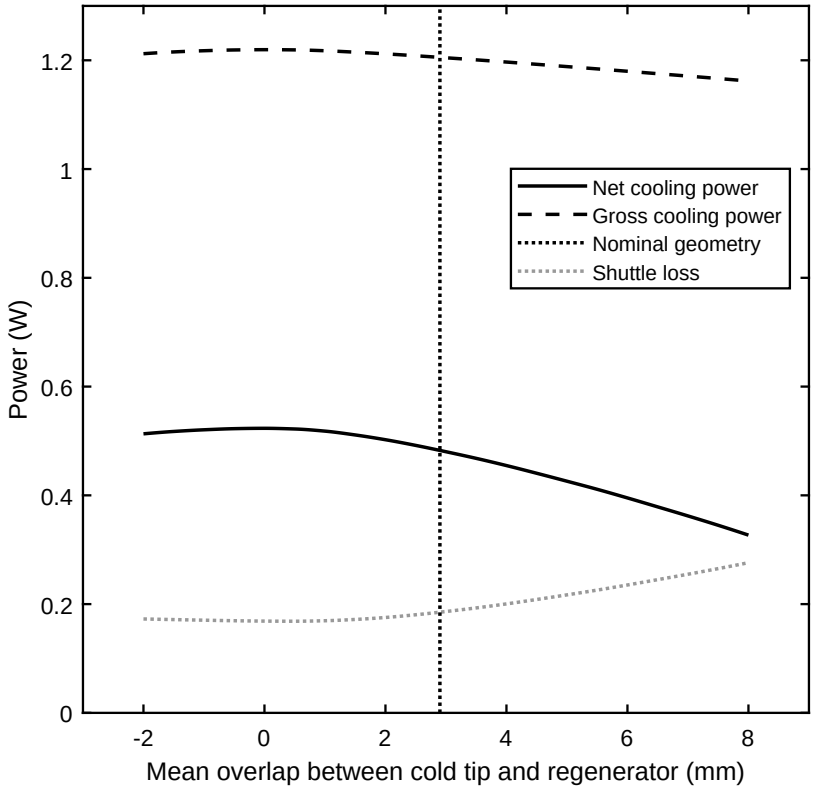

Figure 6.5: A plot of the cooling power predicted by the RAL Third-Order Model as a function of the mean overlap between the cold tip and the cold end of the regenerator. The nominal case is the 78 K case of the 2018 Small Scale Cooler with the clearance seal calibration applied. The vertical dotted line represents the nominal geometry. The plot also displays the gross cooling power and the shuttle loss. The other loss mechanisms are not plotted as they do not vary significantly when the overlap is adjusted.

Figure 6.5 shows that the gross cooling power decreases as the mean overlap increases. This can also be seen in the expansion chamber pressure-volume loops, plotted in Figure 6.7. It was found that this reduction in gross cooling power is caused by a reduction in the pressure swing. The larger mean overlap causes a larger fraction of the gas in the regenerator to be cold. When the gas is compressed and moves towards the cold end, it cools and becomes denser, reducing the system pressure. If there is more cold gas, the pressure swing is reduced. The pressure swing is also reduced in the compression chambers, so the input power is reduced by a similar proportion.

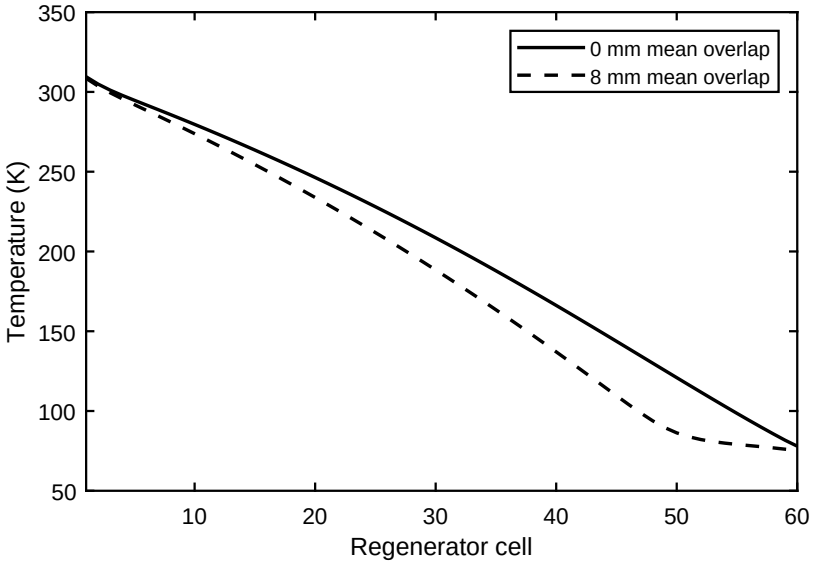

Figure 6.6: A plot showing the cycle-averaged regenerator temperature profile predicted by the RAL Third-Order Model for two different values of mean cold tip overlap. These are two of the cases that are shown in Figure 6.5.

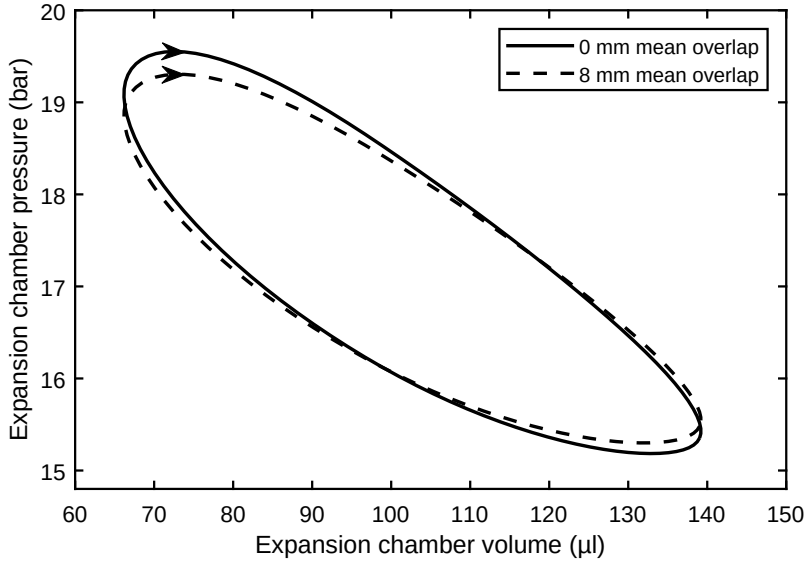

Figure 6.7: A plot of the expansion chamber pressure-volume loops predicted by the RAL Third-Order Model for two different values of mean cold tip overlap. These are two of the cases that are shown in Figure 6.5.

Zero overlap may not be optimal for all coolers. The temperature profile of the regenerator in low-temperature coolers may not be linear, even if the interaction with the static parts of the cold finger is not accounted for. This is because the material properties of the regenerator are temperature dependent which makes the regenerator less effective at the cold end. If this is the case, some cold tip overlap may improve the alignment between the temperature profiles along the displacer and the static parts of the cold finger, reducing the losses.

6.3 Cold Head Body and Regenerator Overlap

A similar analysis has been performed at the warm end of the Small Scale Cooler by adjusting the mean overlap between the cold head body and the warm end of the regenerator. This overlap is shown in Figure 6.8. The metal foam that is used to disperse the gas is not counted as part of the regenerator because it has much less surface area than the wire mesh.

6.3.1 Modelled Cases

The impact of the cold head body overlap on the cooling power was assessed in a similar way to the cold tip overlap. The same nominal case was used, and the length of the cold head body was varied to change the overlap. The cold finger tube length was adjusted to keep the overall length of the cold finger constant.

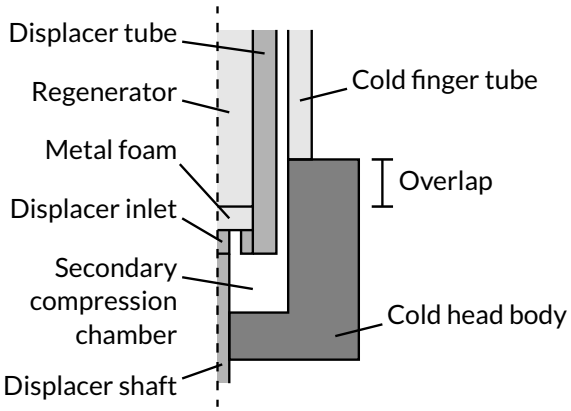

Figure 6.8: A diagram showing the cold head body and regenerator overlap. The dashed vertical line represents the axis of symmetry. The mean overlap is when the displacer is at the midpoint of its motion.

6.3.2 Results

It was found that net cooling power was not as sensitive to the cold head body overlap as it was to the cold tip overlap. This can be seen in Figure 6.9. As the overlap is increased, the shuttle losses increase but so does the gross cooling power. These partly cancel each other out, so the net cooling power is only a weak function of the overlap.

The impact of the overlap on the regenerator temperature profile and the pressure-volume loop in the expansion chamber are shown in Figures 6.10 and 6.11.

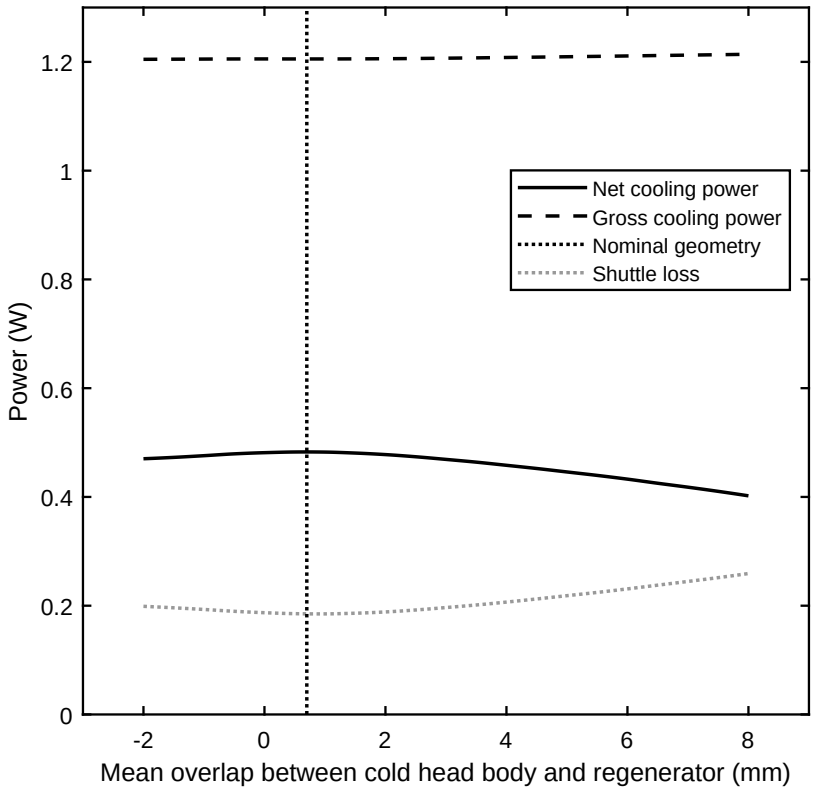

Figure 6.9: A plot of the cooling power predicted by the RAL Third-Order Model as a function of the mean overlap between the cold head body and the warm end of the regenerator. The nominal case is the 78 K case of the 2018 Small Scale Cooler with the clearance seal calibration applied. The vertical dotted line represents the nominal geometry. The plot also displays the gross cooling power and the shuttle loss. The other loss mechanisms are not plotted as they do not vary significantly when the overlap is adjusted.

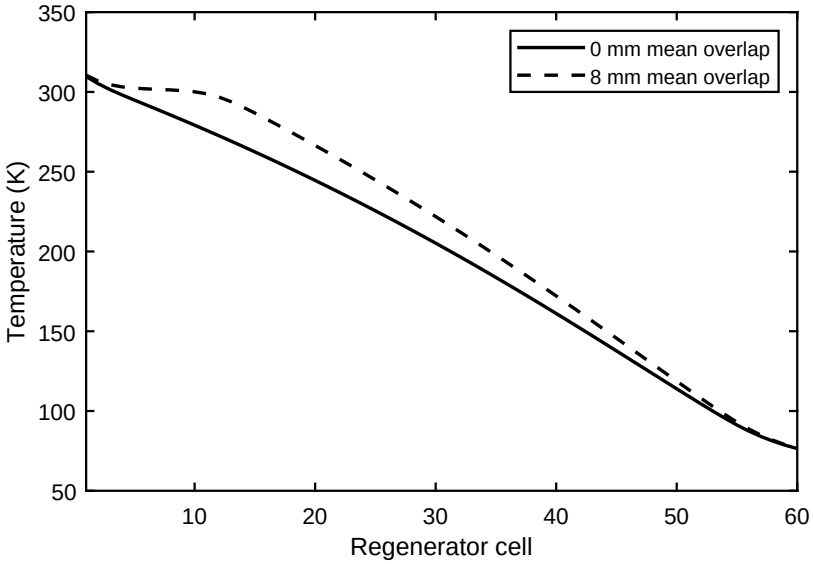

Figure 6.10: A plot showing the cycle-averaged regenerator temperature profile predicted by the RAL Third-Order Model for two different values of mean cold head body overlap. These are two of the cases that are shown in Figure 6.9.

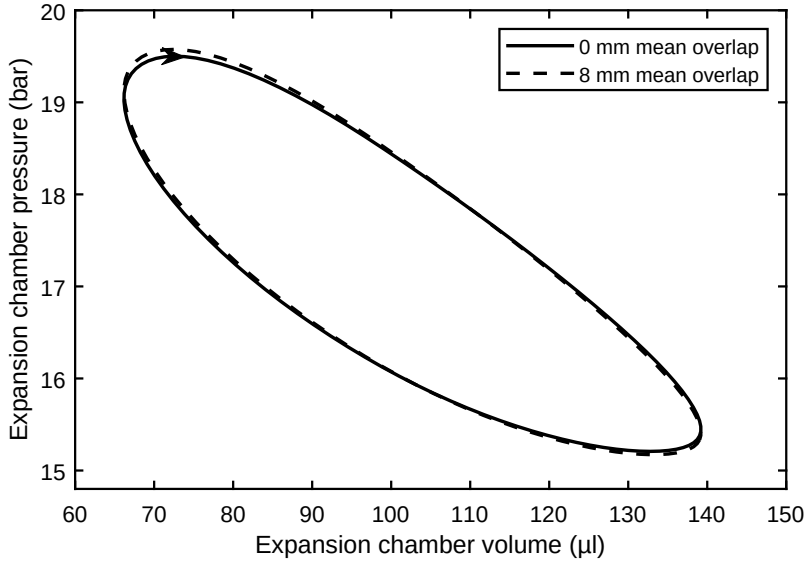

Figure 6.11: A plot of the expansion chamber pressure-volume loops predicted by the RAL Third-Order Model for two different values of mean cold head body overlap. These are two of the cases that are shown in Figure 6.9.

It does not appear that there would be much benefit in changing the cold head body overlap because the nominal geometry of the cooler is already near the optimum predicted by the RAL Third-Order Model.

6.4 Summary of Geometry Modifications

The model predictions indicate that all three geometry modifications have an impact on the cooling power and the loss mechanisms: using a constant appendix gap can greatly increase the appendix gap enthalpy transport; adjusting the cold tip and regenerator overlap affects the gross cooling power and the shuttle losses; and adjusting the cold head body and regenerator overlap also influences the shuttle losses. The RAL Third-Order Model could be used to optimise these aspects of the cold finger geometry. For the Small Scale Cooler, it appears that optimisation of the cold tip and regenerator overlap would be particularly beneficial and could lead to an increase in the cooling power of around 8%.

Chapter 7

Conclusion

A new Stirling cryocooler model, the RAL Third-Order Model, has been developed. It builds on previous models in the literature by simulating the motion of the displacer and modelling the interactions within the entire cold finger. The results of the model have been validated against cryocoolers tested at RAL.

The model meets the requirements set out in Chapter 1. It can accurately simulate the performance of a range of single and two-stage coolers, once a calibration has been applied to improve the simulation of the clearance seals, and it is able to converge quickly, thanks to a robust artificial convergence method. This combination of accuracy and speed will make it useful for designing future coolers at RAL.

7.1 Summary of Work Done

The model was developed following a review of other Stirling cooler models described in the literature. A two-stage breadboard cooler was developed to aid the model validation. The performance results from this cooler, along with results from other coolers previously developed at RAL, were used to assess different aspects of the model. The model was then used to investigate the impact of modifying the cold finger geometry of a single-stage cooler.

7.1.1 Model Development

The model can simulate single-stage and two-stage Stirling coolers. It can simulate regenerators that contain different grades of mesh along their length and can simulate different cold end heat exchanger configurations. The cold finger geometry is fully adjustable, allowing the simulation of complex

appendix gap geometries and overlaps between the displacer and the cold head body or cold tip.

The geometry of the simulated Stirling cooler is split into solid and gas cells, and the finite difference method is used to calculate the rate of change of mass, energy, momentum and turbulence for the gas cells and the rate of change of temperature for the solid cells. The model can use real or ideal equations of state to evaluate the pressures and temperatures of the gas cells.

The model uses state-of-the-art empirical correlations for gas friction factors and heat transfer. It can simulate frictional forces that are out of phase with the bulk gas velocity and heat transfer that is out of phase with the bulk temperature variation. The model can accurately model the turbulence state in pipes and variable volume regions by calculating the rates of turbulence generation and decay. A new method for modelling surface temperature fluctuations for solids of a finite thickness has been derived, and it has been implemented by adding additional cells that represent the wall surfaces. Tracking the surface temperature fluctuations improves the model's accuracy when simulating heat transfer, particularly when the solid has a low thermal conductivity or the cooler operates at a high frequency.

Different interpolation methods have been investigated, and the QUICK method was found to be the most effective of the methods investigated. This method requires the fewest cells to produce an accurate result while preventing unphysical temperature oscillations.

The model runs until it reaches a periodic steady state. It uses a novel method of converging the temperatures of the cold finger cells which combines two convergence techniques, one that works well for effective regenerators and one that is better suited to ineffective regenerators. The combination of these methods ensures that the model converges consistently for every cooler geometry and operating condition that has been tested.

The model is written in the MATLAB programming language. It takes a Microsoft Excel spreadsheet file as an input and outputs another spreadsheet file that reports key information such as the cooling power and the size of each loss mechanism. The model is also able to report the waveforms of the variables over the final cycle. The model typically converges in less than 300 cycles, which takes approximately four hours on a desktop computer. Multiple cases can be run in parallel by using MATLAB's Parallel Computing Toolbox.

7.1.2 Breadboard Cooler Development

A breadboard two-stage Stirling cooler was developed and tested, and the results were used to help validate the model. This Breadboard Cooler is larger than the two-stage coolers that have previously been built at RAL. The cooling power of the Breadboard Cooler is restricted because it uses pre-existing compressor and displacer motors that have different resonant frequencies; this means that they are unable to operate at their full strokes. Despite this, the Breadboard Cooler produced data that was very useful for validating the model, such as cooling powers and pressure measurements at both stages. The Breadboard Cooler was designed so that it is simple to modify its geometry. This will allow it to be adjusted to prototype different cooler designs in the future.

7.1.3 Model Validation

The model was validated against performance measurements of three Stirling cryocoolers that have been tested at RAL: the Small Scale Cooler, a compact single-stage cooler; the CryoBlue Cooler, a larger single-stage cooler; and the Breadboard Cooler that was developed as part of this project.

The model results closely match the measured performance results of the CryoBlue Cooler. However, the agreement was not as good for the Small Scale Cooler and the Breadboard Cooler. It is believed that this is due to inaccuracies in the clearance seal flow friction correlation. The critical clearance seals of the CryoBlue cooler had their leakage measured directly and this measured leakage was used in the model. The leakages of the critical clearance seals of the other coolers were not measured and only the geometries of the seals were measured. Using these geometries in the model appears to underpredict the leakage.

Measurements carried out by other researchers at RAL have indicated that the measured flow rate through clearance seals is often larger than predicted from their geometry alone. It was found that the model could be calibrated to agree with the results of all three coolers if the gap sizes of the clearance seals were increased. This calibration was only applied if the size of the gap had been calculated from measuring the geometry of the seal. A gap increase of 40% gave the closest predictions for the Small Scale Cooler and an increase of 50% was required for the Breadboard Cooler.

The displacer force waveform predicted by the model for the CryoBlue Cooler was compared with a force waveform that had been derived from measurements. There was good agreement between these waveforms; their amplitude, shape and phase were very similar. Accurately knowing the displacer force waveform will allow future coolers to be designed so that the displacer runs on resonance, minimising the required input power.

The predictions of the RAL Third-Order Model for the Small Scale Cooler were compared to the predictions of the commercially available Sage software. It was found that the two models gave similar predictions for the net cooling power. However, the models disagreed on the contributions of the individual loss mechanisms. This is because the RAL model can simulate interactions between the loss mechanisms that are not simulated by Sage.

7.1.4 Model Application

The RAL Third-Order Model was used to investigate modifications to the cold finger geometry of the Small Scale Cooler that would be difficult to assess with other third-order models, such as Sage. The model was used to look at how tapering the appendix gap affected the cooling power. The model predicted different optimum mean appendix gap sizes for the Small Scale Cooler depending on whether the gap was tapered or constant. The model was also used to simulate how the overlap between the regenerator and the cold tip or cold head body affected the cooling power. It was found that the cold tip overlap had a significant effect on the predicted cooling power for the Small Scale Cooler.

7.2 Key Findings

Several key findings from the model development and validation have been identified. These findings may be useful when developing other Stirling cryocooler models or designing Stirling coolers.

- The RAL Third-Order Model formulates the system as an initial value problem and lets the solution variables converge to a periodic steady state over several cycles. An alternative would have been to formulate the model so that the system of equations includes periodic boundary conditions, which is the approach used by Sage [5]. It was believed that

formulating the model as an initial value problem would make it easier to develop as it would allow the differential equations to be solved using a solver built into MATLAB. However, it was found that the main disadvantage with this approach is that it needs a complex artificial convergence method to reliably converge to a periodic steady state; this results in the model taking a significant length of time to converge. If periodic boundary conditions were included as part of the system of equations, any solution to the system of equations would be converged by definition. It is likely that this type of model would have been able to run quicker.

- The RAL Third-Order Model simulates the cold finger of the cooler as a single system and can simulate the heat transfer between the different flow paths. This allows the interactions between the loss mechanisms to be simulated, and these interactions were found to be very significant. However, the RAL Third-Order Model predicted very similar total losses to Sage for the Small Scale Cooler. It appears that the total sum of the loss mechanisms is not strongly influenced by the interactions between the mechanisms, so a model such as Sage would still be accurate enough to perform the initial optimisation of a cooler. However, the fine-tuning of the cold finger geometry discussed in Chapter 6 is only possible with the RAL Third-Order Model.
- It was found that the flow rate through clearance seals is often larger than predicted from their measured geometry alone. A gap size increase of 40-50% is required for the predicted flow to agree with flow test data. Using this calibration results in the RAL Third-Order Model giving accurate performance predictions. The leakage of some of the clearance seals of the coolers used for the model validation had been measured directly using a flow test. When this leakage was used as a model input, the model gave good cooling power predictions. This indicates that the rest of the model is working well and that the issue is limited to how the flow through the clearance seals is simulated.
- The sensitivity analysis of the Small Scale Cooler showed that the size of compressor piston clearance seal gap has a very significant effect on the cooling power. The piston clearance seal gaps of small coolers should be minimised to increase the pressure swing and the gross cooling power.

- The modelling results of the Breadboard Cooler highlighted the challenges that are present when designing long-life two-stage Stirling coolers. When the cooler is running, the entire second stage of the displacer tube is cold, and this causes it to shrink away from the cold finger tube. This increases the appendix gap along the entire length of the second stage, permitting a large amount of gas to leak past the displacer, which severely compromises the performance of the second stage. This issue could be addressed in future coolers by using a material for the displacer tube that has a similar coefficient of thermal expansion to the cold finger tube.
- The investigation of the impact of the overlap between the regenerator and the cold tip and cold head body suggests that the optimum cooling power occurs when there is approximately zero overlap at either end. This helps to keep the temperature profiles of the regenerator and cold finger tube linear, minimising the losses.

7.3 Suggestions for Future Work

The measurements presented in Section 5.4 indicate that the measured flow rate through clearance seals is often larger than predicted. This provides justification for increasing the clearance seals in the model, which improves the model's cooling power predictions. However, the measurements were only carried out for two clearance seals, there was no way of accurately determining the eccentricity and it is not clear what the physical mechanism is behind the increased flow. A study into the leakage past clearance seals would help to provide more information on what calibration factor should be used in the model. A range of different clearance seal geometries would need to be tested with a method for varying the eccentricity of the seals. In addition to physical measurements, it may be useful to model a clearance seal using 3D computational fluid dynamics software. This would allow the simulation of pistons and bores that are not perfect cylinders and would allow the impact of these imperfections to be assessed.

Appendix A

Model Details

This appendix presents further details of the RAL Third-Order Model. It shows how different cooler configurations are simulated by the model, explains how the cooler geometry is defined and lists the inputs and outputs of the model.

A.1 Alternative Cooler Configurations

The RAL Third-Order Model can simulate a variety of different cooler configurations. The configuration presented in Chapter 3 was a two-stage cooler with annular heat exchangers (see Figure 3.3); however, other configurations are possible. For example, Figure A.1 shows the cell connections of a single-stage cooler and Figure A.3 shows the cell connections of a two-stage cooler without annular heat exchangers. Figures A.2 and A.4 show the regions in the cold head that the cells correspond to.

Dedicated warm end heat exchangers are not included in the model as they are not present in any of the RAL coolers used for the model validation; all of the heat rejection in these coolers is carried out in the compression chambers and transfer lines. It would be possible to add optional warm end heat exchangers to the model if they are required.

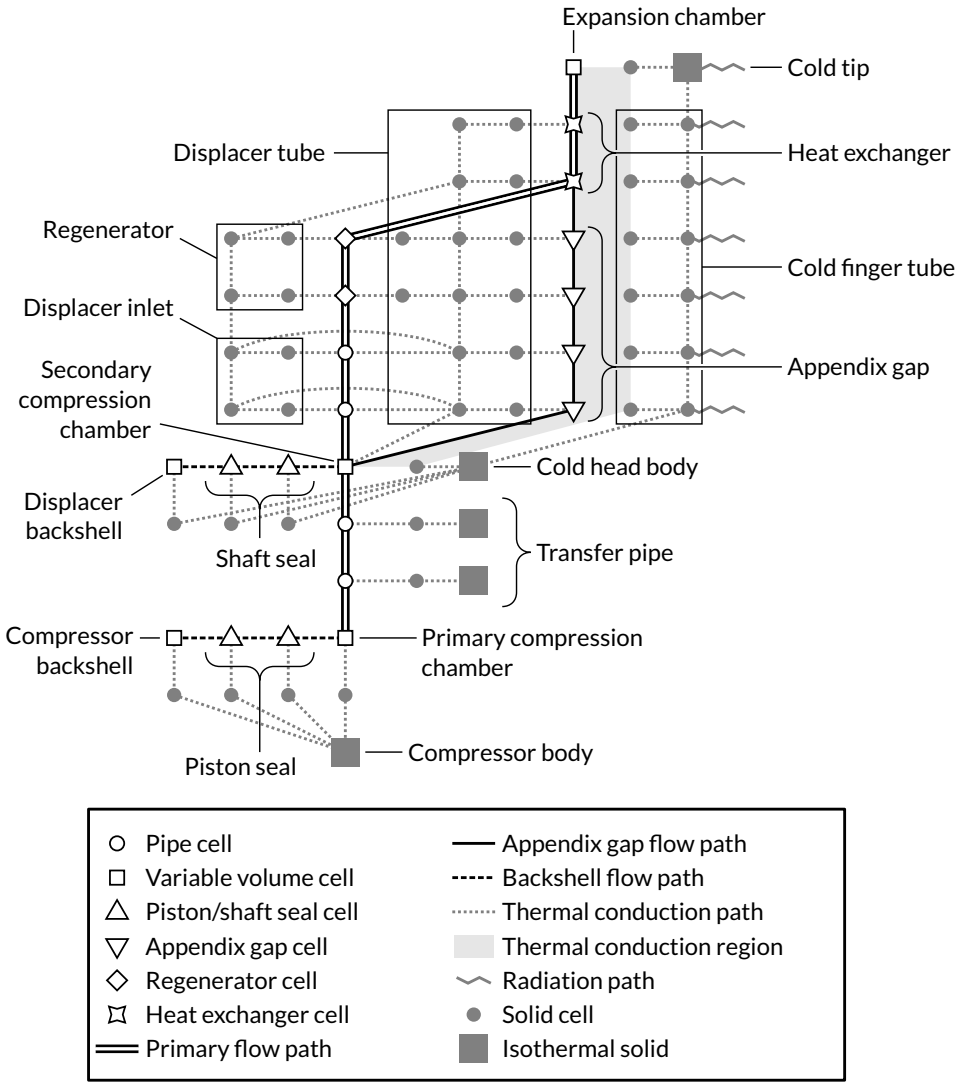

Figure A.1: A diagram showing the connections between cells when simulating a single-stage cooler with an annular heat exchanger. It is possible to adjust the spatial resolution of each section by adjusting the number of cells.

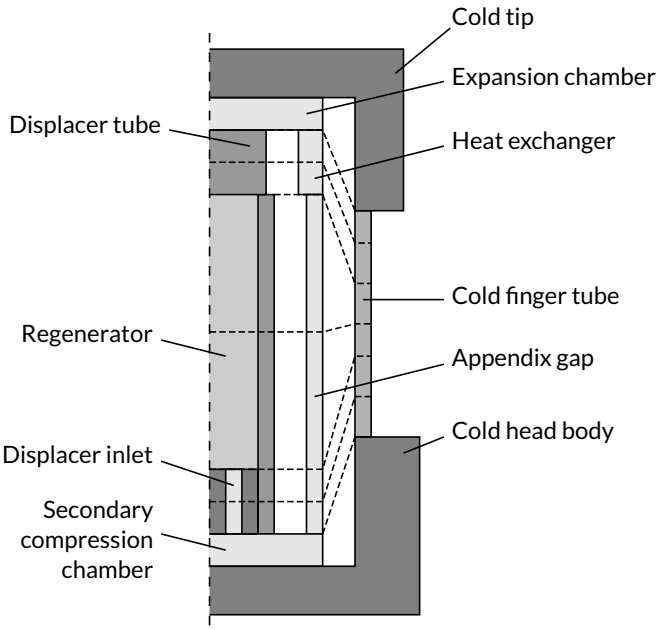

Figure A.2: A diagram showing the physical locations of the cells of a single-stage cold finger with an annular heat exchanger. This section view only shows half of the cold finger; the dashed vertical line represents the axis of symmetry. The cells of this diagram correspond to the cells of Figure A.1. The dashed lines dividing the regions show the boundaries of the cells. These lines also indicate which cells are on the same rows of Figure A.1.

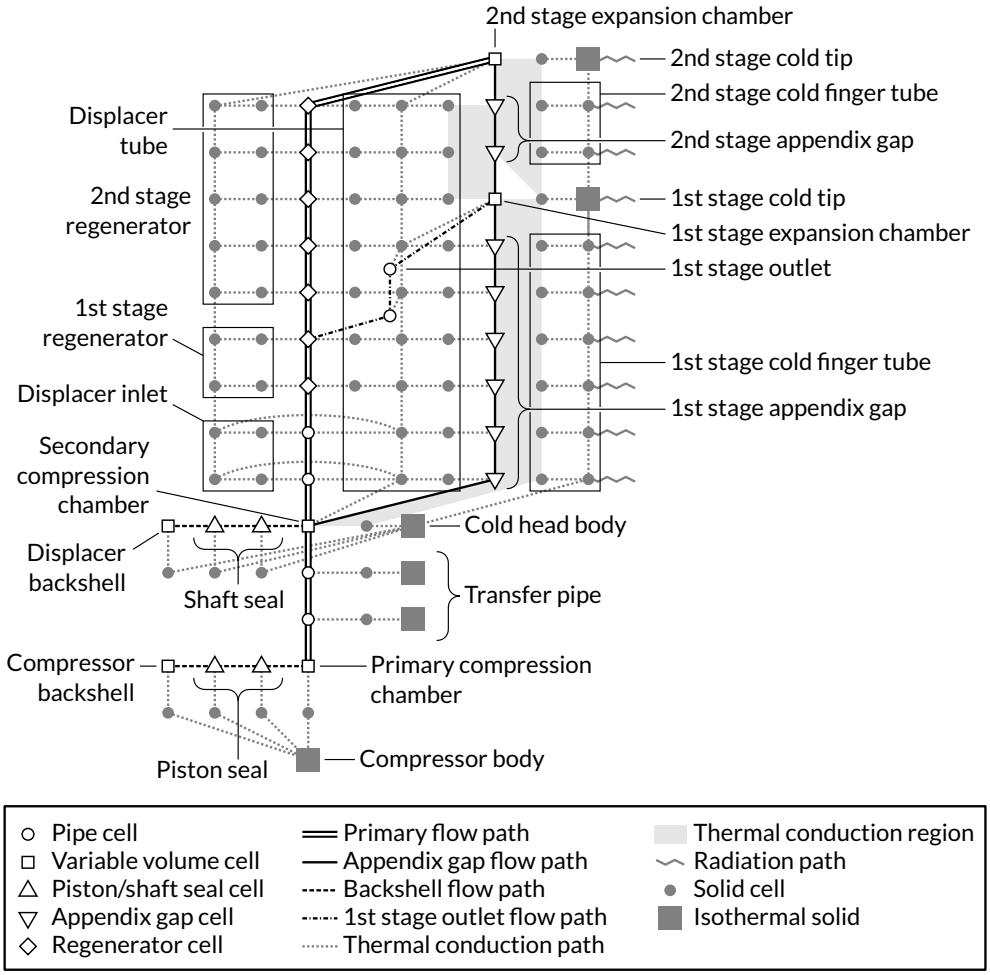

Figure A.3: A diagram showing the connections between cells when simulating a two-stage cooler without annular heat exchangers. It is possible to adjust the spatial resolution of each section by adjusting the number of cells.

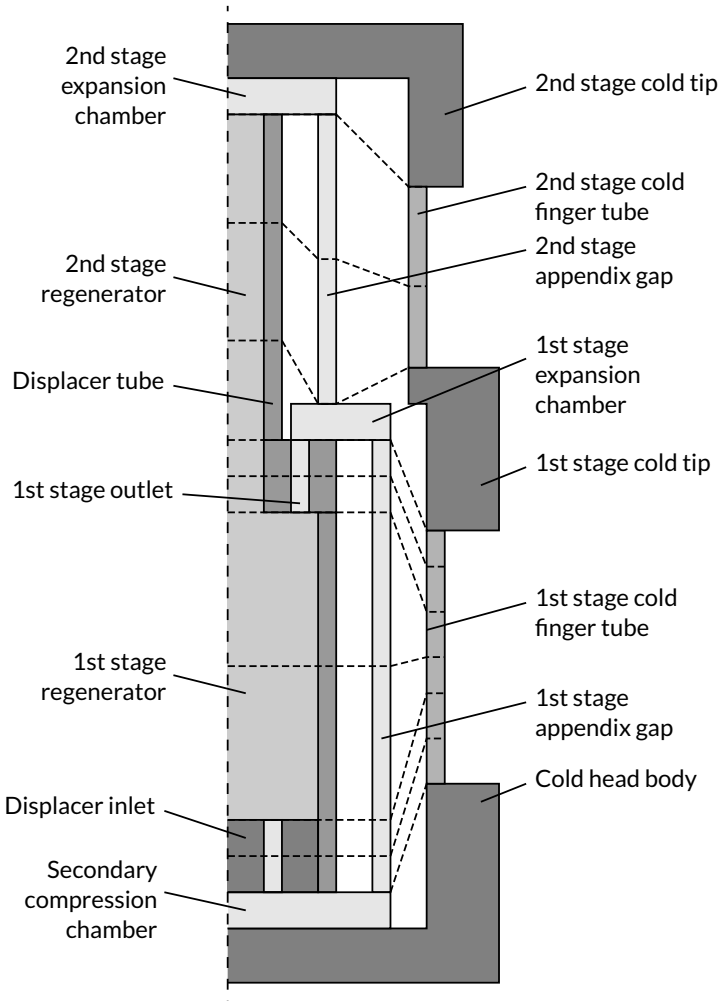

Figure A.4: A diagram showing the physical locations of the cells of a two-stage cold finger without annular heat exchangers. This section view only shows half of the cold finger; the dashed vertical line represents the axis of symmetry. The cells of this diagram correspond to the cells of Figure A.3. The dashed lines dividing the regions show the boundaries of the cells. These lines also indicate which cells are on the same rows of Figure A.3.

A.2 Cold Finger Geometry Definition

The geometry of the cold finger is modelled in full. The model input dimensions have been chosen so that the most important dimensions are the inputs, and the other dimensions are calculated from these. For example, the cold finger tube lengths and the displacer tube wall thicknesses are not defined directly but are derived from the other dimensions. The model input dimensions are shown in Figure A.5.

The model provides flexibility for defining the size of the appendix gap. The simplest option is to define a constant gap along the length. However, in some cases, the cold end of the displacer tube will shrink away from the cold finger tube when it gets cold, increasing the appendix gap at the cold end. This can be modelled by providing two gap sizes as inputs. The model will then taper the appendix gap between these two sizes and use linear interpolation to calculate the sizes of the cells in the appendix gap. There is also the option to provide the appendix gap size for the start and end of each section of the displacer. The length of the first section is defined by the length of the inlet holes and the lengths of the other sections are defined by the regenerator section lengths. Specifying the size of the appendix gap for each section individually allows for the rate of the taper to be controlled or for a stepped appendix gap to be simulated.

The size of the appendix gap can only be varied for single-stage coolers and for the first stage of a two-stage cooler. The second stage of two-stage coolers must have a constant gap. This is because the gas cells in the second stage appendix gap do not move with the displacer but move at different rates depending on their location (see Section 3.5.1). The relative motion of the displacer and gas cells would cause the cross-sectional area of the cells to vary over the cycle and increase the complexity of the simulation. The constant gap requirement is not typically an issue; both ends of the second stage are usually at cryogenic temperatures so will have undergone a similar amount of thermal contraction.

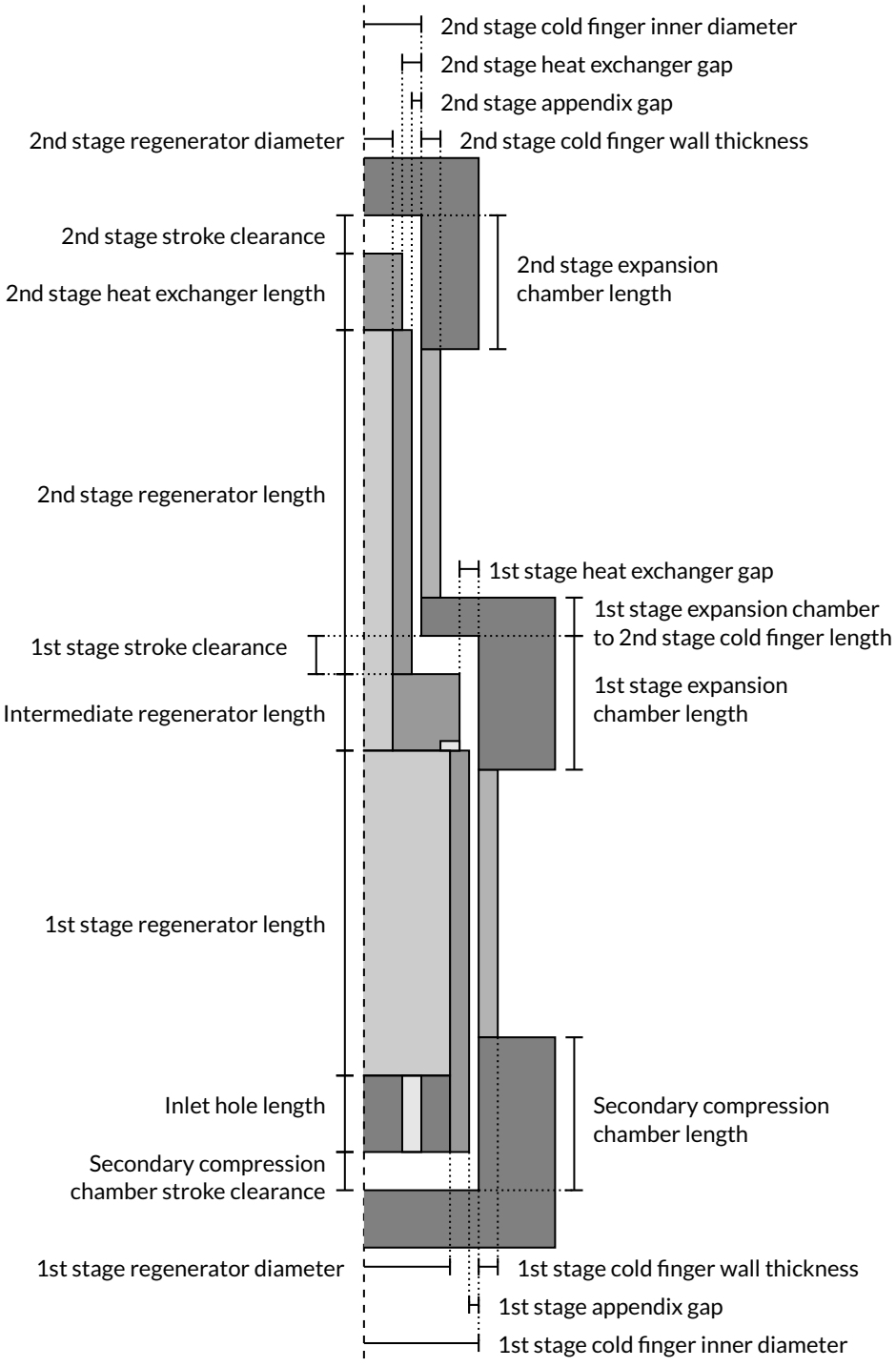

Figure A.5: A schematic showing the model input dimensions of a two-stage cold finger with annular heat exchangers. The cold finger tube lengths and displacer tube wall thicknesses are calculated from these inputs. The dashed vertical line represents the axis of symmetry.

A.3 Model Input and Output Files

The input to the model is a Microsoft Excel `.xlsx` file, with each column of the input file representing an input case. An example of the required inputs is shown in Table A.1. The output file is also an `.xlsx` file. It contains the same data as the input file but appends the outputs of the model (discussed in Section 3.15). An example of the output values reported by the model is shown in Table A.2.

Table A.1: A table showing an example of the input parameters required by the model. These input parameters are for the Breadboard Cooler with a fill pressure of 10 bar, with no cryogenic pressure transducers, and with 1 W and 0.5 W applied to the first and second stages respectively. The calibration discussed in Section 5.3.4 is applied to the appendix gaps. The precision of the input parameters presented here has been reduced and only the first three displacer position harmonics are shown.

Property	Example Input
Primary compression chamber	
Chamber material	Stainless Steel 304
Number of pistons	2
Common bore	True
Piston diameter (m)	4.83E-2
Max amplitude (m)	7.00E-3
Dead volume at max amplitude (total) (m^3)	3.32E-5
Compressor backshell	
Seal radial clearance (m)	1.94E-5
Seal length (m)	1.88E-2
Seal roughness (m)	1.60E-6
Seal eccentricity	0
Backshell material	Stainless Steel 304
Backshell volume per compressor (m^3)	1.97E-3
Transfer line	
Tube materials	Stainless Steel 304, Stainless Steel 304, Copper C103, Copper C103
Number of tubes	1, 1, 1, 1
Lengths (m)	1.96E-1, 7.00E-2, 3.30E-1, 6.70E-2
Inner diameters (m)	15.7E-3, 4.6E-3, 4.8E-3, 4.0E-3
Roughnesses (m)	8E-7, 8E-7, 8E-7, 8E-7
Secondary compression chamber	
Chamber material	Aluminium 6061-T6
Displacer shaft diameter (m)	8.69E-3
Stroke clearance from idle position (m)	4.70E-3
Dead volume when touching end (m^3)	5.41E-6

Table A.1 continued: A table showing an example of the input parameters required by the model.

Length from end stop to start of cold finger tube (m)	5.00E-4
Displacer backshell	
Seal radial clearance (m)	1.42E-5
Seal length (m)	1.70E-2
Seal roughness (m)	1.60E-6
Seal eccentricity	0
Backshell material	Titanium Ti-6Al-4V
Backshell volume (m^3)	6.22E-4
Displacer inlet	
Inlet material	Aluminium 6061-T6
Number of inlet holes	6
Hole length (m)	1.00E-2
Hole diameter (m)	8.00E-3
Hole roughness (m)	1.60E-6
Displacer tube	
Tube material	Nylon 6
1st stage inner diameter (m)	3.40E-2
1st stage regenerator	
Regenerator types	Foam, Mesh
Regenerator materials	Inconel X-750, Stainless Steel 304
Wire diameter (m) (or foam pores per inch)	80, 0.04E-3
Porosity	0.956, 0.680
Section lengths (m)	1.90E-3, 139.6E-3
1st stage appendix gap	
Radial clearances (start and end) (m)	21E-6, 322E-6
Roughness (m)	1.60E-6
Eccentricity	1
1st stage cold finger tube	
Material	Stainless Steel 304
Inner diameter (m)	3.93E-2
Wall thickness (m)	5.40E-4
1st stage MLI	
MLI along cold finger	False
MLI layers	10
MLI thickness (m)	5.0E-3
Mylar thickness (m)	6.0E-6
Aluminium coating thickness (m)	4.00E-8
2nd stage present	True

Table A.1 continued: A table showing an example of the input parameters required by the model.

1st stage outlet	
Number of outlet holes*	12
Outlet hole diameter (m)*	3.00E-3
Outlet hole length (m)*	1.00E-2
Outlet hole roughness (m)*	1.60E-6
Intermediate stage displacer inner diameter (m)*	1.40E-2
Intermediate stage regenerator	
Regenerator types*	Mesh
Regenerator materials*	Stainless Steel 304
Wire diameter (m) (or foam pores per inch)*	3.00E-5
Porosity*	0.743
Section lengths (m)*	1.00E-2
1st stage heat exchanger	
1st stage heat exchanger present*	False
Radial clearance (m)†	N/A
Roughness (m)†	N/A
1st stage expansion chamber	
Cold tip material*	Copper C103
Stroke clearance from idle position (m)*	5.75E-3
Dead volume when touching end (m^3)*	2.28E-7
Distance from end of 1st stage cold finger tube to interior face of 1st stage expansion chamber (m)*	1.40E-2
Distance from interior face of 1st stage expansion chamber to start of 2nd stage cold finger tube (m)*	1.40E-2
Cold tip external diameter (m)*	9.50E-2
2nd stage displacer inner diameter (m)*	1.40E-2
2nd stage regenerator	
Regenerator types*	Mesh
Regenerator materials*	Stainless Steel 304
Wire diameter (m) (or foam pores per inch)*	3.00E-5
Porosity*	0.743
Section lengths (m)*	1.10E-1
2nd stage appendix gap	
Radial clearance (m)*	1.30E-4
Roughness (m)*	1.60E-6
Eccentricity*	1
2nd stage cold finger tube	
Material*	Stainless Steel 304
Inner diameter (m)*	1.60E-2

Table A.1 continued: A table showing an example of the input parameters required by the model.

Wall thickness (m)*	5.00E-4
2nd stage MLI	
MLI along cold finger*	False
Radiation shield present*	True
MLI Layers*	10
MLI Thickness (m)*	5.00E-3
Mylar thickness (m)*	6.00E-6
Aluminium coating thickness (m)*	4.00E-8
Cold end outlet	
Number of outlet holes	5
Hole diameter (m)	2.50E-3
Cold end heat exchanger	
Cold end heat exchanger present	False
Length (m)‡	N/A
Radial clearance (m)‡	N/A
Roughness (m)‡	N/A
Cold end expansion chamber	
Cold tip material	Copper C103
Stroke clearance from idle position (m)	5.48E-3
Dead volume when touching end (m^3)	5.38E-7
Distance from end of cold finger tube to interior face of cold end expansion chamber (m)	0
Cold tip external diameter (m)	6.00E-2
Cold tip external length (m)	2.20E-2
Temperatures	
Radiation background (K)	2.94E+2
Primary compression chamber (K)	3.11E+2
Transfer line (K)	3.11E+2, 3.11E+2, 3.11E+2, 2.95E+2
Secondary compression chamber (K)	2.95E+2
1st stage expansion chamber (K)*	7.94E+1
Cold end expansion chamber (K)	6.95E+1
Gas properties	
Gas Type	Helium-4
Fill pressure (Pa)	1.02E+6
Fill temperature (K)	2.93E+2
Cycle properties	
Frequency (Hz)	2.00E+1
Compressor harmonic amplitudes (m)	3.24E-3
Compressor harmonic phases (°)	-174.9
Compressor offset (forwards) (m)	0

Table A.1 continued: A table showing an example of the input parameters required by the model.

Displacer harmonic amplitudes (m)	2.85E-3, 9.22E-6, 5.01E-5, …
Displacer harmonic phases (°)	-98.6, -44.7, -220.5, …
Displacer offset (towards cold tip) (m)	-1.80E-5
Number of cells in regions	
Compressor seal	2
Transfer line	1,1,6,2
Displacer shaft seal	2
Shaft holes	2
1st stage regenerator	1, 40
1st stage outlet holes†	N/A
Intermediate stage*	2
2nd stage regenerator*	40
Cold end heat exchanger‡	N/A
Heat transfer multipliers	
Primary compression chamber	1
Transfer line	1
Secondary compression chamber	1
Displacer inlet	1
1st stage regenerator	1
1st stage appendix gap	1
1st stage outlet*	1
1st stage heat exchanger†	N/A
1st stage expansion chamber*	1
Intermediate regenerator*	1
2nd stage regenerator*	1
2nd stage appendix gap*	1
Cold end heat exchanger‡	N/A
Cold end expansion chamber	1
Compressor clearance seal	1
Compressor backshell	1
Displacer shaft clearance seal	1
Displacer backshell	1
Friction factor multipliers	
Transfer line	1
Displacer inlet	1
1st stage regenerator	1
1st stage appendix gap	1
1st stage outlet*	1
1st stage heat exchanger†	N/A
Intermediate regenerator*	1
2nd stage regenerator*	1
2nd stage appendix gap*	1

Table A.1 continued: A table showing an example of the input parameters required by the model.

Cold end heat exchanger‡	N/A
Compressor clearance seal	1
Displacer shaft clearance seal	1
Model options	
Gas equations	Real
Enable complex heat transfer	True
Enable complex friction	True
Enable delayed turbulence	True
Number of outputs per cycle	100
Convergence criterion	1.00E-6
Convergence temperature cap (K)	5
Solver tolerance	1.00E-2

* These inputs are only required for two-stage coolers.

† These inputs are only required if a first stage heat exchanger is present.

‡ These inputs are only required if a cold end heat exchanger is present.

Table A.2: A table showing an example of the output values produced by the model. These output values were produced using the input parameters presented in Table A.1. The precision of the output values presented here has been reduced and only the first two harmonics are shown.

Property	Example Output
Forces	
Compressor harmonic amplitudes per piston (N)	1.64E+2, 4.08E+0, …
Compressor harmonic phases (°)	47.1, 267.3, …
Compressor mean force per piston (N)	3.01E+0
Displacer harmonic amplitudes (N)	2.92E+1, 7.61E-1, …
Displacer harmonic phases (°)	210.4, 131.3, …
Displacer mean force (N)	7.96E-1
Pressures	
Primary compression chamber harmonic amplitudes (Pa)	8.56E+4, 2.23E+3, …
Primary compression chamber harmonic phases (°)	229.3, 87.0, …
Primary compression chamber mean pressure (Pa)	1.04E+6
Secondary compression chamber harmonic amplitudes (Pa)	7.36E+4, 1.31E+3, …
Secondary compression chamber harmonic phases (°)	218.6, 81.2, …
Secondary compression chamber mean pressure (Pa)	1.04E+6
1st stage expansion chamber harmonic amplitudes (Pa)	4.64E+4, 9.79E+2, …
1st stage expansion chamber harmonic phases (°)	222.7, 51.6, …
1st stage expansion chamber mean pressure (Pa)	1.04E+6
Cold end expansion chamber harmonic amplitudes (Pa)	4.48E+4, 9.59E+2, …
Cold end expansion chamber harmonic phases (°)	222.9, 48.5, …
Cold end expansion chamber mean pressure (Pa)	1.04E+6
Compressor backshell harmonic amplitudes (Pa)	5.10E+3, 1.35E+1, …
Compressor backshell harmonic phases (°)	7.0, 10.6, …
Compressor backshell mean pressure (Pa)	1.04E+6
Displacer backshell harmonic amplitudes (Pa)	4.92E+2, 1.17E+0, …
Displacer backshell harmonic phases (°)	84.7, 125.5, …
Displacer backshell mean pressure (Pa)	1.04E+6
Mean gas temperatures	
Primary compression chamber (K)	3.12E+2
Secondary compression chamber (K)	3.03E+2
1st stage expansion chamber (K)	7.84E+1
Cold end expansion chamber (K)	6.82E+1
Mechanical work	
Primary compression chamber and compressor backshell (W)	4.46E+1
Secondary compression chamber and displacer backshell (W)	1.03E+1
1st stage expansion chamber (W)	-5.28E+0
Cold end expansion chamber (W)	-9.73E-1
Radiation load	
1st stage (W)	1.96E-1

Table A.2 continued: A table showing an example of the output values produced by the model.

2nd stage (W)	1.00E-4
Heat input	
Warm end (W)	-5.01E+1
1st stage (W)	7.69E-1
Cold end (W)	5.42E-1
1st stage losses	
Regenerator advection (W)	-1.00E-1
Regenerator flow work (W)	6.54E-2
Appendix gap advection (W)	5.77E-1
Appendix gap flow work (W)	3.91E-1
Shuttle (W)	9.60E-1
Regenerator gas conduction (W)	7.00E-1
Appendix gap gas conduction (W)	3.66E-3
Regenerator solid conduction (W)	5.92E-1
Displacer tube conduction (W)	1.50E-1
Cold finger tube conduction (W)	1.28E+0
MLI conduction (W)	0
2nd stage losses	
Regenerator advection (W)	-1.36E-2
Regenerator flow work (W)	-7.75E-4
Appendix gap advection (W)	2.19E-1
Appendix gap flow work (W)	1.63E-1
Shuttle (W)	7.18E-2
Regenerator gas conduction (W)	3.32E-3
Appendix gap gas conduction (W)	3.94E-5
Regenerator solid conduction (W)	2.59E-3
Displacer tube conduction (W)	1.15E-3
Cold finger tube conduction (W)	2.33E-2
MLI conduction (W)	0
Run information	
Number of cycles	210
Mesh convergence	9.86E-7
Wall convergence	5.12E-7
Seal convergence	7.65E-9

Appendix B

Material Properties

This appendix discusses the material properties used by the RAL Third-Order Model. Some key properties are presented, and the data sources are listed.

B.1 Gas Properties

The model uses helium-4 as a working fluid. It can model the gas using the ideal gas approximation or as a real gas.

For the ideal gas approximation, the gas properties used by the model are the specific gas constant $R_g = 2077.1$ [95], the heat capacity ratio $\gamma = 1.667$ [96], the dynamic viscosity μ and the thermal conductivity k. The dynamic viscosity and thermal conductivity are temperature dependent and are linearly interpolated from data taken from REFPROP 9.1 [56]. The lookup tables were generated at a constant pressure of 15 bar and over a temperature range of 10 to 400 K but can be generated at a different pressure and over a different temperature range if required.

Some of the real gas properties are also calculated using lookup tables but these tables use bilinear interpolation with two independent variables to improve their accuracy. The lookup tables for the pressure and temperature factors (f_P and f_T) are functions of specific internal energy u and density ρ and the procedure used to calculate the pressures and temperatures from these factors is described in Section 3.4.1. Once the pressures and temperatures have been calculated, they are then used as the independent variables in the lookup tables for μ and k.

B.2 Solid Properties

The model uses empirical correlations to calculate the thermal conductivity, specific heat capacity and density of solid cells.

B.2.1 Thermal Conductivity

The thermal conductivities of the solids in the model are functions of temperature, and the correlations are taken from multiple sources, listed in Table B.1. The thermal conductivities are plotted in Figure B.1.

Table B.1: A table listing the sources of the thermal conductivity correlations used in the model.

Material	Grade	Source	Notes
Aluminium	1100	[97]	
Aluminium	6061-T6	[98]	
Copper	C103	[99, p. 7-16]	Assume RRR = 50.
Erbium	Pure	[100, p. 89]	
Inconel	X-750	[101, p. 45]	
Mylar	A-PET	[102]	
Nylon	6	[98]	
Phosphor bronze	PB102	[99, p. 21-10]	
Stainless steel	304	[98]	
Titanium	Ti-6Al-4V	[100, p. 1076]	A fit through data from curves 3, 6 and 8.
Vespel	SP-3	[103]	SP-1 data scaled to match measurements of SP-3 taken at RAL.

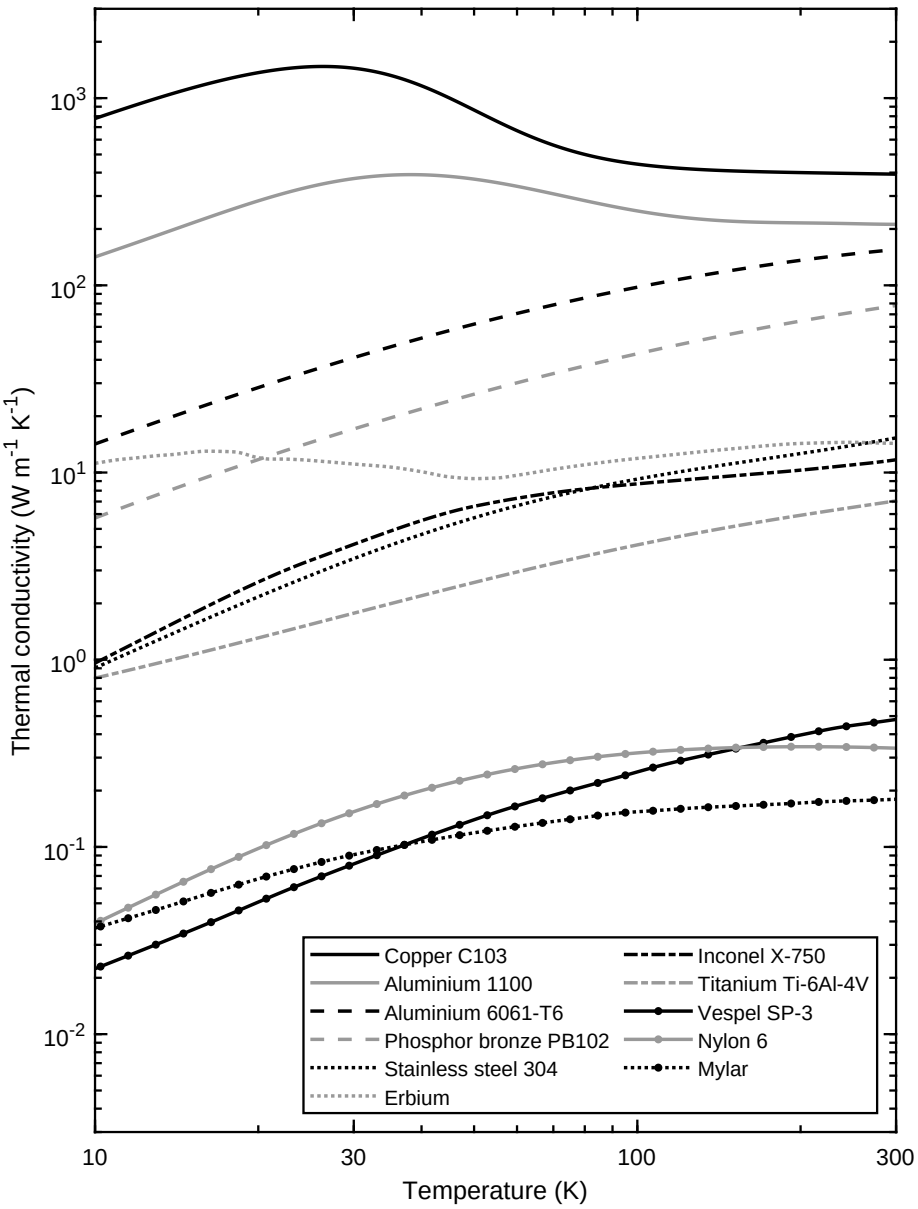

Figure B.1: A plot of the thermal conductivity correlations used in the model.

B.2.2 Heat Capacity

The specific heat capacities of the solids in the model are functions of temperature, and the correlations are taken from multiple sources, listed in Table B.2. The specific heat capacities are plotted in Figure B.2.

Table B.2: A table listing the sources of the specific heat capacity correlations used in the model.

Material	Grade	Source	Notes
Aluminium	6061-T6	[98]	
Copper	C103	[98]	
Erbium		[104]	
Inconel	X-750	[101, p. 341]	
Nylon	6	[98]	
Phosphor bronze	PB102	[99, p. 21-1]	
Stainless steel	304	[98], [105, p. 47]	[98] used below 100 K, otherwise [105] used.
Titanium	Ti-6Al-4V	[101, p. 344], [106, p. 599]	[101] used below 15 K, otherwise [106] curve 2 used.
Vespel	SP-3	[34], [107]	[107] scaled to match [34] for SP-1.

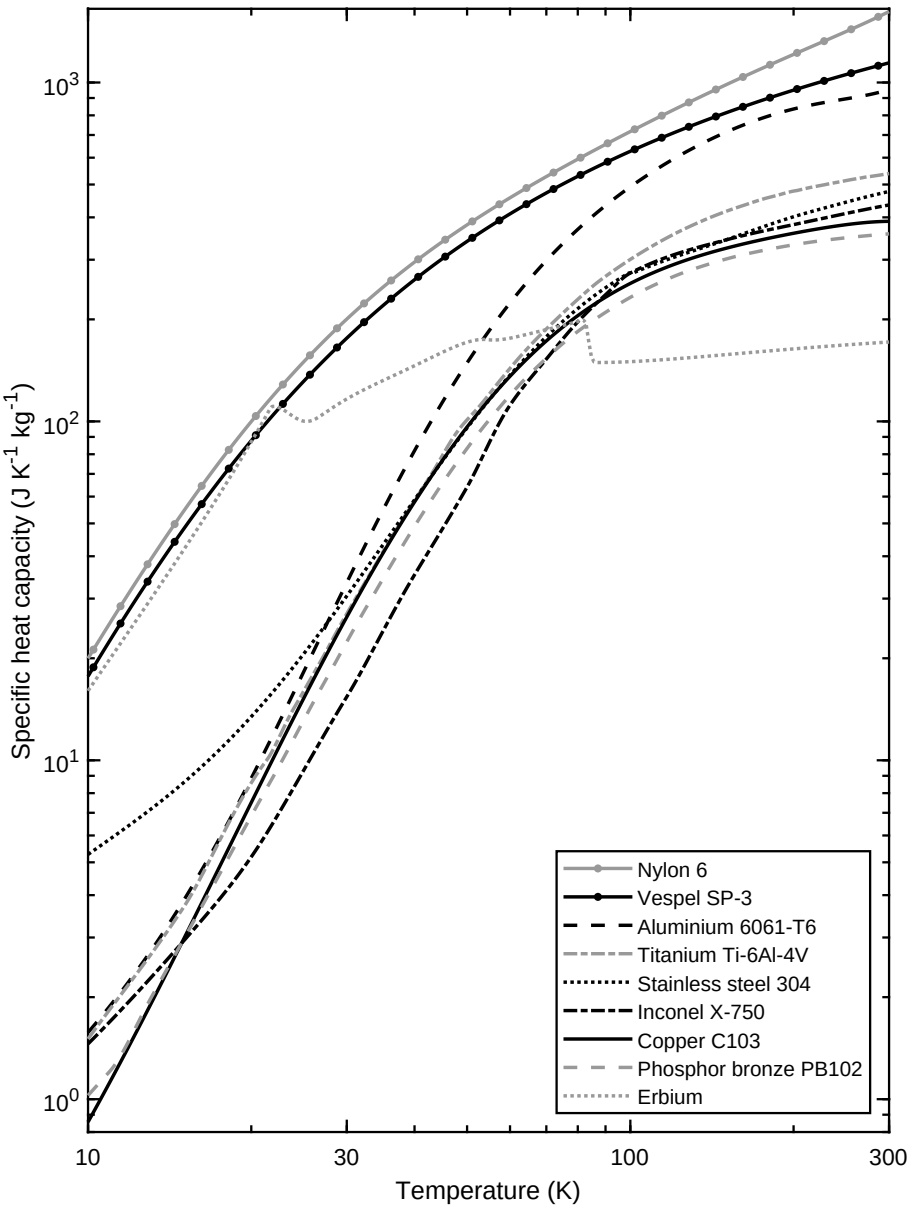

Figure B.2: A plot of the specific heat capacity correlations used in the model.

B.2.3 Density

The densities of the solids in the model are listed in Table B.3.

Table B.3: A table listing the densities of the materials used in the model.

Material	Grade	Density (kg m^{-3})	Source
Aluminium	6061-T6	2720	[108]
Copper	C103	8960	[108]
Erbium		9070	[108]
Inconel	X-750	8250	[109]
Nylon	6	1115	[109]
Phosphor bronze	PB102	8860	[109]
Stainless steel	304	7940	[108]
Titanium	Ti-6Al-4V	4430	[109]
Vespel	SP-3	1600	[34]

References

[1] R. Ross, “Aerospace coolers: A 50-year quest for long-life cryogenic cooling in space”, in *Cryogenic Engineering*, K. D. Timmerhaus and R. P. Reed, Eds. New York, NY: Springer New York, 2007, pp. 225–284.

[2] D. Barret, T. L. Trong, J.-W. den Herder, L. Piro, X. Barcons, J. Huovelin, R. Kelley, J. M. Mas-Hesse, K. Mitsuda, S. Paltani *et al.*, “The Athena X-ray Integral Field Unit (X-IFU)”, in *Space Telescopes and Instrumentation 2016: Ultraviolet to Gamma Ray*, International Society for Optics and Photonics, vol. 9905, 2016, 99052F.

[3] H. Dang, T. Zhang, R. Zha, J. Tan, J. Li, Y. Zhao, B. Zhao, H. Tan and R. Xue, “Development of 2-K space cryocoolers for cooling the superconducting nanowire single photon detector”, *IEEE Transactions on Applied Superconductivity*, vol. 29, no. 5, pp. 1–4, 2019.

[4] S. K. Andersen, “Numerical simulation of cyclic thermodynamic processes”, PhD thesis, Technical University of Denmark (DTU), 2006.

[5] D. Gedeon, *Sage user’s guide*, v11, Gedeon Associates, 2016.

[6] E. R. Cohen, T. Cvitas, J. G. Frey, B. Holström, K. Kuchitsu, R. Marquardt, I. Mills, F. Pavese, M. Quack, J. Stohner, H. L. Strauss, M. Takami and A. J. Thor, Eds., *Quantities, Units and Symbols in Physical Chemistry*. The Royal Society of Chemistry, 2007.

[7] T. W. Bradshaw, A. H. Orlowska and J. Hieatt, “Computer modelling of Stirling cycle coolers”, in *Cryocoolers*, vol. 7, 1992, pp. 772–782.

[8] R. W. Dyson, S. M. Geng, R. C. Tew and M. Adelino, “Towards fully three-dimensional virtual Stirling convertors for multi-physics analysis and optimization”, *Engineering Applications of Computational Fluid Mechanics*, vol. 2, no. 1, pp. 95–118, 2008.

[9] I. Urieli, “A computer simulation of Stirling cycle machines”, PhD thesis, University of Witwatersrand, 1977.

[10] W. R. Martini, “Stirling engine design manual”, Tech. Rep., 1978.

[11] G. Walker, *Cryocoolers: Fundamentals*, ser. International cryogenics monograph. Plenum Press, 1983.

[12] J. Weisend, “Cryostats and cryocoolers”, *Cold Facts*, vol. Winter, 2009.

[13] R. Radebaugh, “Cryocoolers: The state of the art and recent developments”, *Journal of Physics: Condensed Matter*, vol. 21, no. 16, 2009.

[14] M. Donabedian, *Spacecraft Thermal Control Handbook: Cryogenics. Vol. 2*. American Institute of Aeronautics and Astronautics, 2003.

[15] H. J. ter Brake and G. Wiegerinck, “Low-power cryocooler survey”, *Cryogenics*, vol. 42, no. 11, pp. 705–718, 2002.

[16] A. Orlowska, M. Harman and B. Ellison, “Receiver cryogenic system”, in *ALMA Project Book*, Version 4.00, Feb. 2001, ch. 6.

[17] A. Filis, Z. B. Haim, N. Pundak and R. Broyde, “Microminiature rotary Stirling cryocooler for compact, lightweight, and low-power thermal imaging systems”, in *Infrared Technology and Applications XXXV*, B. F. Andresen, G. F. Fulop and P. R. Norton, Eds., International Society for Optics and Photonics, vol. 7298, SPIE, 2009, pp. 421–429.

[18] R. G. Ross Jr and R. F. Boyle, “An overview of NASA space cryocooler programs — 2006”, in *Cryocoolers*, S. D. Miller and R. G. Ross, Eds., vol. 14, ICC Press, 2006, pp. 1–10.

[19] J. A. Tauber, N. Mandolesi, J.-L. Puget, T. Banos, M. Bersanelli, F. R. Bouchet, R. C. Butler, J. Charra, G. Crone, J. Dodsworth *et al.*, “Planck pre-launch status: The Planck mission”, *Astronomy & Astrophysics*, vol. 520, A1, 2010.

[20] W. U. Notardonato, A. M. Swanger, J. E. Fesmire, K. M. Jumper, W. L. Johnson and T. M. Tomsik, “Zero boil-off methods for large-scale liquid hydrogen tanks using integrated refrigeration and storage”, *IOP Conference Series: Materials Science and Engineering*, vol. 278, no. 1, 2017.

[21] R. G. Ross, “Refrigeration systems for achieving cryogenic temperatures”, in *Low Temperature Materials and Mechanisms*, CRC Press, Jul. 2016, ch. 6, pp. 109–181.

[22] T. Finkelstein and A. J. Organ, *Air Engines*, ser. IMechE Conference Transactions. Professional Engineering, 2001.

[23] A. Veprik, S. Zehtzer, N. Pundak and S. Riabzev, “Compact linear split Stirling cryogenic cooler for high temperature infrared imagers”, in *Cryocoolers*, vol. 16, 2011, pp. 121–132.

[24] T. Bradshaw, A. Orlowska, C. Jewell, B. Jones and S. Scull, “Improvements to the cooling power of a space qualified two-stage Stirling cycle cooler”, in *Cryocoolers*, vol. 9, Springer, 1997, pp. 79–88.

[25] R. Radebaugh, “Refrigeration for superconductors”, *Proceedings of the IEEE*, vol. 92, no. 10, pp. 1719–1734, 2004.
[26] R. Z. Unger and J. G. Wood, “Performance comparison of M77 Stirling cryocooler and proposed pulse tube cryocooler”, *Advances in cryogenic engineering*, vol. 45, no. A, pp. 539–544, 2000.
[27] R. Arts, D. Willems, J. Mullié and T. Benschop, “Advantages of high-frequency pulse-tube technology and its applications in infrared sensing”, in *Tri-Technology Device Refrigeration (TTDR)*, International Society for Optics and Photonics, vol. 9821, 2016, p. 982 108.
[28] R. G. Ross Jr, “Vibration suppression of advanced space cryocoolers: An overview”, in *Smart structures and materials 2003: Damping and isolation*, International Society for Optics and Photonics, vol. 5052, 2003, pp. 1–12.
[29] “Optimization of a Brayton cryocooler for ZBO liquid hydrogen storage in space”, *Cryogenics*, vol. 64, pp. 172–181, 2014.
[30] M. Crook, T. Bradshaw, G. Gilley, M. Hills, S. Watson, B. Green, C. Pulker and T. Rawlings, “Development of a 2 K Joule-Thomson closed-cycle cryocooler”, in *Cryocoolers*, vol. 19, 2016, pp. 9–18.
[31] N. R. Gemmell, M. Hills, T. Bradshaw, T. Rawlings, B. Green, R. M. Heath, K. Tsimvrakidis, S. Dobrovolskiy, V. Zwiller, S. N. Dorenbos, M. Crook and R. H. Hadfield, “A miniaturized 4 K platform for superconducting infrared photon counting detectors”, *Superconductor Science and Technology*, vol. 30, no. 11, 2017.
[32] M. Crook, M. Hills, S. Brown, S. Kendall, H. Korswagen and P. Iredale, “Small Scale Cooler - improvements”, in *Cryocoolers*, vol. 20, 2018, pp. 93–101.
[33] M. Crook, M. Hills, S. Brown, S. Cleary, P. Iredale, N. Hardy and H. Korswagen, “CryoBlue — a low-vibration 50 K Stirling cryocooler”, in *Cryocoolers*, vol. 20, 2018, pp. 119–125.
[34] *Vespel SP-3 product data sheets isostatic (ISO)*, VPE-A10869-00-B0614, DuPont, 2014.
[35] K. A. Gschneidner, A. O. Pecharsky and V. K. Pecharsky, “Low temperature cryocooler regenerator materials”, in *Cryocoolers 12*, R. G. Ross, Ed., Boston, MA: Springer US, 2003, pp. 457–465.
[36] *Retimet information sheet*, Meggitt Control Systems, 2016.
[37] G. Walker, *Stirling Engines*, ser. Oxford Science Publications. Clarendon Press, 1980.

[38] K. Liang, M. Dadd and P. Bailey, “Clearance seal compressors with linear motor drives. part 1: Background and system analysis”, *Proceedings of the Institution of Mechanical Engineers, Part A: Journal of Power and Energy*, vol. 227, no. 3, pp. 242–251, 2013.

[39] K. Liang, “A review of linear compressors for refrigeration”, *International Journal of Refrigeration*, vol. 84, pp. 253–273, 2017.

[40] G. Baker, D. Féger, A. Gibson, A. Little, T. Bradshaw, M. Crook, A. Orlowska, B. Tomlinson and A. Sargeant, “Demonstration of a 10K Stirling cooler for space applications”, in *9th European Space Mechanisms and Tribology Symposium*, vol. 480, 2001, pp. 165–170.

[41] T. Finkelstein, “Generalized thermodynamic analysis of Stirling engines”, in *SAE Technical Paper*, SAE International, 1960.

[42] F. J. Zimmerman and R. C. Longsworth, “Shuttle heat transfer”, in *Advances in Cryogenic Engineering: Proceeding of the 1970 Cryogenic Engineering Conference*, K. D. Timmerhaus, Ed. Boston, MA: Springer US, 1971, pp. 342–351.

[43] R. C. Tew, “Computer program for Stirling engine performance calculations”, National Aeronautics and Space Administration, Lewis Research Center, Tech. Rep. NASA TM-82960, 1983.

[44] N. C. J. Chen and F. P. Griffin, “Review of Stirling-engine mathematical models”, Oak Ridge National Lab., TN (USA), Tech. Rep., 1983.

[45] J. P. Clark, W. C. Ward and G. W. Swift, “Design environment for low-amplitude thermoacoustic energy conversion (DeltaEC)”, *The Journal of the Acoustical Society of America*, vol. 122, no. 5, pp. 3014–3014, 2007.

[46] S. Watson, “Design and development of a high power Stirling cooler”, in *European Space Mechanisms & Tribology Symposium—ESMATS 2013*, 2013.

[47] R. Dyson, S. Wilson, R. Tew and R. Demko, “Fast whole-engine Stirling analysis”, in *3rd International Energy Conversion Engineering Conference*, 2005, p. 5558.

[48] H. Rana, M. A. Abolghasemi, R. Stone, M. Dadd and P. Bailey, “Numerical modelling of a coaxial Stirling pulse tube cryocooler with an active displacer for space applications”, *Cryogenics*, vol. 106, 2020.

[49] K. Mahkamov, “Design improvements to a biomass Stirling engine using mathematical analysis and 3D CFD modeling”, *Journal of Energy Resources Technology*, vol. 128, no. 3, pp. 203–215, Sep. 2005.

[50] A. Della Torre, A. Guzzetti, G. Montenegro, T. Cerri, A. Onorati and F. Aloui, “CFD modeling of a beta-type Stirling engine”, Jul. 2014.
[51] D. Gedeon and J. G. Wood, “Oscillating-flow regenerator test rig: Hardware and theory with derived correlations for screens and felts”, Lewis Research Center, Tech. Rep., 1996.
[52] J. Gary, A. O’Gallagher, R. Radebaugh, Y. Huang and E. Marquardt, *REGEN 3.3: User manual*, National Institute of Standards and Technology, 2008.
[53] A. Caughley, M. Sellier, M. Gschwendtner and A. Tucker, “CFD analysis of a diaphragm free-piston Stirling cryocooler”, *Cryogenics*, vol. 79, pp. 7–16, 2016.
[54] S. Patankar, *Numerical Heat Transfer and Fluid Flow*, ser. Series in computational methods in mechanics and thermal sciences. Taylor & Francis, 1980.
[55] MathWorks, *MATLAB primer*, R2020b, Natick, MA, 2020.
[56] E. W. Lemmon, M. L. Huber and M. O. McLinden, *NIST standard reference database 23: Reference fluid thermodynamic and transport properties-REFPROP, version 9.1, National Institute of Standards and Technology*, 2013.
[57] Crane Co. Engineering Division, *Flow of Fluids Through Valves, Fittings, and Pipe: Metric Edition - SI Units*. Crane Company, 2010.
[58] N. Dynamics. (2018). Discharge coefficient for nozzles and orifices, [Online]. Available: `https://neutrium.net/fluid_flow/discharge-coefficient-for-nozzles-and-orifices/` (visited on 08/02/2018).
[59] W. M. Kays and A. L. London, *Compact heat exchangers*. McGraw-Hill,New York, NY, 1998.
[60] J. H. Lienhard IV and J. H. Lienhard V, *A Heat Transfer Textbook*, 4th. Cambridge, MA: Phlogiston Press, 2017, Version 2.11.
[61] F. Incropera and D. DeWitt, *Introduction to Heat Transfer*, 6th. Wiley, 2011.
[62] T. S. Zhao and P. Cheng, “Experimental studies on the onset of turbulence and frictional losses in an oscillatory turbulent pipe flow”, *International journal of heat and fluid flow*, vol. 17, no. 4, pp. 356–362, 1996.

[63] S. Genić, I. Arandjelović, P. Kolendić, M. Jarić, N. Budimir and V. Genić, "A review of explicit approximations of Colebrook's equation", *FME transactions*, vol. 39, no. 2, pp. 67–71, 2011.

[64] F. J. Cantelmi, D. Gedeon and A. A. Kornhauser, "An analytical model for turbulent compression-driven heat transfer", *Journal of heat transfer*, vol. 120, no. 3, pp. 617–623, 1998.

[65] K. Lee, "A simplistic model of cyclic heat transfer phenomena in closed spaces", in *Proceedings of the Eighteenth Intersociety Energy Conversion Engineering Conference*, vol. 2, 1983, pp. 720–723.

[66] K. Nam and S. Jeong, "Investigation of oscillating flow friction factor for cryocooler regenerator considering cryogenic temperature effect", *Cryogenics*, vol. 45, no. 12, pp. 733–738, 2005.

[67] Y. Ju and Q. Shen, "Comparative study of oscillating flow characteristics of cryocooler regenerator at low temperatures", *Frontiers of Energy and Power Engineering in China*, vol. 3, no. 1, pp. 80–84, 2009.

[68] D. Edouard, M. Lacroix, C. P. Huu and F. Luck, "Pressure drop modeling on SOLID foam: State-of-the art correlation", *Chemical Engineering Journal*, vol. 144, no. 2, pp. 299–311, 2008.

[69] S. Mahjoob and K. Vafai, "A synthesis of fluid and thermal transport models for metal foam heat exchangers", *International Journal of Heat and Mass Transfer*, vol. 51, no. 15, pp. 3701–3711, 2008.

[70] M. Lacroix, P. Nguyen, D. Schweich, C. P. Huu, S. Savin-Poncet and D. Edouard, "Pressure drop measurements and modeling on SiC foams", *Chemical Engineering Science*, vol. 62, no. 12, pp. 3259–3267, 2007.

[71] R. E. Booser, *CRC Handbook of Lubrication: Theory and Practice of Tribology, Volume II: Theory and Design*. CRC Press, 1983.

[72] R. Barron and G. Nellis, *Cryogenic Heat Transfer*. CRC Press, 2017.

[73] Y. S. Touloukian and D. P. DeWitt, *Thermophysical properties of matter - the TPRC data series. Volume 7. Thermal radiative properties - metallic elements and alloys*. Defense Technical Information Center, 1970.

[74] R. G. Ross Jr, "Quantifying MLI thermal conduction in cryogenic applications from experimental data", in *IOP Conference Series: Materials Science and Engineering*, IOP Publishing, vol. 101, 2015.

[75] C. W. Keller, G. R. Cunnington and A. P. Glassford, “Thermal performance of multilayer insulations”, Lockheed Missiles & Space Co, Tech. Rep., 1974, NASA Contractor Report CR-134477.

[76] H. Carslaw and J. Jaeger, *Conduction of heat in solids*, ser. Oxford Science Publications. Clarendon Press, 1959.

[77] M. Clifford, K. Simmons and P. Shipway, *An Introduction to Mechanical Engineering: Part 1*. CRC Press, 2009.

[78] H.-D. Kühl and S. Shulz, “Measured performance of an experimental Vuilleumier heat pump in comparison to 3rd order theory”, in *Energy Conversion Engineering Conference, 1990. IECEC-90. Proceedings of the 25th Intersociety*, IEEE, vol. 5, 1990, pp. 436–441.

[79] H. Versteeg and W. Malalasekera, *An Introduction to Computational Fluid Dynamics: The Finite Volume Method*, 2nd. Pearson Education Limited, 2007.

[80] R. J. LeVeque, *Finite Volume Methods for Hyperbolic Problems*, ser. Cambridge Texts in Applied Mathematics. Cambridge University Press, 2002.

[81] P. L. Roe, “Some contributions to the modelling of discontinuous flows”, in *Large-scale computations in fluid mechanics*, 1985, pp. 163–193.

[82] L. Shampine, I. Gladwell and S. Thompson, *Solving ODEs with MATLAB*. Cambridge University Press, 2003.

[83] R. Courant, K. Friedrichs and H. Lewy, “On the partial difference equations of mathematical physics”, *IBM journal of Research and Development*, vol. 11, no. 2, pp. 215–234, 1967.

[84] L. F. Shampine and M. W. Reichelt, “The MATLAB ODE suite”, *SIAM journal on scientific computing*, vol. 18, no. 1, pp. 1–22, 1997.

[85] P. Wynn, “On a device for computing the em(Sn) transformation”, *Mathematical Tables and Other Aids to Computation*, vol. 10, no. 54, pp. 91–96, 1956.

[86] A. Schock, “Stirling engine nodal analysis program”, Fairchild Space and Electronics Company, Germantown, Maryland, Tech. Rep., 1978.

[87] J. P. Harvey, C. S. Kirkconnell and P. V. Desai, “A fast and accurate regenerator numerical model”, in *Cryocoolers*, R. G. Ross, Ed., vol. 13, Boston, MA: Springer US, 2005, pp. 455–461.

[88] J. Ekin, *Experimental Techniques for Low-Temperature Measurements: Cryostat Design, Material Properties and Superconductor Critical-Current Testing*. OUP Oxford, 2006.

[89] "Technology readiness levels handbook for space applications", European Space Agency, Tech. Rep., 2008, TEC-SHS/5551/MG/ap, issue 1, rev. 6.

[90] *2S132W pressure wave generator nominal parameters*, Chart Industries, 2017.

[91] A. Orlowska and G. Davey, "Measurement of losses in a Stirling cycle cooler", *Cryogenics*, vol. 27, no. 11, pp. 645–651, 1987.

[92] K. Liang, R. Stone, M. Dadd and P. Bailey, "The effect of clearance control on the performance of an oil-free linear refrigeration compressor and a comparison between using a bleed flow and a DC current bias", *International Journal of Refrigeration*, vol. 69, pp. 407–417, 2016.

[93] R. Fitzpatrick, *Theoretical Fluid Mechanics*, ser. 2053-2563. IOP Publishing, 2017.

[94] G. Morgante, L. Terenzi, D. D'Ascanio, P. Eccleston, M. Crook, T. Hunt, V. D. Deppo, M. Focardi, G. Malaguti, G. Micela, E. Pace and G. Tinetti, "Thermal architecture of the ESA ARIEL payload", in *Space Telescopes and Instrumentation 2018: Optical, Infrared, and Millimeter Wave*, International Society for Optics and Photonics, vol. 10698, SPIE, 2018, pp. 1346–1359.

[95] Engineering ToolBox. (2004). Universal and individual gas constants, [Online]. Available: `https://www.engineeringtoolbox.com/individual-universal-gas-constant-d_588.html` (visited on 30/05/2021).

[96] Engineering ToolBox. (2003). Specific heat and individual gas constants of gases, [Online]. Available: `https://www.engineeringtoolbox.com/specific-heat-capacity-gases-d_159.html` (visited on 30/05/2021).

[97] D. Mann, "LNG materials and fluids: A user's manual of property data in graphic format", National Bureau of Standards, Cryogenics Division, Tech. Rep., 1977.

[98] E. D. Marquardt, J. P. Le and R. Radebaugh, "Cryogenic material properties database", in *Cryocoolers*, R. G. Ross, Ed., vol. 11, Boston, MA: Springer US, 2002, pp. 681–687.

[99] N. J. Simon, E. S. Drexler and R. P. Reed, “Properties of copper and copper alloys at cryogenic temperatures”, National Inst. of Standards and Technology (MSEL), Boulder, CO (United States). Materials Reliability Div., Tech. Rep., 1992.

[100] Y. S. Touloukian, R. W. Powell, C. Y. Ho and P. G. Klemens, *Thermophysical Properties of Matter - The TPRC Data Series. Volume 1. Thermal Conductivity - Metallic Elements and Alloys*. Defense Technical Information Center, 1970.

[101] Y. Touloukian, “Recommended values of the thermophysical properties of eight alloys, their major constituents and oxides”, Purdue University, Tech. Rep., 1966, NBS Sub-Contract No. CST-7590.

[102] C. L. Choy and D. Greig, “The low-temperature thermal conductivity of a semi-crystalline polymer, polyethylene terephthalate”, *Journal of Physics C: Solid State Physics*, vol. 8, no. 19, pp. 3121–3130, Oct. 1975.

[103] A. L. Woodcraft and A. Gray, “A low temperature thermal conductivity database”, in *AIP Conference Proceedings*, AIP, vol. 1185, 2009, pp. 681–684.

[104] K. A. Gschneidner, A. O. Pecharsky and V. K. Pecharsky, “Ductile, high heat capacity, magnetic regenerator alloys for the 10 to 80 K temperature range”, in *Cryocoolers 11*, R. G. Ross, Ed., Boston, MA: Springer US, 2002, pp. 433–441.

[105] Y. S. Touloukian and C. Y. Ho, “Thermophysical properties of selected aerospace materials. Part 2. Thermophysical properties of seven materials”, Thermophysical and Electronic Properties Information Analysis Center, Lafayette, IN, Tech. Rep., 1977.

[106] Y. S. Touloukian and E. H. Buyco, *Thermophysical Properties of Matter - The TPRC Data Series. Volume 4. Specific Heat - Metallic Elements and Alloys*. Defense Technical Information Center, 1971.

[107] D. L. Rule, D. R. Smith and L. L. Sparks, “Thermal conductivity of a polymide film between 4.2 and 300K, with and without alumina particles as filler”, National Institute of Standards and Technology, Tech. Rep., 1990.

[108] C. L. Yaws, *Yaws’ Critical Property Data for Chemical Engineers and Chemists*. Knovel, 2014.

[109] L. Mordfin, *Handbook of Reference Data for Nondestructive Testing*. ASTM International, 2002.

Related Work

Development of a Stirling Cryocooler Model that Includes a Full Simulation of the Appendix Gap

T. Rawlings, M. Crook and M. Hills

Cryocoolers, vol. 21, 2021, pp. 235–244

Presented at the 21st International Cryocooler Conference, 7-10th December 2020, online virtual conference.

Development of a Stirling Cryocooler Model that Includes a Full Simulation of the Appendix Gap

T. Rawlings, M. Crook, M. Hills

STFC Rutherford Appleton Laboratory
Harwell, Oxford, UK

ABSTRACT

A new Stirling cryocooler model has been developed at the Rutherford Appleton Laboratory. This one-dimensional, finite difference model is able to simulate single and two-stage cryocoolers. The model uses the latest friction factor and heat transfer correlations from the literature and simulates turbulence generation and thermal penetration depths. It runs fast enough to be useful for optimisation, thanks to a robust artificial convergence technique. The model includes a full representation of the cold head, including the displacer motion and the flow past the displacer; this enables the optimisation of certain parameters that could not be assessed previously. The model has been validated against single and two-stage coolers and has been used to investigate changing the cold finger geometry of a single-stage cooler.

INTRODUCTION

A new Stirling cryocooler model has been developed that will be used to optimise the design of the single and two-stage coolers that are produced at the Rutherford Appleton Laboratory (RAL). These coolers are typically designed for use in spacecraft and use flexure bearings and non-contact clearance seals in order to achieve a long lifetime.

Stirling cryocoolers are difficult to model using commercially available 2D or 3D computational fluid dynamics software. The compressible gas, moving mesh and the variable regenerator temperatures make a 2D or 3D model computationally expensive.[1] The approach commonly used by other researchers is to simulate the machine as a network of one dimensional flow paths.[2, 3, 4] Empirical relationships are used to calculate the heat transfer rates and friction factors at different points in the cooler. These models are categorised as third-order[5] and this is the approach used by the new RAL model. The new model is able to run fast enough to be able to optimise over a wide parameter range while still being accurate enough to give useful results.

Most of the third-order models in the literature do not simulate the motion of the displacer; instead, they change the volume of the cells at either end. The RAL third-order model is able to account for the relative motion between the displacer and the cold finger tube and this allows it to simulate effects such as shuttle losses as part of the thermodynamic cycle.

MODEL OUTLINE

The model has been developed using MATLAB. The different regions of the cooler are split up into cells and the finite difference method is used to create a system of ordinary differential

Cryocoolers 21, edited by R.G. Ross, Jr., J.R. Raab and S.D. Miller

equations. For the gas cells, the mass, energy, momentum and turbulence state are tracked over time and, for solid cells, the temperature is tracked. The model solves the differential equations by using a backwards differentiation formula. It runs until the relative changes in the solid cell temperatures over a cycle are below a threshold. The rate of convergence is accelerated by using a method that artificially adjusts the temperatures.

Discretisation

The model splits the cooler into cells, as shown in Figure 1. The Eulerian approach is used, where the cells are fixed relative to the cooler geometry, because different regions can have very different friction factor and heat transfer correlations. The mass and energy equations are evaluated for each gas cell and the momentum equations are evaluated at the nodes between the cells. This is known as the staggered grid technique and helps to keep the simulation stable.[6]

The model uses branching flow paths to simulate appendix gaps, compressor and displacer backshells and the first stage outlet of two-stage coolers. Mass and energy can be transferred between flow paths but momentum is not transferred.

The model simulates the entire cold finger as one system so it is not modular. However, it can be configured to simulate one or two stages of cooling; it allows for optional heat exchanger regions and provides the option to split the regenerator into sections with different properties.

Model Equations

Gas Cells. The rate of change of the mass and energy of each gas cell (i) is given by the following differential equations, derived from the laws of conservation of mass and energy. The rate of change in mass is simply the difference between the mass flow rates at the nodes (j).

$$\frac{dm_i}{dt} = \dot{m}_{j-1} - \dot{m}_j \tag{1}$$

The energy of the gas is the sum of its internal and kinetic energy. The equation for the

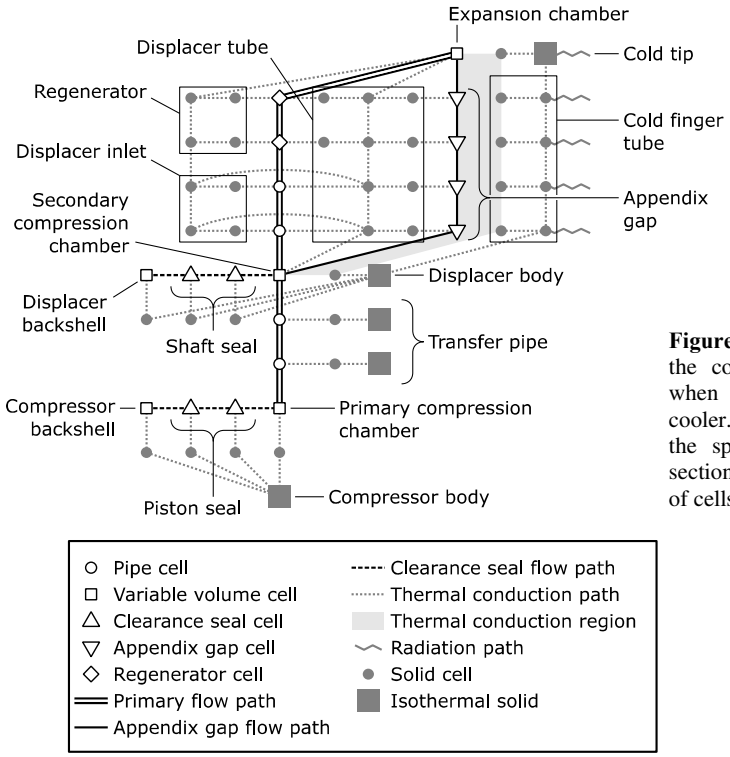

Figure 1. A schematic showing the connections between cells when simulating a single-stage cooler. It is possible to adjust the spatial resolution of each section by adjusting the number of cells.

rate of change of energy accounts for the energy carried by the gas, the flow work, the mechanical work done on the gas, the thermal conduction within the gas and the rate of heat transfer between the gas and its surroundings.

$$\frac{dE_i}{dt} = \dot{E}_{advection_i} + \dot{W}_{flow_i} + \dot{W}_{mechanical_i} + \dot{Q}_{conduction_i} + \dot{Q}_{transfer_i} \tag{2}$$

To convert from masses and energies to temperatures and pressures, the model can either use the ideal gas equation of state or can simulate real gas effects by using a 2D look-up table generated using REFPROP.[7]

The differential equation for the rate of change of momentum at each node is derived from the law of momentum conservation. It accounts for the momentum carried by the gas, the pressure forces, minor losses due to changes in flow area and any frictional forces.

$$\frac{dp_j}{dt} = \dot{p}_{flow_j} + F_{pressure_j} + F_{minor_j} + F_{friction_j} \tag{3}$$

In addition to mass, energy and momentum, the model keeps track of the level of turbulence for some of the cells. For the transfer pipe and other ducts, the mass of gas that is turbulent is tracked.

$$\frac{dm_{\mathcal{T}_i}}{dt} = \dot{m}_{\mathcal{T}_{advection_i}} + \dot{m}_{\mathcal{T}_{generation_i}} + \dot{m}_{\mathcal{T}_{decay_i}} \tag{4}$$

For variable volume cells such as the compression and expansion chambers, the turbulence kinetic energy is tracked.

$$\frac{dK_i}{dt} = \dot{K}_{advection_i} + \dot{K}_{decay_i} \tag{5}$$

Solid Cells. The equation for the rate of change of the thermal energy of the solid cells accounts for conduction between neighboring cells, heat transfer with the gas and thermal radiation. The temperature of each cell can then be calculated from the cell energy.

$$\frac{dE_{s_i}}{dt} = \dot{Q}_{s_{axial_i}} + \dot{Q}_{s_{radial_i}} + \dot{Q}_{s_{transfer_i}} + \dot{Q}_{s_{radiation_i}} \tag{6}$$

Interpolation

To calculate the energy of the gas that is flowing in and out of each gas cell, it is necessary to know the pressures and temperatures of the gas at the boundaries of the cell. Calculating the boundary temperature by simply averaging the temperatures of the neighbouring cells can result in the model producing unphysical temperature oscillations. This is because averaging causes the temperature of the downwind cell to affect the temperature of the gas flowing into it.

A number of different interpolation methods were tested to determine which was able to remove the unphysical oscillations and produce an accurate result with the fewest cells. The QUICK scheme was selected.[8] This is a blend of the average of the neighbouring cell temperatures and an extrapolated temperature from the upwind cells. Simple averages were used for the pressures at the nodes and the velocities at the cell centres as these did not cause oscillations.

Numerical Method

Explicit and implicit solvers were investigated to determine which type was fastest at solving the model's system of differential equations. Explicit solvers must take time steps that are shorter than the time taken for a pressure wave to cross each model cell. This is known as the Courant-Friedrichs-Lewy condition.[9] Implicit solvers are more computationally expensive per step but are not affected by this condition and so are able to take much longer time steps. The overall simulation time was significantly reduced by using an implicit solver. MATLAB's ode15s solver was selected.[10] The backward differentiation formula option was used and the order was set to two to improve its stability.

Convergence Acceleration

The model will naturally approach a periodic steady state where the temperatures at the end of each cycle are the same as the temperatures at the start of the cycle. The model is deemed to have converged when the following condition is met for every solid cell:

$$\frac{|T_{end} - T_{start}|}{T_{end}} < 10^{-6} \tag{7}$$

It can take thousands of cycles for the model to converge naturally. This is because the regenerator mesh cells typically have a much higher heat capacity than the gas passing through them, so it takes many cycles to change the mesh cell temperature. To speed up convergence, Stirling cycle models typically use convergence acceleration methods.

The RAL third-order model combines two techniques: energy flow equalisation and cell temperature adjustment. Using both of these techniques produces a convergence acceleration method that is fast and robust.

Energy flow equalisation. This method has been previously used in the Stirling cycle models of Kühl[11] and Harvey.[12] For a single-stage cooler, it can be assumed that energy only enters or leaves the cold finger at either end. This means that the energy flowing along the cold finger over a cycle must be the same along its length when the model is converged. If this is not the case, the model calculates and applies adjustments to the cell temperatures in order to make the energy flow uniform. The required adjustments vary along the length of the cold finger but the same adjustment is applied to all the cells that are at the same axial position (each row of cells in Figure 1).

Cell temperature adjustment. This method has been used in the Stirling engine model of Urieli.[2] It accelerates the rate of convergence by multiplying the natural temperature change of each cell over the previous cycle by a factor (a) and adding this to the current cell temperature.

$$T_{new} = T_{end} + a(T_{end} - T_{start}) \tag{8}$$

These two methods are effective in different situations. If the cells are well connected thermally, the energy flow equalisation technique can be used because a temperature change of one cell will strongly affect the energy flow to neighbouring cells. This occurs if the regenerator is effective because the temperature of a regenerator cell strongly affects the temperature of the gas flowing through it. If the regenerator is ineffective, temperature changes of cells have little impact on their neighbours and the cell temperature adjustment technique works better.

The model combines the temperature perturbations predicted by these two convergence methods. The cell temperature adjustment perturbations are scaled so that the largest of these perturbations is half the magnitude of the largest energy flow equalisation perturbation. The perturbations for each cell are then added together. To keep the convergence stable, the sum of these perturbations is multiplied by a scale factor before being applied. This scale factor is reduced when necessary to ensure that the largest temperature perturbation does not exceed 5 K. The scale factor is also reduced if the model is not converging because the applied temperature changes are oscillating. The convergence acceleration method is applied every two cycles. The model typically converges in less than 300 cycles which takes approximately four hours on a desktop PC. Multiple cases can be run in parallel by using MATLAB's Parallel Computing Toolbox.

MODEL FEATURES

Solid Surface Temperature

The model tracks the surface temperatures of the solid components separately to their interior temperatures. This reduces the rate of heat transfer, particularly if the solid is a good insulator.

In regions such as the compression chamber, the interior of the chamber wall is assumed to be isothermal. If a sinusoidal heat transfer rate ($\dot{Q} = \dot{Q}_A e^{i\omega t}$) is applied, the wall surface temperature variation (T_W) lags the heat transfer rate by 45°,

$$\frac{T_W}{\dot{Q}} = \frac{\delta}{kA_{gs}(1+i)} \tag{9}$$

where A_{gs} is the surface area, $\delta = \sqrt{2k/(\omega\rho c)}$ is the thermal penetration depth, ω is the angular frequency, k is the conductivity, ρ is the density and c is the specific heat capacity.[13, 4] To simulate this, the model uses the method developed by Kühl.[11] An extra solid cell is added to represent the wall surface and the thermal mass of this extra cell and the resistance between it and the isothermal region are chosen so that the temperature of the cell matches T_W. This is known as a lumped-capacitance model. The thermal mass of the cell must be $C_W = \frac{1}{2}\delta A_{gs}\rho c$ and the thermal resistance must be $R = \delta/(k\,A_{gs})$.

This method has been extended so that the model can also simulate solids of a finite thickness (r) where the temperature of the interior can change. This is particularly important when simulating the regenerator mesh. The surface temperature is then given by equation 10.[13, 4]

$$\frac{T_W}{\dot{Q}} = \frac{\delta}{kA_{gs}(1+i)} \; \frac{1}{\tanh\left(\frac{r}{\delta}(1+i)\right)} \tag{10}$$

By using two solid cells, one representing the wall surface and one representing the interior, it is possible to ensure that the surface temperature in the model responds in the same way as the theoretical surface temperature. The thermal masses of the two cells and the resistance between them is selected so that the response matches equation 10.

Appendix Gap Heat Transfer

The appendix gap is the region between the displacer tube and the cold finger tube. The long-life coolers developed at RAL do not use dynamic seals so require a small appendix gap to reduce the flow of gas past the displacer. However, if the gap is too small, the level of shuttle losses is increased. Shuttle losses occur due to the relative motion of the displacer and cold finger tube. As the displacer and cold finger tube move past each other, their thermal gradients become offset. Thermal energy conducts across the gap. When the displacer moves back, the thermal energy is "shuttled" towards the cold end.

The leakage of gas past the displacer can be simulated with an extra flow path. Simulating the shuttle losses is more difficult. The approach used by the model is to let the mesh of the appendix gap and the cold finger tube move relative to each other. At each time step, the cells are divided into subcells, as shown in Figure 2. The temperatures of the gas and wall subcells are calculated by linearly interpolating the cell temperatures.

The rate of heat transfer is calculated separately for each subcell and the change of energy is applied to the parent cells. The model calculates the rate of heat transfer by using the method suggested by Andersen[3] and recommended by Sauer.[14] A quadratic polynomial is fitted to the

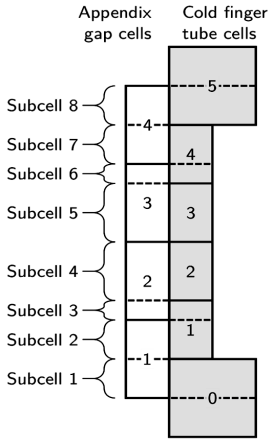

Figure 2. A diagram showing how the appendix gap and cold finger tube are divided into subcells. The solid lines represent the boundaries of the cells. The lengths of the subcells are set so that they do not overlap any cell boundaries. If the cells share the same number, they are in the same row for the energy flow equalisation convergence method. Some subcells span multiple rows so any heat transfer within these is accounted for when calculating the energy flow between rows.

temperatures of the displacer tube wall (T_D), the appendix gap gas (T_g) and the cold finger tube wall (T_F). The thermal gradient of this polynomial at the walls is then used to calculate the rate of heat transfer from the displacer tube and cold finger tube to the gas, given by equations 11 and 12.

$$\dot{Q}_{Dg} = \frac{A_{gs}k}{r}\left(4T_D + 2T_F - 6T_g\right) \tag{11}$$

$$\dot{Q}_{Fg} = \frac{A_{gs}k}{r}\left(4T_F + 2T_D - 6T_g\right) \tag{12}$$

A_{gs} is the surface area of the wall, k is the conductivity of the gas and r is the width of the appendix gap.

Oscillating Flow Correlations

The model makes the assumption that flow through the regenerator mesh, clearance seals and the appendix gap can be modelled using the quasi-static approximation. This is where the heat transfer coefficient and friction factor are calculated using the instantaneous gas properties. This is because the flow channels in these regions are narrow and the steady velocity profiles will develop quickly. This has been shown experimentally.[15]

For gas in variable-volume chambers and ducts, the quasi-static assumption is no longer valid. For these regions, the model uses the oscillating flow correlations that were developed for the Sage model.[4] To enable the use of these correlations, the model tracks the level of turbulence present in these cells. It is also able to simulate heat transfer that is out of phase with the temperature difference and simulate frictional forces that are out of phase with the gas velocity. It does this by phase shifting the temperature and velocity waveforms of the previous cycle and using these in the heat transfer and friction calculations.

MODEL VALIDATION

The model has been validated against single and two-stage Stirling coolers that have been built and tested at RAL.

Single-Stage Cooler Validation

The RAL Small Scale Cooler, shown in Figure 3, was one of the coolers used to validate the model. This compact single-stage Stirling cooler has been developed for use in small satelites.[16] The model was used to replicate a load line where heat loads from 0 W to 1.5 W were applied. Measured temperatures, as well as compressor and displacer motions, were used as inputs into the model; the same cases were also simulated using Sage for comparison.

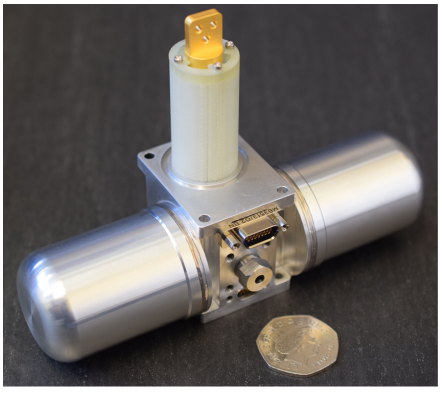

Figure 3. The RAL Small Scale Cooler.

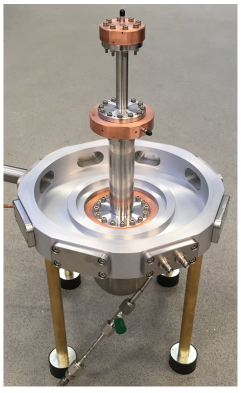

Figure 4. The RAL breadboard two-stage cooler.

It can be seen that both the RAL third-order model and Sage overpredict the cooling power by a similar amount. It is thought that this may be due to the models underestimating the leakage past the compressor clearance seals which have been calculated from the measured sizes of the pistons and bore. Previous measurements taken at RAL have shown that the measured leakage through clearance seals is often higher than is predicted by theory when assuming that the piston and bore are perfect cylinders with the measured diameters. This is the case even when the piston is considered to be fully eccentric within the bore.

The theoretical leakage can be made to agree with the measured leakage by increasing the clearance seal gap by a scale factor. However, it is unclear what scale factor should be used as the required factor has been found to be different for different seals. Increasing the compressor piston and appendix gap clearances seals of the RAL third-order model by 50% gave good agreement with the measured load line. The results can be seen in the right plot of Figure 5. This scale factor is within the range of factors required to match theoretical seal leakages to measured leakages. The gap of the displacer shaft seal was not increased as this gap was calculated from the measured leakage. The calibrated model has good agreement with the measured cooling power over the entire temperature range. This suggests that increasing the clearance seal gaps is a reasonable way of calibrating the model.

The difference in cooling power between the two models appears to be mostly due to the differences in how the appendix gaps are simulated. The RAL third-order model simulates the appendix gap as tapered because the displacer contracts at the cold end. The Sage model assumes a constant gap which is set to the mean of the tapered gap. The constant gap reduces the effectiveness of the seal and increases the enthalpy transport in the appendix gap.

Two-Stage Cooler Validation

The model has also been validated against data from a two-stage cooler. This breadboard two-stage cooler was built specifically to help validate the model and is shown in Figure 4.

Unlike the Small Scale Cooler, the clearance seal leakage was measured for both the compressor piston and displacer shaft clearance seals. This means that a theoretical gap size could be calculated that would give the correct leakage in the model and a scale factor was not required for these seals. However, the leakage was not measured for the appendix gaps. The size of the appendix gaps was calculated from the measured sizes of the displacer and cold finger tube, accounting for thermal contraction. The displacer was assumed to be fully eccentric in the bore.

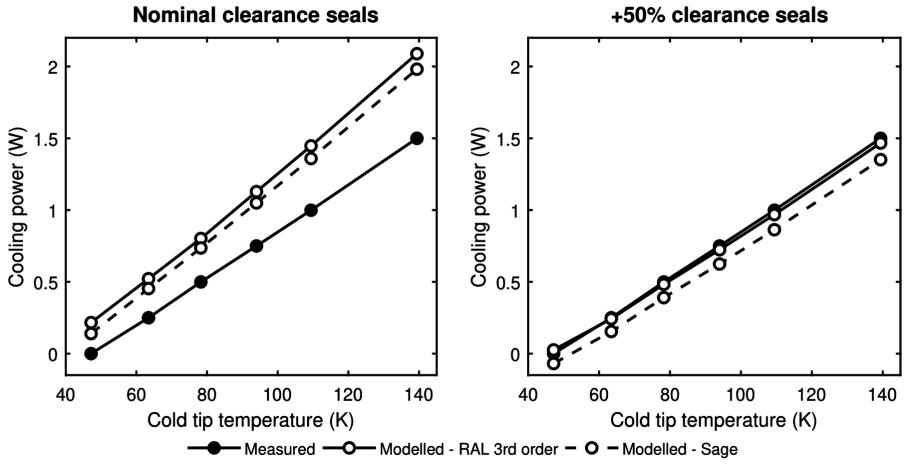

Figure 5. The results of the RAL third-order model and Sage compared to a measured Small Scale Cooler load line. The left plot shows the results of the models with the measured clearance seals. The right plot shows the results of the models with the compressor piston clearance seals and the appendix gap increased by 50%.

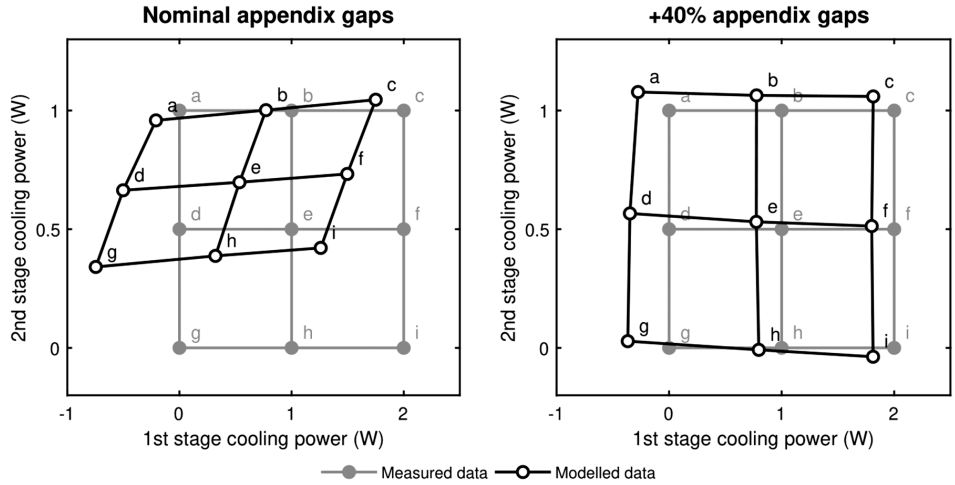

Figure 6. The results of the RAL third-order model when simulating the performance of the breadboard two-stage cooler at a range of temperatures. Each letter correspond to a different case. For example, case "g" has stage temperatures of 59.1 K and 46.4 K for the first and second stages whereas case "c" has stage temperatures of 98.8 K and 99.9 K. The left plot shows the results of the model with the measured appendix gaps and the right plot shows the results of the model with the appendix gaps increased by 40%.

The model was used to replicate a measured load map where different heater powers had been applied to each stage; the measured stage temperatures and compressor and displacer motions were used as inputs into the model. The predicted performance using the measured appendix gaps is shown in the left plot of Figure 6. In addition, a range of clearance seal scale factors for the appendix gaps were investigated, with the same factor being applied to both stages. Increasing the gaps by 40% gave the best agreement and the results are shown in the right plot of Figure 6.

The results show that increasing the size of the appendix gaps greatly improves the accuracy of the model. The larger gaps reduce the modelled cooling power at the second stage because the gas is able to partially bypass the second stage regenerator and transport enthalpy to the cold tip.

Knowing that this calibration factor is required will be invaluable when designing future two-stage coolers. It may result in requiring the displacer to be made from a material with a low coefficient of thermal expansion in order to keep the appendix gap small when the displacer is cold.

MODEL RESULTS

The RAL third-order model works in a similar way to other third-order models in the literature; however, its key feature is that it simulates the entire geometry of the cold finger with cells that interact realistically. These interactions can have a large influence on the modelled performance. Simulating the full geometry allows investigation of aspects of Stirling cooler design that is not possible with other models.

Cold Tip and Displacer Overlap

One aspect of cooler design that can be investigated using the RAL third-order model is how the overlap of the cold tip and the mean displacer position affects the performance. This overlap is shown in Figure 7. Increasing the overlap provides more surface area for the heat transfer to occur which should reduce the temperature difference between the gas and the cold tip. However, it also reduces the length of the cold finger tube, leading to higher thermal conduction. The other key effect is that changing the overlap affects the alignment of the thermal gradients along the displacer and cold finger tube. The shuttle losses are increased if the gradients are not aligned.

Figure 8 shows the effect that changing the overlap would have on the Small Scale Cooler's performance, as predicted by the RAL third-order model. The model predicts that the perfor-

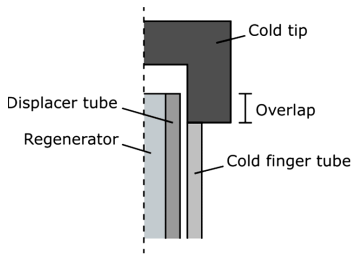

Figure 7. A diagram showing the overlap between the displacer and the cold tip. The overlap is when the displacer is in its mean position.

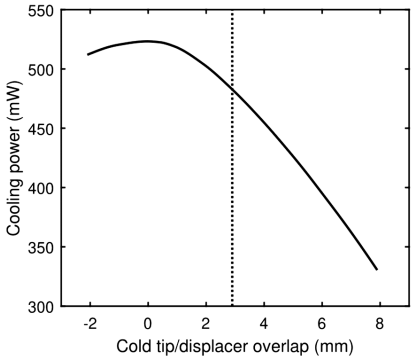

Figure 8. A plot showing the cooling power predicted by the RAL third-order model when the mean cold tip and displacer overlap is adjusted. The other input parameters are taken from the 78 K case of the Small Scale Cooler. The vertical dotted line shows the nominal overlap.

mance can be improved by around 40 mW by reducing the overlap. Making this change aligns the thermal gradients along the cold finger tube and displacer and reduces the shuttle losses.

A similar analysis has been performed at the warm end of the cooler by adjusting the overlap between the cooler body and the warm end of the displacer. It was found that cooling power was not as sensitive to the warm end overlap and the overlap was already near the optimum.

Appendix Gap Geometry

The RAL third-order model is able to simulate coolers where the size of the appendix gap varies along the length of the cold finger. This is often the case for coolers built at RAL; the displacer is typically made from plastic which shrinks more than the metal cold finger tube when cooled, increasing the gap at the cold end. The model was used to investigate the influence a tapered appendix gap has on the Small Scale Cooler's performance.

The results of this investigation are plotted in Figure 9. The tapered gap appears to improve the cooling power at the current gap size by around 90 mW when compared to a constant gap of the same mean size. Because the mean sizes are the same, the shuttle losses should be similar. Therefore, the difference in cooling power is probably due to the reduced seal leakage at the warm end for the tapered gap.

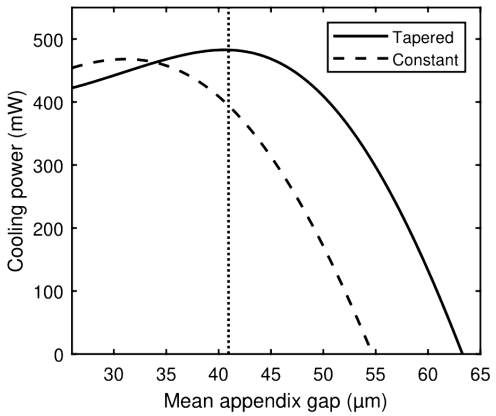

Figure 9. A plot showing how the cooling power predicted by the RAL third-order model is affected by the mean gap size for tapered and constant appendix gaps. The gradient of the tapered gap was fixed and the gap sizes at the warm and cold ends were changed by the same amount. The other input parameters are taken from the 78 K case of the Small Scale Cooler. The vertical dotted line shows the nominal gap size.

CONCLUSION

A new Stirling cryocooler model has been developed that builds on previous models in the literature by simulating the interactions within the entire cold finger. The results of the RAL third-order model are broadly similar to other models in the literature, such as Sage; however, the RAL third-order model is able to investigate aspects of cold finger geometry that are difficult to assess with other models. The results of the model have been validated against performance measurements of coolers taken at RAL. It was found that the model accuracy was improved by using clearance seal gaps that are 40-50% larger than the measured size. This is because the leakage past the seals appears to be greater than is predicted theoretically.

The model will be used to aid the design of future coolers at RAL. Further information about the model will be published in an upcoming PhD thesis.[17]

ACKNOWLEDGEMENT

This work has been funded by the European Research Council under the European Union's Horizon 2020 research and innovation programme (grant agreement: IRIS, no. 648604).

REFERENCES

1. Dyson, R. W., Geng, S. M., Tew, R. C., Adelino, M., "Towards Fully Three-Dimensional Virtual Stirling Convertors For Multi-Physics Analysis and Optimization," *Engineering Applications of Computational Fluid Mechanics*, vol. 2 (2008), pp. 95-118.
2. Urieli, I., *A Computer Simulation of Stirling Cycle Machines*, PhD thesis, University of Witwatersrand (1977).
3. Andersen, S. K., *Numerical Simulation of Cyclic Thermodynamic Processes*, PhD thesis, Technical University of Denmark (2006).
4. Gedeon, D., *Sage User's Guide*, Gedeon Associates, v11 edition (2016).
5. Martini, W. R., *Stirling Engine Design Manual*, United States Department of Energy (1978).
6. Patankar, S., *Numerical Heat Transfer and Fluid Flow*, Taylor & Francis (1980).
7. Lemmon, E.W., Huber, M.L., McLinden, M.O., *NIST Standard Reference Database 23: Reference Fluid Thermodynamic and Transport Properties-REFPROP*, Version 9.1, NIST (2013).
8. Versteeg, H., Malalasekera, W., *An Introduction to Computational Fluid Dynamics: The Finite Volume Method,* 2nd edition, Pearson Education Limited (2007)
9. Courant, R., Friedrichs, K., Lewy, H., "On the Partial Difference Equations of Mathematical Physics," *IBM journal of Research and Development*, vol. 11, issue 2 (1967), pp. 215–234.
10. Shampine, L., Gladwell, I., Thompson, S., *Solving ODEs with MATLAB*, Cambridge University Press (2003).
11. Kühl, H. D., Shulz, S., "Measured Performance of an Experimental Vuilleumier Heat Pump in Comparison to 3rd Order Theory," *Proceedings of the 25th Intersociety Energy Conversion Engineering Conference*, vol. 5 (1990), pp. 436–441.
12. Harvey, J.P., Kirkconnell, C. S., Desai, P. V., "A Fast and Accurate Regenerator Numerical Model," *Cryocoolers 13*, Springer US, Boston, MA (2005), pp. 455–461.
13. Carslaw, H., Jaeger, J., *Conduction of Heat in Solids*, Oxford, Clarendon Press (1959).
14. Sauer, J., Kühl, H. D., Numerical Model for Stirling Cycle Machines Including a Differential Simulation of the Appendix Gap, *Applied Thermal Engineering 111* (2017), pp. 879–833.
15. Gedeon, D., Wood, J. G., *Oscillating-Flow Regenerator Test Rig: Hardware and Theory with Derived Correlations for Screens and Felts*, Tech. rep., Lewis Research Center (1996).
16. Crook, M., Hills, M., Brown, S., Kendall, S., Korswagen, H., Iredale, P., "Small Scale Cooler – Improvements," *Cryocoolers 19*, ICC Press, Boulder CO (2018), pp. 93–101.
17. Rawlings, T., *Numerical Modelling of Stirling Cryocoolers*, PhD thesis, University College London (unpublished).